University of Nottingham
Biodiscovery Institute

BBSRC Doctoral Training Partnerships

New antimicrobial biomaterials based on recombinant spider silks

by Jolanta Beinarovica, BSc

Supervisors: Professor Neil R. Thomas, Professor Sara L. Goodacre

School of Chemistry, Biodiscovery Institute, University Park, University of Nottingham, NG7 2RD

United Kingdom

Thesis submitted to the University of Nottingham

for the degree of Doctor of Philosophy, October 2021

Table of Contents

Abstract

Spider silk is a protein-based material with exceptional mechanical properties together with low immunogenicity and pyrogenicity which makes it useful in biomedical applications. The cannibalistic and highly territorial nature of most spiders prevents high-density farming; therefore, the availability of their silk in a usable form is very limited. Recombinant production of silks is explored as an alternative mean of production. This study uses two miniature recombinant silk proteins (mini-spidroins) with distinct biochemical nature -NT2RepCT and 4RepCT - to create new materials for drug delivery.

A procedure for a column-free, scale up compatible purification of highly water soluble spidroin NT2RepCT has been developed. NT2RepCT was then processed into a colloidal drug delivery system that could be loaded with a model drug and exhibited a pH-dependent controlled drug release profile. It was found that NT2RepCT particles have a polydisperse size range on a micron scale, and that they are unstable in water, which makes them useful for *in situ* and temporary embolic applications.

Further, the 4RepCT^{3Aha} mini-spidroin was expressed and purified. In this construct, each methionine residue is replaced with a synthetic methionine analogue L-azidohomoalanine (Aha) that carries a terminal azide in its side chain. The azide acts as a selectively chemically reactive, bioorthogonal group for bioconjugations using copper-catalysed azide-alkyne cycloaddition (CuAAC) knows as the “click reaction”. Using this methodology, a selection of antimicrobial ligands (triclosan, chloramphenicol, ciprofloxacin, erythromycin, levofloxacin, and nitroxoline) bearing a labile linker with a terminal alkyne were conjugated to 4RepCT^{3Aha}, creating a library of antimicrobial conjugates. The resulting conjugates were processed into films that showed significant antimicrobial activity against the Gram-negative *Escherichia coli* (*E. coli*) and the Gram-positive *Staphylococcus aureus* (*S. aureus*) in a novel plate-based, high throughput-compatible assay. Further, it was found that ‘clickable’ antimicrobial ligands could also be conjugated to pre-formed Aha-bearing silk films. When the antimicrobial ligands were conjugated to pre-formed films, their biocidal activity was lower than that of films made from soluble

4RepCT^{3Aha} -ligand conjugates but the activity was statistically significant compared to films dipped in antibiotic solution.

In addition, the 4RepCT^{3Aha} mini-spidroin was functionalised with quaternary ammonium-based ligands via a non-labile linker prior to processing of the conjugate into a surface coating. In this approach, a cationic, contact-active antimicrobial surface was created that showed significant antimicrobial effect against *E. coli* in a range of conventional microbiological assays. For this material, a tailored high-throughput compatible assay to analyse the metabolic activity and biomass increase of surface-adherent bacteria was developed. In this assay, it was found that quaternary-ammonium bearing ligands have activity against *E. coli*, but not *S. aureus* or *Pseudomonas aeruginosa*.

In conclusion, this work describes a range of new antimicrobial materials based on miniature spider silks that can serve as a drug delivery vehicle in different biomedically relevant scenarios. By combining silk's uniquely biocompatible nature with a tailored functionality and modifiable release kinetics, these novel biomaterials are promising candidates for drug delivery applications.

Acknowledgements

I would like to acknowledge the UKRI BBSRC, the University of Nottingham, and my supervisors Prof Neil R. Thomas and Prof Sara L. Goodacre for the opportunity to work on this exciting and promising research and invaluable guidance throughout the course of my studies.

I would like to sincerely recognise the technical and administrative assistance within the Biodiscovery Institute, Nanoscale and Microscale Research Centre, and the University of Nottingham School of Life Sciences Imaging facility for their help, training, and expertise.

Further thank you goes to the members of NRT and PS research groups, in particular Charlotte Smith, Hannah Betts, Isobel Holden, Dr Rowan Earlam, Dr Tom Armstrong, Dr Alex Holland and Dr Faadil Fawzy, for their practical support and a great sense of camaraderie. This research would not be possible without Dr David Harvey whose hard work in the NRT group led me and other junior researchers by example.

Lastly, I would like to sincerely thank my friends and family - especially Dr David Harvey, Olivia Hillson, Sandra Beinarovica, Elina Uskane - for their love, patience, and profound belief in my abilities.

List of abbreviations

3D – three-dimensional

A. diadematus – *Araneus diadematus*

ADF – *Araneus diadematus* fibroin

AFM – atomic force microscopy

Aha – L-azidohomoalanine

B. subtilis – *Bacillus subtilis*

BSA – bovine serum albumin

cDNA – complementary deoxyribonucleic acid

CFU – colony forming units

CuAAC – copper (I)-catalysed azide-alkyne cycloaddition

DMSO – dimethyl sulfoxide

DNA - deoxyribonucleic acid

E. australis – *Euprosthenops australis*

E. coli – *Escherichia coli*

EDC - 1-ethyl-3-(3-dimethylaminopropyl)carbodiimide

EDTA - ethylenediaminetetraacetic acid

EPM – extracellular polymeric matrix

eSEM – environmental scanning electron microscope

FAM – fluorescein

GA – glutaraldehyde

GC - guanine-cytosine

HAI – hospital acquired infections

HRV – human rhinovirus

IMAC – immobilised metal ion affinity chromatography

IPA – isopropanol

LB – lysogeny broth

Lbl – layer-by-layer

MA – major ampullate

MA – methyl acrylate

MaSp – major ampullate spidroin

MIC -minimum inhibitory concentration

MiSp – minor ampullate spidroin

MMP – matrix metalloprotease

MS – mass spectrometry

MWM – molecular weight marker

NHS - *N*-hydroxysulfosuccinimide

NICE -National Institute for Health & Care Excellence

NMR – nuclear magnetic resonance

OD – optical density

P. aeruginosa – Pseudomonas aeruginosa

P. pastoris – Pichia pastoris

PCR – polymerase chain reaction

PDB – protein data bank

PDDS – polymeric drug delivery system

PEG – polyethylene glycol

PLA – polylactic acid

PLLA – poly(L-lactide)

PDLA – poly(D-lactide)

QAC – quaternary ammonium compound

RFU – relative fluorescence units

RGD – L-arginine, glycine, and L-aspartate integrin-binding peptide sequence

RhB – rhodamine B

RNA – ribonucleic acid

rpm – revolutions per minute

rRNA – ribosomal ribonucleic acid

S. aureus – Staphylococcus aureus

SAAP – synthetic amino acid polymer

SD – standard deviation

SDS - sodium dodecyl sulfate

SDS PAGE – sodium dodecyl sulfate polyacrylamide gel electrophoresis

SEM – scanning electron microscope

SPAAC – strain promoted azide-alkyne cycloaddition

T. clavipes – *Trichonephila clavipes*

$tRNA^{Gly}$ - glycine transfer RNA

TRX – thioredoxin

TSB – tryptic soy broth

TuSp – tubuliform spidroin

UV – ultraviolet light (100-400 nm)

WHO – World Health Organisation

ZOI – zone of inhibition

Naturally occurring amino acid one letter codes (all L isomers except Glycine which is achiral):

Alanine	A	Arginine	R	Asparagine	N
Aspartic acid	D	Cysteine	C	Glutamic acid	E
Glutamine	Q	Glycine	G	Histidine	H
Isoleucine	I	Leucine	L	Lysine	K
Methionine	M	Phenylalanine	F	Proline	P
Serine	S	Threonine	T	Tryptophan	W
Tyrosine	Y	Valine	V		

List of figures

Figure 5.8. *E. coli* NCTC12242 cells stained with propidium iodide and SYTO9 using **A** -594nm (red) and **B**- 488nm (green) laser after 6-hour incubation on glass surfaces coated with 4RepCT^{3Aha} and4RepCT^{3Aha}-QAC (Br). SYTO9 indicates the total cell number as it stains all cells, whereas propidium iodide stains membrane-compromised cells only. A and B are representative images of the same field of vision.

Figure 5.9. Absorbance of **A** – reduced resazurin at 570nm and B -cell turbidity at 600 nm of surface-adherent *E. coli* NCTC12242, *S. aureus* NCTC 6571, and *P. aeruginosa* at 6 hours after the addition of a fresh growth media to a 24-hour biofilm. Absorbance of resazurin at 570 nm indicates cellular metabolism whilst OD600 indicates increase in bacterial biomass.

Figure 5.10. Resazurin (blue) is irreversibly reduced to resorufin (pink) by aerobic respiration of metabolically active cells.

Figure 6.1. Expression of 4RepCT^{3Aha} using methionine depletion protocol. The concentration of methionine is limited so that it can support bacterial biomass growth to the desirable optical density, followed by addition of Aha and IPTG for protein expression.

List of schemes

List of tables

1. General introduction

1.1. Natural spider silk

1.1.1. Overview

Silk is a protein-based fibre spun by arthropods for a range of applications including survival and reproduction. Current evidence shows that silk evolved convergently 23 times in the Insecta class[1] , and at least once each in the Myriapoda, Acari, Pseudoscorpiones, Crustacea, and Aranea[2] . Of these, spiders are one of the most ancient spinners who are uniquely capable of silk production throughout their lifecycle. Spiders spin up to seven types of biochemically distinct silks each composed mainly of one type of protein and secreted by a dedicated silk gland (Fig. 1.1). Most of the research to date has been focused on major ampullate silk (MA) which has become a model for silk property characterisation.

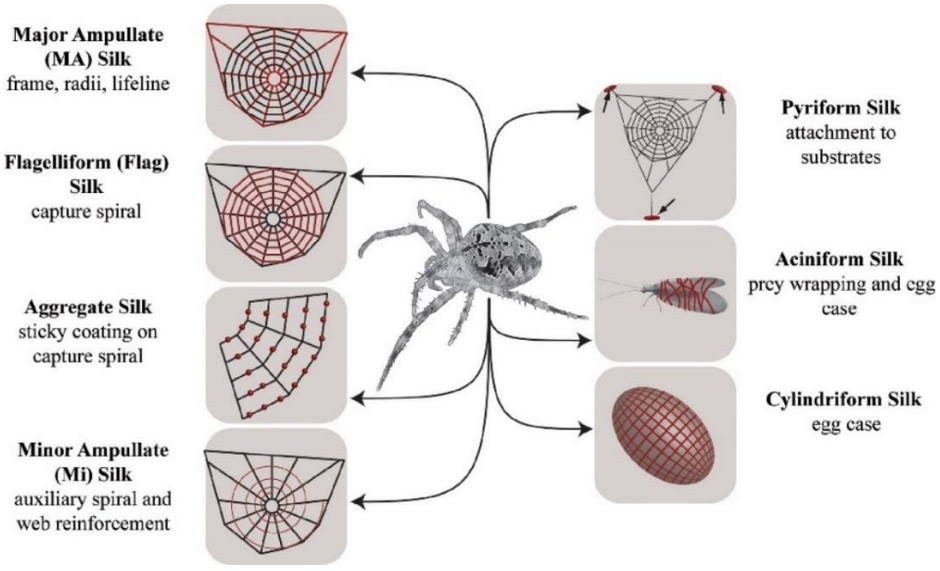

Figure 1.1. Seven types of spider silks and their applications. Reproduced from Eisoldt *et al.*[3].

Spider silk has been used as a wound dressing as early as ancient Greek times[4] . Its mechanical properties have been exploited by processing the webs into fishing nets by the native population of the Solomon Islands (South Pacific); in Malakula (Melanesia, South Pacific), *Trichonephila* silks were

harvested and processed into ritualistic garments, such as hoods and capes[5]. In 2012, artists S Peers and N Godley created a dress made of over three meters of fabric woven from *T. clavipes* silk[6]. These selected examples highlight the appeal and long history of spider silk use in different biomedical and textile applications. It is now known that the combination of silk's mechanical and biological properties is unmatched by materials of natural and synthetic origin.

1.1.2. Spider silk at a protein level

Silk proteins, or spidroins, are large (200-350 kDa)[7,8] proteins composed of repetitive core modules flanked by highly evolutionary conserved, non-repetitive N- and C-terminal domains. Spidroins are grouped into categories based on their unique repetitive amino acid sequences that are called tandem repeats due to their successive arrangement (Table 1.1). The best researched spidroins belong to the major ampullate spidroin family MaSp family and are discussed in more detail below.

Table 1.1. Spidroin tandem repeats based on their type (adapted from Hu *et al.*[9]). Similar motifs are highlighted in identical colours across silk types.

Silk name	**Representative tandem repeat amino acid sequences**
MaSp1	poly(A) blocks >7 residues; GGX; $(GA)_n$
MaSp2	poly(A) blocks >7 residues GGX; $(GA)_n$; GPGXX;
MiSp1	poly(A) blocks (<7 residues); GGX; $(GA)_n$;
MiSp2	poly(A) blocks (<7 residues); GGX; $(GA)_n$; GX spacers
Flag	GGX; $GPGXX_n$; GX spacers
AcSp1	GGX poly(S) blocks;
TuSp1	poly(S) blocks; GX spacers; AAQAASAA; AAAQA; AASQAA; SQ_n

The N-terminal domain of MaSp is known to be responsible for maintaining the solubility of spider silk proteins at high concentrations, and to possesses transport tags that facilitate protein secretion[10]. Different types of silk have 37-63% N-terminal sequence identity and are universally predicted to form a five α-helix bundle (Fig.1.2 A)[10,11]. In addition, the conformation of the N-terminal domain is reported to be salt- and pH-dependent, therefore suggesting that the N-terminal domain contributes to silk

fibre formation and stabilisation in soluble state via non-covalent dimerization[12–15]. There is experimental evidence for N-terminal domain being involved in an asymmetrical dimer formation in *Euprosthenops australis* and *T. clavipes* MaSp1 (Fig.1.2 B).

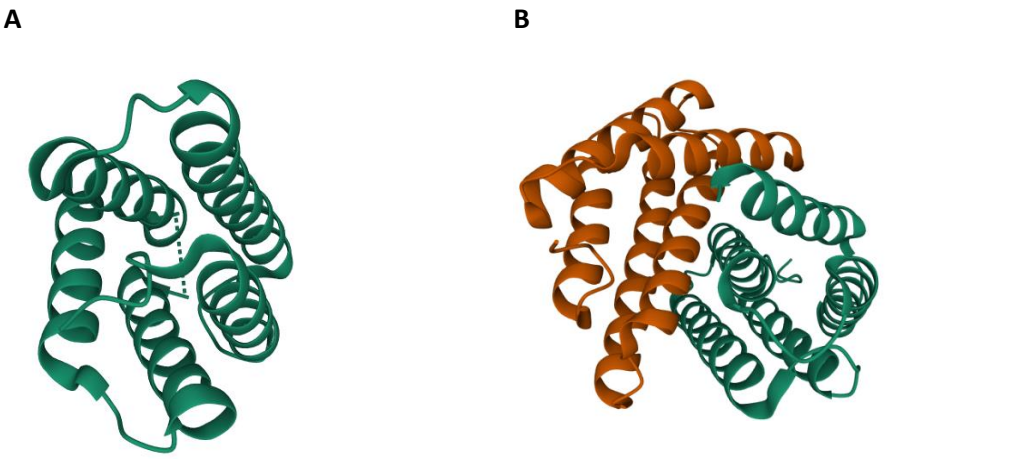

Figure 1.2. N-terminal domain of MaSp1 from *E. australis* **A**: monomer (RSC PBD 4FBS) and **B**: dimer (RCSB PDB 6R9D). Dashed line represents missing diffraction signal.

In MaSp, the central repetitive modules in silk proteins are made of polyalanine repeats (A_n) and glycine-rich motifs such as GGX (X=L, Y, S, A)[16] and GPGXX (X=G, Q, Y, A, S)[17]. Polyalanine repeats are found to form intramolecular β-sheets and crystalline regions that account for fibre formation via hydrogen bonding and hydrophobic forces, therefore contributing to high tensile strength of the silk[16,18]. Glycine-rich modules are thought to assume α-helical structure with 3 residues per turn[19]. These motifs are usually connected with spacer regions whose secondary conformations are yet to be elucidated.

The C-terminal domains of spider silk are found to form 5 α-helices and two antiparallel β-sheets (Fig 1.3 A, B). It has been shown that C-terminal domain plays a critical role in spidroin dimer formation; sometimes via a conserved unique cysteine residue in MaSp although this is not always required [10,20–22].

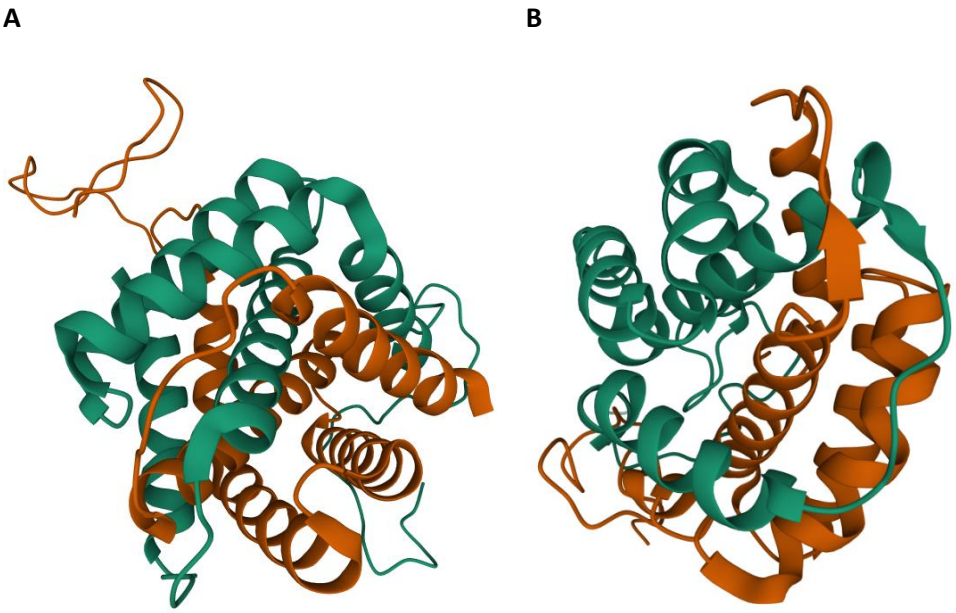

Figure 1.3. C terminal domain dimers of **A**: ADF-3 (*Araneus diadematus*) (RCSB PDB 2KHM); **B**: MiSp1 from *Araneus ventricosus* (RCSB PDB 2MFZ).

1.1.3. Silk spinning

As mentioned previously, each type of spider silk is produced within a dedicated gland located in the abdomen. The glands are divided into three distinct areas: the tail, the sack, and the duct (Fig. 1.4)[23–25].

Spidroins are secreted into the glandular lumen by the epithelial cells in the tail and the proximal and mid-section of the sac to form a highly concentrated (over 30% w/v[26]) solution in water, known as the dope[24] . The dope is acidified in the distal end of the sac and further in the duct by the activity of carbonic anhydrase[27] that catalyses the conversion of carbon dioxide and water into carbonic acid. In the duct, the dope is further acidified via import of PO_4^{3-} ions; active export of Na^+ and Cl^- promotes the dehydration of the dope via osmosis (Fig.1.4A)[28–30]. Import of K^+ ions into the duct promotes nanofibril formation[31] . Finally, the combination of the elongational flow provided by spider pulling the thread and the shear force provided by the decreasing diameter of the duct promotes formation of an insoluble fibre[32]. From there, the fibre exits the abdomen at microscopic orifices at the distal

end of spider's abdomen called spigots; spigots assemble into spinnerets where multiple fibres are combined into a single silk thread.

A

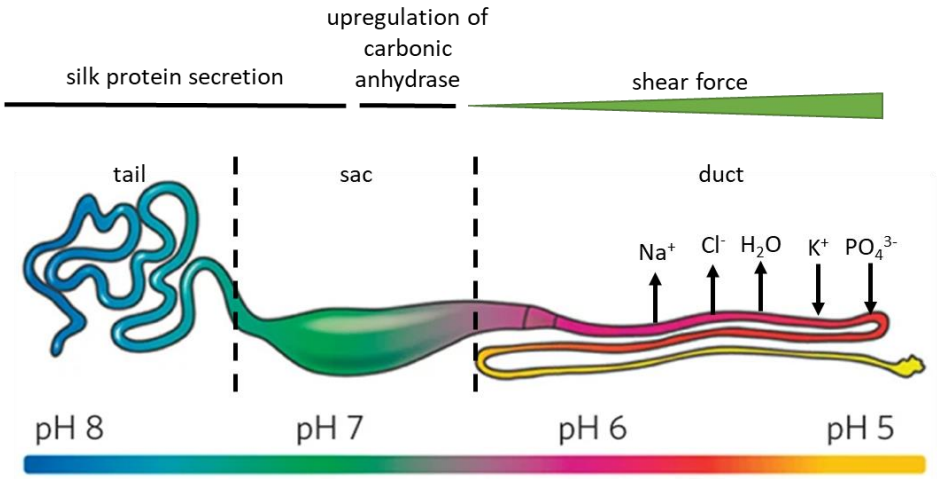

B

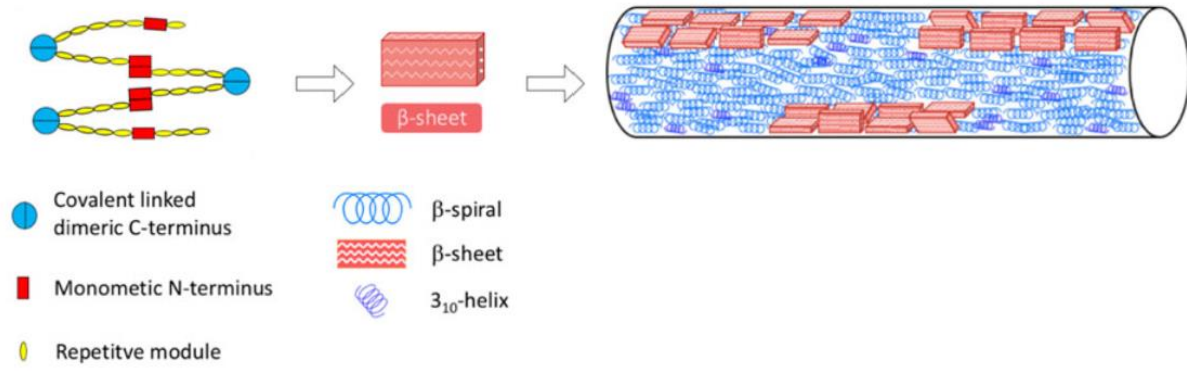

Figure 1.4. Spider silk spinning process. **A**: a schematic of a spider silk gland (adapted from Rising *et al.*[23]); **B**: the structural hierarchy of silk fibre assembly (adapted from Eizoldt *et al.* [3]). .

Current consensus on spider silk fibre formation postulates that C-terminal domains are responsible for initiation of fibre formation. In MaSp, this interaction is mediated via a conserved single cysteine residue that forms an intermolecular disulfide dimer[20,33,34]. Further to this, polymerisation and elongation of a fibre occurs as the intrinsically disordered core domains acquire more ordered β-sheet structure upon shear force (caused by flow), acidification, and dehydration and exposure of hydrophobic residues to the solvent (Fig.1.4B). Increase in the β-sheet content promotes

intermolecular interactions such as van-der-Waals forces and hydrogen bonding[33] . The orientation of the β-sheets is known to be parallel to the fibre axis[35–37].

1.1.4. Mechanical properties of silk

Spider silks have exceptional mechanical characteristics known to be the second toughest (most resistant to breaking after plastic deformation) biopolymer that outperforms most artificial materials, including high-tensile steel, carbon fibre, and Kevlar® [38,39]. Mechanical properties of spider silk are usually described in context of its tensile strength, extensibility, elasticity, and stiffness as expressed by Young's modulus. Below, definitions of each measurement are provided along with some representative examples from natural silk research literature.

Tensile strength is defined as maximum stress that a material can support (when stretched or pulled) before breaking[40]. MaSps range in their tensile strength from 20 MPa in wanderer spiders to 1500 MPa in orb weaver spiders[41]. Malagasy Darwin's bark spider *Caerostris darwini* spins the strongest major ampullate silk so far identified with a tensile strength of 1652 MPa[41].

Extensibility is the ability of a solid material to extend, expressed as a percentage increase compared to the non-extended material or alternatively as extension per unit length (mm/mm)[40]. Extensibility varies dramatically depending on the fibre type, with major ampullate (MA) silk from *T. clavipes* showing 35% extension[42] compared to flagelliform silk from *Araneus diadematus* which is 200% extensible[43].

Finally, Young's modulus is a measure of the ability of the fibre to withstand uniaxial stress, in essence representing the stiffness of the material[40]. Sheet (cobweb) weaving spiders generally have stiffer major ampullate silks with Young's modulus reaching 22.2 GPa in *Kukulancia hibernalis*, compared to 13.8 GPa in *T. clavipes* (orb weaver)[41].

Bioprospecting of natural spider silk samples in search for the most extreme mechanical properties has been a popular research area for decades, however several aspects complicate direct comparison

of silk across studies. Naturally occurring contaminants, spider nutrition and environment, and the conditions of silk spinning have a critical influence on the silk's mechanical properties. For example, artificially reeled *Trichonephila edulis* MA silk was shown to have a decreased breaking elongation (high resistance to the change in shape upon stress) and increased breaking stress (maximum force applied to the material before breaking); in combination with increased Young's modulus (stiffness)[44]. In addition, regenerated silk fibres have significantly poorer mechanical properties than their natural counterparts[45]. Lastly, ambient moisture levels are a critical factor contributing to the variability in the measurements of silk mechanical properties due to supercontraction of the fibre.

1.1.5. Supercontraction

Supercontraction is a phenomenon of spider silk fibre shrinking upon exposure to water[46]. This property has been of great interest in context of biomedical applications due to its self-powered action, such as hydroscopic artificial muscle design[47].

Evidence shows that this unique property is caused by the disruption of hydrogen bonding within the silk's repetitive regions followed by the swelling of the fibre[46,48]. This causes the shrinkage of the fibre (up to 40% decrease in length) subsequently a 1000-fold decrease in the elastic modulus (measure of elastic deformation) which suggests increased stiffness[49].

Due to silk's supercontraction, it is often difficult to directly compare tensile strength and other mechanical properties of the fibres across different studies as the extensibility of silk changes depending on the ambient humidity. It is well documented that humidity modifies mechanical properties of silk, to the extent that air moisture can be used to reproductively tailor the shrinkage or a fibre[46,50–53].

The current research into biomimetic silk fibres suggests that proline and tyrosine residues in the amorphous silk regions are key contributors to supercontraction[47,54]. Some evidence has highlighted that an evolutionarily conserved glutamine motif GPGGX could further contribute to this phenomenon[55]. Silk with higher hydrophobic amino acid content, such as MaSp2 from *E. australis* that

has a relatively high phenylalanine content, supercontracts less than other silks. This is likely to be due to its nonpolar nature which prevents water penetration into the fibre[56,57].

1.1.5. Biocompatibility and immunogenicity of natural spider silks

Natural spider silk is known for its biocompatible and non-immunogenic nature[58], however this property has been show to depend both on silk type and the way the material is processed. Studies have shown that *T. clavipes* MA silk meshes for hernia repair in rat model showed less fluid buildup (seroma) than synthetic meshes made of polypropylene, and only a mild immune response was observed via giant cell accumulation that facilitated material biodegradation within 4 weeks post-implantation[59]. The resorption of the silk mesh was followed by formation of a collagenous scar with a constant tensile strength suggesting a healthy healing process[59]. In contrast to MA silk, egg case silk from *A. diadematus* showed severe immune response in rats, including increased leukocyte infiltration over seven weeks and fibrosis after week 1 post implantation[60]. This reaction was reduced by treating the egg case sac silk with mild proteinase treatment, although the immunogenic motif in this silk type remains undefined[60]. Further, this study showed giant cell infiltration and their involvement in the clearance of the implanted material, which is in agreement with other histological studies. When used as a sciatic nerve graft in rats, MA silk from *T. clavipes s*howed good support of axonal outgrowth and Schwann cell migration with no evidence of an adverse immune response histologically[61,62]. *Trichonephila edulis* MA silk conduit for sheep nerve regeneration showed a temporary immunogenic reaction combined with axonal regeneration and giant cell mediated degradation within 90 days[63].

Blood compatibility and cytotoxicity study by Kuhbier *et al.* [64] has shown that silks are not haemolytic to human erythrocytes but mildly cytotoxic to epithelial cells; the authors concluded that his could be specific to *Trichonephila* silks as their yellow colour components (beta carotenes) leeched into the buffer and could have detrimental effects to cells *in vitro* as they are known chemical modulators of cell viability. Nevertheless, another study from these authors using same type of silk found no adverse

immune responses to the material whilst observing that the silk materials promoted neoangiogenesis and wound healing in sheep model[65].

A major drawback of these studies is a failure to examine the immunogenicity burden of fibre's non-silk components, such as exogenous DNA or lipopolysaccharide contamination post-sterilisation: in this way, it remains unclear whether any immune response that has been mounted is a response to the silk itself or to the contaminants.

1.1.6. Antimicrobial activity of spider silk

In addition to the exceptional range of mechanical properties, biocompatibility, and proteolytic degradation profile, spider silk has been found to have native antimicrobial activity. Studies have shown that *Tegenaria domestica* web silk inhibits the growth of the Gram positive bacteria, *Bacillus subtilis*; this growth-limiting, or bacteriostatic effect was eliminated upon treatment of the silk with proteolytic enzymes which suggests that the bacteriostatic element in the web is a protein[66,67]. Similarly, *Pholcus* spider silk showed antimicrobial activity against food-borne Gram-positive *Listeria monocytogenes* but not Gram-negative *E. coli*[68]. Recent evidence suggests that some spiders coat their webs in venom[69], and this venom could be the factor contributing to the antimicrobial effect seen in these studies as most venoms have broad spectrum antimicrobial effects[70]. Given that all spider venoms are peptides, it would be consistent with previous observations that the antimicrobial effect is eliminated when silk is treated with proteases. Other researchers hypothesise that the bacteriostatic effect is caused by inability of bacteria to digest spider silk which therefore limits their growth[71].

1.1.7. Summary

To conclude, naturally occurring spider silk is a phenomenal biomaterial with exceptional mechanical and biological properties that make silk an excellent candidate for biomedical applications.

Despite this range of highly sought after characteristics, spider silk use in textile and biomedical industries is rare due to the scarcity and heterogenicity of the material supply. Unlike silkworms, most

web-spinning spiders are highly territorial and cannibalistic which prevents their high-density farmng. Silk extraction is not only a time consuming and labour intensive process, but as described previously, artificial silk extraction from the spider and reconstitution of fibres yields a material with poorer mechanical properties. Additionally, biomedical applications require more tailored and customisable functionality, as well as morphological diversity of the material

In order to address these issues, an range of synthetic biology approaches have been developed for recombinant spider silk production for processing into different morphologies and imbue them with desirable properties.

1.2. Recombinant spider silks

1.2.1. Rationale for recombinant production of spider silk

Recombinant protein production is a way to ensure the development of more controlled and consistent process with capability to produce an industrially relevant spider silk supply. Silk genes are being studied using a plethora of genomic and transcriptomic approaches that in combination with established synthetic biology advances have enabled researchers to produce silk up to a gram-scale in the lab without the need for spider farming. To that end, new silk-based proteins with novel characteristics can be designed, such as miniature silks, interspecies and inter-silk type hybrid spidroins, silk fusions with biologically active motifs, as well as incorporation of unnatural amino acids and posttranslational functionalisation of silks via bioconjugation.

In addition to freedom of intelligent protein design, recombinant production has the capability of supplying the researchers with soluble silk protein (similarly to silk dope in the gland). Access to soluble protein allows researchers to process silk into different morphologies not limited to fibres, such as particles, films, and gels, making the material more versatile and applicable in a wider range of biomedical scenarios.

1.2.2. History of recombinant silk production

The first partial MaSp1 cDNA sequences were obtained in 1990[16] and expressed in *E. coli* as 14-58 kDa proteins[72,73]. Since then, a range of hosts has been used for recombinant silk production from single cell organisms to plants and higher animals. The heterologous hosts for silk production are reviewed in Table 1.2.Whilst great advances have been made to support heterologous production, some limitations remain. For example, the extremely high GC content in spider silk genes makes them difficult to manipulate using standard molecular biology techniques such as PCR. Additionally, some eukaryotic hosts are inherently prone to truncate proteins at C-terminal end suggesting that the protein expression machinery terminates prematurely[74],or produce shorter proteins with an intact C-terminal tag suggesting gene rearrangement and deletions in central repetitive regions[75,76].

Table 1.2. Spider silk expression hosts, their advantages, and disadvantages. Adapted from Whitall *et al.*[77].

Host	Advantages	Disadvantages	Ref
Spiders	• Ability to synthesise full size silks due to naturally evolved cellular machinery and larger tRNA pools for sustained full-length protein expression • Spinning apparatus adds to the mechanical properties of a fibre	• Unfeasible to farm due to cannibalistic nature • Mechanical properties of forcibly drawn (too quickly) fibres do not compare to naturally occurring silks • Require harsh solvents to re-solubilise • Produces only fibres (no access to soluble protein) • Little functionality • No commercially available vectors for transfection with heterologous silk genes	[78,79]
Transgenic goats	• Scalable • Uses milk secretion-specific vector • High yields of rMaSp2 (low yields of rMaSp1) • Comparable mechanical properties to other recombinant silks of similar, or greater size	• 65kDa – much smaller than naturally occurring silks • Insoluble in aqueous solution after purification, HFIP used to dissolve which diminishes physical properties of a reconstituted fibre and is cytotoxic; for water solubility, heat and pressure is required that diminishes physical properties due to degradation • Milk is a very complex protein mixture – preparation requires filtration, fat separation, and precipitation • Long development times (18 months until first lactation) • Controversial use of a mammal from ethics standpoint	[80–82]
Transgenic mice	• A proof of principle that mammals can express recombinant spidroins	• Immature expression termination is a concern (three different protein size species observed whilst mRNA is the same size) • Unfeasible to scale up	[74]
Sheep embryos	• Very highly scalable host transfected with a silk gene under hair follicle specific promoter control	• Small size of the silk construct (approximately 500 amino acids) • Viability of the embryo unknown	[83]

Table 1.2 (*continued*). Spider silk expression hosts, their advantages, and disadvantages.

Host	Advantages	Disadvantages	Ref
Transgenic silkworms	• Equipped to sustain repetitive protein expression • Easily scalable • Ability to add additional alanine blocks to further improve mechanical properties	• If fused with *B mori* silk domans: inferior mechanical properties compared to spider silk • Fibres spun by silkworm are in average 2x larger in diameter but have ½ physical properties of naturally occurring silk • Chimeric proteins are closely associated with sericin which is difficult to remove; silk-sericin complex is highly immunogenic • Some studies report comparable mechanical properties to natural spider silk but do not address yields or sericin issue	[84–88]
Higher plants (tobacco, potato, soybean, *Arabidopsis*)	• Scalable • Up to 200 kDa protein • In seed endoplasmic reticulum yields up to 15% total protein	• Truncated species very common suggesting that plant expression machinery is not equipped to sustain repetitive protein expression • Extensive downstream processing • Low overall yields • Uses agricultural land	[76,89–92]
Cultured spider silk glands	• Full sized protein • Sustained expression in basic culture medium	• Survival only up to 5hrs • Gland excision and tissue culture require extensive training and cost	[7,93,94]
Mammalian cell line (MAC-T and DHK)	• Protein size up to 140kDa • Physical properties close to natural fibres	• Very high cost of culture, unfeasible to scale up for materials applications	[95]

Table 1.2 (*continued*). Spider silk expression hosts, their advantages, and disadvantages.

Host	Advantages	Disadvantages	Ref
Insect cell lines	• Silk forms fibres *in cellulo* • Viral expression vector – much faster transformation compared to traditional homologous recombination • Equipped to deal with increased tRNA demand • Expression levels at 1.3% wet weight	• Only studied using miniature spidroin • Cell culture maintenance is expensive, scale up options not investigated	[86,96,97]
Leishmania tarentolae	• Very rapid growth rate • Low cost of culture • Known to secrete large proteins • Unable to infect humans	• Miniature spidroin (N- and C-terminal domains and eight repeats approx. 84 kDa) • No known commercially available vectors	[98]
Yeast (*Pichia pastoris*)	• Constructs are stable 100x generation times • Well characterised extracellular secretion pathways that avoid the need for cell lysis	• Truncated species (intracellular expression) • Poorly researched despite potential scalability	[75]
Salmonella	• Well-researched secretion system with chaperones • 0.7-14mg/L yields of relatively pure protein	• *Salmonella* is a known human pathogen • Only up to 14% expressed protein in secreted but can be resolved by further optimisation	[99]
E. coli	• Best-researched genetics, abundance of expression vectors and auxotrophs available • Easily scalable, cheap to maintain • Most common expression system for various size constructs • Well-researched solubility tagging system • Size up to 556 kDa reported (expression supporting host's tRNA pool and using protein self-splicing ligation sequences)	• Yields and size estimations of the largest reported recombinant proteins inconclusive. • Plasmid instability • Truncations • Insolubility	[100,32]

In spiders, sustained continuous production of these alanine- and glycine-rich proteins is facilitated by additional tissue-specific tRNA expression[94]. This finding inspired host strain engineering approach where co-expression of additional $tRNA^{Gly}$ and silk genes in *E.coli* resulted in production of some of the largest recombinant silks to the date (up to 284.9 kDa), and mechanical properties of such silks are comparable to the natural counterparts [100]. Further, by using $tRNA^{Gly}$ supplemented *E. coli* strain and a gene construct that includes split interin ligation signals, silks up to 556 kDa have been produced[101]. The estimation of the protein size in these studies is carried out using gel-based protein analyses that lack resolution (especially for large molecular weight proteins), therefore the precise size of the recombinantly produced silk remains debatable and mostly calculated from the gene size as opposed to the size of the protein.

Currently, some miniature recombinant proteins include a solubility tag, or a terminal domain known to promote solubility (such as the N-terminal domain), for example miniature spidroin NT2RepCT (Fig. 1.5) that is considered to be one of the highest yielding (>250 mg/L shake flask culture[102]) miniature silk constructs used in research (Chapter 2-3). Similarly, a miniature spidroin composed of 1-4 repeats of aciniform spidroin flanked by N- and C-terminal domains from MiSp (*A. ventricosus*) reports comparable yields to NT2RepCT[103]. Both proteins share presence of an N-terminal domain and a MiSp C-terminal domain; it is possible that these ordered structures play a key role in maintaining silk in the soluble state in a heterologous host.

MGHHHHHHMSHTTPWTNPGLAENFMNSFMQGLSSMPGFTASQLDDMSTIAQSMVQSIQSLAAQGRTSPN
KLQALNMAFASSMAEIAASEEGGGSLSTKTSSIASAMSNAFLQTTGVVNQPFINEITQLVSMFAQAGMNDVSA
GNSGRGQGGYGQGSGGNAAAAAAAAAAAAAAAGQGGQGGYGRQSQGAGSAAAAAAAAAAAAAAGSGQ
GGYGGQGQGGYGQSGNSVTSGGYGYGTSAAAGAGVAAGSYAGAVNRLSSAEAASRVSSNIAAIASGGASALP
SVISNIYSGVVASGVSSNEALIQALLELLSALVHVLSSASIGNVSSVGVDSTLNVVQDSVGQYVG

Figure 1.5. Amino acid sequence of NT2RepCT spidroin. Red: 6xHis tag; orange: N-terminal domain from E. australis MaSp1; green: two repeats from *E. australis* MaSp1 repetitive region. Blue: C-terminal domain from *Araneus ventricosus* MiSp1.

1.2.3. Recombinant spider silk morphologies

Naturally occurring silks are known to form only fibre and glue-like structures. In contrast, recombinant silks are reported to display various morphologies reviewed in Figure 1.6 and discussed below.

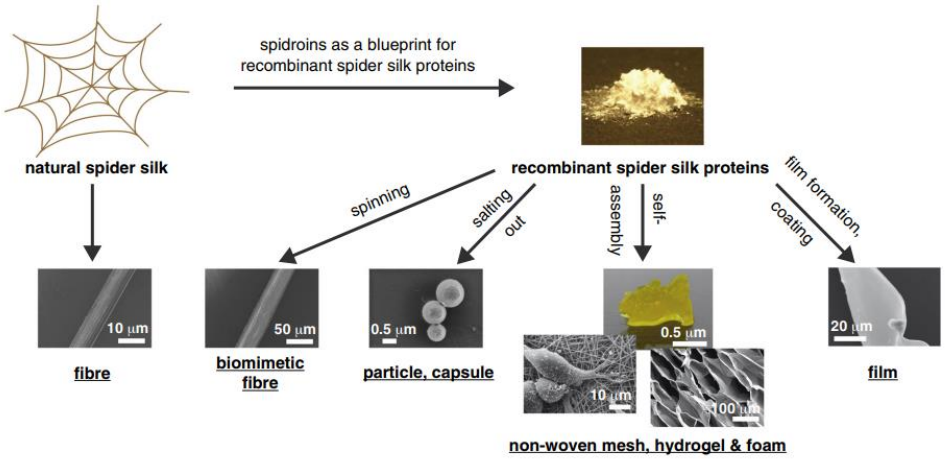

Figure 1.6. Morphologies of naturally occurring and recombinant spider silk proteins. Reproduced from [104].

Fibres

Spontaneous intracellular fibre assembly in a heterologous host has been seen upon silk expression in mammalian cell line[96]. Further, recombinantly produced spidroin 4RepCT produces fibres upon cleavage of a solubility tag (thioredoxin) when shear force is applied (gentle agitation)[105,106]. A pH-sensitive recombinant spidroin NT2RepCT was shown to form fibres upon acidification when shear force (flow) was applied[102]. Lastly, an oscillating expansion/compression-based system with air-liquid interface (a syringe mechanism) has been used to process 4RepCT silk protein derivative into fibres without chemical coagulants[107].

Various coagulation bath extrusion-based approaches have been developed using organic solvents or salts to promote fibre formation. Recombinant egg sac silk protein in $ZnCl_2$ (100 mM) and $FeCl_2$ (1 mM) coagulation bath produced a fibre with 50% higher Young's modulus and 30% higher tenacity (ultimate breaking force of the fibre per denier, a measure of strength) and decreased breaking compared to a

natural egg sac silk which suggests formation of a stronger yet stiffer fibre[108]. Isopropanol-based coagulation baths were shown to produce TuSp1 fibres with tensile strength of 158.6 MPa (twofold decrease compared to naturally occurring force-spun tubuliform silk, around 376 MPa[109]) and 3-5 fold decrease in breaking stress compared to reconstituted egg case silk combined with extensibility up to 35%[110]. Methanol-water coagulation bath produced fibres with lower tenacity than natural dragline silk and similar tenacity to regenerated dragline silk fibres[95] . Methanol bath-coagulated recombinant ADF4 silk with molecular weight of 240 kDa showed tenacity comparable to that of a natural dragline silk. To that end, it is hypothesised that the molecular weight of the monomer is the key contributor to the exceptional mechanical properties of a silk fibre as the largest mini-spidroins assemble into strongest fibres[111]. However, other studies report that even miniature silks can be spun into fibres with tensile strength comparable with their natural counterparts. Study by Hu *et al.*[112] using acidic coagulation baths (17.5mM acetic acid at pH 5.0) report that silks with 16 repetitive domains (up to 70 kDa) can be processed into fibres with tensile strength similar to that of *T. clavipes* MA silk.

Recombinant spidroins have been processed into fibres using electrospinning to create non-woven meshes and coatings, however the mechanical properties of individual electrospun fibres are not commonly assessed, possibly due to the fact that the fibres stick to each other upon a contact with the spinning collector[113]. Nevertheless, such materials are very useful for various biomaterials, such as meshes, scaffolds, and sponges, and highly favoured due to their scalable and reproducible production process[113–116].

Finally, to ensure greater control over flow conditions and by extension, the shear force applied to the material, many microfluidics-based devices have been developed that mimic the flow and ion exchange that occurs in the gland (reviewed in [117]). Addition of oil to the mobile phase of microfluidics device helps to reduce the adhesion of the newly forming fibre to the device whilst providing an interface for fibre formation[118].

Films and coatings

Another unique property of silk is to assemble into continuously accumulating films[12,119]. This assembly can be spontaneous, as in case of 4RepCT[12], or promoted via addition of phosphate salts (ADF-4)[120]. The ability of silk to form films without the need for base surface modification is of great interest in the context of surface functionalisation which will be discussed in depth in Section 1.3 and Chapters 4 and 5. In addition, materials coated with spider silk show better immunocompatibility than base materials alone, such as silicone (See Section 1.2.3).

In addition to continuous accumulation which implies that film thickness can be modified by increasing coating time, properties of a film such as stretchability, transparency, thickness are tuneable. Alcohols and acids have been found to increase β-sheet content of the silk's repetitive domains which promotes supramolecular silk structures[121,122]. However, very high β-sheet content results in a brittle biomaterial; in this context, water acts as a plasticiser whereas an alcohol increases stiffness of the material[122] . To that end, film properties can be finely tuned which is very useful for biomedical applications such as wound healing.

Interestingly, the stability of the film in water prior to treatment with any other chemicals seems to depend on the design of the spidroin: films of spidroins that include N-terminal domain are more prone to resolubilisation in water[123,124], whereas films of 4RepCT that lacks an N-terminal domain do not resolubilise[12].

Notably, silk film and coating surface topographies can be modified using various nano- and micro-patterning approaches, such as dry etching, microcontact moulding, and lithography[125,126]. However, due to specificity of the processing conditions compared to film casting using innate continuous assembly, these emerging methodologies are beyond the scope of this review.

Hydrogels

Hydrogels are three-dimensional porous polymer networks that are extensively swollen with water. These structures are of great interest for cell culture and tissue engineering as 3D cell scaffolds. Spider silk is known to form hydrogels in a manner which involves entanglement of β-sheet-rich nanofibrils induced by addition of alcohol[28], a phosphate salt[127,128], or in a concentration dependent manner[127,129] , or in response to temperatures below 3°C (likely due to water crystal formation) or over 60°C (heat denaturation)[128,130]. Formed hydrogels can be stabilised by other interactions, such as chemical crosslinking[131,132].

Some silk hydrogels, including NT2RepCT, show shear thinning which makes them uniquely applicable for injectable applications [127,132,133]. In addition, NT2RepCT hydrogels were found to form in response to mechanical stimuli such as vortexing and sonication, as well as in ambient conditions at physiologically relevant temperature (37°C)[132,134]. Recent evidence shows that silk hydrogels can be formed in presence of organic solvents, thus not only increasing the β-sheet content that contributes to gel stability, but also aiding encapsulation of highly hydrophobic drugs[135].

Particles

Protein particles are a useful biomaterial morphology for various drug delivery applications. Recombinant silks have been processed into spheres ranging from 250 nm to 3 µm, and their size can be tailored by changing the concentration of protein, concentration of salt, as well as the mixing speed[136]. Spidroin aggregation into particles can be promoted by high concentrations of potassium phosphate[137–139] , sometimes with addition of ionic liquids[136,140,141]. The rationale for using high salt concentrations is to induce β-sheet formation in silk's repetitive domains. Particles are believed to have a higher β-sheet content compared to films, and therefore are thought to be insoluble in water without the need for any further stabilising treatment[139]. Some evidence shows that the method for used for protein purification can influence the properties of the particles, possibly due to β-sheet content within the soluble protein[142].

1.2.3. Biocompatibility of recombinant silk materials

Recombinant spider silk materials have similarly low immunogenicity and pyrogenicity as their natural counterparts. Soluble silk proteins[143], fibres[144–146], films and porous scaffolds[147,148] are known to cause only mild immune responses. The biomolecular reason for low silk immunogenicity remains unknown. Other proteins that are evolutionarily unrelated to silk are known to contain polyalanine repeats, and such proteins often manage to avoid mammalian immune responses. A few additional examples of this phenomenon are EBNA1 protein from Epstein-Barr virus that is overexpressed in virtually all B-cell lymphomas[149], as well as amyloid fibrils now known to contribute to a range of neurodegenerative diseases such as Huntington's disease[150].

The degradation profile of recombinant spider silk materials is thought to depend on the size of the spidroin monomer[151] and degree of material crosslinking[152] . Human matrix metalloprotease 2 and neutrophil elastase were able to digest eADF4(C16) films *in vitro*[152]. *In vivo* degradation of silk based materials was significantly slower than that observed in *in vitro* studies, partially due to lower proteolytic enzyme concentration in physiological environment; further to this, modelling showed that silk material stability *in vivo* is promoted by the inaccessibility of repetitive domains to the solvent and thus to the proteases[151].

1.3. Functionalisation of spider silks and their applications

Recombinantly produced silks can be tailored to a specific application; such modifications are done by passive loading, genetic engineering or applying chemical conjugation techniques. Currently, functionalised silks are researched to create surfaces for cell culture and tissue engineering; deliver drugs, vaccines, DNA; and to create antimicrobial surfaces.

1.3.1. Loading

The simplest strategy for functionalisation of silk material is their loading with a functional molecule. In this approach, the active component is absorbed or encapsulated within the structure using

electrostatic or hydrophobic interactions, and then diffuses down its concentration gradient to display the therapeutic activity.

Recombinant ADF4(C16) particles have been loaded with a range of small molecule drugs[153] and larger biopolymers such as lysozyme[127,154]. The loading likely occurs via electrostatic interactions between negatively charged silk and a positively charged cargo. These studies have found that model drug release from silk particles is inversely correlated to the pH of the release environment in the pH range 2.0-7.4; there was no difference in drug release from ADF4(C16) particles at pH 7.4 and pH 8. Further research using ADF4-based spidroins found that the release of a model molecule fluorescein is salt-dependant: accumulated fluorescein release from ADF4(C16) at 120 minutes was higher at 100-200mM NaCl or KCl compared to 20mM Tris pH 7.2 or 100 mM sodium acetate[155]. Similarly, uptake and release of the highly water soluble model drug rhodamine B from silk particles was found to be dependent on salt concentration and to a lesser extent, the degree of particle crosslinking[156]. This further supports the current agreement that drug loading to silk occurs via electrostatic and hydrophobic interactions. In another study, doxorubicin-loaded silk particles were taken up by mammalian cells in culture and released the drug in response to low pH and proteolytic enzymes present in the lysosomal microenvironment[157].

Silk based hydrogels are another morphology often used for drug loading due to its hydrophilic nature. Model proteins such as lysozyme (16.2 kDa, pI 9.36), bovine serum albumin (69.2 kDa, pI 5.82), and horseradish peroxidase (32.3 kDa, pI 6.10) have been loaded into eADF4(C16) (47.7 kDa, pI 3.13) hydrogels at pH 7.5. The results showed that the silk forms a gel when pre-mixed with cargo, or alternatively the cargo can be adsorbed into pre-made hydrogel[158]. The interaction of silk and cargo is likely an electrostatic interaction in combination with hydrophobic interactions. Diffusion studies showed that lysozyme release profile was notably slower compared to that of other proteins, likely due to electrostatic interactions between positively charged lysozyme and negatively charged silk. Fluorescein and a cytostatic drug 6-mercaptopurine have been loaded into ADF4 based spidroin

hydrogel supplemented with DMSO, and both molecules release kinetics showed 40% total release occurring within 375 minutes in 10 mM Tris pH 7.5 buffer[135].

1.3.2.Genetic approach

Genetic functionalisation of silk involves changing its gene sequence to incorporate additional amino acids, peptide fragments, or other proteins. The non-silk proteins are often added to silk protein as N- or C-terminal fusions, but attempts to engineer functionality within silk's repetitive region is known to interfere with material's mechanical properties[159]. Proteins that would not be naturally expressed as a single amino acid chain are called chimeras or fusions; a comprehensive overview of studies using chimeric spider silk with biologically active domains is presented in Table 1.3. Below, antimicrobial silk chimeras are discussed in more detail.

Silk has been fused to antimicrobial peptides such as human neutrophil defensins at its C-terminal domain[160]. Antimicrobial activity of these chimeras was not concentration-dependent, possibly due to aggregation of silk at higher concentrations. Due to the fact that antimicrobial peptide is not released from the silk, the effects were modest; additionally, mammalian cell cytotoxicity was observed for one of engineered chimeras. Silk and silk-silver binding protein fusions have been shown to direct the formation of silver nanoparticles from silver nitrate solution[161]. These particles leach silver ions known to have antimicrobial activity[162]. When tested by radial diffusion assay (also known as zone of inhibition study or ZOI), such silk films showed small zones of inhibition, however the growth of *E.coli* and *S.aureus* was significantly inhibited in a shaking liquid culture in the presence of silk treated films. Interestingly, in this study untreated silk also exhibited a marginal inhibition of culture growth.

Recently, sortase-mediated protein ligation has been used to attach biofilm-dispersing and antimicrobial proteins to silk scaffold[163]. Sortase-ligated fusions of 4RepCT to dispersin B and SAL-1 endolysin showed excellent antimicrobial and anti-biofilm activity in customised enzyme assay models and against *S. aureus*. Whilst this establishes a novel, more streamlined and highly promising platform

for chimeric protein development, recombinant sortase enzymatic activity is notoriously low[164] and would require further optimisation if this material is to be produced on a larger scale .

Whilst this approach of silk functionalisation is very appealing due to its controllable and reproducible nature of production (as the genetic code dictates the exact composition of the functional chimera), there are inherent limitations of toxic protein production in a recombinant host. During expression of a toxic protein in a bacterial host, the heterologous host cell death increases resulting in very low yields of the final product, as well as truncations and plasmid loss.

Table 1.3. Recombinant silk proteins functionalised via genetic approach.

Modification	Silk type	Added functionality	Findings and comments	Ref
Replacement of glutamic acid residues to lysines	ADF4(C16) from *A. diadematus* expressed in *E. coli*	Positive overall charge	Supported growth of cardiomyocytes, fibroblasts, smooth muscle, and epithelial cells *in vitro*.	[165]
Incorporation of 15-45 lysines at the C-terminus	Hexamer derived from *T. clavipes* expressed in *E. coli*	Cationic domain	Cationic domains bound exogenous DNA. Silk was processed into a film and showed to deliver DNA to mammalian cells for transfection. Silk with 45 C-terminal lysines showed significant cytotoxicity.	[166]
Incorporation of C-terminal lysine and C- and N-terminal RGD repeats	Hexamer derived from *T. clavipes* expressed in *E. coli*	Strongly positive overall charge	Cationic nature of the silk bound exogenous DNA and delivered it to mammalian cells for transfection. Silk without RGD did not increase transfection efficiency (as opposed to . Silk with 11 RGD repeats showed highest transfection but reduced cell viability.	[167]
N- or C-terminal fusion to Tat-peptide	eADF4(κ16) from *A. diadematus* expressed in *E. coli*	Positive overall charge Cell-penetration domain	Silk was processed into spheres with diameter 239-393 nm. Particles up to 200 nm showed good permeability into mammalian cells, as well as low cytotoxicity.	[141]
C-terminal fusion to RGR motif	eADF4(κ16) from *A. diadematus* expressed in *E. coli*	Positive overall charge Cell-adhesion domain	Attachment, survival, and contractility of cultured myocytes (not significantly different from Matrigel)	[168]
N-terminal fusions with RGD, IKVAV and YIGSR	4RepCT from *E. australis* expressed in *E. coli*	Positive overall charge Cell adhesion motif	Functionalised silk supported adhesion and proliferation of fibroblasts, keratinocytes, endothelial cells, Schwann cells *in vitro*	[169]

Table 1.3 (*continued*). Recombinant silk proteins functionalised via genetic approach.

Modification	Silk type	Added functionality	Findings and comments	Ref
N-terminal fusion with fibronectin	4RepCT from *E. australis* expressed in *E. coli*	Cell adhesion motifs	Foam supported expansion of non-differentiated 3D culture of human pluripotent stem cells when supplemented with recombinant laminin and further differentiation into neuronal cell progenitors upon induction signal	[170]
N-terminal fusion with fibronectin	4RepCT from *E. australis* expressed in *E. coli*	Cell adhesion motif	Scaffold supported 3D co-culture of fibroblasts, endothelial and smooth muscle cells (blood vessel model)	[107,171]
N-terminal fusion with fibronectin	4RepCT from *E. australis* expressed in *E. coli*	Cell adhesion motif	Coatings supported pancreatic islet cell growth in vitro	[172]
N-terminal fusion with fibronectin	4RepCT from *E. australis* expressed in *E. coli*	Cell adhesion motif	Silk-coated dressing showed accelerated burn wound healing and better tissue remodelling activity compared to commercial PU dressing in rats	[173]
N terminal fusion with fibronectin and N terminal fusion with lactoferricin fragment	4RepCT from *E. australis* expressed in *E. coli*	Cell adhesion motif Antimicrobial peptide	Silk-coated nanofibrous mat (composed of silkworm silk) showed better re-epithelisation and tissue remodelling in a diabetic wound model in rabbit	[174]
RGD incorporation in repetitive domains	4RepCT from *E. australis* expressed in *E. coli*	Cell adhesion motif	Coating supported pancreatic cell mobility and cluster formation *in vitro*	[175]
C-terminal fusion to fibronectin	Hexamer derived from *T. clavipes* expressed in *E. coli*	Cell adhesion motif	Coatings showed a moderate increase in fibroblast proliferation. Better results obtained when silk-fibronectin was blended with silk-elastin-like protein.	[176]
RGD incorporation into the repetitive domains	15-mer derived from *T. clavipes* expressed in *E. coli*	Cell adhesion motif	Non-functionalised silk promoted differentiation of stem cells into osteoblasts. Functionalised silk did not have any beneficial effect on cell adhesion or proliferation, possibly due to inaccessibility of the RGD sites in the electrospun fibres.	[159]

Table 1.3 (*continued*). Recombinant silk proteins functionalised via genetic approach.

Modification	Silk type	Added functionality	Findings and comments	Ref
Her-2-recognising peptide	MS1 derived from *T. clavipes* expressed in *E. coli*	Drug delivery to Her2 receptor-bearing cells	Silk was processed into spheres. N-terminal conjugates showed considerably higher capacity of binding Her2 compared to C-terminal conjugate.	[157]
C-terminal poly-lysine domain followed by tumour-recognising peptide	Hexamer derived from *T. clavipes* expressed in E. coli	DNA binding Adhesion to cancer cells	Silk chimera delivered exogenous DNA to cancerous cells in vivo with no off-target side effects.	[177]
C-terminal poly-lysine domain followed by ppTG1 peptide	Hexamer derived from *T. clavipes* expressed in *E. coli*	DNA binding Destabilisation of cell membrane	Silk showed gene transfer efficiency comparable to standard transfection reagent, but cell viability was reduced by 31%.	[178]
N-terminal fusion of silk with Human Galectin-3 Carbohydrate Recognition Domain	4RepCT derived from *E. australis* expressed in *E. coli*	Mucoadhesion	Silk shower adsorption of both bovine submaxillary mucin and pig gastric mucin via specific glycan-protein interactions.	[179]
C-terminal fusion to R5 peptide	15-mer derived from *T. clavipes* expressed in *E. coli*	Biomineralisation (silica chelation)	Silk was processed into films and electrospun fibres. Silk-R5 fusion promoter formation of silica particles with diameter of 0.5–2 µm (R5 alone formed particles with diameter of 0.5-10 µm).	[180]
N-terminal fusion to R5 peptide	15-mer derived from *T. clavipes* expressed in *E. coli*	Biomineralisation (silica chelation)	Coated surfaces promoted mesenchymal stem cell differentiation into osteoblasts. Biomineralisation was pH dependent, and a computational model for the biological outcomes of the material were built.	[181]
N-terminal fusion to dentin matrix acidic phosphoprotein DMP1	15-mer derived from *T. clavipes* expressed in *E. coli*	Biomineralisation (hydroxyapatite nucleation)	Silk was processed into films and showed mineralisation in presence of simulated body fluid.	[182]

Table 1.3 (*continued*). Recombinant silk proteins functionalised via genetic approach.

Modification	Silk type	Added functionality	Findings and comments	Ref
N- and C-terminal fusions to osteo tag, and sialo tag,	eADF4(C16) from *A. diadematus* expressed in *E. coli*	Biomineralisation (hydroxyapatite nucleation)	All tags and their combinations promoted mineralisation and mouse preosteoblast adhesion, proliferation, and differentiation into osteoblasts. No significant difference compared to tissue culture plastic.	[183]
N-terminal fusion to magainin and lactoferricin	4RepCT derived from *E. australis* expressed in *E. coli*	Antimicrobial activity	Significant reduction in biofilm formation compared to non-functionalised silk	[184]
Silver-binding protein domains	Hexamer and 15-mer derived from *T. clavipes* expressed in *E. coli*	Antimicrobial activity against *E. coli* and *S. aureus*	Silk-silver binding peptide chimera formed silver nanoparticles on its surface. Chimeras showed antimicrobial activity caused by silver ion leaching into the environment.	[161]
C-terminal fusions to human neutrophil defensins	Hexamer derived from *T. clavipes* expressed in *E. coli*	Antimicrobial activity against *E. coli* and *S. aureus*	Antimicrobial activity of chimeras was not always concentration-dependent, possibly due to inaccessibility of the active domains and silk aggregation. One of the chimeras was significantly cytotoxic against mammalian cells. Chimeras produced a zone of inhibition, but it was not explained how the active domain is released from the silk.	[160]
Endolysin SAL1 and dispersin-1	4RepCT derived from *E. australis* expressed in *E. coli*	Antimicrobial and anti-biofilm activity against *S. aureus*	Dispersin-4RepCT was expressed as a fusion protein or as sortase-mediated fusion. Both proteins showed ability to degrade biofilm matrix in model biofilm and *S. aureus* biofilm. SAL1 was fused to 4RepCT using sortase; fusion protein showed antimicrobial activity against *S. aureus* in suspension.	[163]

1.3.3. Chemical approach

Chemical conjugations of active molecules to the reactive groups present in amino acid side chains is an alternative method to functionalise spider silk. Using activation by 1-ethyl-3-(3-dimethylaminopropyl)carbodiimide (EDC) and *N*-hydroxysulfosuccinimide (NHS), ADF4(C16) silk has been coupled with fluorescein-5-isothiocyanate and β-galactosidase[185] (Scheme 1.1).

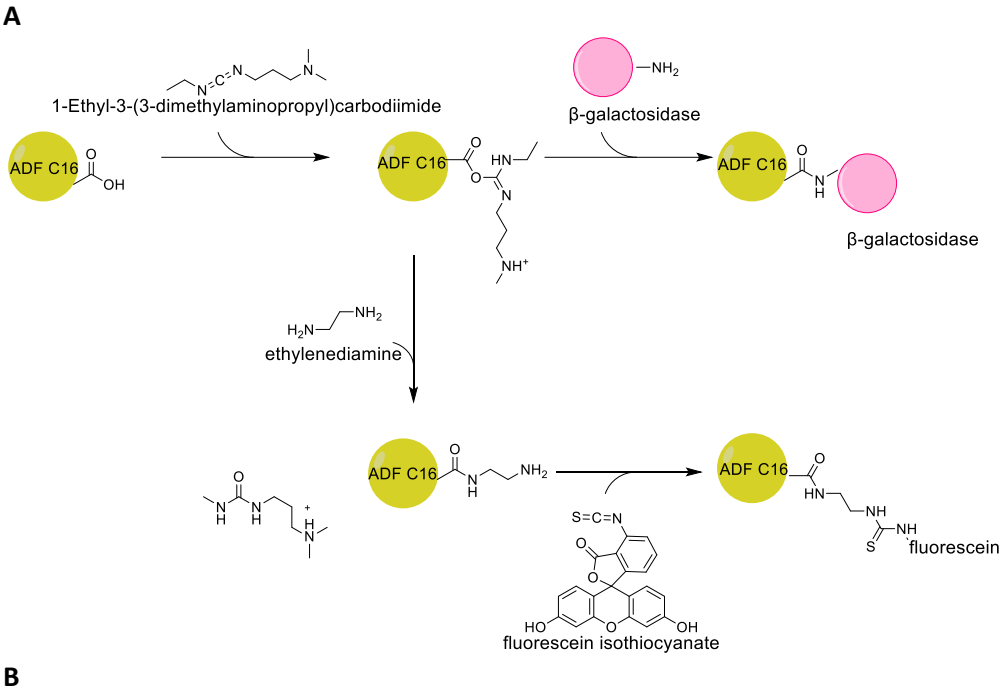

Scheme 1.1. Chemical modification of a recombinant spidroin ADF C16 using A: 1-ethyl-3-(3-dimethylaminopropyl)carbodiimide (EDC) and *N*-hydroxysulfosuccinimide (NHS)[185].

ADF4(C16) N-terminal cysteine-bearing construct has been conjugated to β-galactosidase using maleimide-thiol conjugation (Scheme 1.2A)[186]. In these studies, silk-conjugated molecules maintained their activity (fluorescence and enzymatic activity) showing the potential of silk-based chemical conjugates in biosensor development. N-terminal cysteine-bearing ADF4(C16) has also been used to chemically couple cyclic RGD peptide using a linker for maleimide-thiol conjugation (Scheme 1.2 B). This resulted in similar fibroblast adhesion and proliferation as genetically engineered chimera[187].

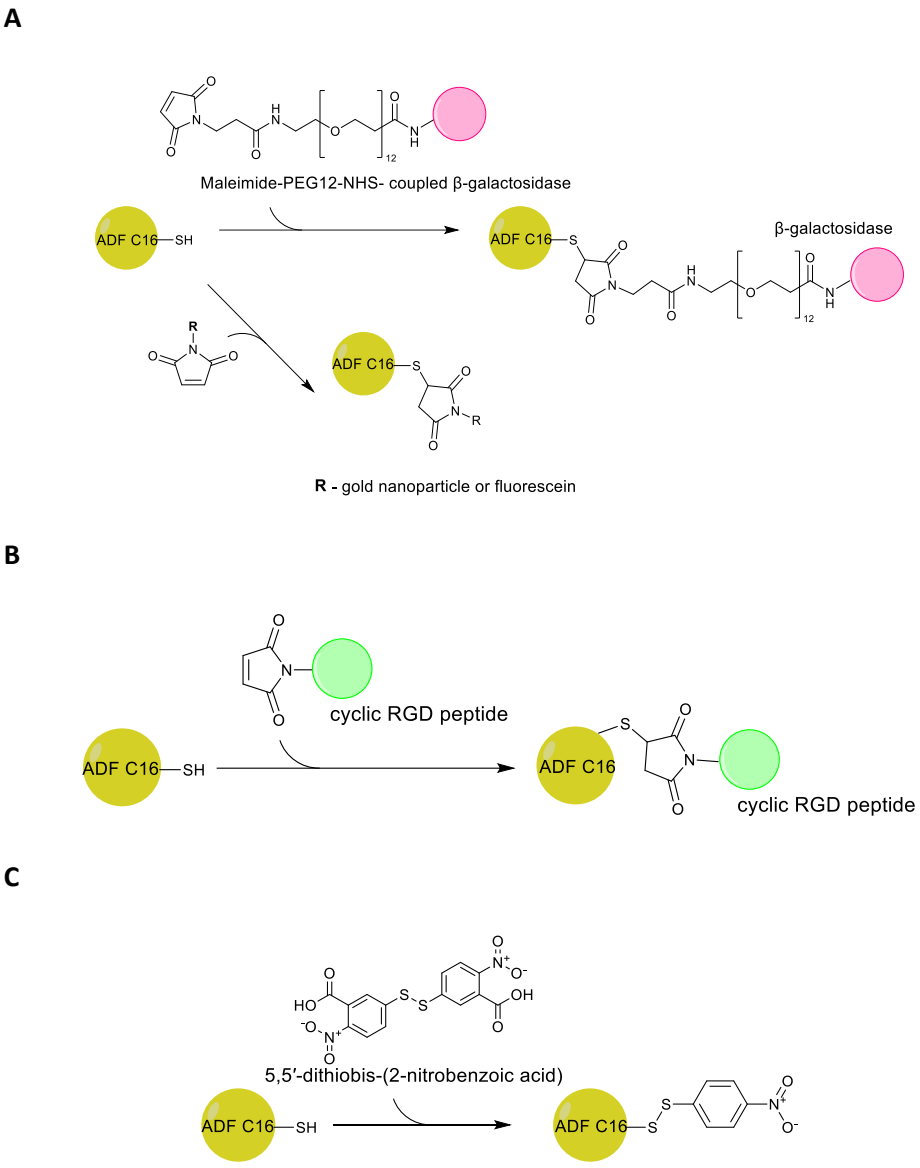

Scheme 1.2. Chemical modification of a recombinant spidroin ADF C16 using **A**, **B**: sulfhydryl-maleimide conjugations; **C**: disulfide bond[186-188].

The same N-terminal cysteine-bearing ADF(C16) (soluble protein, films, and particles) has been modified with thiol-bearing drugs via a disulfide bond, thus creating a redox sensitive, releasable conjugate(Scheme 1.2 C)[188]. In the same study, *para*-dimethylaminobenzaldehyde and doxorubicin was tethered to the silk materials via EDC-hydrazine conjugation thus creating a pH-sensitive drug delivery system (Scheme 1.3)[188].

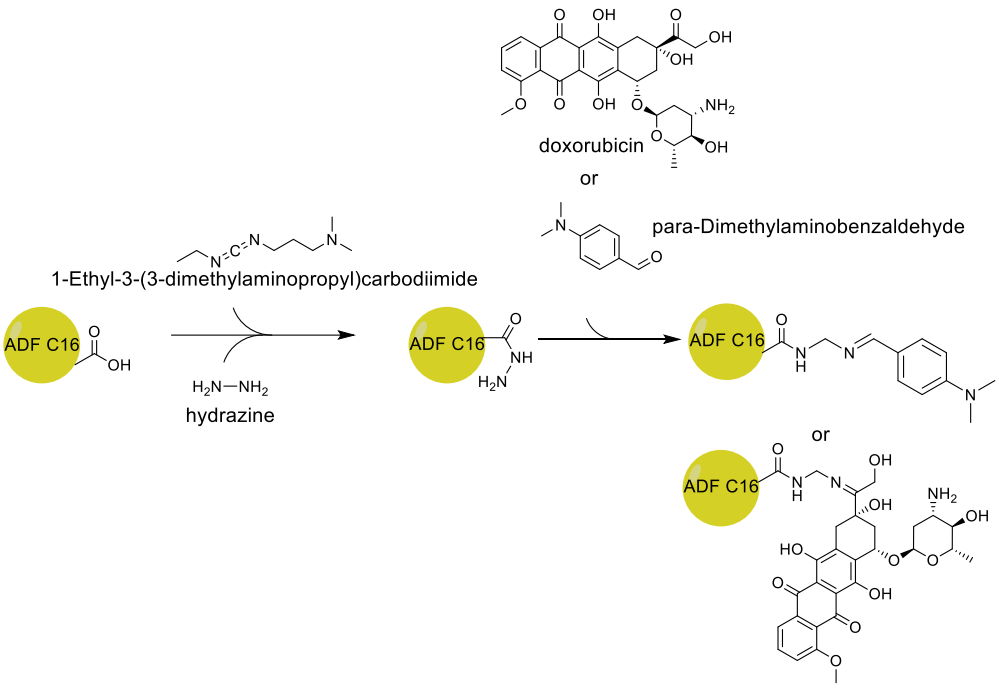

Scheme 1.3. Chemical modification of a recombinant spidroin ADF C16 using EDC-hydrazine-ketone conjugation[188].

Copper-catalysed azide-alkyne cycloaddition (CuAAC) has been employed as a fast and easy method of chemical coupling to silk modified with functional groups (discussed in more detail in Section 1.4 below). The N-terminus (and possibly tyrosine side chain amines) of ADF4(C16) was modified with NHS-activated 6-azidohexanoic acid and conjugated to alkyne-bearing oligonucleotides in the presence of copper yielding a triazole link[189,190]. Such conjugates were shown to assemble into nanofibrils as a proof of principle that spider silk is able to self-assemble and can be used as a versatile platform for immobilisation of functional units, for instance for high density enzyme arrays. In a similar setup, ADFC(16) conjugate to DNA was processed into a fibrillar nanohydrogel that was loaded with thrombin thus describing a novel enzyme-delivery platform[191].

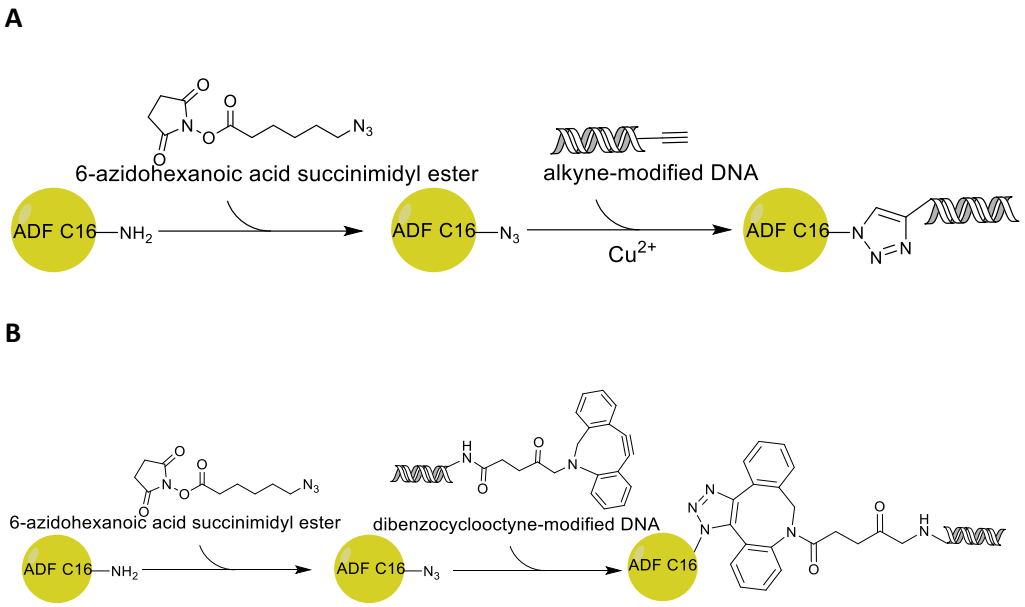

Scheme 1.4. Chemical modification of a recombinant spidroin ADF C16 using the activation of primary amines with 6-azidohexanoic acid followed by **A**: copper (I) catalysed azide-alkyne cycloaddition[189,190]; **B**: strain-promoted azide-alkyne cycloaddition[191].

However, these studies did not exploit CuAAC, or click-chemistry, to its maximum potential and specificity due to the requirement for an additional activation step. To that end, incorporation of a methionine analogue, an unnatural azide-bearing amino acid L-azidohomoalainine (Aha), into 4RepCT silk sequence (4RepCT^{3Aha}) using a methionine-auxotrophic *E.coli* strain has allowed the creation of a ready-to-use platform for further chemical modification whilst skipping the need for amine activation[106]. It was shown that Aha incorporation did not affect silk's ability to form fibres and their mechanical properties whilst allowing 4RepCT^{3Aha} fibres to be conjugated to fluorophores and levofloxacin using a pH-labile linker (Scheme 1.5 A). The 4RepCT^{3Aha} -levofloxacin conjugate fibres showed sustained delivery of the antibiotic in the presence of bacteria (bacterial growth acidifies the environment, thus promoting the linker hydrolysis and the release of the antibiotic)[106].

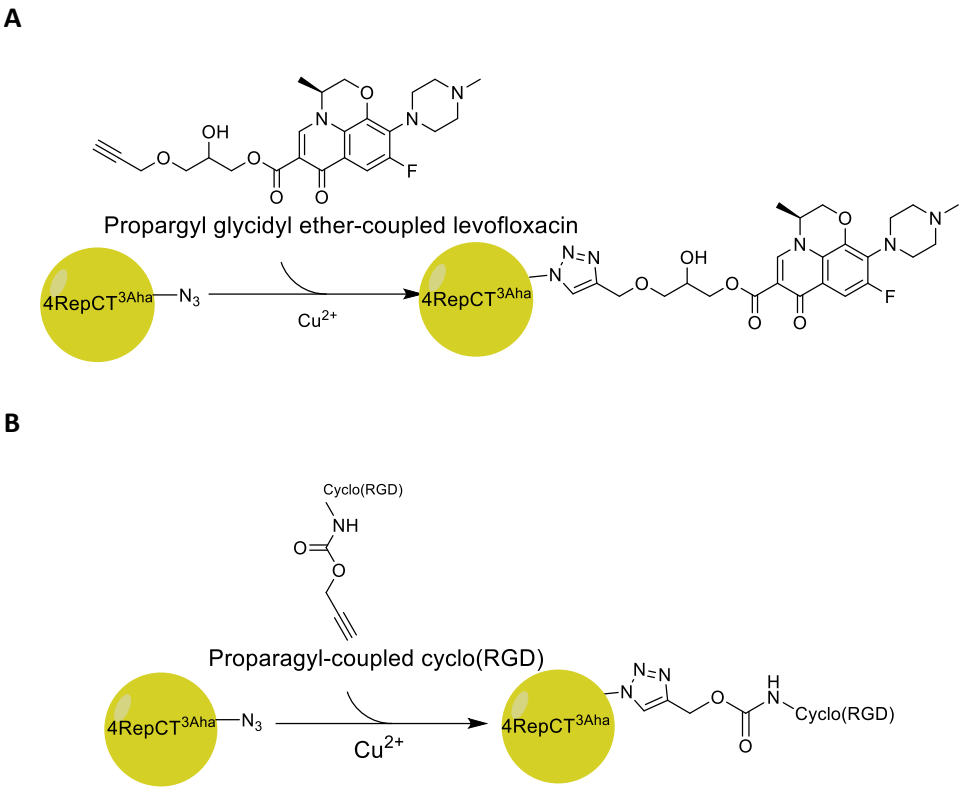

Scheme 1.5. Chemical functionalisation of a miniature spidroin 4RepCT^{3Aha} bearing L-azidohomoalanine residues using copper (I) catalysed azide-alkyne cycloadditions A: small molecule ligand[106]; B: cyclic RGD peptide ligand[192].

As shown in Fig 1.7, a 4RepCT silk construct contains six methionine (Met) residues that can be replaced by Aha. Of note, one methionine residue is within the S-tag (in yellow) and two Met are found within the thioredoxin solubility tag (in green); these residues are only present within the final protein if solubility tag is not proteolytically cleaved. As such, in contrast to previously described studies that use N-terminal modification to incorporate a single azide moiety, the Aha incorporation protocol allows the introduction of several azide-bearing amino acids into silk's primary sequence (wherever a methionine codon is present) which increases the loading of the functional ligand per spidroin.

MAHHHHHHKETAAAKFERQHMDSSSGLVPQGSMSDKIIHLTDDSFDTDVLKADGAILVDFWAEWC

GPCKMIAPILDEIADEYQGKLTVAKLNIDQNPGTAPKYGIRGIPTLLLFKNGEVAATKVGALSKGQLKEF

LDANLAGTDDDDKLVPRGSGNSGIQGQGGYGGLGQGGYGQGAGSSAAAAAAAAAAAAGGQGGQ

GQGGYGQGSGGSAAAAAAAAAAAAAAAGKGQGGYGQGSGGNAAAAAAAAAAAAAAGQGGQ

GGYGRQSQGAGSAAAAAAAAAAAAAAGSGQGGYGGQGQGGYGQSSASASAAASAASTVANSVSR

LSSPSAVSRVSSAVSSLVSNGQVNMAALPNIISNISSSVSASAPGASGCEVIVQALLEVITALVQIVSSSSV

GYINPSAVNQITNVVANAMAQVMG

Figure 1.7. Amino acid sequence of 4RepCT spidroin fusion with a 6xHis purification tag, S-tag epitope, and thioredoxin solubility tag. Construct contains six methionine residues: one within the S-tag (yellow), two within the thioredoxin solubility tag (green), and three within the C-terminal domain (pink). Histidine tag is highlighted in green. The four alanine-glycine rich domains are in blue. Initiator methionine is cleaved upon protein synthesis; therefore, it is not highlighted in the sequence.

This increased capacity of loading is further illustrated by a study of 4RepCT^{3Aha} conjugation to linear (Scheme 1.5 B) and cyclic (Scheme 1.6) RGD peptides modified with an alkyne-bearing non-hydrolysable linker[192]. The 4RepCT^{3Aha} -RGD conjugate showed greatly enhanced mesenchymal stem cell adhesion, and at the date of this review, it remains the only functionalised silk for 2D cell culture applications that outperforms tissue culture-treated plastic.

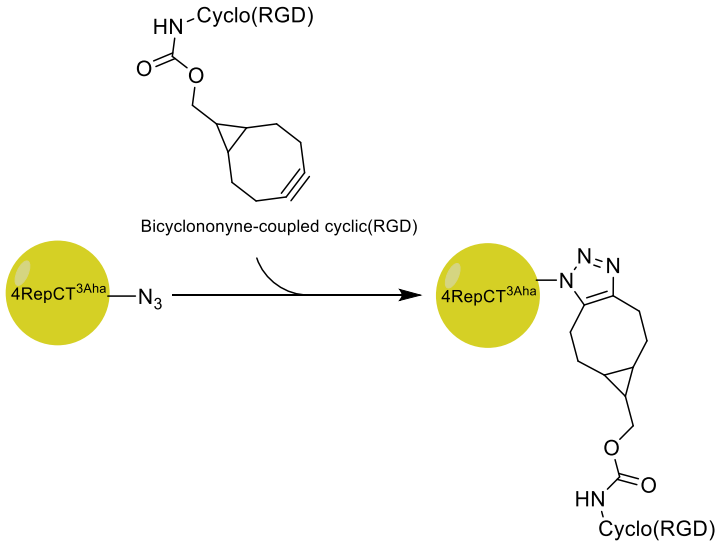

Scheme 1.6. Chemical functionalisation of a miniature spidroin 4RepCT^{3Aha} L-azidohomoalanine residues using strain-promoted azide-alkyne cycloaddition[192].

1.4. Fundamentals of copper (I) catalysed azide-alkyne cycloaddition

Click chemistry is a term coined by Sharpless *et al.*[193] that describes a class of combinatorial chemical reactions characterised by modular nature, wide scope, high yields, non-harmful by-products that can be removed without chromatography, and stereospecificity.

Sharpless *et al.* further describe "click" chemistry as a fast process that involves ambient conditions, readily available reagents and materials, and only benign solvents such as water. The tolerance to a wide variety of substrates, conditions, and user proficiencies has made click chemistry applicable to modification of biologicals, by non-chemists. Click chemistry reactions that are compatible with biological structures and organisms and do not modify the functional groups naturally found in nature are called bioorthogonal click reactions[194].

The two most popular bioorthogonal click chemistries are Cu(I)-catalysed [3+2] azide-alkyne cycloaddition (CuAAC) and strain-promoted [3+2] azide-alkyne cycloaddition (SPAAC). Azide-alkyne cycloadditions are particularly useful for biological applications due to the fact that these selectively chemically reactive groups are very rarely seen in naturally occurring biomolecules[194].

The CuAAC reaction (Figure 1.8 A, B) is exceptionally fast and only requires three components – an azide, an alkyne, and copper(I). Addition of sodium ascorbate (a reducing agent that converts copper(II) to copper(I)[195]), THPTA (a copper(I) stabiliser and a sacrificial reagent that reacts with reactive oxygen species generated by copper[196]), and increased temperature are optional[197].

Copper catalysis is of concern to all conjugated material applications due to known toxicity. Copper is an essential micronutrient in humans with tolerated daily intake of up to 10mg per day (lower for people with copper metabolism deficiencies such as Wilson disease)[198] . In larger quantities and in aquatic environments, copper is toxic; in addition, copper (I) ions can be toxic in their local microenvironment due to free radical generation[198] . Therefore, the CuAAC catalyst needs to be removed from the reaction before the biological application of the material, and the reaction cannot be carried out *in vivo*, however it remains highly applicable for bioconjugations of isolated

macromolecules. Further, the copper (I) sulphate used by Harvey *et al.*[106,192] to catalyse CuAAC can be removed by dialysis to levels below detection limits of energy-dispersive X-ray spectroscopy[106,192].

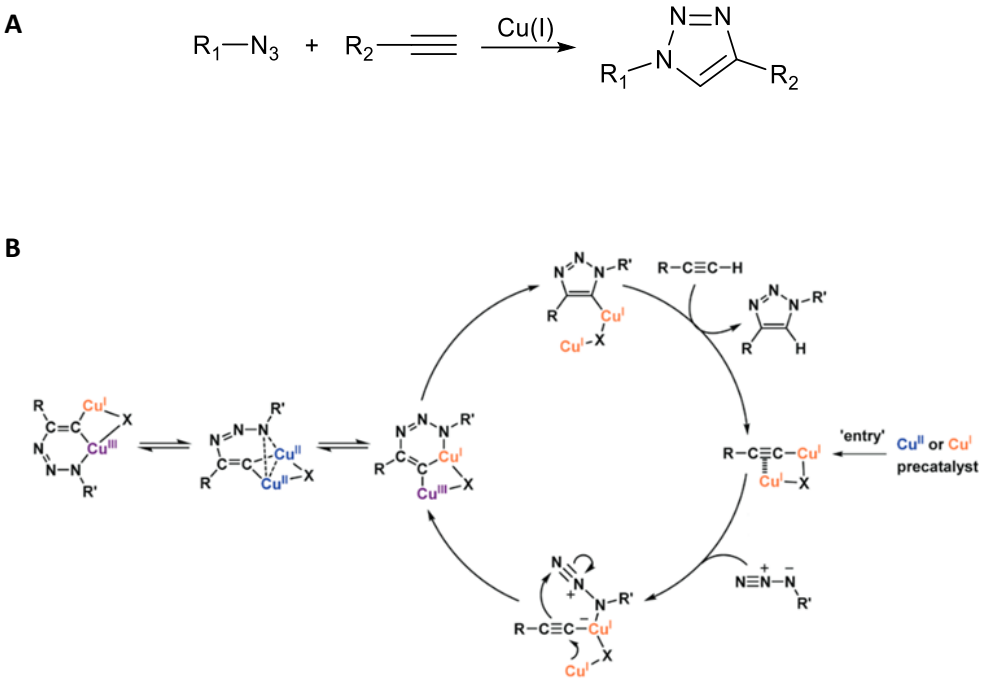

Figure 1.8. Copper (I) catalysed azide-alkyne cycloaddition. **A** – Copper (I)-catalysed [3+2] azide-alkyne cycloaddition (CuAAC) reaction. **B** – Proposed mechanism of CuAAC reaction (adapted from [197]), X is a bridging element [199].

SPAAC is a copper-free click chemistry that employs strained cyclooctynes to promote 3+2 cycloaddition[200] The developers of SPAAC chemistry claim that rate of SPAAC using difluorocyclooctyne (DIFO) is comparable to that of CuAAC[194], however it is argued that SPAAC is considerably slower (CuAAC k_2~10-100 $M^{-1}s^{-1}$ per 10-100µM Cu(I) versus SPAAC k_2~0.001-0.96 M^{-1} s^{-1} depending on the type of the cyclooctyne)[201,202], possibly due to low solubility of cyclooctynes in water. Nevertheless, in practical applications for biological chemistry, it is a highly applicable reaction with a wide scope and potential because it does not require any potentially cytotoxic copper for the catalysis.

1.5. Thesis aims and objectives

This thesis builds upon the existing technologies that allow us to use miniature recombinant spider silks as materials for various antimicrobial applications by expanding the portfolio of drug-loaded silk morphologies and silk-small molecule conjugates.

Chapter 2 describes silk production process optimisation procedures and development of novel column-free and scaleup-compatible purification method for a highly water soluble spidroin NT2RepCT. This approach will enable us to purify NT2RepCT on a gram-scale advancing the progress of research into the applications of this material by removing a bottleneck in the production stages.

Chapter 3 describes the creation and characterisation of an NT2RepCT-based colloidal drug delivery platform at nano-to-micro scale that takes advantage of the pH-responsive nature of the protein and has modifiable release kinetics depending on the degree of particle crosslinking.

Chapter 4 describes an expansion of the library of silk-antimicrobial molecule conjugates whose mechanism of action depends on a labile linker, and the design of a high-throughput compatible plate-based assay that allows to test the antimicrobial activity of these conjugates.

Chapter 5 describes the development of a novel contact-active antimicrobial surface coating based on silk conjugates to cationic quaternary ammonium-bearing ligands.

2. Recombinant production of the spider silk proteins 4RepCT, 4RepCT^{3Aha} and NT2RepCT

2.1 Introduction

As discussed in Chapter 1, recombinant production of spider silk proteins offers several distinct advantages over the use of the animal-derived counterparts, especially in context of the process scalability and protein functionalisation potential using unnatural amino acid incorporation methods. However, there are many challenges associated with heterologous protein production, and significant optimisation procedures are required to ensure high yields of protein per unit biomass (a pre-requisite to scaleup process) and simple and environmentally friendly purification procedures.

This thesis focuses on two miniature spidroins NT2RepCT and 4RepCT^{3Aha} (a derivative of 4RepCT) that both have distinct properties and applications. Below, the main features of each miniature spidroin biochemical nature and production are reviewed in context of their application as a biomaterial.

2.1.1. NT2RepCT

The miniature spidroin NT2RepCT was designed in 2017 by Andersson *et al.*[102] by combining the N-terminal domain from *E. australis* MaSp1 and the C-terminal domain from *A. ventricosus* MiSp flanking two alanine and glycine tandem repeats from *E. australis* (Fig 1.5). The spidroin also features a C-terminal six histidine tag for protein purification using Ni^{2+} affinity chromatography. NT2RepCT is a 33kDa protein with a uniquely hydrophilic nature and very high yields when produced in a heterologous host (125-200 mg/L);- in an aqueous buffer, it maintains a soluble state when concentrated to > 500 mg/ml[102]. NT2RepCT has been shown to be shear and pH-responsive due to its assembly into fibres upon extrusion into an acidified aqueous buffer (pH 5.5)[102].NT2RepCT has also been shown to form self-supporting thermoresponsive and shear sensitive hydrogels[132]. The main limitation of the NT2RepCT use in biomaterial applications is the need for column-based purification

that is inherently limited in volume; currently published methods utilise 5-20 ml columns with a theoretical dynamic binding capacity of 200-800 mg protein (GE Healthcare HisTrap HP).

2.1.2. 4RepCT and 4RepCT^{3Aha}

The miniature spidroin 4RepCT was designed in 2007 by Hedhammar *et al*.[203] This construct features four tandem repeats and the C-terminal domain from *E. australis* modified with an N-terminal histidine tag for protein purification and thioredoxin solubility tag (Fig 1.7). The 4RepCT protein has several unique properties not observed in other types of silk, for instance fibre self-assembly upon the thioredoxin solubility tag cleavage[203,204] and the formation of stable and continuously accumulating films that do not require stabilisation with organic solvents[12]. Further, these features are preserved when 4RepCT is modified on a genetic level by adding biologically active moieties to its N-terminal domain (Table 1.3).

In 2017, a modified version of 4RepCT protein was created by Harvey *et al.*[106] using unnatural amino acid (a methionine analogue L-azidohomoalanine, Aha) incorporation yielding a protein called 4RepCT^{3Aha}. The novel 4RepCT^{3Aha} protein was shown to have identical fibre assembly and mechanical properties as its counterpart 4RepCT. Production of this spidroin uses a methionine-auxotrophic bacterial strain that takes up methionine analogue and incorporates it into silk's amino acid sequence where the genetic code includes a methionine codon. This technology has enabled the modification of 4RepCT^{3Aha} proteins using click chemistry (discussed in more detail in section 1.7) thus broadening the functionalisation potential of silk as a biomaterial. The ability of 4RepCT^{3Aha} to carry three Aha moieties has not been repeated with NT2RepCT that failed to produce the heterologous protein in a methionine-auxotrophic host (Dr D. Harvey, unpublished observations).

The limitations of 4RepCT^{3Aha} use include the time-consuming use of a slow-growing methionine auxotrophic bacteria that reach protein induction density in eight hours compared to four hours for non-auxotrophic strains; and need to perform a time-consuming media swap protocol whereby the bacterial biomass is grown in a methionine-supplemented media that is then removed exchanged for

the Aha-supplemented media where protein expression is induced (described in detail in 2.2. Methods). Further to this, incorporation of Aha into other proteins required for the heterologous host's survival can have detrimental effects on the biomass increase and thus result in relatively low protein yields averaging 9 mg/L culture.

2.1.3. Aims and objectives

The work described in this chapter aims to empirically optimise the existing production and purification procedures for 4RepCT, 4RepCT^{3Aha} and NT2RepCT proteins with the goal to increase yields and overcome time-consuming and cost-inefficient processing steps.

The key objective for the optimisation of 4RepCT and 4RepCT^{3Aha} expression and purification was to increase yields of protein per unit biomass. This chapter describes technical details for the improvement of bacterial biomass growth conditions, along with protocols for cobalt affinity and anion exchange chromatography purification methods in order to increase the yield of the 4RepCT and 4RepCT^{3Aha}. Further genetic modifications of the 4RepCT genetic construct are described; these procedures will-optimise fibre preparation and diversify the unnatural amino acid incorporation ability.

A new precipitation-based protocol for NT2RepCT purification is developed to bypass the column chromatography thus tackling the most rate-limiting factor for thNT2RepCT purification.

2.2. Materials and methods

All chemicals were from Sigma-Aldrich (now Merck) unless indicated otherwise. All immobilised metal affinity (IMAC) columns were acquired from GE (now Cytiva). Detailed instrumentation lists with their application range along with media, buffer, and gel compositions can be found in the Appendix 1.

2.2.1. Expression of 4RepCT^{3Aha}

An overnight culture of *E. coli* DL41 pjE401_TRX-4RepCT was grown in 10 ml of LB broth supplemented with 50 µM kanamycin for 18 hours at 37°C with shaking at 200 revolutions per minute (rpm). The 10 ml overnight culture was used to inoculate 990 ml M9 media (Appendix 1) supplemented with 0.1 mg methionine and 1 ml kanamycin (50 mg/ml) and incubated for 8 hours at 37°C, 200 rpm until it reached OD_{600} = 1. The biomass generated was harvested by centrifugation at 4500 *g* for 15 minutes. The supernatant was discarded, and the pellet was washed by resuspension in 50 ml 1 x M9 salt solution (pH 7). Resuspended cells were centrifuged at 4500 *g* for 15 minutes, and the wash step was repeated three times. Washed biomass was resuspended in 10 ml 1 x M9 salt solution and used to inoculate fresh M9 media (990 ml) supplemented with azidohomoalanine (0.1 g), 1 ml kanamycin (50 mg/ml), and 1 ml IPTG (1 M) and grown for 18 hours at 25 °C, 200 rpm. Cells were harvested by centrifugation at 5000 *g* for 20 minutes. The supernatant was discarded, and the pellet was resuspended in 40 ml Buffer A (Appendix 1) and stored at -20°C until purification.

2.2.2. Purification of 4RepCT^{3Aha}

E. coli DL41 pjE401_TRX-4RepCT suspension was thawed at room temperature and sonicated using MSE Soniprep 150 sonicator (Sanyo) at 4°C. The sonicator probe was immersed 5 cm into the bacterial suspension and sonicated for 30 seconds followed by a 30 second cool-down ten times. After sonication, the lysate was cleared by centrifugation for 45 min at 35,000 *g*. Cleared lysate was loaded onto a nickel charged HiTrap column (5 ml) using an AKTA START (via UNICORN software) at 5 ml/min flow speed. The column was washed with increasing concentrations of Buffer B (Appendix 1), and TRX-4RepCT^{3Aha} was eluted at a 40% Buffer B. For purification using Co^{2+} affinity, cleared lysate was loaded

onto a cobalt-charger HiTrap TALON column (5 ml), washed with increasing concentrations of Buffer B Co^{2+} (Appendix 1), and TRX-4RepCT^{3Aha} was eluted at 40% Buffer B Co^{2+} concentration.

2.2.3. Sodium dodecyl-sulfate polyacrylamide gel electrophoresis (SDS PAGE)

For protein analysis by sodium dodecyl-sulfate polyacrylamide gel electrophoresis (SDS PAGE), eluted protein fractions were combined with 4 x SDS loading buffer (Appendix 1), boiled at 95°C for 10 minutes and loaded on a 15% polyacrylamide gel (Appendix 1), then run at 200 V for 50 minutes. As a molecular weight marker (MWM), PageRuler Plus Prestained Protein Ladder (Thermo Scientific) 10-250 kDa was used. After electrophoresis, the gel was stained with GelSafe Blue gel stain (Thermo) according to manufacturer's instructions. The gel was destained by washing the gel three times in MilliQ water and visualised using Geneflow GBox (Syngene) under visible light.

2.2.4. Protein dialysis procedure

Fractions containing TRX-4RepCT^{3Aha} protein (37 kDa) were pooled into a SpectraPor dialysis bag with 6 – 8 kDa pore size (Spectrum Lab) and dialysed against 20 mM Tris pH 8 at 4°C overnight.

2.2.5. Q-column based 4RepCT^{3Aha} purification procedure post-dialysis

For additional purification of the 4RepCT^{3Aha} protein sample after dialysis, the dialysed protein solution was loaded onto a Q column (diameter 1.6 × length 2.5 cm, volume 5 ml). The loaded column was washed with 20 mM Tris pH 8 followed by stepwise-increasing concentrations of Buffer BQ (Appendix 1). Column-bound 4RepCT^{3Aha} was eluted at 20% Buffer BQ concentration. The sample was dialysed as described in Section 2.2.4.

2.2.6. Concentration and storage of 4RepCT^{3Aha} protein

Dialysed protein solution was concentrated to 2 mg/ml using a buffer exchange column with 10 kDa molecular weight cut-off (MWCO) (Satorius Vivaspin). The final concentration of the protein was measured using a microvolume spectrophotometer at 280 nm. The protein solution was aliquoted into 1 ml aliquots, snap-frozen using liquid nitrogen, and stored at -80°C.

2.2.7. Procedure for 4RepCT_iso159met mutation

For the mutagenesis of the unique isoleucine residue to methionine, glycerol stock of *E. coli* NEB5α pJE401_TRX-4RepCT was streaked onto a fresh LB agar plate supplemented with 50 µg/ml kanamycin and incubated overnight at 37°C. A single colony of *E. coli* NEB5α pJE401_TRX-4RepCT was used to inoculate 5 ml LB media supplemented with 50 µg/ml kanamycin and incubated overnight at 37°C, 200 rpm. The culture was harvested by centrifugation at 5000 *g* for 10 minutes. The pJE401_TRX-4RepCT plasmid was purified using NEB Monarch Plasmid Prep Kit according to the manufacturer's instructions. The purified plasmid was stored at -20°C.

Polymerase chain reaction (PCR) was carried out using the following components:

Component	**Volume (µl)**
Q5 2x Master Mix (NEB)	12.5
Forward primer ACTCGGGTATgCAAGGCCAAG (10µM)	1.25
Reverse primer TACCGGATCCACGCGGAA (10µM)	1.25
Plasmid DNA (20 ng/ml)	1
Nuclease-free water	9

Lowercase g highlighted in green represents the mutation that changes isoleucine residue to methionine (ATC to ATC). The initial denaturation step included incubation 98°C for 30 seconds followed by 25 cycles of 98°C for 10 seconds, 68 °C for 20 seconds, 72°C for 120 seconds. The final extension was carried out at 72°C for 2 minutes. A 5 µl aliquot of the reaction was mixed with 6 x Loading Dye (NEB) and loaded on a 1% agarose gel supplemented with 1 µg/ml ethidium bromide. The gel was run at 120 V for 20 minutes and visualised using SynGene G:Box under UV light.

The reaction was purified using PCR CleanUp Kit (Promega) according to the manufacturer's instructions, then treated with kinase, ligase and DpnI enzymes (NEB) according to the manufacturer's instructions. The treated reaction was transformed into chemically competent *E. coli* NEB5α using 30 second heat shock at 42°C, followed by the addition on 1 ml LB media and 1 hour recovery incubation at 37°C, 200 rpm. Transformed cells were plated on LB agar supplemented with 50 µg/ml kanamycin and incubated overnight at 37°C. The plasmid was extracted from the successful clones as described

above, and successful introduction of the desired mutation was confirmed by sequencing. The mutated clones were transformed into chemically competent *E. coli* DL41 as described above, and protein was expressed from them as described in the Section 2.2.1.

2.2.8. Fluorescein conjugation

Purified 4RepCT^{4Aha} protein was conjugated with fluorescein alkyne (FAM) by combining 100 µl 4RepCT^{4Aha} (1 mg/ml), 10 µl THPTA (50 mM), 10 µl sodium ascorbate (50 mM), 5 µl FAM in DSMO (50 mM) and 3 µl $CuSO_4$ (50 mM). The reaction was incubated for 3 hours at room temperature with gentle agitation and protected from light, then stopped by addition of 2 µl 0.5 M ethylenediaminetetraacetic acid (EDTA). The conjugation reaction and a 4RepCT^{4Aha} control sample was analysed by SDS PAGE as described in the Section 2.2.3. These samples were visualised using UV light prior to staining with GelSafe Blue, destaining, and visualisation under visible light.

2.2.9. Expression of 4RepCT^{3Hpg}

Alkyne-bearing 4RepCT^{3Hpg} was expressed and purified as described in the Section 2.2.1-2.2.4 with exception that M9 media was supplemented with 0.07 g/L L-homopropargylglycine (HPG). HPG powder was dissolved in 10 ml 1 x M9 media and filter-sterilised using 0.2 µm filter. Purified 4RepCT^{3Hpg} was conjugated to fluorescein azide and analysed as described in Section 2.2.8.

2.2.10. Solubility tag cleavage using 3C protease

A construct pjE401_TRX-3C-4RepCT was provided by SpiBer Technologies. Solubility tag removal was carried out using Recombinant HRV 3C Protease kit (Sino Biological). The plasmid was transformed into chemically competent *E. coli* DL41 as described in the Section 2.2.7, and TRX-3C-4RrpCT was expressed and purified as described in the Section 2.2.1-2.2.2. For the cleavage reaction, 0.3 ml 4RepCT^{3Aha} (1.5 mg/ml), 50 µl 3C Protease (100 U) and 150 µl Reaction Buffer were combined and incubated at room temperature for 2 hours. The reaction was analysed for the cleavage of the sample by SDS PAGE as described in the Section 2.2.3.

2.2.11. Cloning of 4RepCT gene into pET22b vector

The pjE401_4RepCT plasmid was purified as described in the Section 2.2.7. PCR of the 4RepCT gene for HiFi ligation into pET22b vector was carried out using the following components:

Component	Volume (µl)
Q5 2x Master Mix (NEB)	12.5
Forward primer (10µM) ctttaagaaggagatatacatATGGCACATCATCACCACCACC	1.25
Reverse primer (10µM) agtggtggtggtggtggtgctcgaGCCCAGGGGGTCACTCGA	1.25
Plasmid DNA (20 ng/ml)	1
Nuclease-free water	9

The initial denaturation step included incubation at 98°C for 1 minute followed by 30 cycles of 98°C for 10 seconds, 68°C for 20 seconds, 72°C for 20 seconds. The final extension was carried out at 72°C for 2 minutes. The excess reactants were removed using PCR CleanUp Kit (Promega) according to the manufacturer's instructions.

An empty pET22b vector was incubated with 1 µl NdeI and 1µl XhoI enzyme supplemented with CutSmart Buffer (NEB) for 30 mins at 37°C followed by enzyme heat inactivation at 70°C for 10 minutes. The PCR product and the digested vector backbone were run on 1% agarose gel supplemented with 10 µg/ml ethidium bromide at 120 V for 20 minutes prior to visualisation under UV light. The UV- fluorescent band representing the vector backbone was excised from the gel using Zymoclean Gel DNA Recovery Kit (Zymo Research). DNA concentrations were measured using absorbance at 260 nm.

HiFi assembly of the PCR product and the vector backbone was carried out at the molar ratio of 1:2 which corresponds to 50 ng vector (2 µl of 25 ng/ul stock) and 11.6 ng of the PCR product (0.52 µl of 28 ng/ul stock). The reaction was supplemented with 10 µl 2 x HiFi Assembly Master Mix and 7.48 µl nuclease free water, then incubated at 50°C for 1 hour. The reaction was used to chemically transform *E. coli* NEB5α as described in the Section 2.2.7. Transformed cells were plated on LB agar

supplemented with 100 µg/ml ampicillin and incubated overnight at 37°C. The successful clones were confirmed by sequencing and transformed into chemically competent *E. coli* BL21DE3 (ThermoFisher).

2.2.12 Protein expression using pET22b_4RepCT

E. coli BL21 DE3 pET22b glycerol stock was streaked onto an LB agar plate supplemented with 100 µg/ml ampicillin and incubated overnight at 37°C. A single colony was used to inoculate 10 ml LB media supplemented with 100 µg/ml ampicillin and incubated overnight at 37°C, 200 rpm. The starter culture was used to inoculate 990 ml M9 media with 100 µg/ml ampicillin and incubated at 37°C, 200 rpm until OD_{600} = 0.7 . The following protein expression and purification procedure carried out was as outlined in the Section 2.2.1-2.2.4. Concentrated protein was conjugated to fluorescein alkyne as described in the Section 2.2.8.

2.2.13. Expression of NT2RepCT protein

E. coli BL21 DE3 pET22b_NT2RepCT glycerol stock was streaked on an LB agar plate supplemented with 100 µg/ml ampicillin and incubated overnight at 37°C. A single colony was used to inoculate 10 ml LB media with100 µg/ml ampicillin and incubated overnight at 37 °C, 200 rpm. The starter culture was used to inoculate 1 L LB media (100 µg/ml ampicillin) and incubated at 30°C until OD_{600} = 0.7. Protein expression was induced by adding 0.3 ml IPTG (1 M) following by incubation at 20°C, 200 rpm overnight. The biomass was harvested by centrifugation at 5000 *g* for 20 minutes. The supernatant was discarded, and the pellet was resuspended in 30 ml Buffer A (Appendix 1). The pellet was stored at -20°C until purification.

2.2.14. Purification of NT2RepCT using metal affinity chromatography

E. coli BL21DE3 pellet was thawed at room temperature and sonicated as described in the Section 2.2.2. After centrifugation at 35,000 *g* for 45 minutes, the cleared supernatant was loaded on a 20 mL HiTrap column. Further processing was carried out as described in Sections 2.2.2-2.2.5. The protein solution was dialysed against 2 L MilliQ water overnight, then snap-frozen using liquid nitrogen and freeze dried over 72 hours using MudolyoD freeze dryer (Thermo Scientific).

2.2.15. Purification of NT2RepCT using ammonium sulfate precipitation

E. coli BL21 DE3 pET22b_NT2RepCT biomass aliquot (10 ml) was lysed with 10 ml 30ml 5% v/w SDS, 50 mM Tris pH 8 and incubated at room temperature with stirring for 25 minutes. The lysate was clarified by centrifugation at 35,000 *g* for 45 minutes and the resulting supernatant (0.5 ml) was incubated with 55 µl saturated ammonium sulfate (to 10% w/v total ammonium sulfate concentration) for 5 minutes with gentle agitation before being centrifuged at 14,000 *g* for 5 minutes. The supernatant was removed, and the pellet was resuspended in 50 µl 20 mM Tris pH 8. The process was repeated using 0.5 ml supernatant and increasing total concentrations of ammonium sulfate: 62 µl (to 20% w/v); 71 µl (30% w/v);83 µl (40%w/v); 100 µl (50% w/v); 125 µl (60% w/v) and 166 µl (70% w/v) (concentrations extrapolated from Sigma Aldrich Ammonium Sulfate Precipitation Guide). Resolubilised precipitants were analysed using SDS PAGE.

2.2.16. Purification of NT2RepCT using solvent precipitation

E. coli BL21DE2 pET22b_NT2RepCT cell pellet (biomass from 1 L culture) was resuspended in 30 ml 5% v/w SDS, 50 mM Tris pH 8 and incubated at room temperature with stirring for 25 minutes. The lysate was clarified by centrifugation at 35,000 *g* for 45 minutes, and 1 ml supernatant aliquots were exposed to increasing concentrations of isopropanol (IPA) 10-60% v/v. The precipitate was collected by centrifugation at 14,000 *g*, resuspended in 20 mM Tris pH 8 and analysed using SDS PAGE. The purity of the protein band in each lane was determined using ImageJ gel analysis software.

2.2.17 Purification of NT2RepCT using HCl precipitation with and without KCl treatment

E. coli BL21DE2 pET22b_NT2RepCT cell pellet (biomass from 1 L culture) was resuspended in 30 ml 5% v/w SDS, 50 mM Tris pH 8 and incubated at room temperature with stirring for 25 minutes. The lysate was clarified by centrifugation at 35,000 *g* for 45 minutes and treated with 40% v/v isopropanol with constant stirring for 20 minutes following by centrifugation at 35,000 *g* . The clarified lysate was divided into two samples each representing biomass derived from 0.5L growth culture. Sample 1 was treated with addition of neat hydrochloric acid dropwise until white precipitate was formed (approx.

15% v/v). Sample 2 was treated with addition of 1M KCl dropwise until white precipitate formed. The precipitate was removed by centrifugation at 35,000 *g* for 20 minutes at room temperature, and the supernatant was treated with addition of neat HCl dropwise until white precipitate formed (approx. 15% v/v). Final precipitates of both samples were collected by centrifugation at 35,000 *g* for 30 minutes, dialysed against 5 L of ultrapure water for 48 hours with water change at 24 hours. Dialysed solutions were snap frozen using liquid nitrogen and freeze dried.

2.2.17. Determination of NT2RepCT protein concentration in the HCl-purified samples using Pierce BCA assay

Pierce™ Detergent Compatible Bradford Assay Kit (Thermo) was used following the manufacturer's instructions. In short, 150 µl of bovine serum albumin dilutions 0-2 mg/ml were added to a microplate well, supplemented with 150 µl of Bradford reagent and mixed by pipetting up and down three times. The plate was incubated at room temperature for 10 minutes, and the absorbance values were read using a TECAN Spark plate reader at 595 nm. Lyophilised protein samples were diluted to 5 mg/ml, and the protein concentrations in these samples was calculated using simple linear regression.

2.2.18. Determination of NT2RepCT protein concentration using SDS PAGE band densitometry

A serial dilution (0.125-1 mg/ml) of Ni^{2+} IMAC-purified NT2RepCT protein was used as standards. NT2RepCT samples from HCl precipitation were dissolved to 5 mg/ml. The samples were analysed by SDS PAGE. Band density was analysed using ImageJ gel analysis software by measuring the area under the curve for each peak.

2.3. Results and discussion

2.3.1. Expression of 4RepCT^{3Aha}

The recombinant mini-spidroin 4RepCT^{3Aha} was expressed in the heterologous host *E. coli* DL41.The average yields of 4RepCT^{3Aha} when biomass growth was carried out in baffled glass Erlenmeyer flasks were 9 mg/L culture. In comparison, 4RepCT^{3Aha} yields when biomass was grown in TunAIR flasks averaged 12mg/L (both samples were purified using Ni^{2+} affinity).

2.3.2. Purification of 4RepCT^{3Aha}

The 4RepCT^{3Aha} protein (37kDa) was purified using either Ni^{2+} or Co^{2+} IMAC. The use of Co^{2+} reduced the loss of protein typically seen using Ni^{2+} IMAC at 30% Buffer B wash step (Fig 2.1 A, B; 30% Buffer B lanes). Both approaches produced samples with similar final protein purity. The average 4RepCT^{3Aha} yield after Co^{2+} IMAC was 20 mg/L compared to 12 mg/L after NI^{2+} IMAC. In addition, Co^{2+} IMAC uses 57% less imidazole compared to Ni^{2+} IMAC.

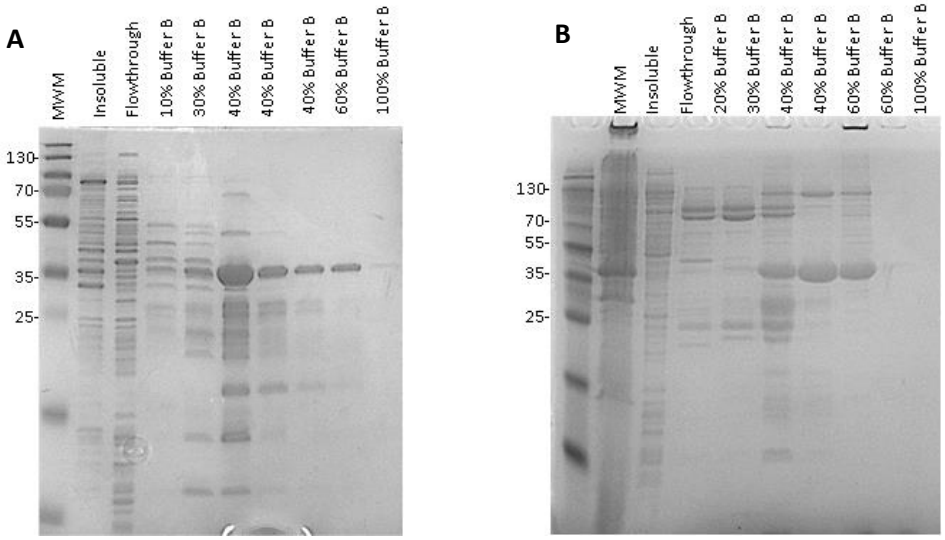

Figure 2.1. SDS-PAGE analysis of 4RepCT^{3Aha} protein (37kDa) purified using **A**: Ni^{2+} and **B**: Co^{2+} immobilised metal ion affinity chromatography. MWM – molecular weight marker, kilodaltons.

2.3.3. Q column-based purification of 4RepCT^{3Aha}

Anion exchange chromatography was conducted using a Q column. This showed that the 4RepCT^{3Aha} purity after Co^{2+}IMAC could be increased to 87% (Fig.2.2). The protein eluted at 20% Buffer B concentration (200 mM NaCl).

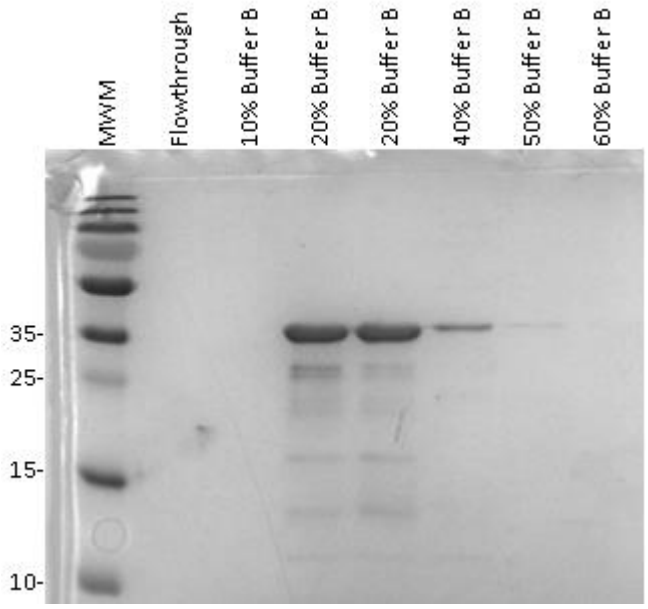

Figure 2.2. SDS PAGE analysis of 4RepCT^{3Aha} protein using two-step purification protocol (Co^{2+} affinity and Q column affinity). MWM – molecular weight marker, kilodaltons.

2.3.4. Purification and TRX tag cleavage of TRX-3C-4RepCT

Human rhinovirus 3C protease is a high precision cysteine protease commonly used in biotechnology as an enzyme to remove solubility tags from recombinant proteins. Unlike thrombin, 3C protease can be produced recombinantly which would significantly reduce the cost of large-scale material processing. The pJE401_TRX-3C-4RepCT was provided by SpiBer Technologies, and the TRX-3C-4RepCT^{3Aha} protein was successfully purified (with yields of 9 mg/L, Fig. 2.3 A) and as expected, azidohomoalanine incorporation did not interfere with TRX tag cleavage using 3C protease (Fig 2.3 B).

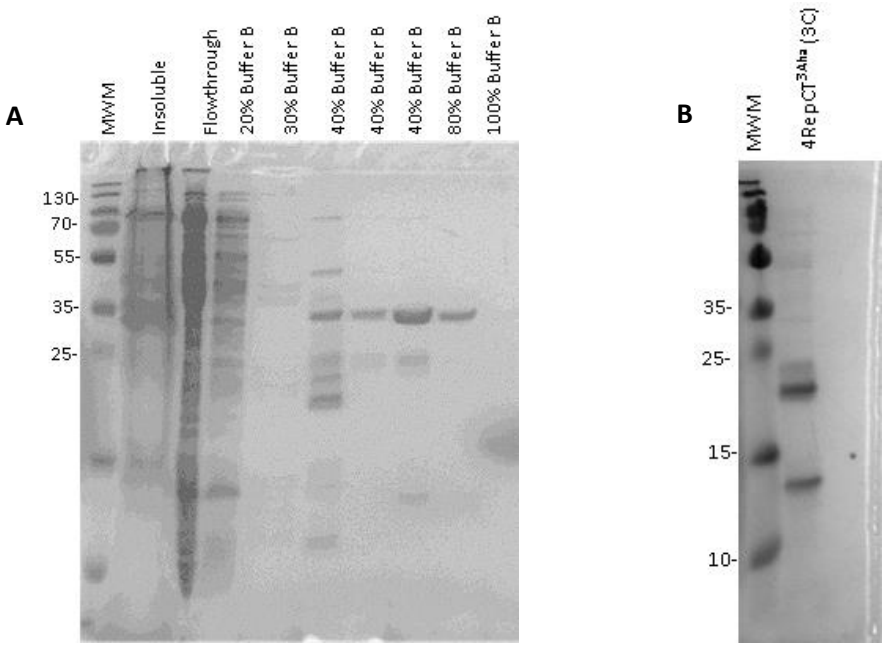

Figure 2.3.SDS PAGE analyses of TRX-3C-4RepCT^{3Aha}**A**-purification and **B** – TRX cleavage using 3C protease. MWM – molecular weight marker, kilodaltons.

2.3.5. Creation, purification, and conjugation of 4RepCT^{4Aha}

The unique isoleucine residue in the 4RepCT repetitive region (ILE_10) was mutated to methionine to provide an additional site for conjugation reactions upon incorporation of azidohomoalanine. Figure 2.4 A shows a successful PCR product using mutation-bearing primers. The protein was expressed and purified successfully (Fig 2.4 B), followed by conjugation to alkyne fluorescein that is shown as a bright band in Fig 2.4 C when illuminated with UV light (Fig 2.4 C) Non-conjugated protein showed no fluorescence under UV light. Fig 2.4 D shows a stained gel from Fig 2.4 C under visible light confirming protein presence in both lanes. This construct could be used in future to increase the loading capacity of the conjugate.

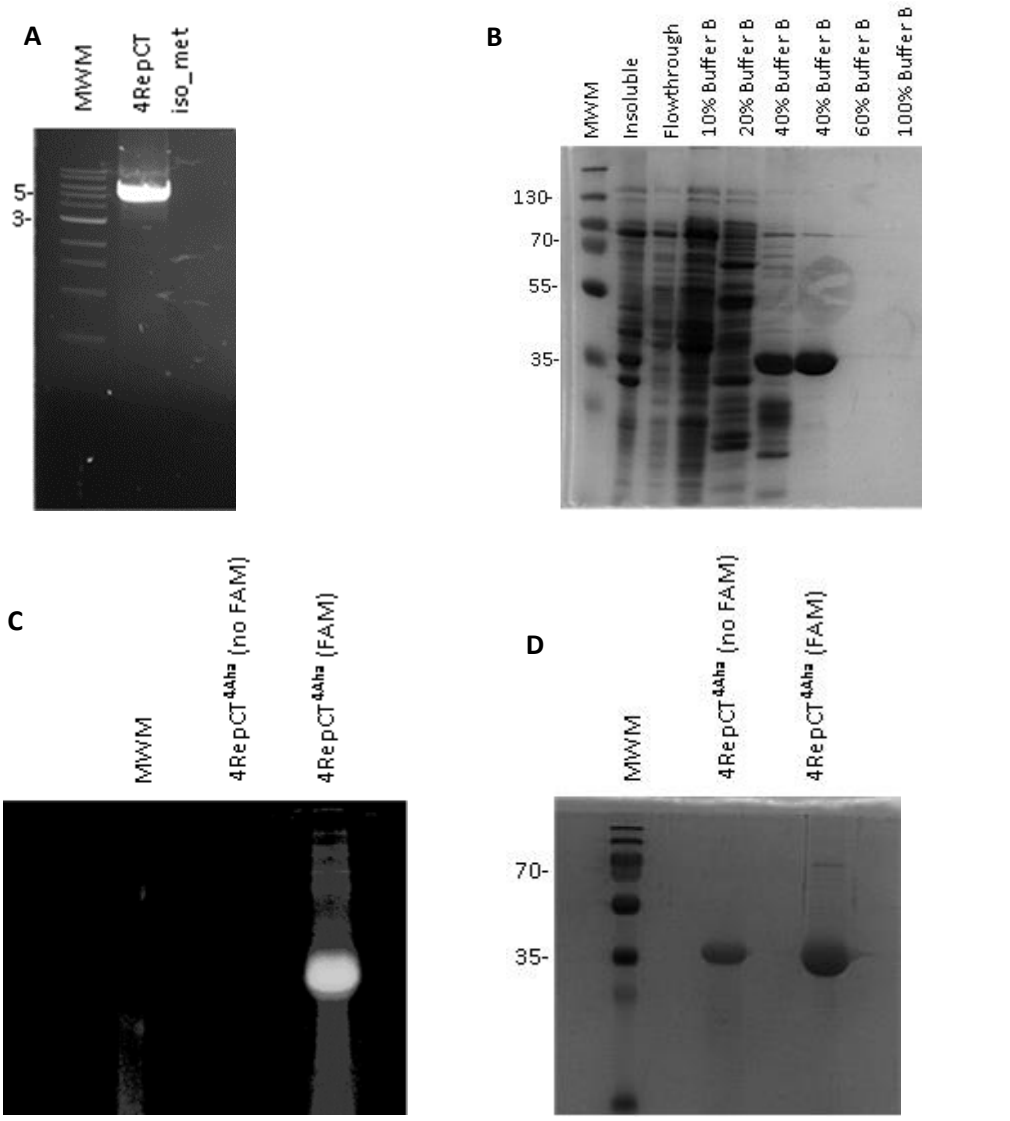

Figure 2.4. Production of 4RepCT^{4Aha} protein. **A**: 1% agarose gel showing a PCR product produced using mutant primers. MWM -1 kB ladder, kilobase pairs. **B**: SDS PAGE analysis of 4RepCT^{4Aha} purification. **C**: 4RepCT^{4Aha}-FAM conjugate under UV light; D: 4RepCT^{4Aha} and 4RepCT^{4Aha}-FAM conjugate under visible light. MWM – molecular weight marker, kilodaltons.

2.3.6. Purification and conjugation of 4RepCT^{3Hpg}

L-Homopropargylglycine is a methionine analogue bearing a terminal alkyne in its side chain. The yields of 4RepCT^{3Hpg} using the protocol developed for 4RepCT^{3Aha} expression were considerably lower (5 mg/L culture; Fig. 2.5 A). The 4RepCT^{3Hpg} could be conjugated to fluorescein azide (Fig 2.5 B), although the quantification of the relative fluorescence intensity using densitometry and comparison to 4RepCT^{3Aha} -FAM conjugate was not successful due to a strong background signal.

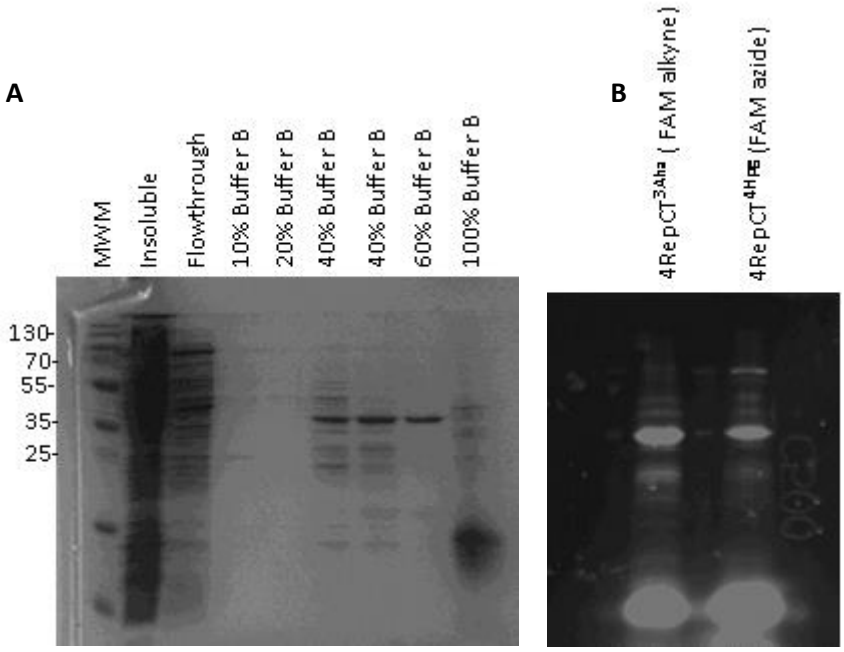

Figure 2.5. SDS PAGE analyses of **A**: purification of 4RepCT^{3Hpg} under visible light and **B**: fluorescein conjugation to 4RepCT^{3Aha} and 4RepCT$^{3Hpg.}$ under UV light. MWM – molecular weight marker, kilodaltons.

2.3.7. Cloning, purification, and conjugation of 4RepCT and 4RepCT^{3Aha} using the pET22b plasmid

Figure 2.6 A shows a PCR product of 4RepCT gene amplified from pJE401_4RepCT plasmid and a restriction enzyme digest of an empty pET22b vector. These two components were combined to create pET22b_4RepCT that was verified by sequencing.

This plasmid was used to produce 4RepCT (Fig 2.6 B) and 4RepCT^{3Aha} (Fig. 2.6 C) proteins. Whilst 4RepCT was produced at greatly enhanced yield (36 mg/L), the expression of 4RepCT^{3Aha} was very low (3 mg/L). This establishes pET22b_4RepCT as an optimal platform for work that involves non-functionalised 4RepCT silk.

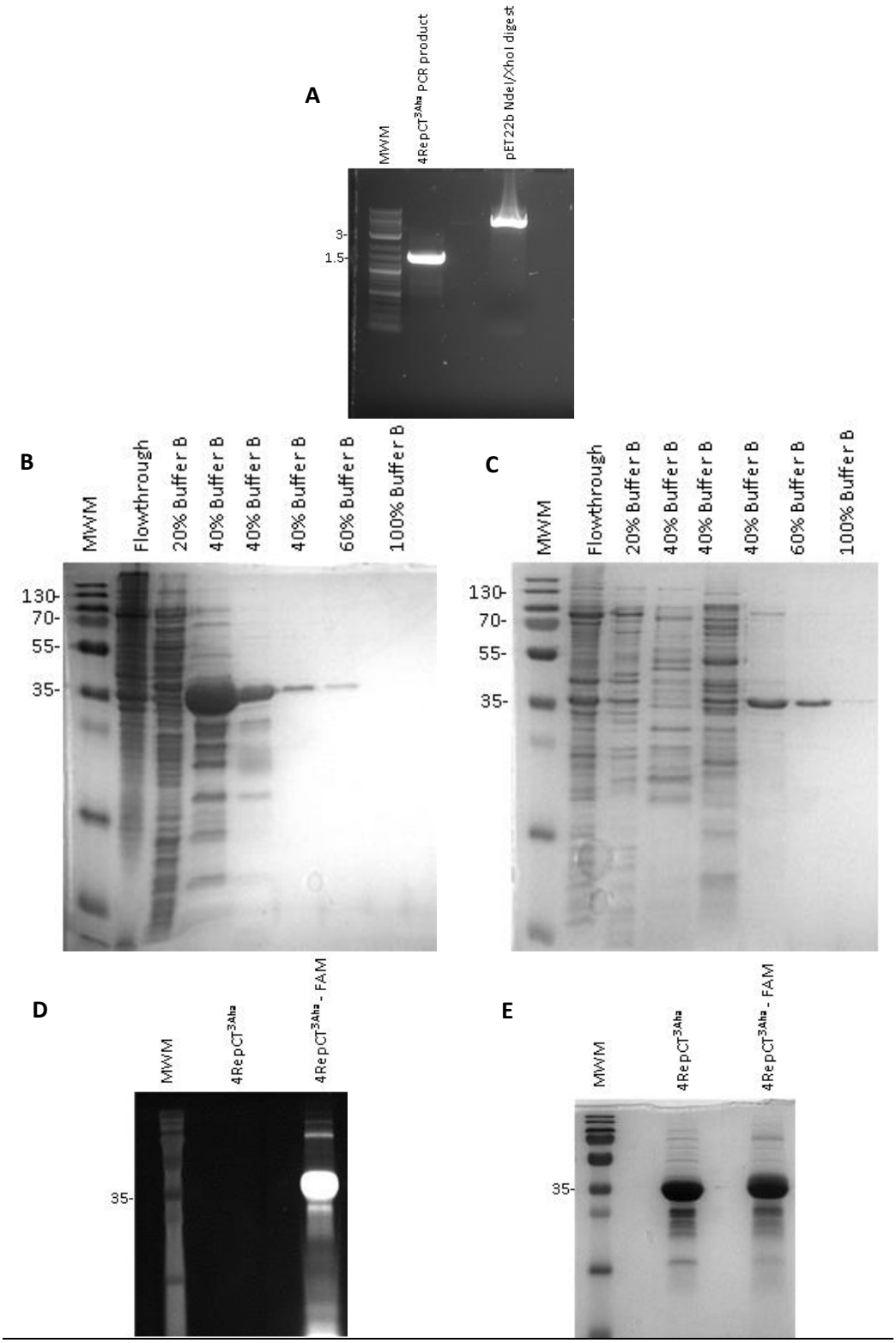

Figure 2.6. The pET22b_4RepCT design and protein expression. **A**: agarose gel analysis of 4RepCT gene PCR fragment and restriction enzyme digest of pET22b. **B**: SDS PAGE analysis of 4RepCT produced from pET22b_4RepCT. **C**: SDS PAGE analysis of 4RepCT^{3Aha} protein produced from pET22b_4RepCT. **D**: SDS PAGE analysis of pET22b_4RepCT-produced 4RepCT^{3Aha} conjugated to fluorescein (FAM) alkyne under UV light. **E**: stained SDS PAGE gel from panel D confirming the presence of protein in both lanes. MWM – molecular weight marker, kilodaltons.

2.3.8. Purification of NT2RepCT using Ni^{2+} IMAC

NT2RepCT protein was purified using Ni^{2+} IMAC with an average yield of 230 mg/L (Fig. 2.7).

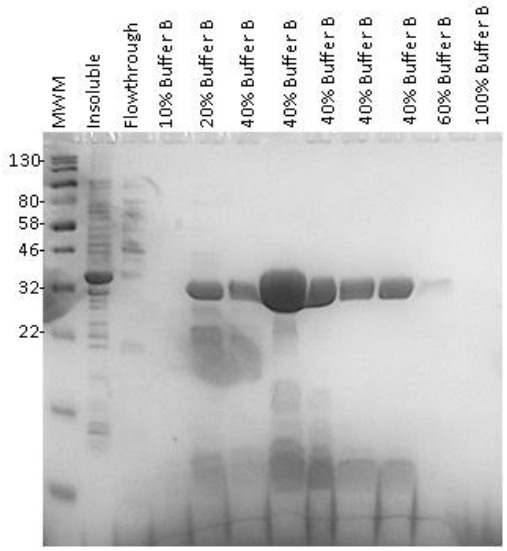

Figure 2.7. SDS PAGE analysis of NT2RepCT protein purified using Ni^{2+} IMAC. MWM – molecular weight marker, kilodaltons

2.3.9. Purification of NT2RepCT using ammonium sulfate precipitation

The majority of NT2RepCT (32kDa) in a sample precipitated at 70% ammonium sulfate (Fig. 2.8), however the sample was highly viscous and difficult to resolubilise indicating the co-precipitation of carryover nucleic acids. In addition, 70% w/v ammonium sulfate co-precipitates most cellular proteins which makes it unsuitable for scaled up purification.

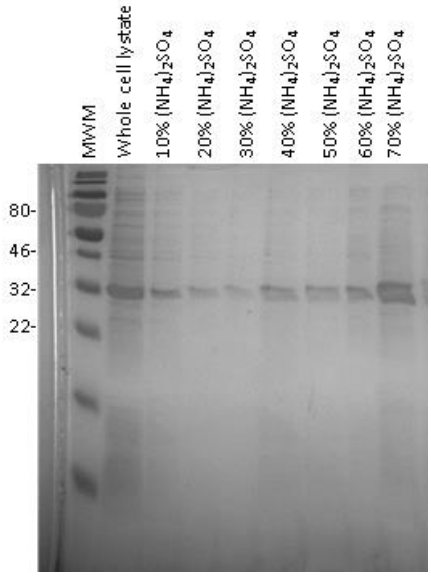

Figure 2.8. SDS PAGE analysis of the precipitation of NT2RepCT protein using increasing concentrations of ammonium sulfate.

2.3.10. NT2RepCT precipitation using isopropanol.

Sample treatment using organic solvents was tested as a potential way for NT2RepCT protein due to the ability of alcohols to precipitate nucleic acids. Whole cell lysate was treated with increasing concentrations of isopropanol, and it was found that NT2RepCT is highly solvent-tolerant and remains in solution when exposed up to 60% v/v isopropanol (IPA) (Fig. 2.9), thus not being applicable as a precipitation method. Despite this, the IPA samples were not viscous which indicates successful precipitation of nucleic acids whilst NT2RepCT remains in solution. In addition, cellular contaminant proteins precipitated as the IPA concentration was increased.

In silico band densitometry analysis showed that the purity of the protein sample was the highest at 40% IPA (Table 2.1).

Table 2.1. Purity of NT2RepCT in solution when treated with 10-50% isopropanol.

Isopropanol concentration (v/v)	**Soluble NT2RepCT purity**
0%	14%
10%	17%
20%	32%
30%	29%
40%	80%
50%	55%

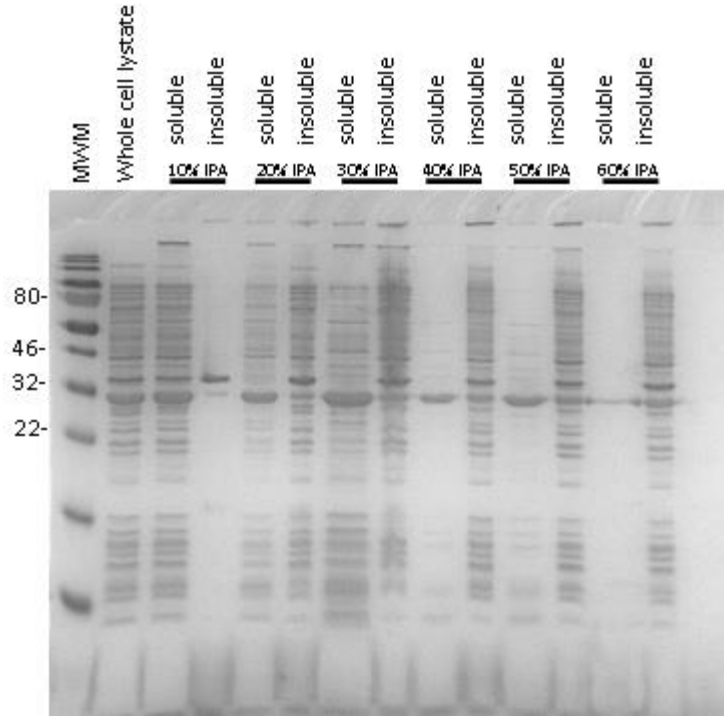

Figure 2.9. SDS PAGE analysis of NT2RepCT solubility in increasing concentrations of ispropanol (IPA). MWM – molecular weight marker, kilodaltons.

2.3.11. Precipitation of NT2RepCT using hydrochloric acid

After the sample was lysed with SDS-containing buffer and treated with 40% IPA to remove the nucleic acids, concentrated hydrochloric acid or KCl[205] followed by hydrochloric acid treatments were used to precipitate NT2RepCT protein from the solution. The samples were then extensively dialysed to remove carryover salts and lyophilised. The samples were freeze dried. The absolute mass of the lyophilised samples was 115 mg (HCl treatment only) and 391 mg (KCl and HCl treatment) per 0.5 L culture each (in comparison to 250 mg/L when using column chromatography).

To investigate the concentration of the protein in the lyophilised sample, Bradford chromogenic assay was used. Lyophilised samples were dissolved to 5 mg/ml. A linear regression plot (using bovine serum albumin as a standard, Fig.2.10) showed that the concentration of protein in the samples was 0.773 mg/ml and 0.53 mg/ml which equates to 60.5 mg and 12.19 mg of protein in KCl +HCl treatment and HCl treated sample, respectively. However, instability and precipitation of the colorimetric reagent was observed during the measurement. This is indicative of the SDS interference with the assay

despite using a BCA kit that contains proprietary additives that decrease detergent sensitivity of the assay (Thermo).

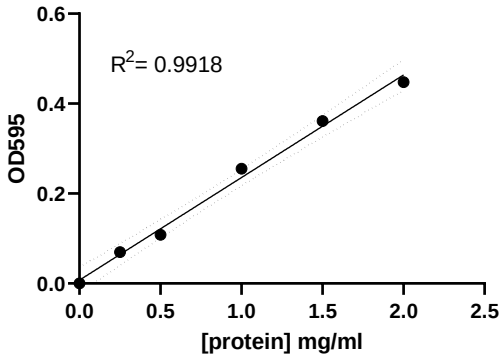

Figure 2.10. Linear regression of OD_{595} bovine serum albumin serial dilutions in the Bradford colourimetric assay.

Gel band densitometry was carried out using the area-under-the curve of column-purified NT2RepCT serial dilutions as a standard (Fig 2.11 A). Only the linear portion of the curve was used to create linear regression (Fig.2.11 B).

The linear regression showed that the protein concentration in HCl-treated sample was 0.929 mg/ml versus KCl+HCl treated sample had 0.441 mg/ml protein. The purity of the HCl sample was 98% compared to 55% purity in KCl +HCl sample.

From this follows that a HCl treatment recovered 104 mg pure protein with 10.3 mg salt and KCl+HCl treatment recovered 94 mg NT2RepCT protein with carryover of 77.59 mg contaminant proteins and 218.57 mg salt (each representing 0.5 L culture biomass). This is in comparison with the recovery of NT2RepCT protein using column chromatography of 250 mg/L. HCl treated sample recovered a comparable amount of NT2RepCT protein to column purification whilst not being limited by column volume. This protocol could form basis for future investigations of scaled up NT2RepCT expression and purification for applications in such as 3D printing.

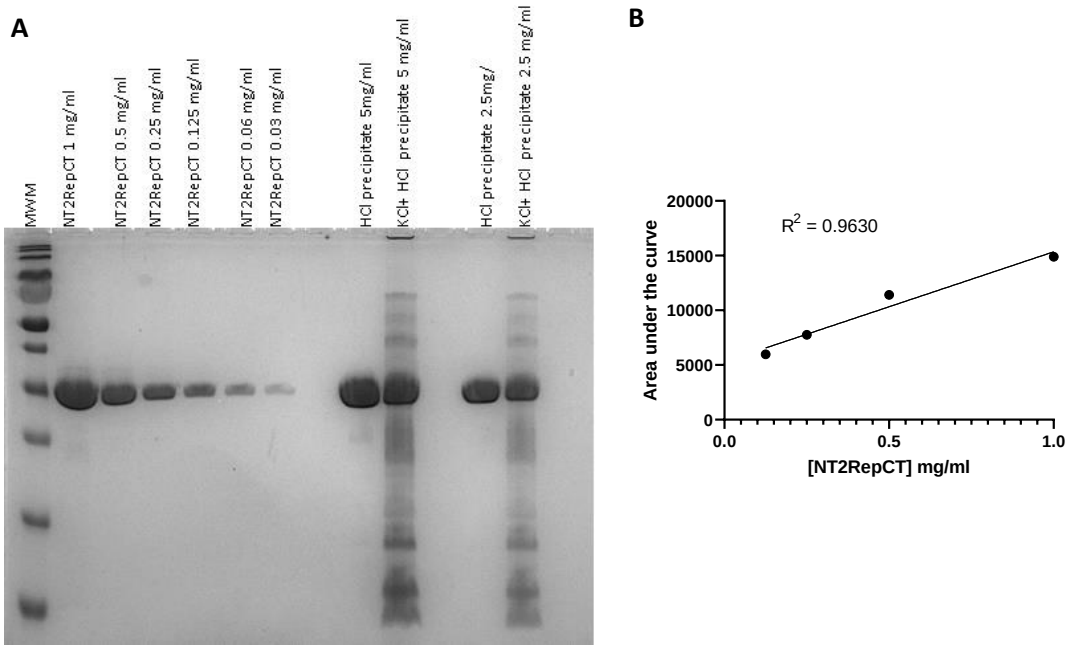

Figure 2.11. Column purified NT2RepCT protein standards (0.03-1 mg/ml). **A**: SDS PAGE gel containing a serial dilution of NT2RepCT standards, HCl treated sample, and KCl+HCl treated sample. MWM – molecular weight marker, kDa. **B**: Simple linear regression of NT2RepCT serial dilution standard band densitometry measurement (area under the curve).

2.3. Conclusions

In conclusion, this chapter summarises technical details of silk protein expression and purification for use in antimicrobial biomaterial applications as described in chapters 3-5. The previously established procedures were carried out to produce a highly hydrophilic protein NT2RepCT, as well as the more hydrophobic spidroin 4RepCT and its l-azidohomoalanine bearing counterpart ^{4RepCT3Aha}.

A selection of empirically selected modifications was carried out to prepare the processes for a scaled-up production and purification of both ^{4RepCT3Aha} and NT2RepCT proteins. It was shown for the first time that 4RepCT and ^{4RepCT3Aha} can be purified using cobalt affinity chromatography that reduces the consumption of imidazole by 57% and increases the yield of protein by 67% compared to the standard nickel affinity chromatography. The ability of 3C protease to cleave 4RepCT^{3Aha} solubility tag was confirmed; the impact of this result will allow further research to bypass the use of a more expensive protease thrombin.

In addition, it was shown that 4RepCT can carry three or four l-azidohomoalanine residues without decrease in the protein yield. On the other hand, the protein yields were significantly reduced when the incorporation of a different methionine analogue homopropargylglycine (Hpg) was carried out. Overall, these findings contribute to cost and yield optimisation of the production of 4RepCT^{3Aha} with the overarching goal to produce this protein at a multi-gram scale.

Further to this, a novel and efficient protocol for column-free purification of NT2RepCT spidroin was developed. This is the first reported approach to reversibly precipitate NT2RepCT spidroin as a means of purification. With yields comparable to that of the standard column-based purification method, this protocol is not limited to column volume and thus can provide opportunity for purification of gram quantities of NT2RepCT for applications such as colloid systems and 3D printing.

3. Colloidal particles based on a highly hydrophilic recombinant spidroin NT2RepCT as a polymeric drug delivery system

3.1. Introduction

A polymeric drug delivery system (PDDS) is a polymer-based colloidal formulation, usually on nano-to-micro scale, that enables delivery of a payload to the target site (intracellular or tissue-localised). The advantages of using a PDDS include increased stability of the payload in the serum, increased cellular uptake, lower immunogenicity, and targeted delivery that ensures reduction in systemic toxicity, controllable release rate, and increased efficacy of the therapeutic payload[206–208]. As a result of these advantages, a variety of PDDS have been developed over the last 50 years and include non-degradable synthetic polymers, biodegradable synthetic polymers, biopolymers, as well as various blends and modifications of these materials to provide the desirable properties for the desired application[207].

The introduction to this chapter focuses on nano-to-micro scale PDDS, specifically spherical and semi-spherical morphologies (nanoparticles, microspheres, micelles, nano/microhydrogels). Although irregularly shaped and larger PDDS are common in medical applications as biomaterials (medicated stents, screws, implants, and films; for films, see chapter 4 and chapter 5 of this thesis)[206], spherical and semi-spherical particles are favoured as PDDS due to the largest surface area which is expected to give the largest loading capacity per unit of material.

Various PDDS materials and means of particle production are discussed highlighting their unique biochemical properties. Lastly, the interplay of particle size, material, and morphology that dictates the application and *in vivo* fate of the PDDS is reviewed.

3.1.1. Polymeric materials

The particle material plays a crucial role for PDDS applications *in vivo*. Depending on the desired administration method, PDDS require plasticity (in the bloodstream) or hardness (*in situ* orthopaedic application), good hydrophilicity for applications in aqueous environment combined with ability to capture hydrophobic payload; and well characterised degradation rates and the metabolic fate of the monomers that must not be cytotoxic[209]. Polymeric materials need to have good immunocompatibility and a benign biochemical nature . High numbers of electrostatic charges are usually disfavoured due to cellular toxicity; however an overall positive charge (or high pI) increases cellular uptake and protein corona adsorption, which determines the pharmacokinetic fate of the particle[210]. To this end, a variety of materials and material modifications are used for specific applications (Fig.3.1).

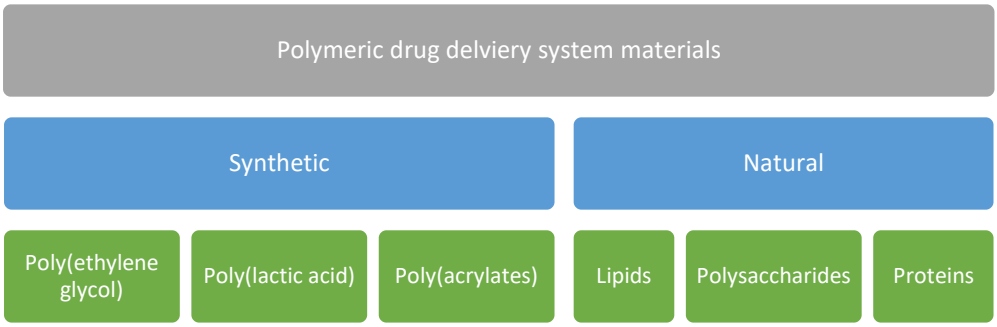

Figure 3.1. Overview of materials used as polymeric drug delivery systems (excluding composites and blends).

Synthetics

Synthetic polymers are widely researched PDDS due to their commercial availability, well characterised chemical nature, and ease of processing into various morphologies (chemical structures shown in Fig. 3.2). Synthetic polymers tend to have good biocompatibility. However, their respective monomers are often toxic, therefore there is a risk of cytotoxicity from incomplete polymerisation. Synthetic polymers can be engineered to include biologically labile chemical bonds such as esters and ethers, therefore making them biodegradable. Below, the key advantages and disadvantages of synthetic polymers as a PDDS are discussed.

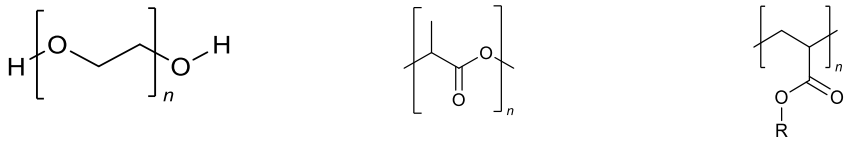

poly(ethylene glycol) (PEG) **poly(lactic acid) (PLA)** **poly(acrylate)**

Figure 3.2. Chemical structures of common synthetic polymeric drug delivery system materials.

PEG: a hydrophilic example

Poly(ethylene glycol) (PEG) is one of the most popular synthetic polymers for drug delivery due to its low immunogenicity, water solubility, tuneable properties, and commercial availability (chemical structure shown in Fig. 3.2). PEG resists plasma protein adsorption, thus conferring a "stealth effect" of increased half-life and reduction in particle opsonization and subsequent aggregation due to its highly hydrophilic nature[211–213]. PEG-based embolization microparticles of tunable diameter are available commercially (LifePearl® and HydroPearl®, Terumo[214–216]). A variety of drug delivery particles, especially lipid-based particles, are coated with PEG (PEGylated) to improve their stability in circulation and reduce immunogenicity with their status ranging from clinical trials to FDA-approved formulations[213,217].

Often, PEG is incorporated into a PDDS as a copolymer or a blend, such as PEG-poly(caprolactone) (PEG-PCL) nanoparticles with diameter 20-220 nm (reviewed in [211]), and PEG- poly(L-lactide) (PEG PLLA) particles[218–221]. PEG is considered partially biodegradable, however the mechanism for its degradability in mammals is unclear; there is evidence for PEG oxidation to PEG-aldehyde and PEG-carboxylate followed by depolymerisation to oxoacetic acid that enters TCA cycle[222].

The widespread use of PEG as a biocompatibility and water-solubility enhancer has raised concerns regarding its immunogenicity. Current evidence has shown that PEGylated particle clearance becomes more rapid upon repeated exposure in an IgM-dependent response[223]. Further, anti-PEG antibodies

have been found in individuals who have never received PEGylated therapeutics, resulting in consequences as severe as an anaphylaxis[213,224], for instance in severe reactions to the Pfizer/BioNTech mRNA COVID-19 vaccine that contains PEG for lipid particle stabilisation[225]. This highlights the need for new biocompatible and hydrophilic materials for polymeric drug delivery systems.

Lactic acid and lactic acid derivatives: biodegradable example

Various poly(lactic acid) (PLA) isomers (such as poly(L-lactic acid), poly(D,L-lactic acid), and poly(D,L-lactic acid; chemical structure shown in Fig. 3.2) are commonly used PDDS due to their biodegradable nature and the potential for production from renewable resources[226] . These polymers are available for clinical use as microspheres and implants; PLA nanoparticles are in clinical development (reviewed in [227]). Lactic acid and its derivatives have low toxicity, however the acidic nature can have detrimental biological effects including triggering of the inflammatory cascade; this is of concern in applications where the PLA is implanted *in situ*, for example in orthopaedic applications, or when material encapsulation has occurred[228]. Prolonged localised acidification as a consequence of the material breakdown can impair tissue repair mechanisms leading to chronic inflammation.

Acrylic acid derivatives: an example of a mechanical resistance

Poly(acrylates) and poly(acrylamides) (Fig. 3.2) are transparent and rigid plastics with a bioinert nature and a long history of use as bone cement in dentistry and orthopaedics. Thermal plasticity and hardness of these materials (depending on the formulation) allow for manufacturing for a range of particle sizes and morphologies from nanometre particles to millimetre pellets and tablets[229].

Poly(acrylate)-based beads with diameter up to 4mm are routinely loaded with silver and gentamycin and implanted on joint replacements and bone grafts to serve as a drug delivery vehicle to the surgical site[230,231]. Methacrylate particles are used in sustained oral drug delivery as a pH-independent, digestion-resistant and mucoadhesive vehicle (Eudragit and Carbopol, EVONIK[232,233]).

However, acrylic acid polymers are non-biodegradable, and non-polymerised monomers are highly cytotoxic and genotoxic despite relatively low immunogenicity[234–236]. Therefore, the search for new PDDS aims to discover new materials that combine mechanical properties of acrylates with biocompatibility of other polymers.

Biologicals

Natural polymers are appealing PDDS due to the biodegradable, non-toxic nature of both monomers and whole polymers, and good aqueous solubility. Many biologicals are sourced from naturally occurring materials, such as lobster shell chitin; others can be produced at scale in recombinant hosts, therefore reducing the use of petrochemicals and environmentally hazardous chemical processes. Further, natural polymers can take advantage of various targeting, transport and uptake systems present in biological systems.

Lipids

Lipid particles are the most common class of FDA-approved nanomedicines with a range of products already available for clinical applications[237,238]. Lipid particles have been created from waxes, free fatty acids, paraffin, and most commonly, phospholipids[237,239,240](Fig.3.3). Due to similarity with the cellular lipid bilayer, phospholipid liposomes have very high bioavailability[237]. The success of liposomes in various clinical applications highlights amphiphilic molecules as a favoured PDDS due to the ability of the lipophilic domains to bind a drug, and the ability of the hydrophilic domain to maintain water solubility and biocompatibility.

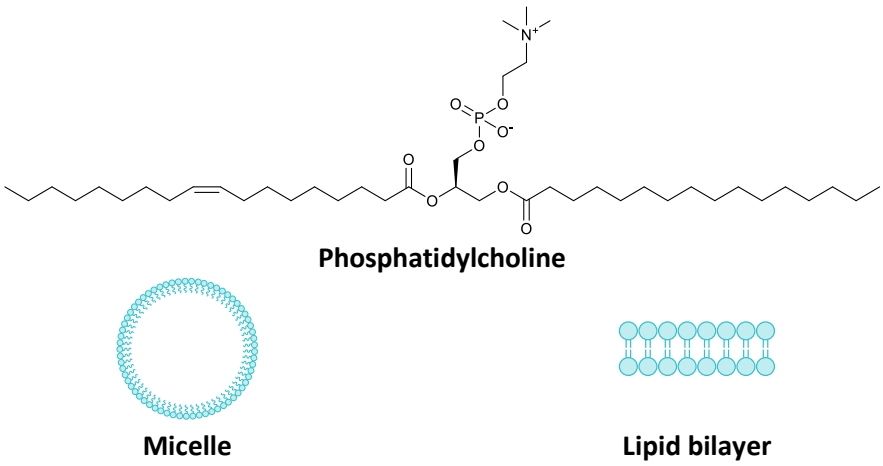

Figure 3.3. Phospholipids are organic molecules composed of a phosphate group and fatty acid chains joined by a glycerol backbone. These molecules can arrange into single-layer or bilayer micellar structures.

Further lipid-based biologicals such as viral capsids, extracellular vesicles, and resealed erythrocytes are an emerging lipid-based delivery vectors due to their favourable size and shape, as well as excellent biocompatibility and the capability of scalable recombinant production. Despite these advantages, the current processes for these material manufacturing and isolation are expensive and relatively time-consuming.

Polysaccharides

Polysaccharides are biodegradable, highly water-soluble, naturally occurring and highly abundant polymers with great variety in their size and biochemical nature making them highly applicable as a PDDS. For example, cellulose is routinely used in various biomedical applications as embolic particles[241], and cellulose nanoparticles have been tested for the delivery of various in a range of clinical trials (reviewed in [242]). The most popular polysaccharides used in PDDS development are alginate, cellulose, hyaluronic acid and chitosan[243](Fig 3.4). Further, polysaccharides are an appealing PDDS due to abundance of chemically reactive groups (especially hydroxyls) that allow for chemical functionalisation and fine-tuning of biochemical characteristics of the material. This potential has encouraged researchers to employ polysaccharides for drug bioconjugations; however, seeing as

these conjugates are technically prodrugs as opposed to drug delivery vehicles or materials, they are beyond the scope of this discussion.

Similarly to PEG, polysaccharides are often used in composite materials to change their overall charge, increase biodegradability and decrease immunogenicity[244]. Polysaccharide PDDS require additional stabilisation due to their highly water-soluble nature; this is achieved by chemical crosslinking, pH modification, and chemical modification resulting in water-swollen hydrophilic structures called nanohydrogels and microhydrogels.

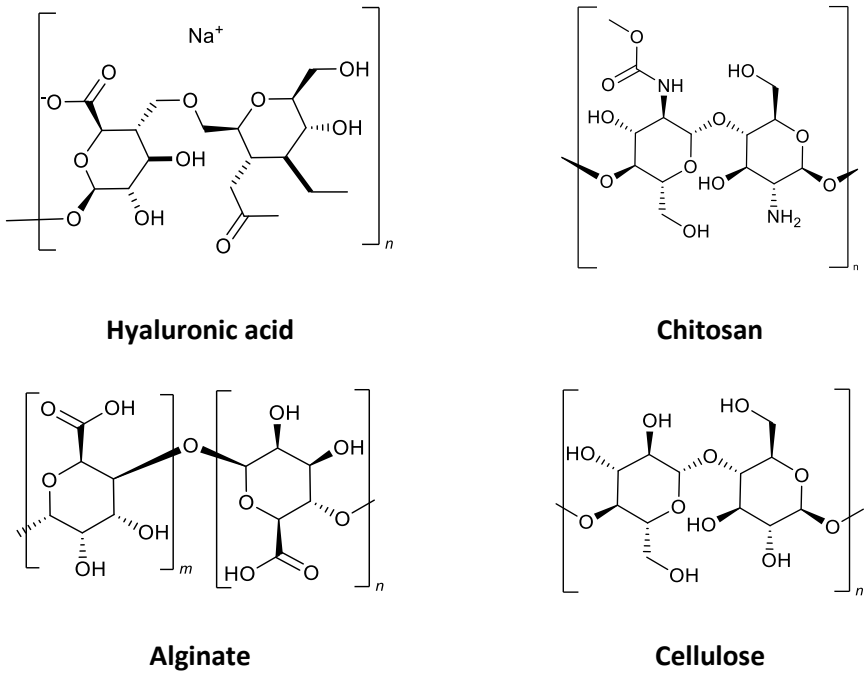

Figure 3.4. Polysaccharides commonly used as polymeric drug delivery systems.

Some drawbacks of use of polysaccharides as a PDDS include short biological half-life and poor shelf life, which is often addressed by crosslinking the particles using chemical or physical methods. Some polysaccharides, typically plant-derived, can be highly immunogenic thus highlighting the need for a polymeric material that can be produced and purified using better controlled methods.

Proteins as a PDDS

Proteins that are used as a PDDS can be broadly divided into synthetic peptides (such as poly(lysines)), naturally occurring proteins, and recombinant proteins. The interest in amino acid polymers as a PDDS stems from their biodegradable nature and non-toxic breakdown products. Amino acids have a variety of chemically reactive motifs in their side chains (hydroxyls, amines, thiols, carboxyls) allowing for easy chemical modification. Further, some proteins and peptides have an inherent structure and functionality that can be deployed in a drug delivery system. Using synthetic biology and recombinant protein expression procedures, proteins can be engineered into chimeras combining naturally occurring functionalities, such as targeting, with a drug delivery capability.

Synthetic peptides

Synthetic peptides (SP) are usually produced using solid-phase synthesis, which allows for very high control of the manufacturing conditions, thus minimising the presence of biological contaminants and ensuring low polydispersity of the final product. SP typically contain charged amino acids such as lysine, arginine, asparagine, and glutamic acid, often as homopolymers with < 100 amino acid residues[245] . SP are usually processed into micellar structures thus taking advantage of their amphiphilic character[245]. A range of SP are in clinical development, and polyglutamate and polyleucine-based amphiphilic platform Medusa (Flamel Technologies) is an approved slow-release system for protein (interferon alpha) delivery for renal cancer and hepatitis[246]. Poly(lysine) SP are researched as a gene delivery vehicle as their positive overall charge helps to bind poly-negatively charged nucleic acids and also increase cell permeability[247].

Despite these advantages, solid-phase synthesis remains a poorly scalable process that involves environmentally damaging reactants and solvents, therefore new and greener processes are continuously sought after.

Naturally occurring proteins

Naturally occurring proteins are inexpensive materials that can be derived from plants (zein, soy protein, gliadin) or animals (albumin, keratin, collagen, elastin, silk). Most proteins used in PDDS have hydrophobic nature that encourages protein aggregation and thus entrapment of the payload. Some proteins have an innate functionality as delivery platforms, and they tend to assemble into cages, for example apoferritin, heat shock proteins, vault proteins, and bacterial encapsulins[248]. These proteins assemble into structures with hollow interiors that can be used for drug loading, uptake, and intracellular release.

Plant-derived proteins

Plant-derived proteins are among the most abundant proteins in nature with good scalability potential. For example, zein is a water-insoluble structural protein (prolamin) derived from maize. Due to zein's hydrophobic nature, it can be processed into a range of morphologies that have good retention of hydrophobic therapeutics (reviewed in [249,250]). Zein can be immunogenic in individuals with maize-protein allergy including those with gluten allergies[249]. Further, zein is naturally associated with xanthophyll (carotenoids) which can be immunogenic, as well as reduce drug loading capacity of zein-based PDDS and cause broader size distribution in particle manufacturing[249] . The size of zein PDDS is directly correlated with its immunogenicity with some evidence showing low immunogenicity of zein nanoparticles with 100-400 nm diameter and significant increase in immunogenicity in mice when particles with > 400nm diameter were administered subcutaneously[249,251] .

Animal-derived proteins

The most commonly used animal derived protein in biomedicine is keratin and its hydrolysed counterpart gelatin. Keratins are water insoluble fibrous proteins that compose hair, skin, feathers, nails, horns, and wool of animals, as well as various intracellular structural components[252] (Fig.3.5 A). As a by-product of farming, keratin-containing materials are cheap and widely available. Keratin resists digestion but is resorbable and has excellent biocompatibility[253]. From the biochemical perspective,

keratins are rich in cell-adhesive motifs that can be used to promote wound healing[252]. Further, they are rich in cysteine, a thiol-bearing amino acid that can be used in bioconjugations.

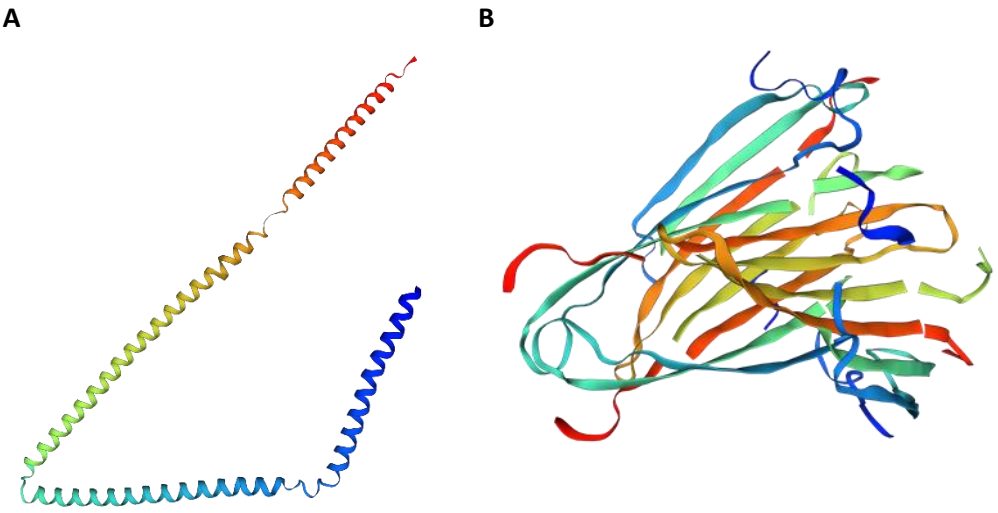

Figure 3.5. Animal-derived products used as a polymeric drug delivery system. **A** - bovine cuticular keratin Type I (fragment; homology model) Q0P5J7 (KRT35_BOVIN); **B**-Silkworm heavy chain fibroin N-terminal domain P05790 (FIBH_BOMMO).

Keratin's self-assembly into 3D structures has been studied in depth for various applications from drug delivery to tissue culture, and huge variety of porcine and bovine gelatin products are routinely used in clinic from wound dressings to stents, sponges, meshes, and tissue scaffolds. Gelatine microparticles are widely available for embolization purposes, for example Embosphere PRO (Terumo), QuadraSphere and EndoSphere (Merit Medical Systems)[254]. In 2000, an estimated 50,000 tons of gelatin were produced for medical applications alone[255] . Gelatin nanoparticles are intensively researched as a drug delivery vehicle (reviewed in depth in [256]), however currently no keratin or gelatin based nanomaterials are being tested in clinical trials.

Another animal derived protein that has a long history of use in medical applications is silk fibroin from *Bombyx mori* (Fig.3.5 B). Conventionally used in surgical sutures and tissue scaffolds, silk fibroin materials have low immunogenicity, good mechanical properties, and optimal biodegradability profile

in vivo[257,258]. Due to these characteristics, fibroin is a highly appealing candidate for PDDS in nano-to-microscale in various morphologies[259–261]. Fibroin microparticles are currently in clinical trials for drug delivery in vocal cord paralysis (NCT03790956). No fibroin nano-PDDS are being trialled in clinic.

There are several challenges associated with the use of naturally occurring proteins as PDDS. Some proteinaceous materials exist in nature as heterogenous mixture of polymers with different molecular weights which results in batch-to-batch variation and unpredictable loading and release kinetics. For instance, natural silkworm silk is strongly associated with silk sericin that in combination with silk fibroin is known to provoke a severe immune response despite not being immunogenic on its own[262,263]. The removal of sericin is a three step process that includes partial degradation of fibroin resulting in broad distribution in the molecular weight of proteins; this distribution complicates processing of fibroin into materials due to inconsistencies in their nature, as well as affecting the mechanical properties of the regenerated fibroin materials[259]. Similarly, keratin extraction involves harsh processing conditions that can introduce heterogenicity in the final material and uses environmentally toxic chemical like mercaptoethanol to reduce cysteine disulfide bonds[252].

Lastly and most importantly, use of animal-derived proteins can contribute to zoonotic disease transfer as a side effect of intensive farming practices. Lyophilised keratin samples are routinely found to contain various potentially pathogenic species such as *Salmonella typhi* and *Klebsiella pneumoniae and Bacillus spp*[264–266]. In bovine keratin, bovine spongiform encephalopathy -causing prions are a major concern as they also cause Creutzfeldt-Jacob disease in humans, a poorly understood and fatal condition[267,268].

Recombinant proteins

Recombinant protein production aims to enable the use of the uniquely biocompatible nature of proteins in PDDS applications by addressing a range of concerns associated with animal-derived protein use.

Recombinantly produced proteins materials can have better homogenicity in light of the capability for introduction of affinity tags and other motifs that aid purification under mild conditions. Various targeting moieties (antibodies, cell penetration domains) and secondary functionalities can be added to the base protein to complement the drug delivery capacity (such as antimicrobial peptides). Further, recombinant protein expression enables the design of proteins for specific applications by designing the size of the protein or combining motifs of known tertiary structures and biological activities. For example, nature-inspired miniature proteins based on silk and elastin amino acid motifs have gained considerable interest as a PDDS due to their "near ideal" elastic behaviour (ability to return most of the energy upon relaxation), predictable and controllable phase-separation properties and structural similarity to human extracellular matrix components[269]. Lastly, highly controlled conditions of recombinant protein production minimise the risk of carryover of zoonotic diseases.

Recombinant collagen and keratin

Recombinant collagens and keratins (full and partial length) have been produced in a range of expression systems from bacterial to eukaryotic cells to transgenic animals. In *Pichia pastoris*, recombinant collagen yields up to 1 g/L have been reported[270] . Mammalian cells are uniquely capable of producing full length, fully hydroxylated collagen identical to mammalian collagen with yields up to 20 mg/L[270] . Recombinant keratins are usually purified from their expression systems as insoluble inclusion bodies[271] which means that the material needs to be resolubilised and reconstituted prior to application in processes similar to those used in resolubilisation of natural keratin. Recombinant human keratins and collagens have excellent biocompatibility as PDDS[271,272]. Despite these advances, recombinant human collagen and keratin manufacturing is prohibitively expensive for PDDS development using current technology, with the material price for pure, full length human collagen reaching £500 per 10 µg (AbCam). This is due to the cost of material production in mammalian cell culture combined with the fact that non-mammalian production is disfavoured due to the protein folding requirements (for correct disulfide bond formation) and extensive posttranslational

modification of human structural proteins (including hydroxylation, and potentially different glycosylation patterns).

Recombinant silks

Whilst recombinant full length silk production poses a technical challenge due to repetitive and hydrophobic nature of the core domains, miniature fibroins and spidroins can be produced in bacterial and fungal expression systems with high yield, relatively cheap consumables, mild processing conditions, and short generation times. Recombinant spider silk PDDS are discussed in Chapter 1 Introduction, and in short their morphological diversity, scalability of production, and exceptionally immunocompatible nature in combination with tunable mechanical and biological properties make silks very appealing candidates for PDDS[137,153,167]. Similarly, recombinant fibroin micro-to-nano materials are successfully used as drug delivery vehicles *in vitro*[257,273].

3.1.2. Methods for polymeric drug delivery system production

The preparation of colloid particles often involves a two-phase system composed of a solvent phase that contains dissolved base material and a dispersing phase where the base material is insoluble. The dispersing phase is often subjected to some type of mechanical force, such as magnetic stirring, microfluidics, or ultrasound to increase the energy of the system. Techniques for PDDS manufacturing are reviewed in Table 3.1.

Further, a variety of approaches are used to stabilise particles to ease the removal of the dispersing phase and increase particle shelf life. These approaches include physical methods (heating/drying, ultraviolet light irradiation); chemical crosslinking with reactive linkers (formaldehyde, glutaraldehyde), and enzymatic approaches (transglutaminase)[243,256,274,275].

Despite the variety of the available colloidal PDDS preparation methods, the main issues of inconsistency in particle sizes and shapes remain a major problem complicating the progress of colloid PDDS to the clinic. This is often addressed by advanced filtering techniques and particle stabilisation additives that require tailoring on the basis of the polymer properties[238]. Further, the crosslinking

methods are often inconsistent which increases batch to batch variability and impairs the ability to predict particle pharmacokinetic behaviour. Some crosslinking agents can also be toxic *in vivo*.

Table 3.1. Polymeric drug delivery system particle preparation techniques and principles.

Method	Principle	Materials	
Polymerisation-induced self-assembly	Material monomers undergo polymerisation in liquid phase or on solid substrate (printing and lithography)	Acrylates, acrylamides, other synthetics	[276,277]
Emulsion-based methods (including nanoprecipitation)	Colloidal dispersion of two immiscible liquids (oil and water, or immiscible organic solvent and water).	Most polymers	[278,279]
Salting out	High charge density causes precipitation via electrostatic interactions and enhancement of hydrophobic effect around an organic molecule.	Protein-based materials, PLA, acrylate polymers	[280,281]
Drying-based methods	Polymer is dissolved in a solvent which is then removed by evaporation. Often carried out by spray drying, electrospraying, or using various casting techniques	Most polymers dissolvable in volatile solvents	[282–285]
Sol-gel transition	Polymer swells in water and an applied mechanical force encourages hydrogel separation into smaller particles	Nanohydrogels and microhydrogels	[191,286,287]
Innate assembly	Biologically programmed affinity for other subunits	Viral particles, protein cages, nucleic acid nanostructures	[248,288]
Supercritical fluids	Supercritical fluid is saturated with a solid substrate and depressurised (into a gaseous or liquid phase) resulting in a rapid nucleation of the substrate	Metals, PLLA, carbon nanotubes, cellulose, and other biological polymers	[289]

3.1.3. Particle size and shape

Size has a critical importance for determining the PDDS application *in vivo*. For applications that require cellular uptake of the payload, such as chemotherapy, the PDDS must be in nanometer range (1-1000 nm)[290]. In eukaryotic cell transfection, particles ranging from 100 nm to <1 µm can be taken up by a cell. Cellular internalization of microspheres with a diameter < 200 nm involve passive process (clathrin-coated pits) whereas particles up to 500 nm can be taken up by non-phagocytic cells in an

energy dependent (caveolae-mediated) internalisation processes such as macropinocytosis[291–293]. Particles > 1 µm are called embolic as the injection of such material into the bloodstream causes occlusion of smaller blood vessels and subsequently cessation of blood perfusion to the affected area[294]. Whilst such occlusion can have a serious detrimental effect to the healthy tissue, these materials are widely used in surgery as an intervention for hypervascular tumours such as uterine fibroids and arteriovenous malformations[294–296]. Embolization particles are often loaded with a chemotherapy agent or a radioactive material. The diameter of embolization particles currently used in surgical applications vary from 20 to 1500 µm; smaller aggregation-prone particles are also applicable[295,297,298]. Further, microparticles are widely used in various *in situ* applications (injected into the site as opposed to the bloodstream) where they serve as a local prolonged drug delivery system[299].

Lastly, particle size influences its removal from the system: particles smaller than 6 nm are excreted by renal filtration, whilst 6 nm – 3 µm particles are removed from blood circulation by reticulo-endothelial system and hepatic clearance[300]. Alongside these clearance mechanisms, biodegradable particles can be metabolised into their monomer components and resorbed by the body[301]. Figure 3.6 summarises the *in vivo* fate of particles from localisation to excretion depending on the diameter.

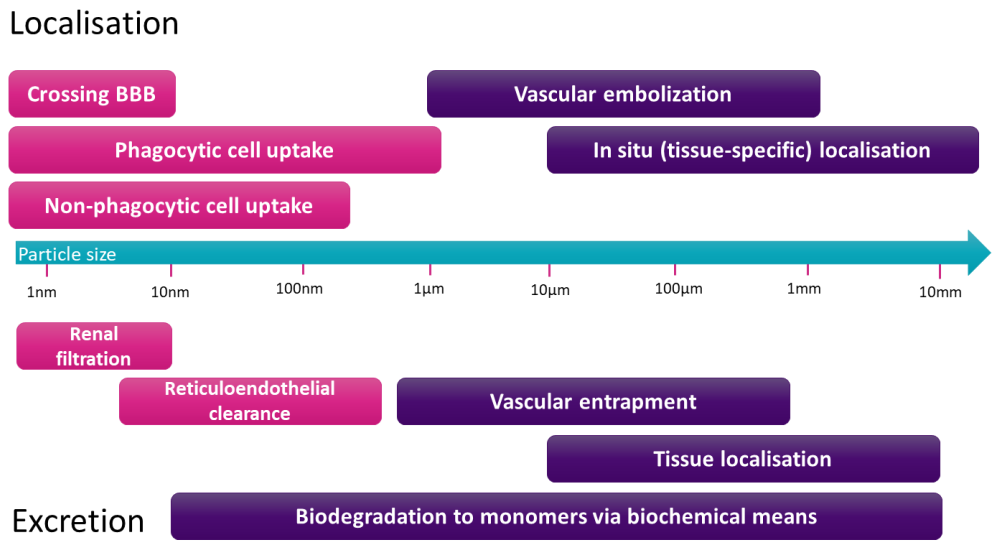

Figure 3.6. Particle *in vivo* fate (localisation and excretion) based on their diameter. BBB- blood-brain barrier. Pink rectangles denote intracellular particle uptake and purple rectangles denote *in situ* tissue localisation.

3.2. Aims and objectives

The existing literature highlights the need for new non-toxic, non-immunogenic, and hydrophilic materials for polymeric drug delivery systems. New polymers need to be manufactured using processes that are highly controlled, scalable, and environmentally benign. From a biochemical perspective, amphiphilic molecules are highly favoured for drug delivery as their hydrophilic moieties ensure water solubility whilst hydrophobic regions help to bind the drug.

This chapter proposes the use of a recombinant mini-spidroin NT2RepCT as a new candidate for PDDS. NT2RepCT is a recombinant spider silk protein with a hydrophilic N-terminal domain followed by two hydrophobic alanine and glycine rich domains from *E. australis* MaSp1 and a C-terminal domain from *A. ventricosus* MiSp1 that exhibits high expression levels in *E. coli* (Fig.1.5). NT2RepCT was designed from naturally occurring silk protein motifs that are known to have good immunocompatibility (see Chapter 1). Recombinant production of this protein uses environmentally benign processes that can be adapted to circular economy workflows. These qualities offer an alternative solution to drawbacks with other materials discussed in the introduction to this chapter.

The aim of the research reported in this chapter was to produce and characterise NT2RepCT particles generated by an established methodology for spherical particle production using 1M KH_2PO_4 pH 8 solution[137,139,302] with different degrees of chemical crosslinking using glutaraldehyde.

In this chapter, fully hydrated size distribution and stability of NT2RepCT particles is analysed using traditional particle sizing techniques. NT2RepCT particle morphology is assessed using electron microscopy. Further, the assessment of NT2RepCT particles as a PDDS is assessed using rhodamine B and antibiotic release from the particles.

3.3. Methods

3.3.1. Sphere preparation and crosslinking

NT2RepCT (60 mg) was dissolved in MilliQ water to the concentration of 1 mg/ml and added dropwise to 2 L 1M KH_2PO_4 pH 8 with constant stirring. The suspension was stirred overnight at room temperature followed by crosslinking of 200 ml suspension aliquots with the addition of 25% v/v glutaraldehyde to 0.001%, 0.01%, and 0.1% v/v and stirring for 3 hours at room temperature.

3.3.2. Zeta potential and laser particle sizing

Zeta potential analysis was carried out using a Malvern Zetasizer Nano ZS with a Zetasizer folded capillary cell (1 ml) using 633 nm laser with 13° scattering angle at 25°C.

Particle sizing was carried out using ORIBA LA-960 Laser Particle Size Analyzer (HORIBA Scientific) using 650 nm red laser and 405 nm blue LED at room temperature using 1 M KH_2PO_4 pH 8 as a blank measurement.

Data acquisition was carried out by the technical staff of the University of Nottingham Interface and Surface Analysis Centre (ISAC).

3.3.3. SEM imaging

For high salt imaging, 50 µl of NT2RepCT particle suspension in 1 M KH_2PO_4 was placed onto an aluminium SEM stub, frozen using liquid nitrogen and dried in the freeze dryer. For salt-free imaging, 30 ml NT2RepCT particle suspension was harvested by centrifugation at 10,000 *g* for 30 minutes, resuspended in 5 ml MilliQ water, and 50 µl of the suspension was placed onto aluminium SEM stub and dried as described above.

Samples were coated with gold using a Polaron SC7640 sputter coater with coating time of 90 seconds. Electron microscopy was carried out using JEOL 6060 Scanning Electron Microscope (accelerating voltage 10 V, working distance 10 mm, 40 nm spot size) with JEOL software.

3.3.4. Rhodamine B release assays

NT2RepCT particles were harvested by centrifugation at 10,000 *g* for 30 minutes and resuspended in 5 ml MilliQ water. The particle concentration was determined by placing 100 µl aliquots of harvested samples into pre-weighed 200 µl tubes, followed by freeze-drying and weighing using the analytical balance. The concentration of the particulates was normalised to 50 mg/ml using MilliQ water.

The particles were loaded with rhodamine B (RhB) by adding 100 µl of 50 mg/ml particulate suspension to a 200 µl tube, harvesting the material by centrifugation at 14,000 rpm on a benchtop microcentrifuge for 10 mins, and adding 200 µl 0.1 mg/ml rhodamine B in MilliQ water followed by incubation for 1 hour at room temperature. All of the following centrifugation steps were carried out at 18,626 *g* for 5 minutes. As a negative control of the amount of dye absorbed by the plastic, dye was incubated in empty 200 µL tubes without protein particles. After incubation, all samples were centrifuged, and the rhodamine B solution was carefully aspirated ensuring that the pellet is not disturbed.

Pellets were resuspended in 200 µl 50 mM MES pH 5.5, 50 mM TRIS pH 8 or 50 mM CAPS pH 10 and incubated with gentle agitation at room temperature for 15 mins, 1 h, 3 h, 5 h, and 24 h. The experiment was carried out in triplicate at each timepoint (three samples of particle pellets for each timepoint). Following the incubation time, protein particles were removed from suspension by centrifugation, and 100 µl of supernatant was transferred into a black clear-bottom 96 well plate well. Relative fluorescence intensity was measured at 560/595 nm (excitation/emission) with the gain set at 30 using TECAN Spark plate reader. The relative fluorescence readings were normalised against the readings from RhB only samples without protein particles (negative control); data was analysed using Prism 9 software. Statistical analysis was carried out using one-way ANOVA with Tukey's multiple comparisons test.

3.3.5. Zone of inhibition assay

NT2RepCT particles (10 mg wet weight) crosslinked with 0.01% v/v glutaraldehyde (GA) were incubated with 1 ml 1 mg/ml chloramphenicol solution for 1 hour. As a control, an equal mass of wet cellulose paste was incubated with 1 ml 1 mg/ml chloramphenicol. Cellulose paste was made by partial dissolution of 0.1 g Wattman paper using 10 ml of NaOH (5 M) overnight, washed three times using MilliQ water and harvested by centrifugation at 5000 *g*.

A single *E. coli* NCTC12242 colony was used to inoculate 5ml LB media and grown overnight, then 100µl of a fully grown culture was plated on an LB agar plate and allowed to dry in sterile environment.

Chloramphenicol-loaded samples (1 ml) were harvested by centrifugation at 18,626 *g*, then the wet material was placed in the middle of the plate. Plates were incubated at 37°C for seven days with daily measurements of the zone of inhibition (ZOI). Images of the plates were taken using SynGene gel doc system using upper white light.

3.4. Results

3.4.1. Sphere preparation and crosslinking

NT2RepCT protein was produced recombinantly in *E. coli* BL21 DE3 Rosetta (NEB) and purified using Ni^{2+} IMAC or isopropanol precipitation strategy described in the chapter 2. Upon addition of protein solution to 2L of 1M KH_2PO_4 pH7 solution, white precipitate formed immediately. Occasionally, white thread-like structures were observed floating on the water surface, however these fibres disintegrated overnight.

3.4.2. Zeta potential and laser particle sizing

Estimated zeta potential of the NT2RepCT particles ranged from -9.20 (±6.66) to -6.37 (±2.03) mV with the highest variability observed in the particle preparation crosslinked with 0.001% GA (Fig. 3.7A) .Similarly, particle electrophoretic mobility ranged from -0.721 (± 0.521) to -0.499 (±0.16) (Fig.3.7B). The differences in zeta potential or electrophoretic mobility were not statistically significant (p>0.05, one-way ANOVA).

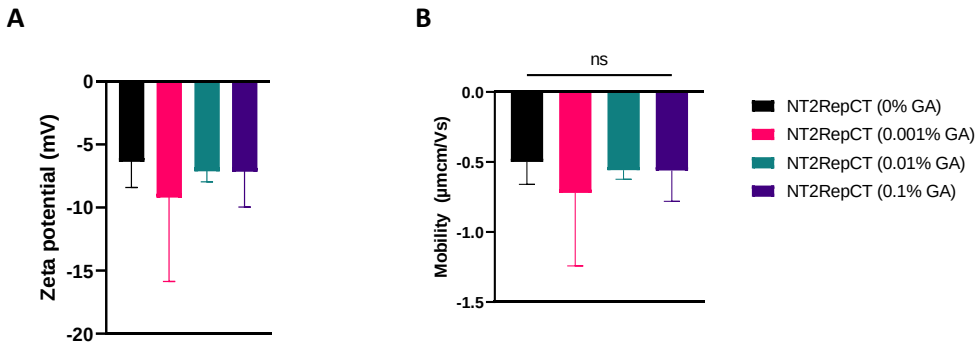

Figure 3.7. Zeta potential (**A**) and the electrophoretic mobility (**B**) of NT2RepCT particles crosslinked with 0-0.1% GA. Error bars denote standard deviation; ns – not significant (p>0.05).

Laser diffraction number weighted distribution data showed that the diameter of the predominant particle species was in the range from 0.389 µm up to 39.26 µm:

- NT2RepCT 0% GA: 0.584-3.9 µm
- NT2RepCT 0.001% GA: 6.72 - 34.3 µm
- NT2RepCT 0.01% GA: 3.41 - 39.2 µm
- NT2RepCT 0.1% GA: 0.389 - 0.877 µm (Fig 3.8 A)

The mean hydrodynamic diameter of NT2RepCT particles (as measured by number distribution) was in the range from 0.49 (± 0.10) to 14 (± 5.18) µm (Fig 3.8 B). NT2RepCT particles crosslinked with 0.001% and 0.01% GA showed a higher variability of the diameter of the predominant particle species compared to 0% and 0.1% GA.

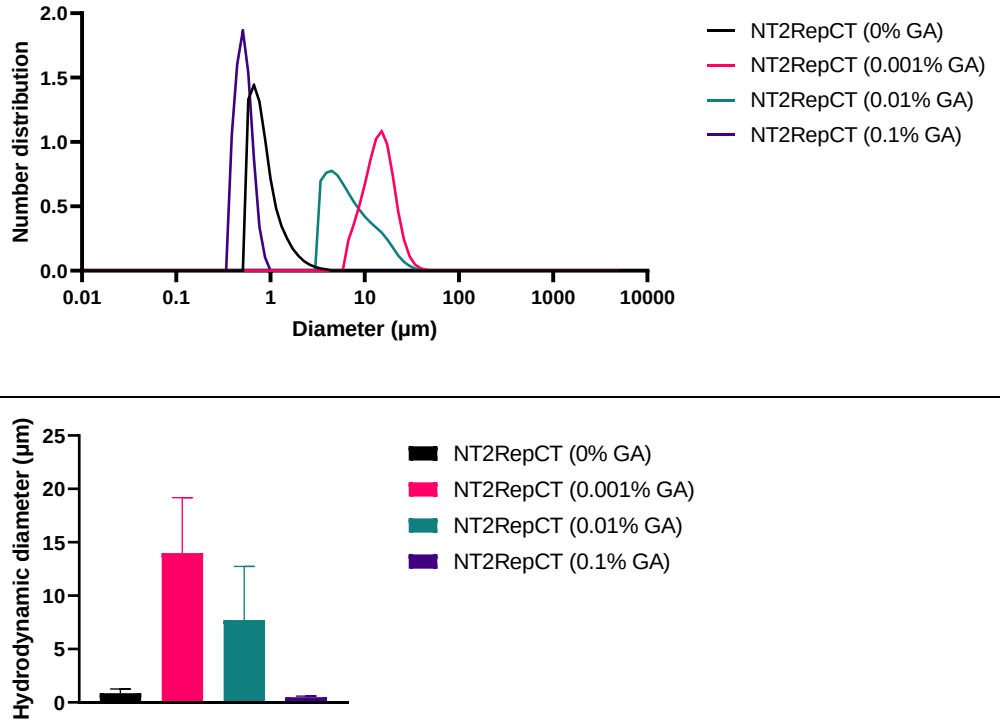

Figure 3.8. The (**A**) number weighted diameter distribution and (**B**) the mean hydrodynamic diameter of NT2RepCT particles crosslinked with 0-0.1% GA. Error bars denote standard deviation.

Volume weighted distribution showed that the particle sizes within each preparation were polydispersed and ranged from

- NT2RepCT 0% GA: 0.389 µm – 1.53 mm
- NT2RepCT 0.001% GA: 0.01 - 0.025 µm
- NT2RepCT 0.01% GA: 0.013 – 452 µm
- NT2RepCT 0.1% GA: 0.389 – 517 µm (Fig 3.9)

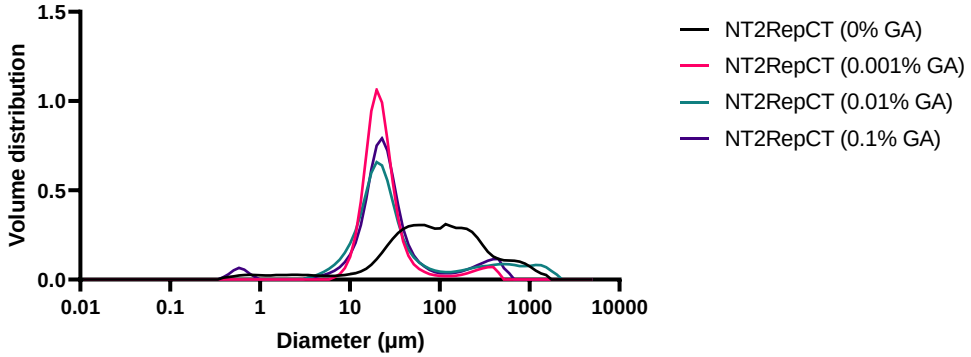

Figure 3.9. Volume weighted particle size distribution of 1M KH_2PO_4-precipitated NT2RepCT particles crosslinked with 0-0.1% GA.

3.4.3. SEM

Scanning electron microscopy in combination with gold coating was used to observe the particle shape and morphology. NT2RepCT 0% GA particles were recovered from the 1 M KH_2PO_4 solution by freeze-drying the suspension onto the aluminium SEM stub, then imaged using SEM. As expected, salt carryover interfered with the imaging by coating the particles; however, spherical structures of polydisperse size could be observed (Fig.3.10).

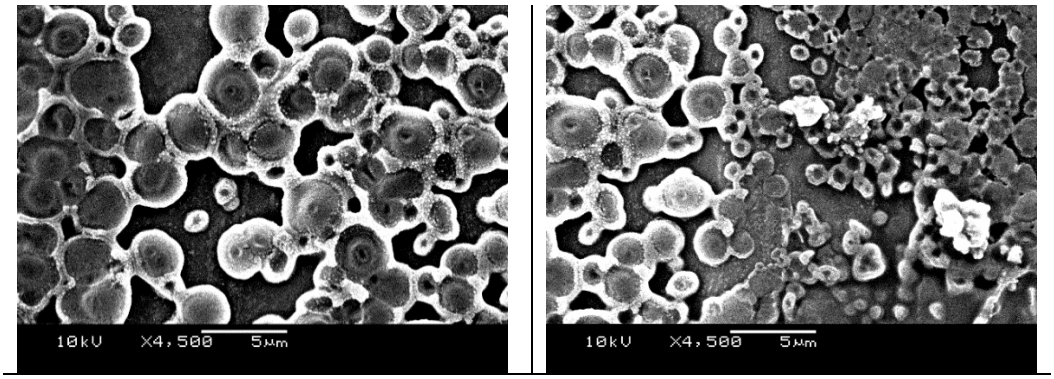

Figure 3.10. Scanning electron microscopy images of NT2RepCT 0% GA particles prior to salt removal from the sample. Scale bar: 5µm.

The removal of salt buffer was attempted by dialysis against low salt buffer and MilliQ water, however the particles resolubilised in the dialysis tubing overnight. To minimise sample exposure to liquid water, the particles were harvested by centrifugation, resuspended in water, snap-frozen using liquid nitrogen and freeze-. dried onto SEM stubs. Further imaging showed minimal carryover of salt crystals into the final sample.

The SEM analysis of 0-0.1% GA-crosslinked samples showed evidence for spherical particles of polydisperse size, as well as fibrous morphologies, and semiregularly shaped particles with diameter ranging from sub-micron size to hundreds of microns (Fig 3.11).

NT2RepCT 0% GA sample had abundantly present features suggesting collapsed spherical particles with approximately 10 µm diameter (Fig 3.11, 0% GA). Some fibres were observed in the sample under 100x magnification.

NT2RepCT particles crosslinked with 0.001% GA showed the poorest stability during the sample preparation with mostly irregularly shaped, poorly defined and collapsed features observed within the sample (Fig 3.11, 0.001% GA). Protein formed sheet-like structures resembling porous films or small samples of a collapsed aerogel as shown under 500x magnification.

NT2RepCT particles crosslinked with 0.01% GA displayed good stability during sample preparation. Discrete spherical particles with a heterogenous diameter size range <10 µm were observed (Fig 3.11, 0.01% GA). A subpopulation of particles with diameter less than 1 µm were present. Areas of collapsed spherical particulates were abundant. In addition to spherical particles, fibrous features were observed under x100 magnification.

NT2RepCT 0.1% GA crosslinked particles showed a strongly interconnected fibrous morphology with few discrete spherical particles (Fig 3.11, 0.1%GA). Some collapsed spheroid features could be observed at x 500 magnification.

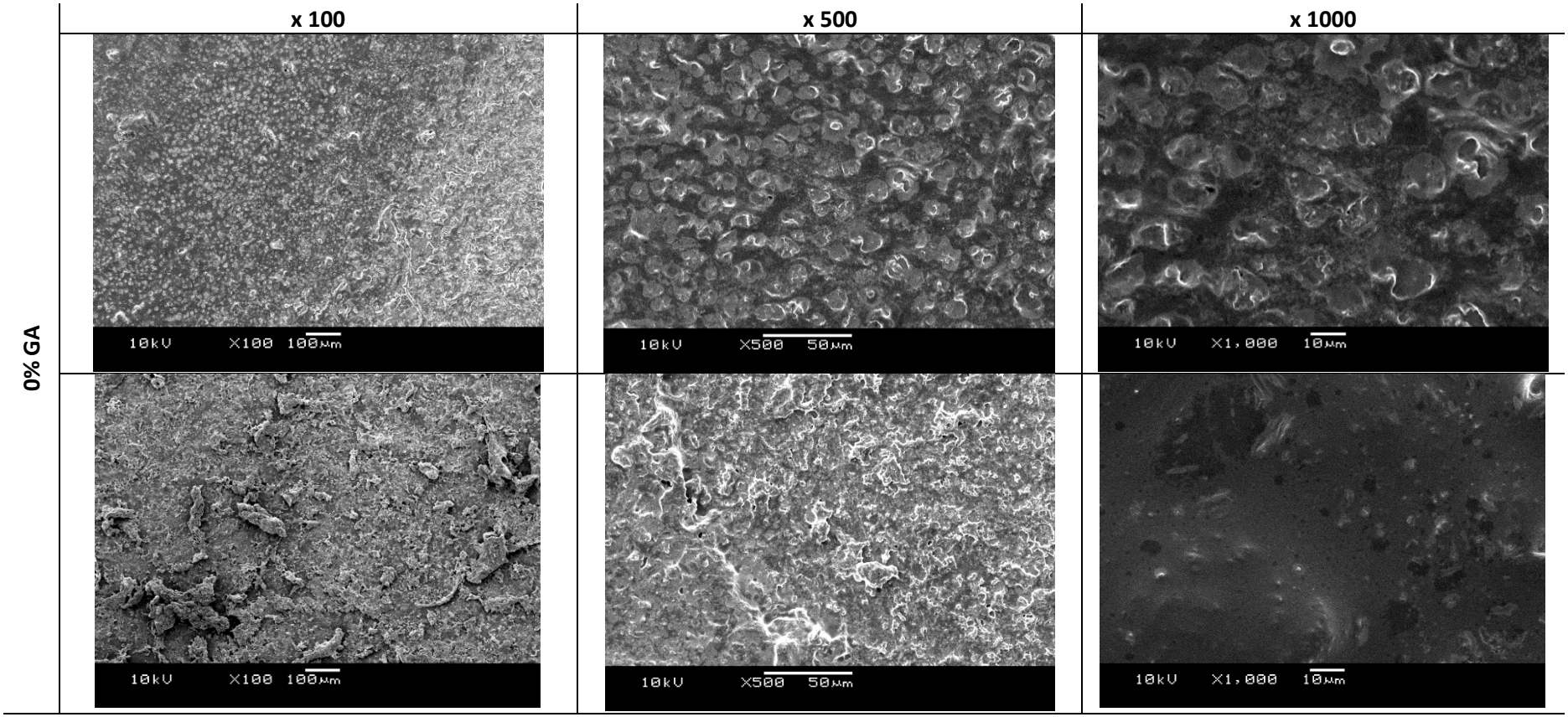

Figure 3.11. Scanning electron microscopy images of NT2RepCT particles under 100-1000x magnification.

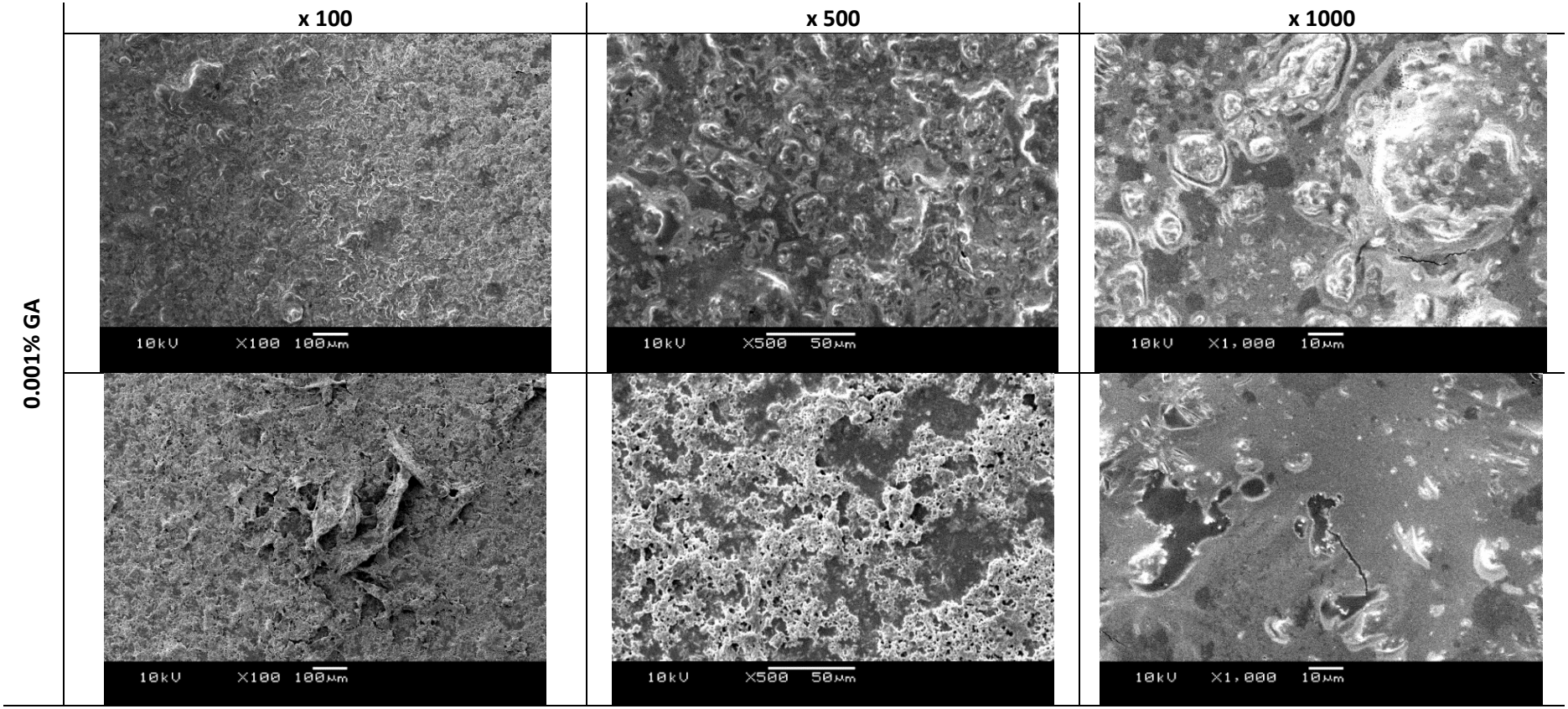

Figure 3.11 (*continued*). Scanning electron microscopy images of NT2RepCT particles under 100-1000x magnification.

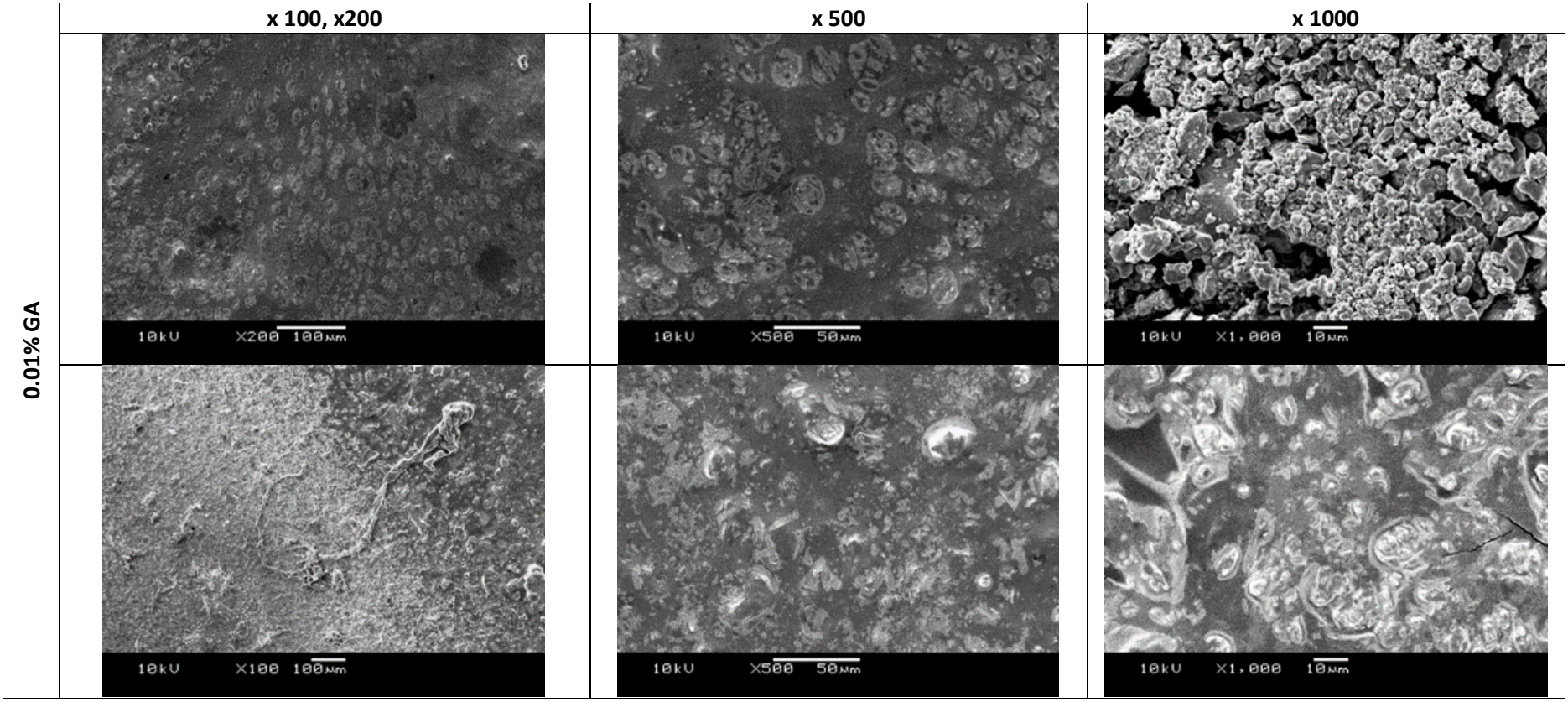

Figure 3.11 (*continued*). Scanning electron microscopy images of NT2RepCT particles under 100-1000x magnification.

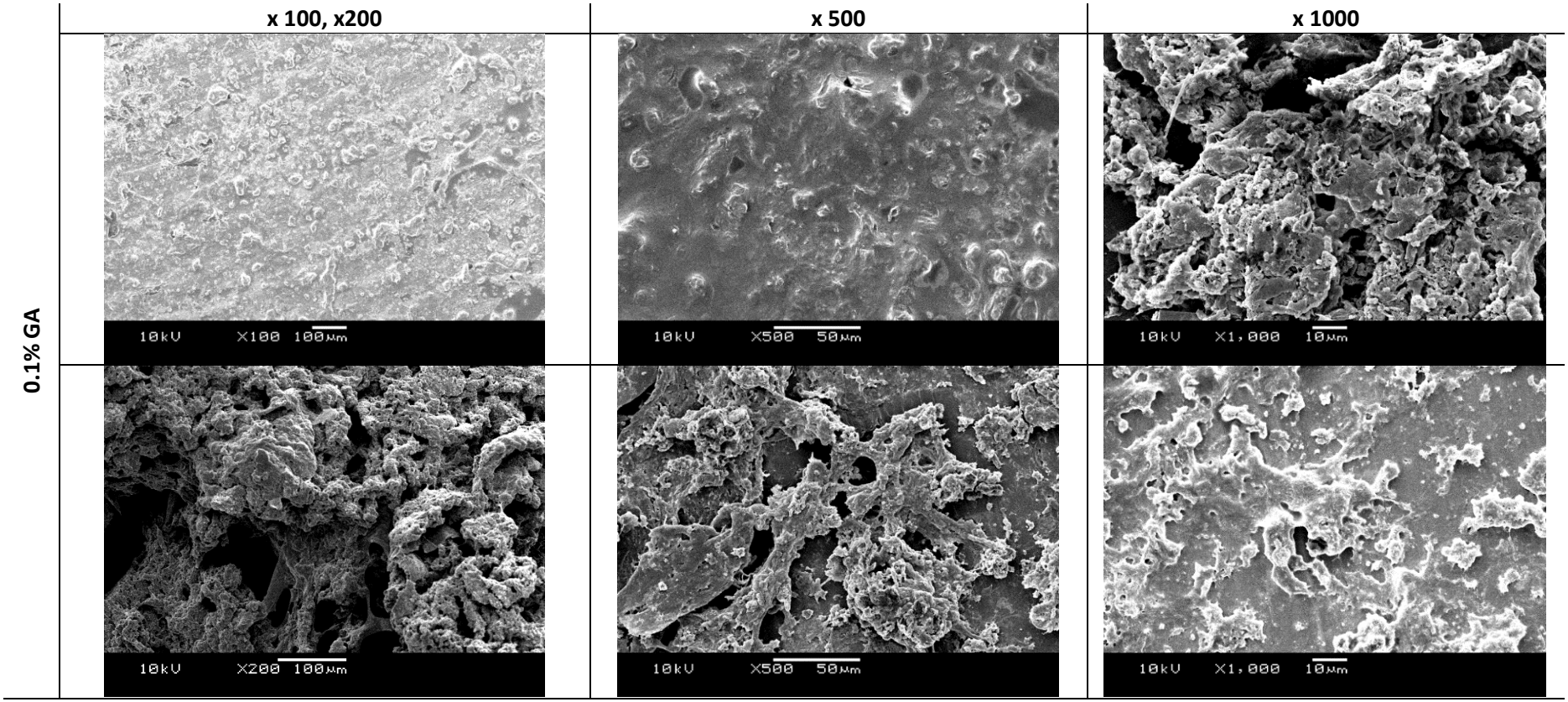

Figure 3.11 (*continued*). Scanning electron microscopy images of NT2RepCT particles under 100-1000x magnification.

Further, the SEM samples were studied for the presence of discrete, well-defined, and non-collapsed spherical particulates (microspheres), as well as any particulates with regular or semiregular shapes (including nano-sized particles).

Few individual particles could be found in the samples crosslinked with 0% and 0.001% GA, and these particles were ranging in their estimated diameter from 2um up to 12 μm (Fig.3.12 A, B). Particles crosslinked with 0.001% GA showed some irregularities and porosity in their shape, whereas 0% GA particles were spherical, and their surface was smooth.

NT2RepCT 0.01% GA samples had the highest abundance of well-defined spherical features, as well as particulates of variable diameter with an irregular shape (Fig.3.12 C). The particle size was highly heterogenous – particle diameters ranged from sub-micron (450-700 nm) to 2 μm in diameter, and larger aggregates over 30 μm in diameter were present.

NT2RepCT 0.1% GA samples showed highly crosslinked nature with large (> 100 μm) aggregation and some evidence for micron-sized spherical particles that were embedded into larger aggregates of irregular shape (Fig.3.12 D). Fibrous structures were observed along with spherical and irregularly shaped aggregates.

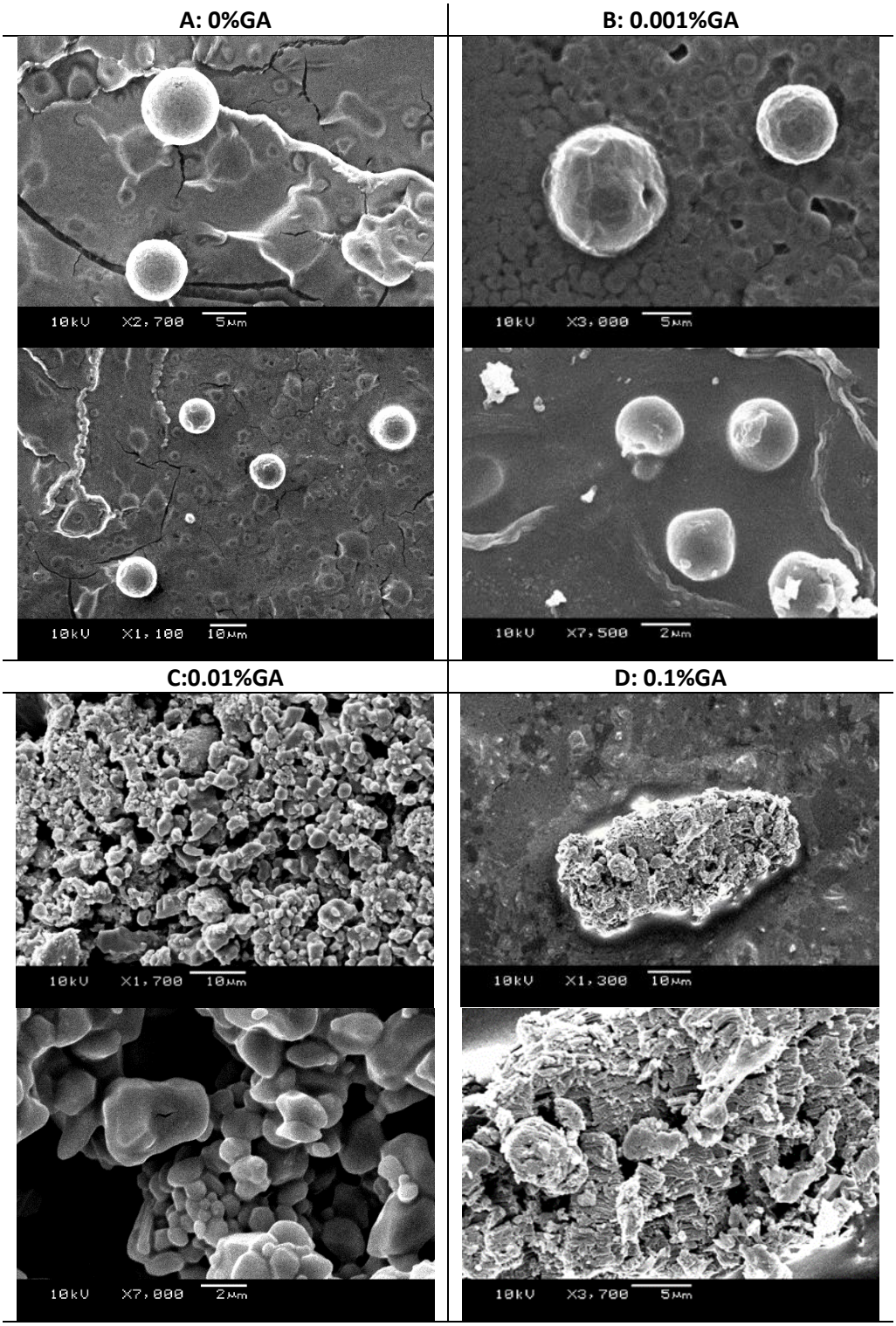

Figure 3.12. Scanning electron microscopy images of NT2RepCT particles of a spherical or semi-regular shape. Crosslinker concentration: **A** -0% GA; **B** – 0.001% GA; **C** -0.01% GA; **D** – 0.1% GA.

3.4.4. Rhodamine B release kinetics

The characteristics of NT2RepCT particles as a potential drug delivery vehicle were investigated by loading the material with a model drug rhodamine B (RhB) and monitoring the release kinetics of the drug hourly over 6 hours and at the 24 hours using relative fluorescence intensity (RF). The relative fluorescence intensity at 24 hours was used as the total cumulative measurement.

Rhodamine B fluorescence at pH 5.5, pH 7 and pH 10 was measured using a standard curve, and no significant pH-dependent fluorescence difference was observed (Fig.3.13).

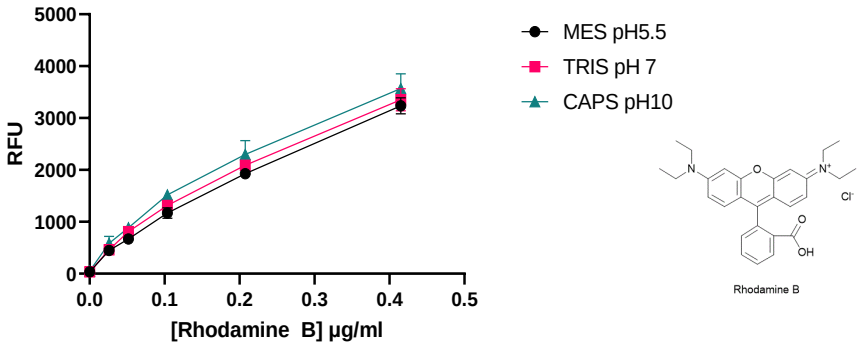

Figure 3.13. Relative fluorescence intensity of rhodamine B serial dilution in MES pH 5.5, TRIS pH 7 and CAPS pH 10. Error bars denote standard deviation.

All NT2RepCT particles regardless of the amount of crosslinker showed similar burst release pattern: 51-96% of the total RhB was released within the first 15 minutes (Fig.3.14 A-D, red arrows). Further peaks in release were arbitrarily defined as 25% increase from the previous timepoint. A second peak of the RhB release was observed in samples at pH 5.5 which occurred at the three-hour timepoint in NT2RepCT 0% and 0.001% GA samples and one-hour timepoint in NT2RepCT 0.01% GA sample (Fig 3.14 A-C, green arrows). No secondary release peaks were observed in NT2RepCT 0.1% GA sample (Fig.3.14 D).

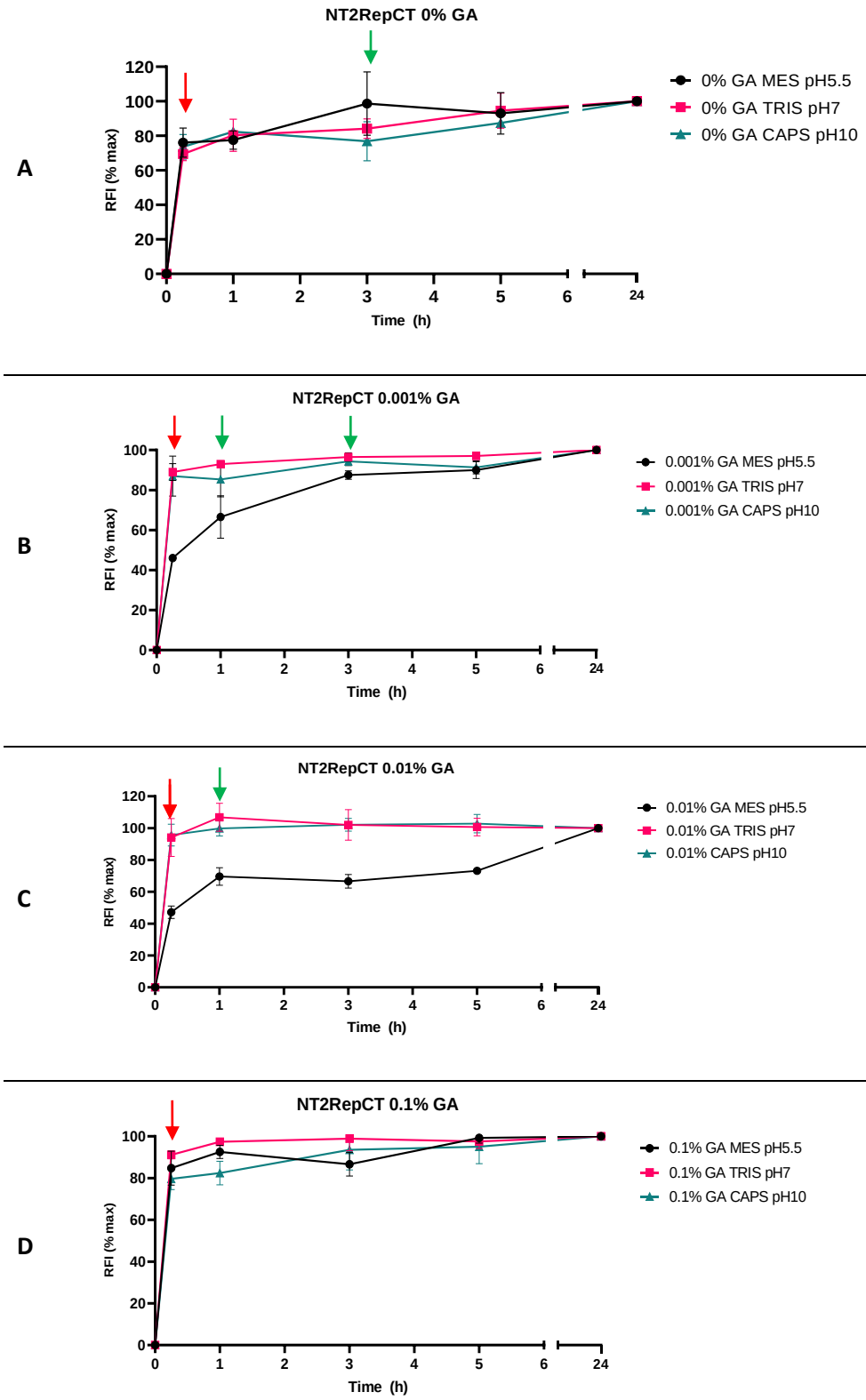

Figure 3.14. Relative fluorescence intensity (RFI) (expressed as a percentage of the maximum RFI at 24 hours) of rhodamine B released from NT2RepCT particles crosslinked with **A**: 0% GA, **B**: 0.001% GA, **C**: 0.01%, **D**: 0.1% GA.
Red arrows indicate peak burst release and green arrow indicates a secondary release peak (defined as a 25% increase compared to the previous timepoint; MES pH5.5 only). Error bars denote standard deviation.

NT2RepCT 0% GA particles in MES pH 5.5 burst-released 76% of the cumulative relative fluorescence within 15 minutes compared to 69% in TRIS pH 7 and 74% in CAPS pH 10 (Fig 3.14 A). The difference in the RhB burst release among these samples was not statistically significant ($p > 0.05$, two-way ANOVA). At three-hour timepoint, the relative fluorescence of the released RhB in MES pH 5.5 increased to 98% of the cumulative relative fluorescence compared to 84% in TRIS pH 7 and 77% in CAPS pH 10. The difference in RF in MES pH 5.5 compared to TRIS pH 7 and CAPS pH 10 at three hours was highly statistically significant ($p < 0.001$, two-way ANOVA).

Similarly, NT2RepCT 0.001% GA particles in MES pH 5.5 burst-released 56% of the cumulative relative fluorescence within 15 minutes compared to 89% in TRIS pH 7 and 87% in CAPS pH 10 (Fig 3.14 B). This difference was statistically significant ($p<0.05$). At the three-hour timepoint, the relative fluorescence intensity of RhB released from the particles in MES pH 5.5 was 93% of the cumulative relative fluorescence compared to 96% in TRIS pH 7 and 92% in CAPS pH 10, however it was not statistically significantly different ($p > 0.05$).

In line with previous release assays, NT2RepCT 0.01% GA spheres in MES pH5.5 released 47% of the cumulative fluorescence within 15 minutes compared to 94% in TRIS pH 7 and 96% CAPS pH 10 (Fig 3.14 C). Within one hour, the released RhB fluorescence intensity then increased to 70% of the cumulative fluorescence in MES pH 5.5 (47% increase), 107% in TRIS pH 7 (14% increase; likely an error in the material handling as the fluorescence at 24-hour timepoint is lower than that at 1 hour), and 100% in CAPS pH 10 (4% increase).

Lastly, NT2RepCT 0.01% GA spheres burst-released 85%, 91% and 80% of the cumulative fluorescence in MES pH 5.5, TRIS pH 7 and CAPS pH 10, respectively (Fig 3.14 D). No second peak of RhB release was observed. RhB RF in CAPS pH 10 at all time points was significantly lower than that of MES or TRIS.

Cumulative rhodamine B release at 24 hours

The 24-hour cumulative fluorescence was measured to investigate the effects of pH and the degree of crosslinking on the rhodamine release from NT2RepCT particles.

Cumulative release of RhB from NT2RepCT 0% GA and 0.001% GA particles was not statistically significantly different at pH 5.5, pH 7, or pH 10 (Fig.3.15). In contrast, cumulative release of RhB from NT2RepCT 0.01% GA particles was inversely correlated with the pH as the highest relative fluorescence intensity was observed at pH 5.5, followed by pH 7 and the lowest RFI was detected at pH 10. Similarly, RhB cumulative release from NT2RepCT 0.1% particles was higher at pH 5.5 and pH 7 compared to pH 10, however there was no statistically significant difference in relative fluorescence intensity of samples at pH 5.5 and pH 7 (Fig.3.15).

The relative fluorescence intensity of RhB released from NT2RepCT particles was inversely correlated with the degree of crosslinking. Rhodamine B released from NT2RepCT 0.1% GA particles showed the highest cumulative fluorescence intensity, followed by NT2RepCT 0.01% GA, 0.001% GA and 0% GA (Fig.3.15).

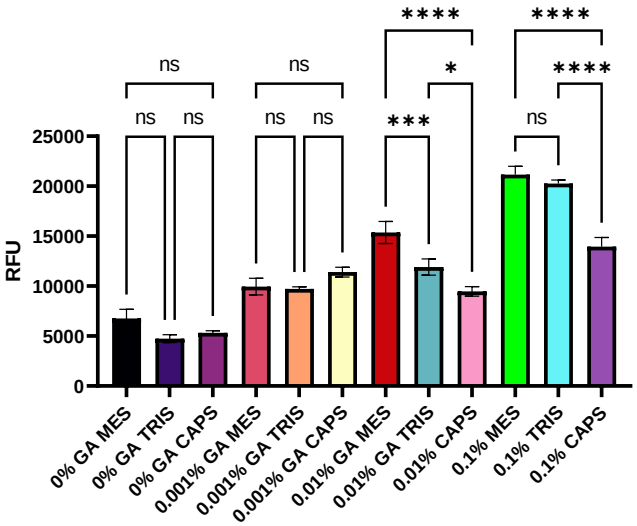

Figure 3.15. Cumulative relative fluorescence intensity of rhodamine B released from NT2RepCT 0-0.1% GA particles after 24-hour incubation. Error bars denote standard deviation, ns – not significant ($p>0.05$), * - $p<0.05$, *** - $p<0.001$, ****- $p<0.0001$, one-way ANOVA.

3.4.6. Zone of inhibition assay

The zone of inhibition assay against *E. coli* NCTC12242 was used to further investigate drug releasing properties of NT2RepCT particles. NT2RepCT 0.01% GA particles were used in this experiment as they showed good stability during centrifugation and loading in the previous experimental procedures.

Chloramphenicol is a broad-spectrum bacteriostatic agent used in local applications due to its systemic toxicity (notably bone marrow suppression)[303]. Therefore it was used as a model antimicrobial drug for a local drug delivery system.

NT2RepCT 0.01% GA particles were loaded with chloramphenicol, and an equal mass of partially dissolved cellulose loaded with chloramphenicol was used as a positive control. As a negative control, non-loaded NT2RepCT 0.01% GA particles were used.

Chloramphenicol-loaded NT2RepCT 0.01% GA spheres produced a zone of inhibition against *E. coli* NCTC12242 with diameter greater than non-loaded NT2RepCT 0.01% GA particles or chloramphenicol-loaded cellulose (Fig.3.16 A). This ZOI was sustained over the course of six days (Fig.3.16 B). A statistically significant decrease in ZOI produced by chloramphenicol-loaded NT2RepCT was observed from day 5 ($p<0.05$, one-way ANOVA) compared to ZOI produced by chloramphenicol-loaded cellulose that showed decrease from day 6 ($p<0.05$, one-way ANOVA). From day 7, there was no statistically significant difference in the ZOI produced by chloramphenicol-loaded NT2RepCT particles and chloramphenicol-loaded cellulose (Fig.3.16 B).

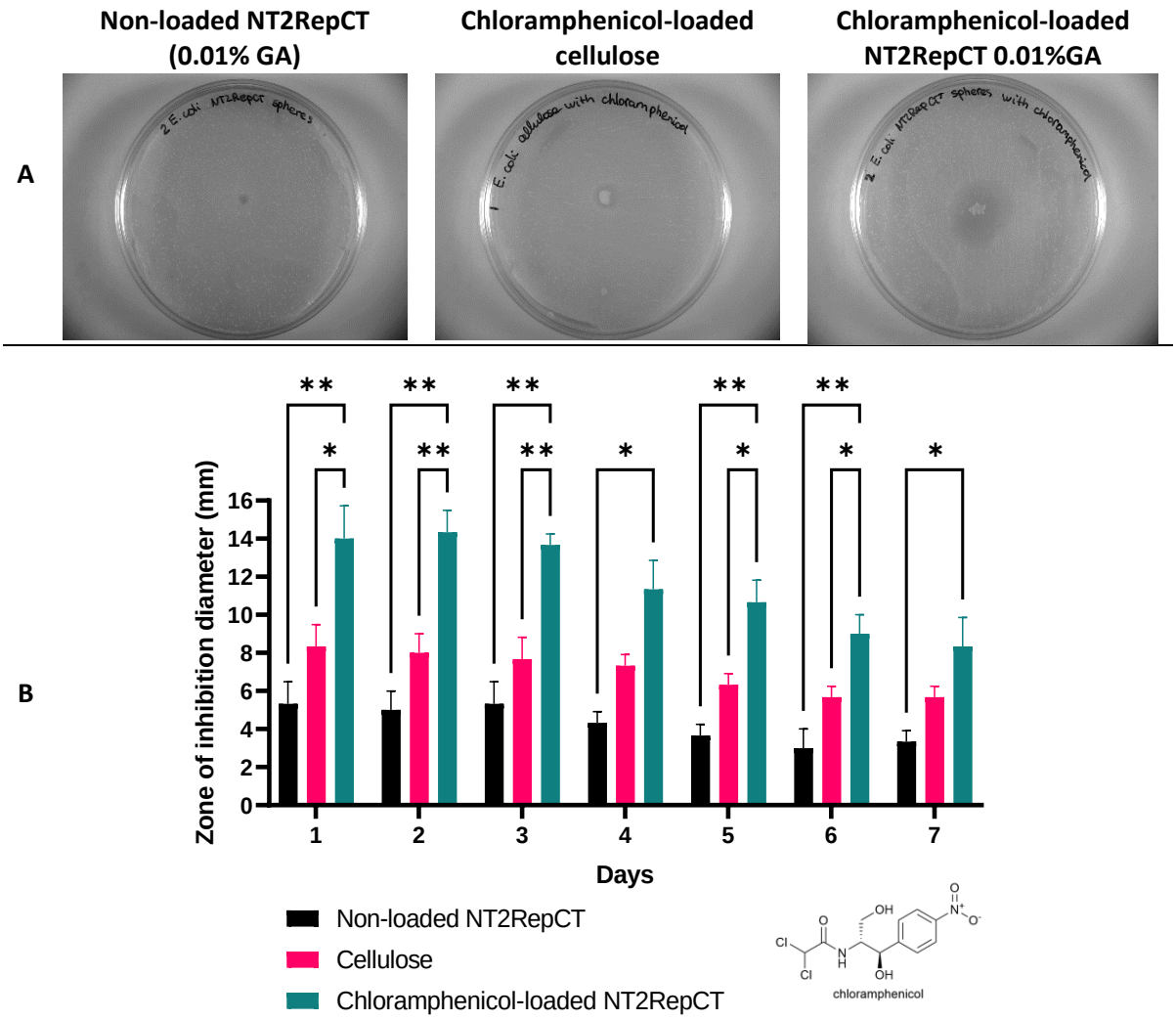

Figure 3.16. Zone of inhibition against *E. coli* NCTC12242 of non-loaded NT2RepCT 0.01% GA particles, chloramphenicol-loaded cellulose, and chloramphenicol-loaded NT2RepCT 0.01% GA particles. **A**: plates illustrating the zone of inhibition after three-day incubation. **B**: Diameter of the zone of inhibition over seven-day incubation, * - p<0.05, ** -p<0.01, n=3, one-way ANOVA. Error bars denote standard deviation.

3.5. Discussion

3.5.1. Particle preparation and overview

This chapter assessed the preliminary characteristics of NT2RepCT properties as a novel polymeric drug delivery system with a resorbable, temporary nature and pH-dependent drug release profile that could be employed in a range of biomedical applications.

NT2RepCT particles were produced using the methodology that has been previously reported in the literature[139,185,304]. In this established protocol, silk protein solution at relatively low concentration (1 mg/ml) was added dropwise to a stirred solution of high concentration of potassium phosphate (1M KH_2PO_4) which is called the coagulation bath. The particles formed instantaneously upon addition of the NT2RepCT solution to a stirred 1 M KH_2PO_4 pH 8 coagulation bath. These particles showed spherical morphology of polydispersed diameters from 389 nm to 39 µm. Electron microscopy showed that material was prone to agglomeration when centrifuged to remove salts, and the spherical morphologies collapsed when freeze-dried suggesting that the spheres are relatively soft and potentially porous. The resulting particles were stabilised using glutaraldehyde crosslinking. Crosslinker concentrations were selected empirically starting at the highest concentration of crosslinker as 0.1% volume/volume that resulted in almost immediate aggregation of the discrete colloid particles into macroscopic aggregates that tended to adhere to each other and the walls of the beaker containing the 1 M KH_2PO_4 pH 8 coagulation bath solution. Crosslinker titration (tenfold decrease steps from 0.1 to 0.001% v/v) showed that 0.01% v/v glutaraldehyde was an optimal concentration to stabilise the spherical particle morphologies. Particles were loaded with an excess of model drug rhodamine B, and the release studies showed that the majority of the drug is released within the first 15 minutes regardless of the pH of the release environment. NT2RepCT particles with 0%-0.01% GA crosslinking showed biphasic release curve with a secondary release peak (25% increase or more) within 1-3 hours after the burst release. No secondary release peak was observed in NT2RepCT 0.1% GA particles suggesting that higher degree of crosslinking interferes with biphasic

release. Particles with lower degree of crosslinking released less drug compared to 0.01-0.1% GA crosslinked particles; this could either be due to less drug loading in particles with lower crosslinker concentration, or very likely to be a consequence of particle resolubilisation during the drug loading in salt-free environment. As an antibiotic delivery vehicle, NT2RepCT 0.01% GA particles showed a sustained zone of inhibition against *E. coli* NCTC 12242. This ZOI was larger than that of an equal mass of cellulose fibres loaded with the same antibiotic suggesting that NT2RepCT particles can carry more antibiotic than fibrous cellulose.

3.5.2. Zeta potential and laser particle sizing

Particles in a colloidal solution are strongly electrostatically bound to a thin layer of counterions called the Stern layer, and Stern layer is, in turn, loosely associated with the second layer of counterions. The electrical potential between these two layers is called zeta potential[305] . Zeta potential is therefore a predictor of a colloidal stability. Zeta potential of NT2RepCT particles in 1 M KH_2PO_4 pH 8 was on average from -9.20 to -6.37 mV (Fig.3.7). This classifies particle as unstable and prone to flocculation/agglomeration[306]. In a high salt concentration at pH 8, there was no statistically significant difference in particle zeta potential across the degrees of crosslinking. This number should be taken as an estimate due to inherent assumptions of the classical theory of electrophoresis based on spherical, uniformly-charged, and rigid particles which might not apply to the NT2RepCT materials[307] Further, the measurements in high salt content where the particles are most stable might not be replicated in other, physiologically relevant salt concentrations.

Laser diffraction showed the predominant particle species sizes ranging from as small as 300 nm and up to 18 µm (Fig.3.8). This suggests that whilst the smaller population of the NT2RepCT particles could be useful in some intracellular applications, the majority of the particle population would not be taken up by non-phagocytic eukaryotic cells. Particles with 1-18 µm diameter could be used as transient embolization particles due to their agglomeration-prone and unstable nature. Volume-weighted

distribution showed that NT2RepCT 0% GA particles have the broadest size distribution compared to crosslinked particles (Fig.3.9)

Further analytical characterisation on NT2RepCT particles should include particle charge and size at physiological salt concentrations as high salt content can decrease apparent hydrodynamic size of particles.

3.5.3. SEM

Scanning electron microscopy shows a variety of different morphologies present in NT2RepCT particle preparations ranging from nano-to-micro sized spherical particles to flakes, porous films, and fibres. Imaging of particles in the precipitation buffer was technically challenging due to salt carryover as salt crystals coated the NT2RepCT morphologies, however these images indicate the presence of spherical particles of polydisperse diameter ranging from sub-micron to single micron (Fig.3.10). This is consistent with the data from laser scattering experiments (Fig 3.8) whilst being in contrast to previous findings that report stable and monodisperse particle species using 1 M KH_2PO_4 pH8 precipitation as visualised by electron microscopy[28,139,304] This variability could be due to considerably more highly hydrophilic nature of NT2RepCT compared to eADF4(C16) that contains 16 hydrophobic core domain repeats.

Further salt removal procedures involving centrifugation and buffer wash steps caused agglomeration of the material. The best stability of spherical particles was observed in NT2RepCT 0.01% GA samples; lower concentrations of crosslinking yielded collapsed spherical morphologies, whereas higher concentration of GA resulted in large, interlinked particulates with fibrous interconnected structure that could be GA polymers (Fig.3.11). This data suggests that the size of NT2RepCT spheres and their stability in the buffer can be tuned using various concentrations of crosslinker.

NT2RepCT 0% GA and NT2RepCT 0.001% GA particles showed areas of flake-like morphologies (Fig 3.11). Whilst for the PDDS, a spherical morphology is usually favoured due to highest surface area available for drug loading, irregularly shaped materials can have merits in certain applications

depending on their biochemical properties. For example, Bearing nsPVA Embolization Particles (Merit Medical) and PVA Foam Embolization Particles (Cook Medical) are described as “irregularly shaped”, and Contour PVA Embolization particles (Boston Scientific) are “small and irregular flakes”. These irregularly shaped morphologies can perform as well as spherical particles whilst using less material[308].

Despite particle instability in SEM sample preparation, likely during salt removal by centrifugation, regions of spherical particles were observed in all samples, with smallest particles observed in NT2RepCT 0.01% GA (Fig.3.12C). This suggests that 0.01% GA concentration was most suitable for submicron sized particle stabilisation whilst preventing GA-induced aggregation (Fig.3.12 A, Fig. 3.12 D). Most particles over 1 μm in diameter showed smooth and regular surface morphology; in contrast, submicron particles had both spherical and irregular morphologies. These observed morphologies highlight the limitations of scattering-based analytical techniques for particle measurement because despite the favourable resolution, scattering data provides a radial average measurement of not perfectly spherical or deforming (aggregating) PDDS material.

Centrifugation might simulate some potential *in vivo* behaviour of particles, such as aggregation under pressure or flow to block a blood vessel for applications as occlusive material. More assessment is needed to clearly define the morphologies created by salting out NT2RepCT protein solution. Based on their soft, collapsible nature, it could be hypothesised that the NT2RepCT particles are microgels or microcapsules[309,310]. Microgels are known for having a dense core and a disperse corona (fuzzy sphere model[310]). To study fully hydrated size and behaviour such particles, super-resolution microscopy techniques such as 3D-stochastic optical reconstruction microscopy or single-molecule localization microscopy could be employed. Microcapsules are defined as particles with hollow interior, and this can be investigated by transmission electron microscopy (TEM), or focused ion beam scanning electron microscopy (FIB SEM). Both techniques use ion beam to investigate internal details of the sample by either forcing an ion beam through the sample or using ion milling to remove upper layers of the sample and scan the freshly exposed surfaces.

3.5.4. Rhodamine B release assays

Release of model drugs from spider silk particle spheres has been previously measured in the increments of days[137,153] however little is known about shorter time-frame release kinetics or within the initial "burst release" period. Further, NT2RepCT particles were expected to have different drug release kinetics compared to previously researched miniature silk proteins due to its uniquely hydrophilic nature. Rhodamine B is a zwitterionic compound that could interact with both positively and negatively charged amino acid side chains on NT2RepCT.Rhodamine B fluorescence at different pH was measured to ensure that pH does not affect its fluorescence, and in accordance with the literature, there was no statistical significance in RhB fluorescence intensity at pH 5.5, pH 7, and pH 10 (Fig.3.13).

Burst release

Majority of the drug was released from NT2RepCT particles of all degrees of crosslinking within the first 15 minutes of incubation in all samples regardless of the pH (Fig 3.14 A-D, red arrows).

Secondary release

Secondary release peak was defined arbitrarily as at least 25% percentage increase compared to the previous time point. Secondary release peak was observed in MES pH5.5 buffer in samples NT2RepCT 0% GA at 3 hours; NT2RepCT 0.001% GA at 1 hour and 3 hours; and NT2RepCT 0.01% GA at 1 hour (Fig.3.14 A-C, green arrows). No secondary release peak was observed from the NT2RepCT particles in TRIS pH7 or CAPS pH10, or NT2RepCT particles with 0.1% GA crosslinking in any of the release buffers. This suggests that particles have some pH sensitivity that is eliminated as the degree of crosslinking increases. NT2RepCT is designed from N-terminal domain from *E. australis* MaSp1 and C-terminal domain from *A. ventricosus* MiSp1; both domains are known for their pH-responsiveness in context of silk fibre formation[27,102,311]. The pH sensitivity of these domains is due to the salt bridges between positively and negatively charged amino acid residues (D40-K65 and D39-R60 in N-terminal domain[312] and between R43–D93 and R52–E101 based on sequence similarity with *A. diadematus* C

terminal domains[22]). This pH sensitivity results in N terminal dimer formation at pH 5.5 whilst C terminal domain gradually unfolds below pH 5.5[311]. This chemical shift could be contributing to the release of rhodamine B in the secondary release peak by causing the particles to lose their structural integrity.

Whilst GA crosslinking mechanism in proteins remains debatable, it is thought to crosslink via reaction of aldehyde groups with non-protonated amines with high preference for primary amines [313–315]. This crosslinking at N-terminal domain D40-K65 (and possibly arginine [316,317]) could interfere with the unfolding behaviour of the individual NT2RepCT proteins, thus no secondary peak was observed in drug release from NT2RepCT 0.1% GA particles.

Interestingly, a secondary release peak at 1hr in MES pH5.5 was observed in particles crosslinked with 0.001-0.01% GA. This release peak was not seen in non-crosslinked particles. In 0.001% GA, this peak was observed along with secondary release at 3hr, however in 0.01% GA particles, it was the only secondary release peak. The release peak could happen due to reversibility of GA crosslinking at acidic pH (< pH 7.0)[314], however, the exact cause of this particle behaviour remains to be investigated using analytical techniques such as FTIR and CD.

Overall, the innate pH-responsiveness of NT2RepCT and the crosslinker interactions with the NT2RepCT particles show some pH dependency in drug release in acidic environment within the first three hours of incubation.

Cumulative release at 24 hours

The cumulative drug release from NT2RepCT particles was measured at 24 hours. No pH-dependant difference in rhodamine B release was observed from particles crosslinked with 0-0.001%GA (Fig.3.15). In contrast, the amount of rhodamine B released from NT2RepCT 0.01% GA particles showed inverse correlation with the buffer pH. This difference was highly statistically significant, suggesting that the drug release kinetics in these particles are pH dependent. These findings are consistent with the results by Lammel *et al.* who showed that the drug release from particles prepared

from a miniature recombinant spidroin eADF(C16) using KH_2PO_4 precipitation was increased at lower pH (from pH 2.2 to pH7.4) over the course of five days[153].

Similarly, more rhodamine B was released from NT2RepCT 0.1% GA particles at pH 5.5 and pH7 compared to pH10, however there was no statistical significance in the relative fluorescence intensity of TRIS pH 7 and MES pH 5.5. Some evidence shows that high GA concentration can induce deformation of a solid protein sample[318] and decrease sample swelling capacity[319] at higher pH. This evidence could provide an explanation why NT2RepCT 0.1%GA in CAPS pH 10 released the lowest amount of rhodamine B as the impaired swelling behaviour might negatively impact the ability of the particles to both uptake and release the drug.

Overall, the data in Fig.3.15 showed higher fluorescence intensity in particles with higher degree of crosslinking. This behaviour could be explained by several hypotheses:

- Particles with lower degree of crosslinking uptake less rhodamine B
- Particles with lower degree of crosslinking uptake comparable amount of rhodamine B as those with higher degree of crosslinking, but do not release it as efficiently
- Particles with lower degree of crosslinking disintegrate during the loading with rhodamine B in aqueous solution, therefore introducing an error where the mass of particles is not equal across degrees of crosslinking in the experimental dataset.

This study used an excess of rhodamine B to ensure the drug availability is not a limiting factor, and the percentage of drug uptake was not measured. The loading behaviour needs to be investigated further to draw conclusions. Further, during material processing, dialysis of the particles against ultrapure water was attempted, however the spheres of up to 0.01% GA crosslinking resolubilised in the dialysis tubing as observed visually by decrease in the turbidity of the suspension. This observation suggests that the removal of salts destabilises the particles and causes resolubilisation of NT2RepCT protein either as individual proteins or smaller aggregates.

Considering the material properties that were observed during this set of experiments, it is important to further study the mechanism of the drug release that could be due to various phenomena such as particle dissolution, erosion, diffusion, or swelling[320]. Each of these behaviours can be characterised using well-established kinetic equations, for example Higuchi model that describes drug release by matrix (that is, particle) dissolution, or the Ritger–Peppas and Korsmeyer–Peppas model that studies the diffusion of the drug from the PDDS taking into consideration the burst effect[321]. To apply these models to drug release from NT2RepCT particles, high performance liquid chromatography could be used to quantify the amount of the released drug.

3.5.5. Zone of inhibition assay

Zone of inhibition assays against *E. coli* NCTC12242 using chloramphenicol loaded NT2RepCT 0.01% GA spheres were carried out to observe whether the particles could be used as an antibiotic drug delivery platform. NT2RepCT 0.01% GA particles were used in this experiment based on the previous data that showed these particles had best preserved spherical morphologies with good stability in water and pH-dependent release. Chloramphenicol is thought to interact with the hydrophobic repeat regions of NT2RepCT, however some electrostatic interaction with the positively charged amino acid side chains (particularly lysines) is possible as chloramphenicol has an overall slightly negative charge (due to the alcohol groups).

NT2RepCT particles showed a sustained zone of inhibition with an average ZOI diameter of 14 mm on Day 1 (Fig.3.16). This ZOI was stable for 5 days with a statistically significant decrease in diameter from Day 6 ($p<0.01$).

As a control, an equal mass of partially dissolved cellulose was used. Partially dissolved cellulose forms swollen fibrillar nanostructures that resemble a gel[322].The zone of inhibition produced by chloramphenicol-loaded cellulose material was significantly smaller than ZOI of loaded NT2RepCT 0.01% GA particles (Fig.3.16). This is in line with assumption that spherical particles with highest surface area are able to deliver larger amount of payload.

3.6. Conclusions and future work

In conclusion, this chapter has reported the use of a hydrophilic recombinant spidroin NT2RepCT as a potential material for polymeric drug delivery system.

Using the existing salting-out protocols, colloidal NT2RepCT particles with a range of diameters from sub-micron to single-micrometre were generated. Particles were characterised as unstable and prone to aggregation, and a titration of a crosslinking agent was carried out to investigate the optimal stabilisation conditions. NT2RepCT particles were loaded with a hydrophilic model drug surrogate rhodamine B and a hydrophobic antibiotic drug chloramphenicol. NT2RepCT particles with lower crosslinking levels showed a biphasic, pH-dependent rhodamine B releasing properties that could have use in transient embolization of tumours and other biomedical applications. Chloramphenicol-loaded NT2RepCT particles showed a sustained zone of inhibition against *E. coli* NCTC 12242.

Further research is needed to characterise both the exact morphology and the size distribution of the colloid particles that were created using the discussed coagulation method. NT2RepCT has a potential to form hydrogels[132], therefore it is plausible that the particles described in this chapter are microgels (water-swollen structures) rather than microspheres (non-swollen particles). The size and size distribution of these structures is likely to be influenced by the variables that were not changed in the current work, for example the speed of particle mixing in the coagulation bath and the protein concentration that is added to the salt solution. Higher speeds of mixing could create smaller and more homogeneous particle sizes, whereas higher protein concentrations might create larger morphologies, however an empirical assessment is required because the existing literature that describes similar experimental approaches is focused on highly hydrophobic silk proteins in contrast to highly hydrophilic NT2RepCT.

Additionally, the mechanisms by which the particles uptake and release the drug are to be described. Particle stability and resolubilisation in absence of salt needs to be investigated for developing more suitable methodologies for drug loading in NT2RepCT particles. To further characterise NT2RepCT

particle behaviour in water, the material could be placed in decreasing concentrations of salt, and the particle dissolution could be measured spectrophotometrically as decrease in turbidity (potentially OD_{600} so as to not interfere with protein absorptivity at 280 nm). Similar assays could be carried out to describe particle behaviour in other biologically relevant fluids, such as cell culture media or simulated plasma and interstitial fluid.

4. A plate-based methodology for screening 4RepCT^{3Aha}-tethered antimicrobial ligands conjugated via a labile ester-bearing linker.

4.1 Introduction

4.1.2. Biofilms and hospital acquired infections

Biofilms are surface-associated bacterial communities that are the primary cause of hospital acquired infections (HAIs) and corresponding morbidity, as well as being responsible for implant and indwelling medical device failure and a major contributor to antibiotic resistance in the clinical setting[323]. According to the WHO, the prevalence of HAIs in high income countries is 3.5-12% compared to 5.7% to 19.1% in medium- and low-income countries [324]. This translates to a huge economic burden of up to US$ 45 billion in the USA[325] and £2.7 billion in the UK for the NHS[326]. Gram-positive bacteria such as *S. aureus* (including methicillin-resistant *S. aureus*) and *Enterococci* spp (including vancomycin-resistant Enterococci) are accountable for approximately 41% of HAIs compared to Gram-negative pathogens such as *E. coli*, *P. aeruginosa, Enterobacter* spp, and *K. pneumoniae* that account for 33%[327]. Fungal infections such as *Candida* spp that account for 9% HAI overall[327] are among most common causes of HAI in neonatal medicine leading to mortality rates as high as 40%[328].

The key characteristics that makes surface-associated bacterial infections particularly dangerous to human health is their inherent resistance to antibiotics, host defences and other stresses compared to free flowing, or planktonic, bacteria[329]. Biofilms are found to be more resistant to antibiotics and broad-spectrum antimicrobials due to their extracellular polymeric matrix (EPM) and close interaction of cells within the matrix resulting in concerted genetic and metabolic responses. EPM is made of richly hydrated interlinked polysaccharides and lipids, as well as cell debris, extracellular DNA and enzymes. This structure provides mechanical protection against antimicrobials due to reduced diffusion rates[330]. In addition, it has been suggested that penetration of antimicrobial agents is decreased due to the charge of the EPM, a phenomenon named the bioelectric effect[331]. The sublethal

exposure to antibiotics is an optimal environment for development of antibiotic resistance. As microbial cells reside in close proximity to each other, a biofilm facilitates the transfer of resistance genes. Additionally, a sublethal exposure to stress can induce the formation of persister cells – metabolically dormant cells that can re-establish an active infection once the environmental conditions become more favourable[332]. All factors considered, it has been reported that microorganisms within a biofilm are up to 1000 times more resistant to antibiotics than their planktonic counterparts[333].

4.1.3. Antimicrobial surfaces

A fully formed, mature biofilm is exceptionally difficult to clear, therefore a logical methodology for tackling this issue is to prevent bacterial growth on the surfaces in the early stages of microbial attachment before the extracellular matrix has formed. From a medical perspective, this can be facilitated by using biomaterials with surfaces that have anti-biofilm and/or antimicrobial properties for 2-3 weeks post-implantation[334]. Antimicrobial surfaces can be broadly divided by their mechanism of action into active and passive branches depending on whether the active molecule is released from the surface to exhibit its effects (active) or exhibits the antimicrobial activity whilst tethered to the surface (passive) (Fig.4.1).

This chapter focuses on active, controlled-release antimicrobial surfaces and coatings (passive contact killing antimicrobial surfaces are discussed in Chapter 5). For in depth discussion of burst releasing, colloidal polymeric drug delivery systems see Chapter 3.

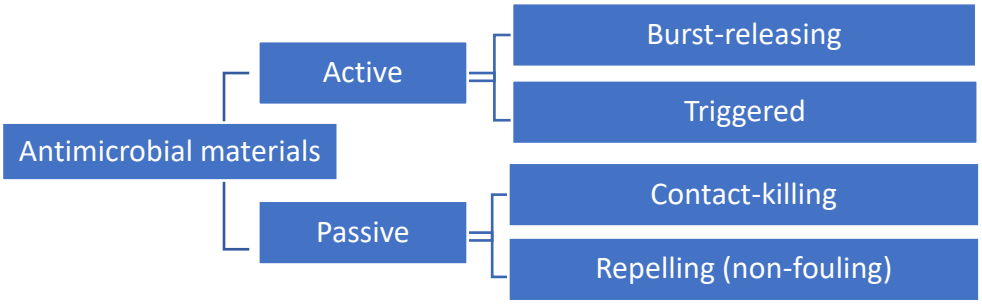

Figure 4.1. Classification of antimicrobial materials by their principle of action. Adapted from [335].

4.1.4. Active agents for antimicrobial surfaces.

Base biomedical materials rarely have a significant antimicrobial/antibiofilm action of their own, therefore they are imbued with antimicrobial ligands that facilitate the desired activity.

Burst release surfaces

Biocide-releasing materials leach ligands that have been loaded onto a substrate. In a burst release system, the active molecule diffuses down its concentration gradient into its surroundings therefore killing microorganisms within the area. Examples of the most commonly used biocides are heavy metals (silver and copper), furanones, halogens (particularly iodine and bromine), triclosan, hypochloride, or surfactants, as well as conventional antibiotics[336] .

Burst release systems are appealing due to their simplicity, however the main argument against the use of such systems is the fact that the materials become exhausted as the antimicrobial agent diffuses to sub-lethal concentrations, which can facilitate antimicrobial resistance development. Various methodologies of modifying the release kinetics have been described, for example using a layer-by-layer (LbL) deposition technique that employs electrostatic interactions to immobilise the active molecules[337]. LbL systems exhibit slower diffusion rates, therefore retaining more killing capacity over time[338]. Packaging biocidal materials into a porous material (commonly PEG, PMMA, PLA; Table 3.1 in Chapter 3) is another approach used to modify the rate of ligand release depending on the porosity, swelling and biodegradability of the matrix. Natural and synthetic materials are often blended to

create composite materials with tailored biological activity, biodegradability, and release kinetics of the drug of interest.

Burst-releasing antibiotic-loaded materials have become a standard practice in medicine, particularly dentistry and orthopaedics that routinely employ prophylactic antibiotic-loaded bone cements and resins[339]. Commonly used antibiotics in such materials are gentamycin, vancomycin, clindamycin, as well as teicoplanin, cefotaxime and meropenem. Further, triclosan-loaded surgical sutures are currently the recommended best practice by the WHO[327] and NICE[340]. However, the optimal dosage of each antibiotic per unit of material is yet to be characterised taking into consideration synergistic effects of material with each drug, as well as the release kinetics and the *in vivo* fate of the material (such as encapsulation or inflammation)[341]. Use of an active burst releasing system as a drug delivery vehicle is discussed in Chapter 3.

Triggered release antimicrobial materials.

Triggered, or controlled-release antimicrobial materials aim to alleviate concerns of nonspecific release of the antimicrobial agent by tethering it onto (or into) a signal-responsive material that breaks down upon an infection/inflammation specific biochemical signal. The main two approaches for triggered release include:

A) Cleaving of a labile linker that secures a ligand to the material

B) Breaking down of the base, or carrier, material.

A biochemical signal that aids the release of the antimicrobial ligand can be an enzyme or a metabolite associated with an infection, or alternatively change in pH or ionic strength that causes swelling of the base polymer and subsequent release of an active antibiotic. Light and electricity also have been used as release signals [342,343]. Representative examples of various triggered release antimicrobial materials are reviewed in Table 4.1.

Unlike burst releasing systems that passively diffuse down their concentration gradient, material-tethered antibiotics create a high local concentration of the biocide that exceeds minimum inhibitory concentration (MIC). Studies have shown that controlled release systems do not contribute to development of antimicrobial resistance in *S. aureus in vitro* at 45 passages and high local concentration of tetracycline antibiotic leads to biocidal effect against tetracycline resistant *E. coli*[344–346]. This phenomenon suggests that triggered release antimicrobial surfaces maintain a bactericidal concentration of the molecule at the surface, thus alleviating some concerns associated with the passive diffusion systems discussed above. Overall, medical device bulk materials usually lack chemically reactive moieties available for conjugation unless they are activated (oxidised). To that end, bulk materials are often functionalised using self-assembling films that deliver a desired activity.

Table 4.1. Examples of common controlled release antibiotic-conjugated materials.

Base material	**Antimicrobial agent**	**Release mechanism**	**Key findings**	**Ref**
Polyvinyl alcohol (PVA) hydrogel	Gentamycin	Thrombin cleavage of the peptide linker that contains thrombin cleavage site	Sustained ZOI against *S. aureus*	[347]
Clickable PEG (hydrogel)	Clickable levofloxacin, clickable ciprofloxacin	Cleavage of a photolabile linker (nitrobenzyl carbamate)	ZOI against *S. aureus*. No cytotoxicity against fibroblasts *in vitro.*	[348,349]
Titanium	Tetracycline Vancomycin Daptomycin	Cleavage of the ester bond within the linker	53-91% decrease in *S. aureus* survival. Activity against TET resistant *E.coli.* Non-cytotoxic	[342,344–346,350]
Hyaluronic acid (gels)	Ciprofloxacin Vancomycin Nisin	Cleavage of the ester bond within the linker; degradation of hyaluronic acid by bacterial enzymes	Significant sustained (over 1 week) antimicrobial effect against MRSA	[351,352]
Bone allograft	Vancomycin	Cleavage of the ester bond within the linker	Significant resistance to *S. aureus* colonisation; 90% reduction in bacterial survival	[353]

4.1.5. Antimicrobial ligands for 4RepCT^{3Aha} conjugation

This section reviews antimicrobial ligands used for functionalisation of the azide-bearing miniature spidroin 4RepCT^{3Aha}. Antimicrobial molecule selection was guided based on examples previously reported in the literature and supplemented with further, less commonly described antibiotics with diverse mechanisms of action, some of which are particularly applicable for local drug delivery (due to their systemic toxicity). Table 3.2 summarises the structures and mechanisms of action of the selected antimicrobial ligands

Triclosan

Triclosan is an antimicrobial molecule widely used in consumer products (toothpastes, soaps), as well as in prescription drug (for topical applications) and pesticide formulations[354]. Its mechanism of action includes inhibition of NADH-dependent enoyl-acyl carrier protein reductase FabI, a rate-limiting enzyme in fatty acid biosynthesis[355]. At higher concentrations, it is thought to non-specifically interact with bacterial cell walls[356]. The MIC of triclosan varies among species; triclosan sensitive *E. coli* and *S. aureus* strain MIC of triclosan is 0.5-1 mg/L[357,358], whereas all *Pseudomonas* spp are highly resistant to triclosan[359]. Since its discovery in 1960s, triclosan has been thoroughly scrutinised in a range of toxicity and efficacy studies that confirmed excellent tolerability, low immunogenicity, and excellent antimicrobial effect that has no observable antimicrobial resistance *in situ*[360]. Triclosan has been previously reported to be tethered to poly-(sulphobetaine methacrylate) and UV-treated siloxanes via its single alcohol group[361–364].

Chloramphenicol

Chloramphenicol is a broad-spectrum antibiotic used to treat bacterial meningitis, respiratory tract infections such as resistant pneumonia and bronchitis, as well as Mediterranean spotted fever and most importantly enteric fever[303]. Chloramphenicol exhibits bacteriostatic activity by inhibiting 23S ribosomal RNA of the large 50S ribosomal subunit thus inhibiting protein translation[365]. Due to its systemic toxicity, which causes bone marrow suppression in virtually all recipients[366], it is not a

recommended first line of treatment, however it is still widely used in localised infections such as conjunctivitis. Chloramphenicol's MIC against sensitive strains of *E. coli* and *S. aureus* is 8 mg/ml[367]. There are several mechanisms of chloramphenicol resistance, such as enzymatic inactivation by acetyltransferases or chloramphenicol phosphotransferase, target site mutation, decreased membrane permeability, or multidrug efflux pump activity rendering it inactive against *Pseudomonas* spp[368]. Chloramphenicol has been conjugated to various polymers and surfaces via its single alcohol group, for example polyamines and whole bacteriophage capsules [369,370].

Ciprofloxacin and levofloxacin

Ciprofloxacin and levofloxacin are two types of fluoroquinolone antibiotics (ciprofloxacin is a second-generation quinolone, and levofloxacin is a third-generation quinolone). They are broad-spectrum antibiotics that inhibit type II topoisomerases and DNA gyrases thus interfering with DNA replication[371]. Fluoroquinolones are often used to treat pneumonia, bacterial sinusitis, complicated urinary tract infections, and pyelonephritis[372]. Fluoroquinolone antibiotic MIC against sensitive strains of *E. coli* is 0.25mg/L and that of *S. aureus* is 0.5 mg/L[367] Fluoroquinolone resistance mechanisms include mutations in the target enzymes, decreased membrane permeability, and multidrug efflux pumps[371]. Levofloxacin has been conjugated to chitosan[373], hyaluronic acid[374], an acidic oligopeptide[375] and 4RepCT^{3Aha} spider silk protein[106] , whereas ciprofloxacin has been conjugated to hyaluronic acid[351], poly(L-lactic acid)[376], poly(2-oxazoline)s and PEG[377] with all conjugates showing antimicrobial activity superior to base material alone.

Erythromycin

Erythromycin is a macrolide antibiotic commonly used for skin and pulmonary infections[378] that works by binding bacterial ribosomes causing a premature dissociation of peptidyl-tRNAs thus inhibiting protein translation [379]. MIC of erythromycin against sensitive *E. coli* is 140 mg/L (high MIC against Gram-negative organisms)[380] and 2 mg/L against *S aureus*[280367].The resistance mechanisms include 23R

rRNA mutations, as well as structural modifications of the molecule by erythromycin esterase[381]. Erythromycin has been conjugated to PEG-citric acid and poly(amidoamine) dendrimers[382,383].

Nitroxoline

Nitroxoline is a quinolone antibiotic very effective against biofilms and often prescribed for recurrent urinary tract infections[384]. Its mechanism of action involves divalent cation chelation that results in inhibition of bacterial attachment that, in turn, promotes the clearance of bacteria by acidification of the environment and host's immune responses [385]. Recent reports on nitroxoline include significant anti-cancer activity[386,387]. The MIC of nitroxoline against sensitive *E. coli* strains is 4 mg/L compared to 16 mg/L against S. aureus[388].

Table 4.2. Clickable antimicrobial ligands used for conjugations with 4RepCT^{3Aha}, their mechanism of action and current medical applications. R and R' are the linker attachment positions. Linker structures are shown in the grey cells below.

Antimicrobial ligand	Mechanism of action	Medical applications	Ref
Triclosan 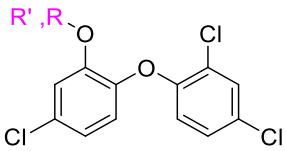	FabI inhibition, nonspecific membrane interaction	Consumer products (mouthwash, toothpaste), topical creams, surgical wash	355,357 ,359,36 0,389
Chloramphenicol 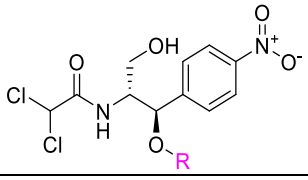	Inhibition of 23S rRNA	Typhoid fever, bacterial meningitis, plague, cholera. Commonly used for conjunctivitis. Severe systemic side effects (bone marrow suppression)	380
Ciprofloxacin 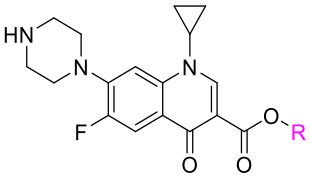	DNA gyrase and type II isomerase inhibition	Broad-spectrum antibiotic for bone, skin, urinary tract, airway infections; very effective against *Pseudomonas* spp	390
Erythromycin 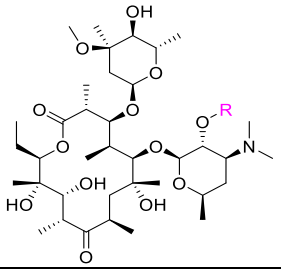	Inhibition of 23S rRNA	Airway, urinary tract, and skin infections; chlamydiosis	380
Levofloxacin 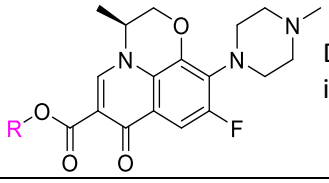	DNA gyrase inhibitor	Bacterial bronchitis, bacterial sinusitis, skin and skin structure infections, acute pyelonephritis, multispecies urinary tract infections	372
Nitroxoline 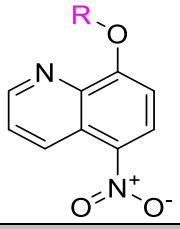	Divalent cation chelation	Urinary infections (*E. coli*, *Pseudomonas* spp)	384,385
R = 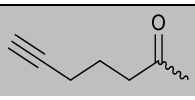 (ester)		R' = 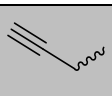 (ether)	

4.2. Aims and objectives

Local release antimicrobial agents are a safer way to prevent surface associated bacterial infections, however, due to the evolution of antimicrobial resistance, new materials carrying different biocides are required. Although passive loading of the material with a drug is very simple and widely used in biomedical applications, it tends to quickly lose its antimicrobial effect due to diffusion of the active ligand, sometimes resulting in local toxicity. Therefore, surface-conjugated trigger-releasable biocides are highly preferred due to less nonspecific leaching that results in lower local toxicity and is known to have lesser contribution to antimicrobial resistance development.

This chapter builds on the previous technology of levofloxacin conjugation to 4RepCT^{3Aha} protein by expanding the library of 4RepCT^{3Aha} - antimicrobial ligand conjugates using CuAAC. For this library, a broad scope of antimicrobials has been selected, some of which have a documented systemic toxicity which usually prevents them from being administered as a therapeutic.

To allow for a series of conjugates to be tested in parallel, a plate-based spectrophotometric assay was designed and developed. This assay helps to screen the conjugate against series of microorganisms, as well as to validate a dose-dependent behaviour of the coating.

Using novel 4RepCT^{3Aha} conjugates in the high-throughput compatible plate assay is validated against two clinically relevant microorganisms, a Gram-negative *E. coli* and a Gram-positive *S. aureus.* Soluble 4RepCT^{3Aha} -biocide conjugates are processed into films, and the capacity for ligand conjugation to a pre-formed 4RepCT^{3Aha} film is shown.

4.3.Methods

4.3.1. Conjugation reaction

The procedure for modification of antimicrobial ligands, MS and NMR spectra can be found in Appendix B. Synthesis and analysis was carried in full by Dr Tom Armstrong (University of Nottingham, School of Chemistry, NRT group). All ligands (Table 4.2) were dissolved in acetonitrile to create 50µM stocks and stored at -20°C. Triclosan ligand was modified with both ester- and ether-linker (Table 4.2, R and R'). All other ligands were modified with ester linker only (Table 4.2, R)

Soluble 4RepCT^{3Aha} conjugation to antimicrobial ligands

A stock of 2 mg/ml of 4RepCT^{3Aha} was defrosted at room temperature. The conjugation reaction was set up by combining 800 µl 4RepCT^{3Aha} (2 mg/ml), 10 µl antimicrobial ligand stock (50 µM), 90 µl THPTA (50 µM), 90 µl NaAsc (50 µM) and lastly adding 10 µl $CuSO_4$ (50 µM). The reaction was incubated at room temperature with gentle agitation for four hours, then quenched with 3 µl 0.2M EDTA and dialysed against 1 L 20 mM Tris pH 8 as previously described. The concentration of protein in the dialysed solution was calculated taking into consideration the final volume and adjusted to 1 mg/ml with 20 mM Tris pH 8.

Conjugation to pre-formed 4RepCT^{3Aha} films

To conjugate antimicrobial ligands to pre-formed 4RepCT^{3Aha} films, a reaction mixture was set up combining 800 µl 20 mM Tris pH 8, 10 µl antimicrobial ligand stock (50 µM), 90 µl THPTA (50 µM) and lastly adding 10 µl $CuSO_4$ (50 µM). To each coated well, 200µl of the reaction solution was added and incubated for four hours at room temperature with gentle agitation, then aspirated.

4.3.2. Film formation and washing procedure

Films were formed in 96 well plates (Corning sterile, non-tissue culture-treated) by adding 50 µl of 4RepCT^{3Aha} or 4RepCT^{3Aha}-conjugate solution (1 mg/ml) to each well. For nonconjugated control experiments, a 96 well plate was coated by adding 50 µL 4RepCT^{3Aha} supplemented with 0.5 mM antimicrobial ligand. Plates were dried in a desiccator filled with $CaCl_2$ pellets under ambient pressure

overnight. Dry plates were washed by pipetting 300 µl isopropanol into each well, then aspirating the solvent followed by pipetting 300µl of ultrapure water to each well and aspirating it three times to remove any non-conjugated ligands and remaining water-soluble reagents. After the wash, the plates were dried in the desiccator overnight.

4.3.3. Plate-based antimicrobial assays

E. coli NCTC12242 and *S. aureus* NCTC 6571 strains were acquired from Dr A Cockayne (University of Nottingham). *E. coli* NCTC12242 glycerol stock was streaked on an LB agar plate and *S. aureus* "Oxford" NCTC6571 glycerol stock was streaked on a tryptic soy agar. Plates were grown at 37°C overnight. A single colony of *E. coli* NCTC12242 and *S. aureus* NCTC 6571 was used to inoculate 5ml LB or TS broth, respectively. Overnight cultures were grown at 37°C, 200 rpm, overnight and serially diluted 1000 times in their respective media. To each well, 200µl of cell dilution was added. The plate was covered with the lid and incubated at 37°C overnight without agitation. Final cell survival at 24 hours was measured using optical density measurement at 600 nm using TECAN Spark microplate reader.

4.3.4. Statistical analysis

Data was visualised using GraphPad Prism 9 software. The two distributions were compared using one-way ANOVA followed by Dunnet's or Tukey's multiple comparisons test and descriptive statistics. Values were rounded up to three significant figures.

4.4. Results

4.4.1. Antimicrobial activity of 4RepCT^{3Aha} conjugates to antimicrobial ligands processed into films

The antimicrobial ligands were conjugated to a the 4RepCT^{3Aha} in solution, and the resulting conjugate was processed into films by adding the reaction mixture to a 9 well plate wells and allowing the water to evaporate under ambient conditions in a desiccator. The removal of non-conjugated ligand was carried out by pipetting isopropanol into each well and then aspirating; this wash was followed by pipetting water into each well and aspiration. The retention of the film inside the wells could be visible as a cloudy coating that persisted after the washing steps.

All 4RepCT^{3Aha}-antimicrobial ligand conjugate films bearing an ester linker showed statistically significant antimicrobial activity against *E. coli* NCTC12241 over a 24-hour period whereas the 4RepCT^{3Aha}-triclosan ether conjugate did not exhibit statistically significant antimicrobial effect against the bacteria (Fig. 4.2). The low optical density of *E. coli* cultures grown in wells coated 4RepCT^{3Aha} -triclosan, 4RepCT^{3Aha} - ciprofloxacin and 4RepCT^{3Aha} -levofloxacin suggests that the antibiotic concentration in these samples is equal or above the minimum inhibitory concentration (0.25-0.5 mg/L; Section 4.1.5). The growth inhibition in wells coated with 4RepCT^{3Aha} -chloramphenicol, 4RepCT^{3Aha} -erythromycin, and 4RepCT^{3Aha} -nitroxoline ranged from 10 to 20% suggesting a very low antimicrobial activity or inherently higher relative resistance (for erythromycin Section 4.1.5.).

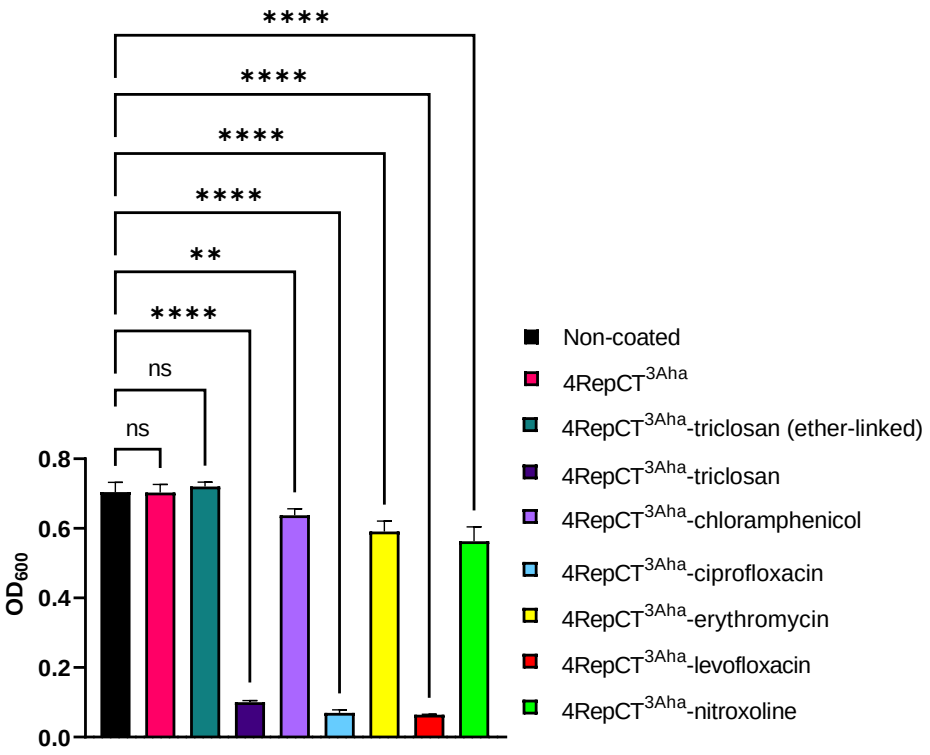

Figure 4.2. Optical density (at 600nm) of *E. coli* NCTC 12241 grown in wells coated with 4RepCT^{3Aha}-antimicrobial ligand conjugates after 24-hour incubation shows significantly inhibited bacterial growth in all wells coated with ester-bearing linkers.

Coating types: 4RepCT^{3Aha}; 4RepCT^{3Aha}-triclosan (ether-linked); 4RepCT^{3Aha}-triclosan (ester-linked); 4RepCT^{3Aha}-chloramphenicol; 4RepCT^{3Aha}-ciprofloxacin; 4RepCT^{3Aha}-erythromycin; 4RepCT^{3Aha}-levofloxacin; 4RepCT^{3Aha}-nitroxoline. Number of experiments N=1, number of replicates n=12. **** - $p<0.0001$, **-$p<0.01$, ns-$p>0.05$ (One-way ANOVA with Dunnet's multiple comparisons test).

The most potent antibacterial effect against *E. coli* NCTC 12241 wells coated with 4RepCT^{3Aha}-triclosan ester, 4RepCT^{3Aha}-ciprofloxacin, and 4RepCT^{3Aha}-levofloxacin was calculated as 86%, 90% and 91% growth inhibition, respectively (Table 4.4).

Table 4.3. Mean OD_{600} of *E. coli* NCTC12241 grown in wells with 4RepCT^{3Aha}-antimicrobial ligand conjugate coatings and the mean difference, percentage decrease and statistical significance of OD_{600} in coated wells compared to non-coated wells.

Coating	Mean (±SD)	Mean difference compared to non-coated wells (percentage decrease)	Significance of the mean difference compared to non-coated wells
Non-coated	0.706 (± 0.03)	-	-
4RepCT^{3Aha}	0.703 (± 0.02)	0.00134 (0%)	NS (p>0.05)
4RepCT^{3Aha}-triclosan (ether-linked)	0.720 (± 0.01)	-0.0158 (-2%)	NS (p>0.05)
4RepCT^{3Aha}-triclosan	0.100 (± 0.005)	0.605 (86%)	**** (p<0.0001)
4RepCT^{3Aha}-chloramphenicol	0.638 (±0.02)	0.0671 (10%)	**** (p<0.0001)
4RepCT^{3Aha}-ciprofloxacin	0.0697 (± 0.009)	0.635 (90%)	**** (p<0.0001)
4RepCT^{3Aha}-erythromycin	0.591 (± 0.03)	0.114 (16%)	**** (p<0.0001)
4RepCT^{3Aha}-levofloxacin	0.0645 (± 0.001)	0.640 (91%)	**** (p<0.0001)
4RepCT^{3Aha}-nitroxoline	0.563 (± 0.04)	0.142 (20%)	**** (p<0.0001)

The antimicrobial effect of 4RepCT^{3Aha}-chloramphenicol was the lowest (10% inhibition, Table 4.3) however, this conjugate showed sustained bacteriostatic effect over 72-hour incubation (Fig 4.3).

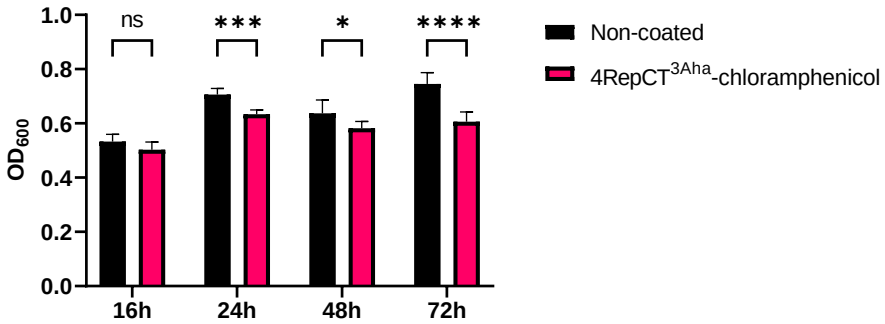

Figure 4.3. Optical density (at 600nm) of E coli NCTC12241 at 16h, 24h, 48h, and 72h time points in uncoated or 4RepCT^{3Aha}-chloramphenicol coated wells showing sustained bacteriostatic effect of 4RepCT^{3Aha}-chloramphenicol coated wells.

Number of experiments N=1, number of replicates n=9, *-p<0.05, **-p<0.01, ***-p<0.001, ****-p<0.0001, ns-p>0.05 (one-way ANOVA and Dunnet's multiple comparisons test).

Similarly, all ester-linked 4RepCT^{3Aha}-antimicrobial molecule conjugate films showed statistically significant antimicrobial activity against *S. aureus* NCTC 6571 at 24-hour timepoint (Fig.4.4). Growth inhibition of *S. aureus* in wells coated with 4RepCT^{3Aha}-ciprofloxacin and 4RepCT^{3Aha}-levofloxacin (91%, Table 4.5) was comparable to the levels of *E. coli* growth inhibition (91%, Table 4.4.) and likely equal or above to the minimum inhibitory concentrations of these antibiotics (Section 4.1.5)..

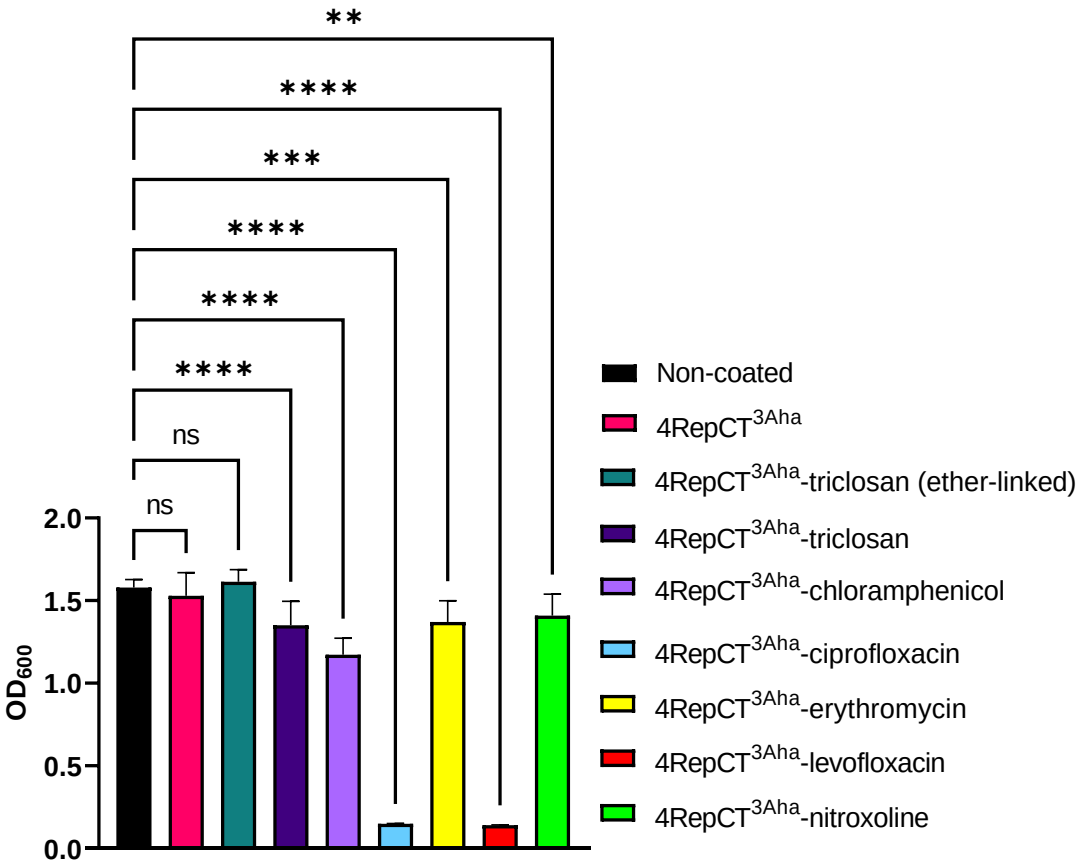

Figure 4.4. Optical density (at 600nm) of *S. aureus* NCTC 6571 grown in wells coated with 4RepCT^{3Aha}-antimicrobial ligand conjugates after 24-hour incubation shows significantly inhibited bacterial growth in all wells coated with ester-bearing linkers.

Coating types: 4RepCT^{3Aha}; 4RepCT^{3Aha}-triclosan (ether-linked); 4RepCT^{3Aha}-triclosan (ester-linked); 4RepCT^{3Aha}-chloramphenicol; 4RepCT^{3Aha}-ciprofloxacin; 4RepCT^{3Aha}-erythromycin; 4RepCT^{3Aha}-levofloxacin; 4RepCT^{3Aha}-nitroxoline.Number of experiments N=1, number of replicates n=12. **** - p<0.0001, ***-p<0.001, **-p<0.01, ns-p>0.05 (One-way ANOVA with Dunnet's multiple comparisons test).

The growth inhibition of *S. aureus* caused by 4RepCT^{3Aha}-chloramphenicol was 2.6 times greater than that of *E. coli* (26% and 10%, respectively; Table 4.5. and Table 4.4.). The least *S. aureus* growth

inhibition was observed in the wells coated with 4RepCT^{3Aha}-nitroxoline (11%) followed by 4RepCT^{3Aha}-erythromycin (13%) and then 4RepCT^{3Aha}-triclosan ester (14%).

Table 4.4. Mean OD_{600} of *S. aureus* NCTC6571 grown in wells with 4RepCT^{3Aha}-antimicrobial ligand conjugate coatings and the mean difference, percentage decrease and statistical significance of OD600 in coated wells compared to non-coated wells.

Coating	Mean (±SD)	Mean difference compared to the non-coated wells (percentage decrease)	Significance of the mean difference compared to non-coated wells
Non-coated	1.58 (± 0.05)	-	-
4RepCT^{3Aha}	1.53 (± 0.1)	0.0489 (3%)	NS (p>0.05)
4RepCT^{3Aha}-triclosan (ether-linked)	1.61 (± 0.07)	-0.0359 (-2%)	NS (p>0.05)
4RepCT^{3Aha}-triclosan	1.35 (± 0.1)	0.228 (14%)	**** (p<0.0001)
4RepCT^{3Aha}-chloramphenicol	1.17 (± 0.1)	0.407 (26%)	**** (p<0.0001)
4RepCT^{3Aha}-ciprofloxacin	0.149 (± 0.002)	1.430 (91%)	**** (p<0.0001)
4RepCT^{3Aha}-erythromycin	1.37 (± 0.1)	0.208 (13%)	*** (p=0.0001)
4RepCT^{3Aha}-levofloxacin	0.141 (± 0.002)	1.43 (91%)	**** (p<0.0001)
4RepCT^{3Aha}-nitroxoline	1.40 (± 0.1)	0.170 (11%)	** (p=0.0024)

4.4.2. Antimicrobial activity of ligands conjugated to a pre-formed 4RepCT^{3Aha} film

To investigate whether antimicrobial ligands can be conjugated to a pre-formed 4RepCT^{3Aha} film, silk protein solution was pipetted into each well and dried under ambient conditions. A reaction mixture containing the ligand, copper sulfate, and other click reagents in water was pipetted into each silk-coated well followed by incubation, aspiration, and wash as described previously.

When the conjugation reaction was carried out on a pre-formed 4RepCT^{3Aha} film, a statistically significant *E. coli* NCTC 12241 growth inhibition at the 24-hour timepoint was observed in the wells where films were conjugated to triclosan ester, ciprofloxacin, erythromycin, and levofloxacin (Fig.4.5).

The percentage decrease in OD_{600} in these wells was 69% (triclosan ester), 42% (ciprofloxacin), 53% (erythromycin), 58% (levofloxacin) (Table 4.6). Crucially, none of these optical densities indicate reduction in bacterial growth that would suggest that the concentration of the antibiotics is close to the minimum inhibitory concentration that was observed when ligands were conjugated to soluble silk protein.

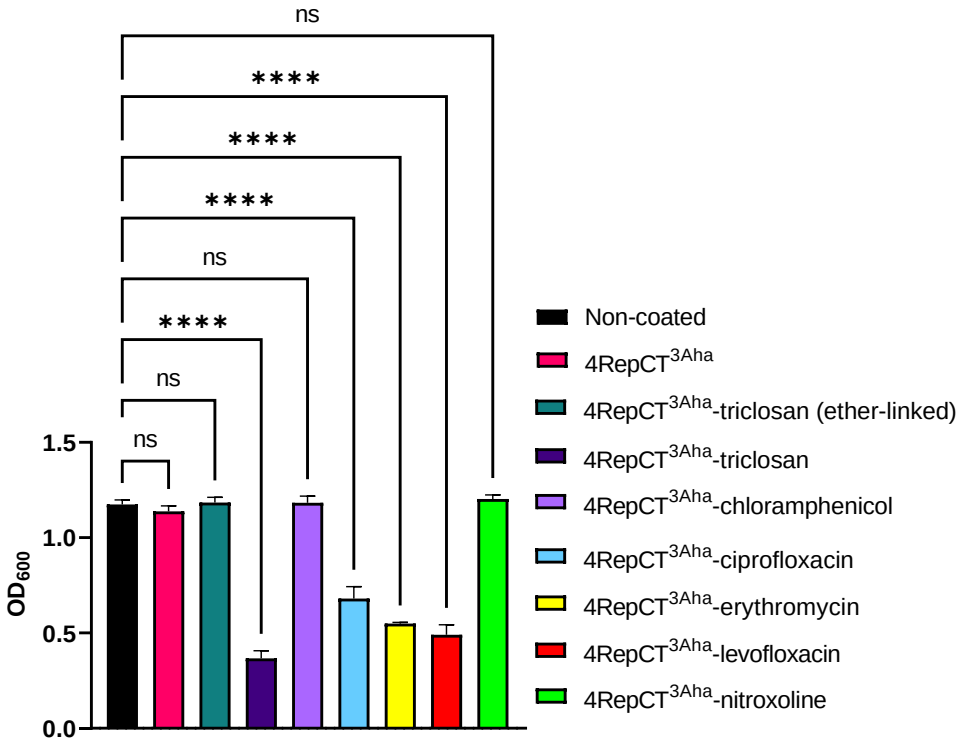

Figure 4.5. Optical density (at 600nm) of *E. coli* NCTC 12241 grown in wells coated with 4RepCT^{3Aha}-antimicrobial ligand conjugates where the conjugation was carried out to a pre-formed 4RepCT^{3Aha} film. After 24-hour incubation, OD600 shows significantly inhibited bacterial growth in wells coated with 4RepCT^{3Aha}-triclosan ester, 4RepCT^{3Aha}-ciprofloxacin, 4RepCT^{3Aha}-erythromycin, and 4RepCT^{3Aha}-levofloxacin.

Coating types: 4RepCT^{3Aha}; 4RepCT^{3Aha}-triclosan (ether-linked); 4RepCT^{3Aha}-triclosan (ester-linked); 4RepCT^{3Aha}-chloramphenicol; 4RepCT^{3Aha}-ciprofloxacin; 4RepCT^{3Aha}-erythromycin; 4RepCT^{3Aha}-levofloxacin; 4RepCT^{3Aha}-nitroxoline. Number of experiments N=1, number of replicates n=12. **** - $p<0.0001$, ***-$p<0.001$, **-$p<0.01$, ns-$p>0.05$ (One-way ANOVA with Dunnet's multiple comparisons test).

There was no statistically significant antimicrobial effect in wells where 4RepCT^{3Aha} films were conjugated with triclosan ether, chloramphenicol, and nitroxoline.

Table 4.5. Mean OD_{600} of *E. coli* NCTC12241 grown in wells with 4RepCT^{3Aha}-antimicrobial ligand conjugate coatings where the conjugation was carried out to a pre-formed film, and the mean difference, percentage decrease and statistical significance of OD_{600} in coated wells compared to non-coated wells.

Coating	Mean (±SD)	Mean difference compared to non-coated wells (percentage decrease)	Significance of the mean difference compared to non-coated wells
Non-coated	1.18 (± 0.02)	-	-
4RepCT^{3Aha}	1.14 (±0.03)	0.0363 (3%)	NS (p>0.05)
4RepCT^{3Aha}-triclosan (ether-linked)	1.18 (±0.03)	-0.00940 (-1%)	NS (p>0.05)
4RepCT^{3Aha}-triclosan	0.367 (±0.04)	0.808 (69%)	**** p<0.0001
4RepCT^{3Aha}-chloramphenicol	1.18 (±0.04)	-0.00875 (-1%)	NS (p>0.05)
4RepCT^{3Aha}-ciprofloxacin	0.680 (±0.06)	0.494 (42%)	**** p<0.0001
4RepCT^{3Aha}-erythromycin	0.549 (±0.006)	0.626 (53%)	**** p<0.0001
4RepCT^{3Aha}-levofloxacin	0.491 (±0.05)	0.684 (58%)	**** p<0.0001
4RepCT^{3Aha}-nitroxoline	1.20 (±0.02)	-0.0283 (-2%)	NS (p>0.05)

4.4.3. Soluble 4RepCT^{3Aha} conjugate exhibits dose-dependent behaviour

A dose-dependent antimicrobial effect against *S. aureus* was observed in wells coated with 50 µg and 100 µg of 4RepCT^{3Aha}-triclosan conjugate (Fig.4.6). *S. aureus* growth inhibition in the wells coated with 50 µg 4RepCT^{3Aha}-triclosan showed 14% inhibition compared to non-coated wells, whereas 100 µg 4RepCT^{3Aha}-triclosan coated wells inhibited bacterial growth by 37%. The mean difference between growth inhibition in wells coated with 50 µg and 100 µg 4RepCT^{3Aha}-triclosan coated wells was 26%, p<0.0001.

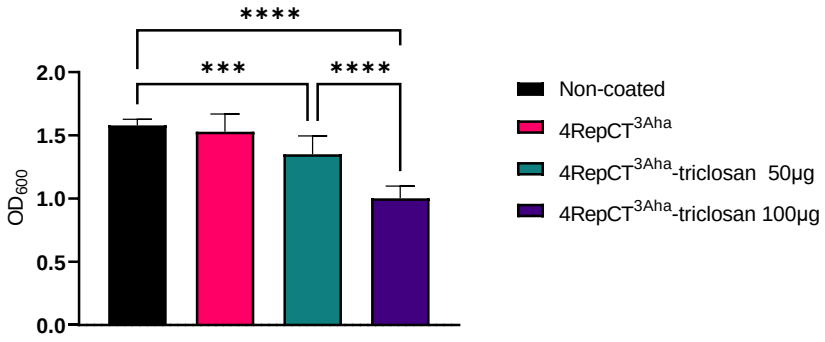

Figure 4.6. Optical density (at 600nm) of *S. aureus* NCTC6751 grown in wells coated with 50µg and 100µg of 4RepCT^{3Aha}-triclosan conjugate at 24 hours. Films made of 4RepCT^{3Aha}-triclosan conjugate exhibits dose-dependent behaviour. N=1,n=10, ***-p<0.001, ****-p<0.0001 (one-way ANOVA with Tukey's multiple comparisons)

In contrast, when triclosan was conjugated to a pre-formed 4RepCT^{3Aha} film (50 µg or 100 µg of protein), there was no statistically significant difference in antimicrobial activity between two samples (Fig.4.7). Mean difference between wells coated with 50 µg and 100 µg 4RepCT^{3Aha} film-triclosan conjugate was 11% with p=0.250 (non-significant).This data suggests that whilst a 100 µg 4RepCT^{3Aha} film theoretically offers more azide side chains available for conjugation than 50 µg 4RepCT^{3Aha}film, these side chains might not be accessible for the ligand to conjugate to. This finding suggests that silk-drug conjugate shows dose dependency whereby more conjugate offers more antimicrobial activity, whereas silk film-drug conjugate does not follow the same pattern of behaviour.

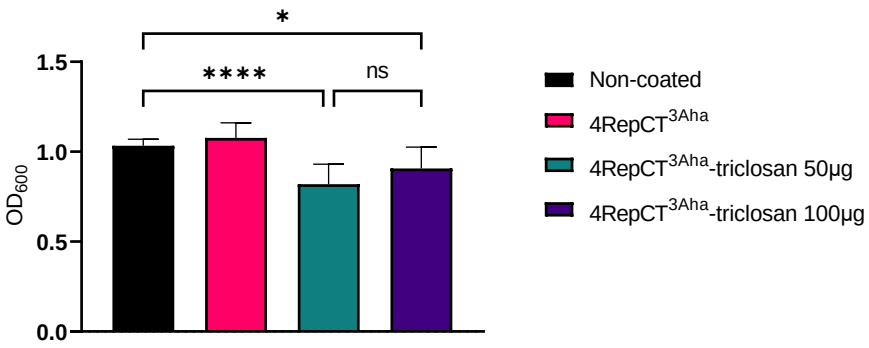

Figure 4.7. Optical density (at 600 nm) of *S. aureus* NCTC6751 at 17 hours grown in wells coated with 50µg and 100µg of 4RepCT^{3Aha} where a pre-formed film was conjugated with triclosan ester. The conjugate to a pre-formed film did not significant show dose dependency.
N=1, n=10, ****-p<0.0001, *-p<0.05, ns-p>0.05 (one-way ANOVA with Tukey's multiple comparisons)

4.4.4. The antimicrobial activity of molecules that are passively released from 4RepCT^{3Aha} films following a washing protocol is negligible.

To assess whether the antimicrobial activity of 4RepCT^{3Aha} -drug conjugate films were caused by covalently attached ligands or the passive diffusion of non-covalently attached (non-reacted) residual ligand, 4RepCT^{3Aha} was mixed with the antibiotics and processed into films as described before and subjected to a wash with isopropanol and water.

Very small (1-3%) but statistically significant inhibition of *E. coli* NCTC12241 was observed in wells coated with 4RepCT^{3Aha} that was mixed with each antimicrobial ligand except levofloxacin (Fig 4.8). This result could be due to some unreacted ligand remaining in the film after the wash, or could be a non-specific variability among the bacterial populations. Whilst the result is statistically significant, it is unlikely to be relevant in a more advanced infection model due to minor growth inhibition.

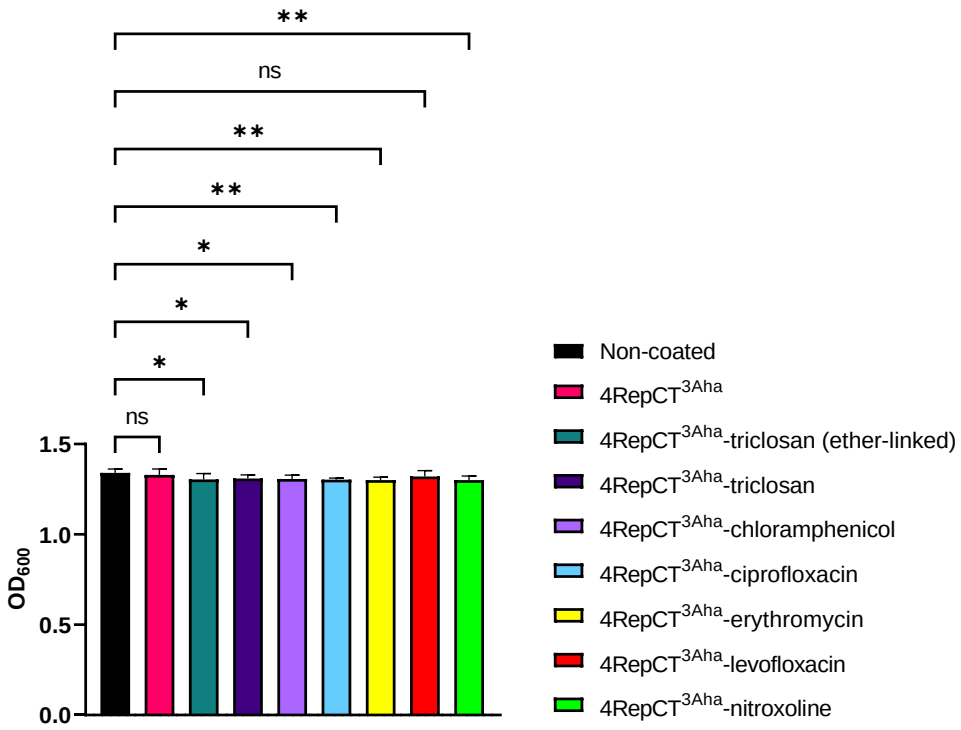

Figure 4.8. Optical density (at 600nm) of *E. coli* NCTC 12241 grown in wells coated with 4RepCT^{3Aha}-antimicrobial ligand nonconjugated mixtures subjected to isopropanol-water wash protocol. After 24-hour incubation, OD600 shows minor but statistically significant bacterial growth inhibition in wells coated with all 4RepCT^{3Aha}-antimicrobial ligand mixtures except levofloxacin.

Number of experiments N=1, number of replicates n=12. **** - p<0.0001, ***-p<0.001, **-p<0.01, ns-p>0.05 (One-way ANOVA with Dunnet's multiple comparisons test).

The growth inhibition ranged from 1% to 3% compared with non-coated wells (Table 4.7). The coating of 4RepCT^{3Aha}-levofloxacin mixture did not cause a statistically significant growth inhibition with 2% percentage decrease, p=0.3326 (Table 4.7).

Table 4.6. Mean OD_{600} of *E. coli* NCTC12241 grown in wells with 4RepCT^{3Aha}-antimicrobial ligand mixtures and the mean difference, percentage decrease and statistical significance of OD_{600} in coated wells compared to non-coated wells.

Coating	Mean (±SD)	Mean difference compared to non-coated wells (percentage decrease)	Significance of the mean difference compared to non-coated wells
Non-coated	1.34 (±0.02)	-	-
4RepCT^{3Aha}	1.33 (±0.03)	0.0106 (1%)	NS (p>0.05)
4RepCT^{3Aha}-triclosan (ether-linked)	1.30 (±0.03)	0.0361 (3%)	* p= 0.0118
4RepCT^{3Aha}-triclosan (ester-linked)	1.31 (±0.02)	0.0306 (2%)	* p=0.0456
4RepCT^{3Aha}-chloramphenicol	1.31 (±0.02)	0.0334 (2%)	* p=0.0234
4RepCT^{3Aha}-ciprofloxacin	1.30 (±0.009)	0.0377(3%)	** p=0.0076
4RepCT^{3Aha}-erythromycin	1.30 (±0.02)	0.0398 (3%)	** p=0.0042
4RepCT^{3Aha}-levofloxacin	1.32 (±0.03)	0.0202 (2%)	NS p=0.3326
4RepCT^{3Aha}-nitroxoline	1.30 (±0.02)	0.0398 (3%)	** p=0.0042

No statistically significant growth inhibition of *S. aureus* was observed in wells coated with 4RepCT^{3Aha} mixed with antimicrobial ligands (Fig.4.9). The mean difference of growth inhibition ranged from -5% to 4% with p>0.05 (Table 4.8).

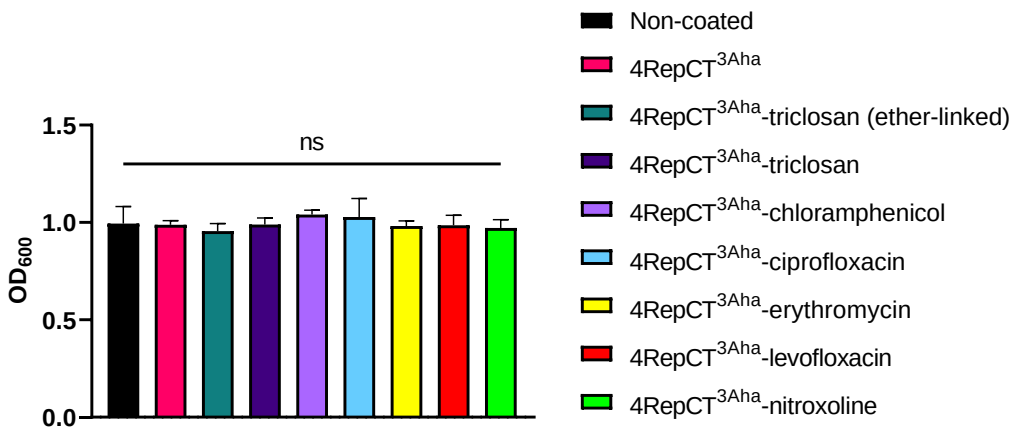

Figure 4.9. Optical density (at 600nm) of S.aureus NCTC 6571 grown in wells coated with 4RepCT^{3Aha}-antimicrobial ligand nonconjugated mixtures subjected to isopropanol-water wash protocol. After 24-hour incubation, OD600 shows no statistically significant bacterial growth inhibition in wells coated with any 4RepCT^{3Aha}-antimicrobial ligand mixtures.
Number of experiments N=1, number of replicates n=12. ns-p>0.05 (One-way ANOVA with Dunnet's multiple comparisons test).

Table 4.7. Mean OD600 of *S. aureus* NCTC6751 grown in wells with 4RepCT^{3Aha}-antimicrobial ligand mixtures and the mean difference, percentage decrease and statistical significance of OD_{600} in coated wells compared to non-coated wells.

Coating	**Mean (±SD)**	**Mean difference compared to non-coated wells (percentage decrease)**	**Significance of the mean difference compared to non-coated wells**
Non-coated	0.994 (±0.09)	-	-
4RepCT^{3Aha}	0.988 (±0.02)	0.00668 (1%)	NS (p>0.05)
4RepCT^{3Aha}-triclosan (ether-linked)	0.955 (±0.04)	0.03926 (4%)	NS (p>0.05)
4RepCT^{3Aha}-triclosan (ester-linked)	0.990 (±0.03)	0.00472 (0%)	NS (p>0.05)
4RepCT^{3Aha}-chloramphenicol	1.041 (±0.02)	-0.04674 (-5%)	NS (p>0.05)
4RepCT^{3Aha}-ciprofloxacin	1.03 (± 0.09)	-0.03400 (-3%)	NS (p>0.05)
4RepCT^{3Aha}-erythromycin	0.982 (±0.03)	0.0120 (1%)	NS (p>0.05)
4RepCT^{3Aha}-levofloxacin	0.986 (±0.05)	0.00848 (1%)	NS (p>0.05)
4RepCT^{3Aha}-nitroxoline	0.972 (±0.04)	0.0221 (2%)	NS (p>0.05)

4.5. Discussion

This chapter describes a plate-based method to evaluate antimicrobial activity of small molecules conjugated to 4RepCT^{3Aha} via a labile linker. This data builds on the previous evidence that levofloxacin can be conjugated to 4RepCT^{3Aha} fibres via a pH/esterase sensitive linker and shows sustained antimicrobial effect in solution and on solid media[106].

Five antibiotics (chloramphenicol, ciprofloxacin, erythromycin, levofloxacin, nitroxoline) and an antimicrobial ligand triclosan were conjugated to soluble 4RepCT^{3Aha} protein. The selection of molecules represents well established drugs and antiseptics that are widely used in medicine in both systemic and topical applications.

One of the properties that is unique to 4RepCT (and its azide-bearing counterpart 4RepCT^{3Aha}) is the ability to form stable and continuously accumulating films that do not require additional treatment, in contrast to other silk films that require stabilisation using high salt concentrations or an organic solvent[12,80,125,165,192]. Chemical conjugation of large molecules to 4RepCT^{3Aha} might have a detrimental influence on silk's ability to form such films via mechanisms such as electrostatic repulsion in case of charged ligands, or steric hindrance. Therefore, the conjugates were used to coat 96 well plate wells. Figure 4.10 shows a 96 well plate coated with 4RepCT^{3Aha}-conjugate films stained with a protein-specific dye. All 4RepCT^{3Aha} conjugates formed an observable film on tissue culture treated plastic suggesting that conjugation of molecules up to 700 Da (erythromycin) did not interfere with continuous assembly of 4RepCT^{3Aha} films[12].

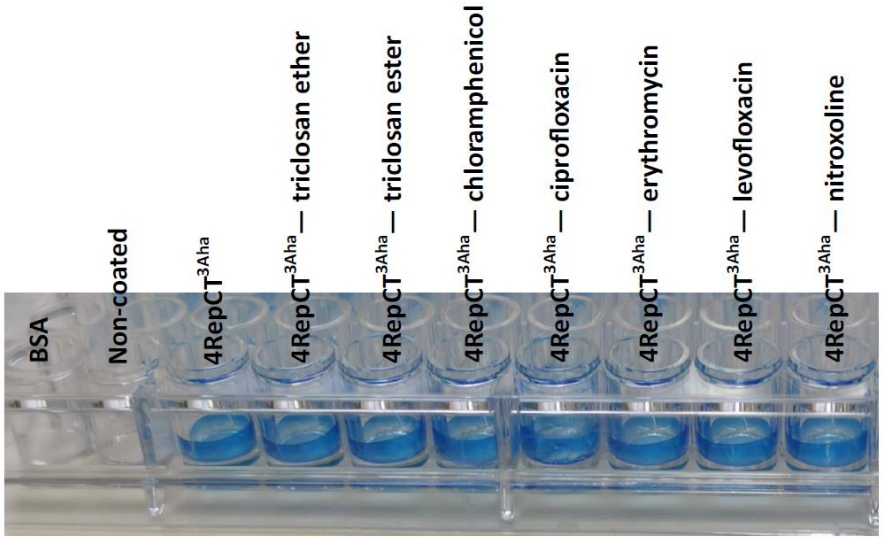

Figure 4.10. Coomassie Brilliant Blue stained films of 4RepCT^{3Aha} conjugates with antimicrobial ligands. BSA – bovine serum albumin, negative control; protein film was unstable.

All coatings of 4RepCT^{3Aha}-antimicrobial ligand conjugates bearing an ester linker showed antimicrobial effects against both *E. coli* NCTC12241 and *S. aureus* NCTC6751 at 24-hour timepoint (Fig.4.2; Fig.4.4). Both strains are antibiotic-sensitive with no described mechanisms of resistance[391]. Therefore, the differences in growth inhibition follow from the respective concentrations of the released antimicrobial ligand. Films made of fluoroquinolone ligands (levofloxacin and ciprofloxacin) showed inhibition at the level over 90% for both *E. coli* and *S. aureus* (Table 4.3; Table 4.4). Other antimicrobial conjugates except chloramphenicol were more effective against *E. coli* than *S. aureus*, despite the fact that *E. coli*, a Gram-negative organism, is generally believed to be more resistant to antimicrobials than the Gram-positive *S. aureus* due to the double cell membrane. Further to this, whilst 4RepCT^{3Aha}-chloramphenicol films caused a minor growth inhibition in *E. coli* at 24-hour timepoint, further measurements at 24-hour intervals showed that the bacteriostatic effect is sustained over three days (Fig.4.3). This is consistent with chloramphenicol's mechanism of action which is a strongly bacteriostatic effect via inhibition of protein translation[365].

Coatings of 4RepCT^{3Aha}-triclosan ether conjugate showed no antimicrobial effect (Fig.4.2; Fig.4.4). suggesting that a labile ester linker is required for activity of an antimicrobial molecule with an

intracellular target. Interestingly, literature reports of surface-tethered triclosan via an ether linkage were found to exhibit antimicrobial effect[362,392]. Both referenced studies use water washes to remove non-reacted triclosan ligand from the surfaces. In contrast, the data presented in Fig. 4.2, Fig.44, and Fig.4.5 strongly suggests that ether-tethered triclosan does not exhibit antimicrobial activity after the material is washed with isopropanol and water. Considering the very poor water solubility of triclosan (5-10mg/L[360]), water is unlikely to efficiently remove non-conjugated triclosan that adheres to surfaces (possibly through hydrophobic interactions with polystyrene or other hydrophobic components), thus the antimicrobial result reported in [362,392] could have been due to non-covalently attached triclosan.

Further, to optimise the workflow compatibility with high-throughput testing, the antimicrobial ligands were conjugated to a pre-formed 4RepCT^{3Aha} film. This approach would save time with upstream processing of the conjugation reactions by excluding manual handling and time required for dialysis (which is used for removal of copper which, if not removed, can cause protein aggregation). Films of 4RepCT^{3Aha} are stable, can tolerate a range of chemical conditions, and the reaction mixture after the conjugation can be removed during the normal washing protocol. By avoiding the dialysis procedure, the method would become applicable for use with high-throughput plate robotics.

The 4RepCT^{3Aha} film conjugates showed antimicrobial activity against *E. coli* NCTC12241 (Fig 4.5). The antimicrobial activity of antimicrobial ligands conjugated to film compared to those conjugated to soluble 4RepCT^{3Aha} was decreased by 47%- 80% (with exception to erythromycin that showed 331% increase in antimicrobial activity). This overall decrease in antimicrobial activity compared to films made of soluble 4RepCT^{3Aha} conjugates suggests that the antimicrobial loading is decreased, potentially because the ligands do not penetrate into the film. Further analysis of 4RepCT^{3Aha} film porosity is required to assess whether film is permeable for antimicrobial ligands of Mw = 200-700 g/mol.

It is important to note that, in case of erythromycin, the absolute mean optical density values were 0.591 (± 0.0298) soluble conjugate and 0.549 (±0.00640) for conjugate to a pre-formed film (Table 4.3,

Table 4.5). These absolute values suggest that both types of conjugation caused a comparable bacteriostatic effect, whereas the apparent difference in antimicrobial values is caused by lower optical density of control samples shown in Fig.4.2 complicating a direct comparison between the two sets of experiments. A smaller scale, higher-throughput assay can be designed to ensure all comparable samples are run in parallel, for example in a 384 well format, thus ensuring the samples are directly comparable.

Films formed from 4RepCT^{3Aha}-triclosan conjugate show a dose-dependent antimicrobial activity as the antimicrobial effect increased when the amount of 4RepCT^{3Aha}-triclosan ester conjugate was doubled (Fig 4.6). This data shows that by increasing the amount of 4RepCT^{3Aha}-antimicrobial ligand conjugate per well, it is possible to reach MIC90 of the antimicrobial ligand as it will be released from the film. The dose-dependency of the conjugates allows the ability to tune the dosage required for the application, for example to use minimum necessary amount of material to reach bacterial growth inhibition *in vivo* without causing local cytotoxicity. In contrast, when triclosan was conjugated to a pre-formed 4RepCT^{3Aha} film, it does not show increase in activity when the amount of 4RepCT^{3Aha} in the film is increased (Fig.4.7). As discussed above, this further suggests that the ligand does not penetrate into the 4RepCT^{3Aha} film to reach Aha reactive side chains for conjugation. Therefore, for further evaluation of releasable antimicrobial ligands, conjugation to soluble 4RepCT^{3Aha} is a preferred way to ensure maximum conjugation efficiency. Alternatively, it is possible that by increasing the coating area, more Aha side chains would be exposed and available for conjugation leading to higher loading of the biocide and better antimicrobial effect. This approach could involve different types of coating method, for example wet coating commonly employed in functional spider silk research effectively using comparable amounts of silk to coat larger area with a thinner film[169].

Lastly, to investigate whether any residual non-conjugated ligand contributes to growth inhibition observed in previous assays, films were made using a non-conjugated mix of 4RepCT^{3Aha} and an antimicrobial ligand in absence of Cu(I) and other click reagents. A minor (1-3%) but statistically

significant antimicrobial effect against *E. coli* NCTC12241 was observed in all wells coated suggesting that some non-specifically attached antimicrobial ligand can remain after the wash cycles and contribute to growth inhibition (Table 4.6). Interestingly, growth inhibition was also observed in wells coated with 4RepCT^{3Aha}-triclosan ether mix which was not seen in other assays. This suggests that washing protocol introduces variability and should be optimised further. Despite the statistical significance observed between some of the datasets in these experiments, this difference is unlikely to be meaningful in the context of a clinical application of this material. There was no statistically significant difference in the optical densities of *S. aureus* growth in this experiment (Fig.4.9).

4.6. Conclusions and future work

One major aspect of 4RepCT^{3Aha} conjugates that remains to be investigated is development of an analytical methodology to observe and quantify Aha incorporation efficiency, as well as ligand conjugation efficiency and the number of ligands that can be conjugated to a single 4RepCT^{3Aha} molecule. This topic is discussed in the General discussion in Chapter 6.

Further, as the activity of an antimicrobial molecule with an intracellular target is dependent on the release from the surface, it is important to characterise the kinetics of linker hydrolysis. Ester-bearing linkers can be hydrolysed by chemical means as the bacterial growth causes a decrease in the pH[393,394], or by enzymatic reaction involving promiscuous bacterial esterases that are abundantly secreted into the environment[395]. In the non-enzymatic scenario, the rate of the ester bond hydrolysis significantly depends on the pKa of the leaving group (the lower its pKa, the better it is as a leaving group). As such, ciprofloxacin and levofloxacin (pKa = 6) are better leaving groups compared to chloramphenicol or erythromycin (pKa = 7.5-8) which might contribute to the difference in their relative antimicrobial potency that was seen in the assays described above. In case of enzymatic hydrolysis, the release of a free antibiotic would depend on the ability of the molecule to fit in the enzyme binding pocket due to steric hindrance caused by a relatively short linker length and the proximity of the material surface. Whilst both mechanisms are feasible, there is no agreement on which mechanism of action is

predominant .With this in mind, further research should focus on obtaining experimental evidence of the rates of ester hydrolysis in these antimicrobial ligands, especially under especially under physiologically relevant conditions. Further, analytical methods would provide greater insight into the kinetics of the drug release (especially as to whether all conjugated ligands are released simultaneously or in increments). This could be done by incubating "clickable" molecules in buffer at different pH or bacterial growth media and then observing the hydrolytic stability of the ligands by mass spectrometry, hydrophobic interaction chromatography and HPLC[396]. Further, it could be possible to observe both the conjugation reaction and linker hydrolysis using real-time NMR[397,398]. These experiments would require extensive method development that is beyond the scope of this chapter.

In conclusion, this chapter describes the first 96 well plate-based method for testing 4RepCT^{3Aha}-antimicrobial conjugate films that are designed to release a drug via hydrolysis of an ester-bearing ligand. Soluble 4RepCT^{3Aha} was conjugated to a selection of antimicrobial ligands and processed into films that showed antimicrobial activity against *E. coli* and *S. aureus*. These conjugates showed a dose-dependent antimicrobial effect that allows for dosage tailoring. Further, it was shown that ligands can be conjugated to pre-formed 4RepCT^{3Aha} films, however the loading of the compound was lower as shown by decrease in antimicrobial effect (compared to 4RepCT^{3Aha} that was conjugated to the ligands in solution). These films did not show dose-dependent antimicrobial effect. Finally, it was observed that antimicrobial effect in these assays is not caused by non-specifically adsorbed ligand because non-conjugated 4RepCT^{3Aha} mixed with the antimicrobial ligand in absence of copper did not have the same antimicrobial effect as the conjugates, thus validating the washing protocol and strongly suggesting that the antimicrobial effect is due to a successful CuAAC reaction.

5. Contact-killing surface coatings of 4RepCT^{3Aha} conjugates to quaternary ammonium ligands using click chemistry.

5.1. Introduction

As discussed in Chapter 4, an established, fully surface adherent biofilm is exceptionally difficult to clear due to variety of bacterial adaptation strategies. An emerging methodology for tackling bacterial attachment is the surface functionalisation with permanently surface tethered biocides, creating a passive contact-killing surface (Fig.4.1). This approach avoids the concerns about diffusion to sub-biocidal concentrations and eventual exhaustion of the antimicrobial surface as seen in burst releasing and controlled release surfaces. The main drawback of this approach is that the ligand options are limited to those that exhibit their antimicrobial effect via membrane interactions. Further, such surface can be inactivated when the biocidal moieties are covered with proteins or bacterial debris as it physically hides the ligands from bacteria.

This introduction reviews the use of a well-established family of cationic biocidal ligands called quaternary ammonium compounds (QAC) in clinical applications and contact killing surface design.

5.1.1. QAC overview

QACs are cationic compounds with a long history of use as antiseptics. The QAC representative formula is $N^{+}R_1R_2R_3R_4X^{-}$ where R can be a hydrogen, alkyl group, or other substituent, and X- is an anion, usually a halide (Fig. 5.1 A)[399]. At least one R group is commonly a lipophilic substituent.

A

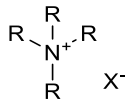

B

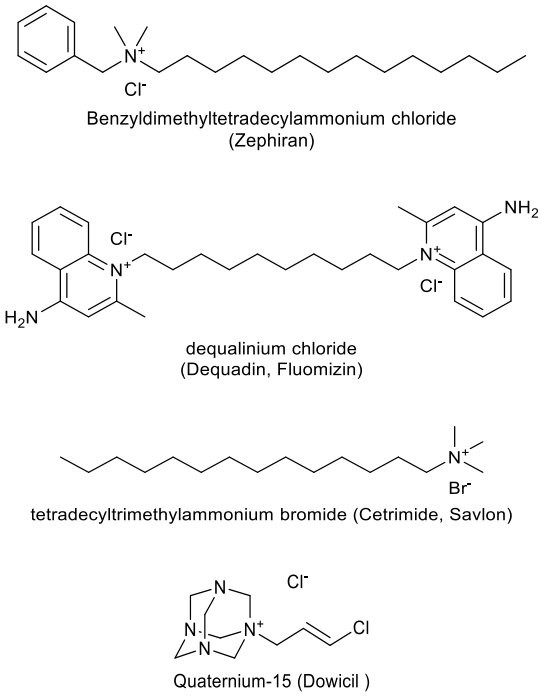

Figure 5.1. Structures of quaternary ammonium compounds; **A** : generic QAC formula where R – H, CH_3, or another substitute and X- is an anion (usually a halide). **B**: Examples of QAC compounds used as antiseptics in commercially available products (brand names stated in the brackets).

QACs are biocidal against a broad spectrum of bacteria including Gram positive, Gram negative, and vegetative cells, as well as fungi, parasites, and enveloped viruses such as Influenza[400]. To that end, soluble QACs are used in surgery under a variety of brand names as hard surface cleaner and wound disinfectant, and as an antimicrobial agent in oral and gynaecological applications (Fig 5.1 B).

A substantial amount of work has been performed focusing on different architectures of surface immobilised QAC ligands, notably by teams of Prof J C Tiller and Prof A Klibanov among many others (reviewed in [401,402]). A representative sample of QAC-functionalised materials exemplifying the diversity of ligand architectures is outlined in Table 5.1.

Table 5.1. Representative examples of surface-grafted quaternary ammonium ligands.

Quaternary ammonium compound	Base material	Findings	Ref
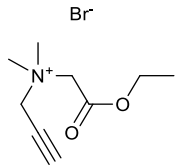	Cellulose	90% reduction *in E. coli* CFU count after a liquid culture was exposed to 1.6mg material	403
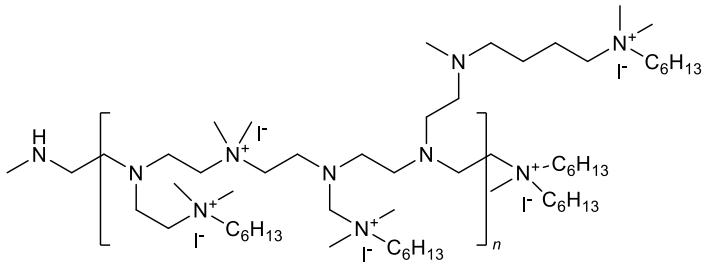	Silicon and hyperbranched polyurea	87-99.99% reduction in *Staphylococcus epidermidis* ATCC 12228 CFU on solid media	404
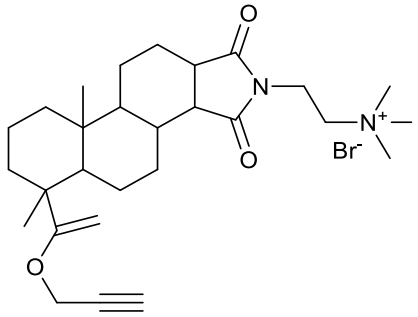	Azide-polydimethylsiloxane	No antimicrobial activity in the diffusion assays. 86% reduction of surface-adherent *S. aureus*; 47% reduction of surface-adherent *E. coli* 77% decrease in *S. aureus* biofilm biomass at 2 days of incubation	405

Table 5.1 (*continued*). Representative examples of surface-grafted quaternary ammonium ligands.

Quaternary ammonium compound	Base material	Findings	Ref
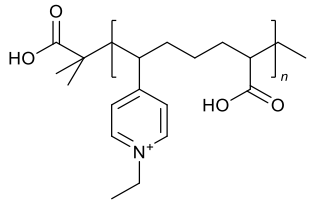	polystyrene and latex particles	88-99% reduction in *S. aureus*, *E. coli*, *S. epidermidis*, *P. aeruginosa*, *S. cerevisiae*, *C. albicans* CFU	[406]
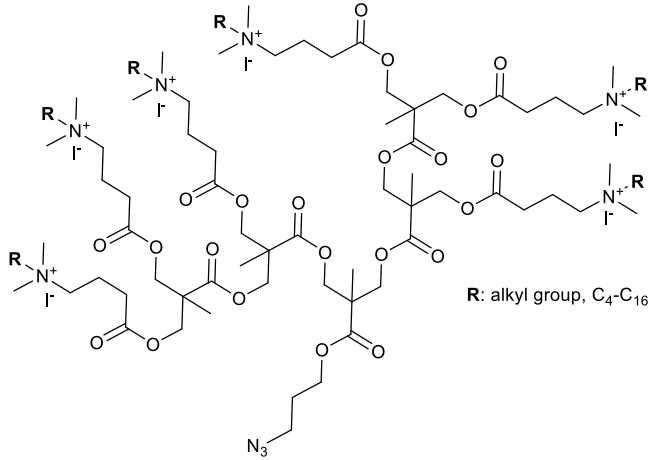	Alkyne polydimethylsiloxane	99% reduction in *E coli* and *S aureus* within 5 minutes of exposure	[407–409]
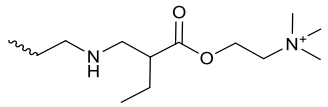	Chitosan	No zone of inhibition against *S. aureus*, *K. pneumoniae*, however growth on the coated material is reduced. Minimal activity against *A. fumigatus*. Material retains the activity after washing	[410]

5.1.2. QAC mechanisms of action

Despite the abundance of QAC use in clinical applications, the mechanism of QAC action remains unclear. Some evidence suggests that QAC alkyl chains penetrate bacterial cell walls whilst the cationic charge disrupts the membrane-associated ion balance resulting in bacterial cytoplasmic leakage and eventually cell death[411,412] . This theory is called the polymeric spacer effect and it is supported by observations that in solution, QAC compounds with alkyl chain length <4 carbons are virtually inactive[413]. Further, QAC with chain lengths of 12-14 carbons have shown the best activity against Gram-positive bacteria and yeast, whereas 14-16 carbon chain length is most effective against Gram-negative bacteria[414] which reflects the differences in cell wall thickness. However, this does not explain the activity of surface tethered QAC ligands that show an antimicrobial effect regardless of the alkyl chain length and even have a better biocidal effect compared to a longer alkyl chain-bearing QAC[415,416].

The second proposed QAC mechanism of action is called the ion-exchange mechanism which states that the strong cationic charge of a QAC disrupts divalent cations present on bacterial membranes to stabilise phospholipid interactions (usually Ca^{2+} and Mg^{2+}). This hypothesis is supported by consistent evidence that a higher charge density of QAC is correlated with increased antimicrobial effect[417,418]. These studies have extended into a field of polycationic dendrimers and brushes that contain quaternary ammonium moieties, however the increase in charge density on a single molecule is logically achieved by increasing the size of the molecule (see Table 5.1) therefore these two hypotheses are not mutually exclusive. Further to this, some research proposes that the QAC counter anion dissociates from QAC molecule in solution and acts as the biocidal agent, however there is little evidence to support this claim because despite known cytotoxicity of halides, this assumption implies that the ion diffuses into the solution which would not account for biocidal activity exclusively at the surface[399].

Lastly, the phospholipid sponge hypothesis states that quaternary ammonium interacts directly with the negatively charged phosphates in the bacterial cell membranes leading to removal of whole

phospholipid molecules and resulting in a cell content leakage[418]. This proposed mechanism of action is related to the ion-exchange mechanism described above in that both are reliant on the unique charged feature, and evidence shows that QAC-grafted surfaces can be inactivated by anionic surfactants and lipids but not by non-charged liposomes[404].

Overall, there is no agreement on the specifics of QAC-induced biocidal effects, although evidence shows that surface-tethered QAC are biocidal via different effect than soluble QAC, and that strong cationic charge is a fundamentally important biocidal feature.

5.1.3. QAC: other bioactivities

Apart from their broad range antimicrobial activity, QAC compounds exhibit inhibition of matrix metalloproteases (MMPs)[419,420]. MMPs are a large family of collagenolytic enzymes, and regulation of their activity can be useful in resolving chronic wounds[421], as an adjuvant therapy in extracellular matrix-degrading tumours such as chondrosarcomas[422,423]. QAC use is very popular in dentistry where it serves a dual purpose of inhibiting caries and preventing biofilm formation on dental materials[424,425]. The mechanism of action in MMP inhibition by QAC could be via metal ion displacement (similarly to their antimicrobial ion-exchange mechanism discussed above), however to the date, there is little understanding of the biochemical basis of these interactions.

5.1.4. QAC resistance

Historically, QAC have been thought not to provoke antimicrobial resistance due to their nonspecific membrane targeting effect. However, more recently, it has been shown that a multitude of adaptations and resistance mechanisms can evolve in microorganisms upon sublethal exposure to QAC[426,427]. Adaptations include alterations in the cell wall composition as well as upregulated secretion of amine oxidases[428]. Resistance mechanisms are mostly based on nonspecific efflux pumps and porins. Interestingly, the antimicrobial resistance to surface tethered QAC have not been observed *in vitro* at 11 passages[429]. This could be due to the fact that immobilised QACs do not diffuse down the concentration gradient to sublethal concentrations. Further, majority of literature reports over 90%

reduction in bacterial growth on QAC-functionalised surfaces thus minimising the risk of resistance development because nearly all microorganisms coming into the contact with the surface are inactivated (Table 5.1). In addition, as discussed previously, it could be that immobilised QAC have a distinct mechanism of action compared to QAC in solution, thus slowing down the evolution of resistance.

5.1.5. QAC surface-grafting techniques and their limitations

Although quaternary ammonium-bearing compound design allows for great morphological diversity, the challenge of grafting QAC onto a solid, biomedically relevant surface remains a technical challenge. Most bulk materials, such as titanium, silicone, and plastics have no functional chemical groups available for QAC grafting without pre-treatments termed surface activation. The activated surface usually introduces hydroxyl groups that are available for further chemical modifications, however the conditions used in surface pre-treatment can be extreme, such as plasma, flame, or ozone gas treatment; electrodeposition; and chemical vapour deposition are among the most popular (reviewed in [430]). Whilst these methodologies are acceptable for lab-scale research, their translation into a larger scale medical device manufacturing is slow. To that end, thin films and coatings composed of a polymer that naturally carries a chemically reactive group and a QAC are becoming increasingly common, for example, chitin-QAC[402,410,431,432] and cellulose-QAC[432,433] coatings. This is a very useful approach as it allows to functionalise materials without the need of fundamentally changing the bulk material processing where the bulk material does not have chemically reactive groups that lend themselves to QAC grafting.

5.2. Aims and objectives

Section 5.1 Introduction highlights that whilst QAC compounds are highly versatile biocides, new approaches are required to install QAC on medical surfaces post-manufacturing as most current approaches can only functionalise the surface during the material manufacturing.

The aim of the research described in this chapter is to create a biocidal surface coating based on 4RepCT^{3Aha} conjugates to a QAC ligand. The unique ability of 4RepCT^{3Aha} to form stable films using only water as solvent and ambient temperature in combination with the presence of three azide groups available for CuAAC conjugation offers itself to creation of a versatile polycationic molecule for surface coating.

To the date, attempts to analytically characterise the conjugations of 4RepCT^{3Aha} to a small ligand have been technically challenging. To that end, three surface characterisation approaches – water contact angle, scanning electron microscopy, and atomic force microscopy with applied electrical bias- are used in order to characterise and seek out features unique to 4RepCT^{3Aha}-QAC conjugate films.

The biocidal effect of 4RepCT^{3Aha}-QAC films is characterised using traditional microbiological methods - zone of inhibition study and a colony forming unit count.

Building on the assay used for releasable ligand testing described in Chapter 4, a high-throughput compatible plate-based assay for investigating 4RepCT^{3Aha}-QAC coated surface-adherent bacterial survival is developed using two established parameters associated with bacterial growth: metabolic reduction of a dye and biomass increase as a function of the increase in turbidity.

5.2. Methods

5.3.1. Clickable QAC synthesis and conjugation

QAC (Br), QAC (I) and QAC (tosylate) (Table 5.2) were prepared in house by Tom Armstrong following the method of Xu *et al.*[403] . The synthesis procedure can be found in the Appendix B.

Ligand stocks were prepared in Milli Q water to 50mM and stored at -20°C.

Table 5.2. Clickable quaternary ammonium ligands for conjugations to 4RepCT^{3Aha}.

Structure & abbreviated name	Chemical name
QAC (Br) 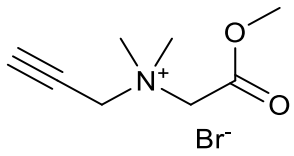	*N*-(2-methoxy-2-oxoethyl)-*N*,*N*-dimethylprop-2-yn-1-aminium bromide
QAC (I) 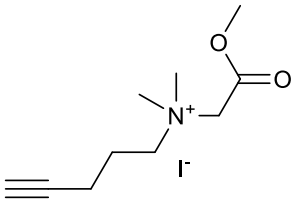	*N*-(2-methoxy-2-oxoethyl)-*N*,*N*-dimethylpent-4-yn-1-aminium iodide
QAC (tosylate) 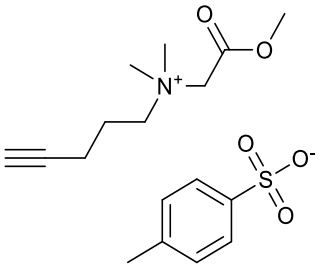	*N*-(2-methoxy-2-oxoethyl)-*N*,*N*-dimethylpent-4-yn-1-aminium tosylate

An aliquot of 2 mg/ml 4RepCT^{3Aha} was thawed at room temperature. The reaction was set up by combining 800 µl 4RepCT^{3Aha} (2 mg/ml), 10 µl QAC ligand (50 mM), 90 µl NaAsc (50 mM) and lastly slowly adding 10µl $CuSO_4$ (50 mM). The reaction was incubated at room temperature with gentle agitation for 4 hours and stopped by addition of 3µl EDTA pH 8 (0.2 M) followed by dialysis against 2 L 20 mM Tris pH 8 at 4 °C overnight. The concentration of protein in the dialysed solution was calculated taking into consideration the final volume and adjusted to 1 mg/ml with 20 mM Tris pH 8.

5.3.2. Investigation of the 4RepCT^{3Aha} and 4RepCT^{3Aha}-QAC wettability

Films of 4RepCT^{3Aha} and 4RepCT^{3Aha}-QAC (Br) were made by pipetting 50 µl 1 mg/ml solution on an aluminium stub and 100 µl 1 mg/ml protein solution on a microscope slide and allowing water to evaporate in a desiccator at ambient pressure at room temperature overnight. Films were washed with MilliQ water to remove residual salts and dried in the desiccator as described previously. Coated metal stubs were used for eSEM analysis using FEI Quanta 650 ESEM. The sample was freeze dried *in situ* followed by gradual rehydration until discrete water droplets were observed.

Coated glass slides were used for liquid contact angle measurement. The measurement was carried out by adding 1µL water droplet onto the coated glass slide(the sessile drop method) using KSV CAM200 goniometer at 20°C. Each sample was measured ten times from each camera (left, right, centre) and expressed as an average +- standard deviation.

5.3.3. Scanning electron microscopy assessment of the film surface morphology

Films were formed on aluminium pin stubs by pipetting 50 µl of protein solution (1 mg/ml) onto the stub and drying in a desiccator overnight, then washed in MilliQ water and freeze-dried using Thermo Scientific ModulyoD freeze dryer. Dried films were coated with gold using Polaron SC7640 sputter coater at 90 second coating time. Samples were visualised using JEOL 6060LV SEM with JEOL Scanning Electron Microscope software.

5.3.4. Atomic force microscopy for surface topology and conductive behaviour

Films were formed on glass microscope slides (VWR Hydrolytic Class 1 glass) by pipetting 100 µl of protein solution onto a glass slide followed by incubation for 10 minutes at room temperature. The remaining protein solution was aspirated, and slides were rinsed with MilliQ water, then dried in the desiccator overnight at ambient pressure. Imaging was carried out on Dimension Icon AFM (Bruker) with Peak Force TUNA Module attachment using Peak Force TUNA Tips (Bruker) as probes. Measurements were carried out at room temperature.

5.3.5. Zone of inhibition study

Fibres were made by incubating 1 ml of 1 mg/ml 4RepCT^{3Aha} and 4RepCT^{3Aha}-QAC(Br) with 50 µL 100U human thrombin with gentle agitation at 37°C for 1 hour. Fibres were collected by centrifugation at 14,000 *g* for 5 minutes. A single colony of *E. coli* NCTC 12242 was used to inoculate 5 ml LB media and grown overnight at 37°C, 200 rpm. A 100 µl aliquot of the overnight culture was spread on an LB agar plate and allowed to dry in sterile environment. Fibres were placed in the middle of the inoculated LB agar plates. Plates were incubated at 37°C for 6 days with daily inspection of the zone of inhibition.

5.3.6. Bacterial survival on coated glass beads: colony forming unit count

Borosilicate plating beads (5 mm diameter, Merck) were sterilised by autoclaving and coated with 4RepCT^{3Aha} or 4RepCT^{3Aha}-QAC (Br) by placing 5 beads into a 1 ml of the protein solution (1 mg/ml) followed by incubation with gentle agitation overnight at room temperature. Coated beads were washed with MilliQ water and dried in the desiccator. The formation of a film was confirmed by Coomassie staining.

An overnight culture of *E. coli* NCTC12242 was used to inoculate 5 ml aliquots of LB media at a hundredfold dilution. One bead was added to each aliquot and incubated overnight at 37°C, 200 rpm (experiment was performed in triplicate to enable statistical analysis). Beads were removed from liquid culture and placed in individual sterile 20 ml universal tubes and washed thrice with 5 ml PBS to remove loosely attached bacterial cells. Washed beads were placed in 1.5 ml tubes, and 1 ml sterile PBS buffer was added. Tubes were secured in a floating foam tube rack and sonicated in the RS Pro ultrasonic water bath at 40 kHz for 3 minutes at room temperature. The beads were removed from the buffer, and serial dilutions of bacterial suspensions were plated on LB agar solid medium and incubated at 37°C. Grown colonies were counted using Fiji with the Cell Counter plugin. The data was compared using Student's t-test.

5.3.7. Live-dead microscopy of *E. coli* NCTC12242 incubated on slides coated with 4RepCT^{3Aha} and 4RepCT^{3Aha}-QAC (Br)

Microscopy slides were wet-coated with 4RepCT^{3Aha} and 4RepCT^{3Aha}-QAC(Br) by pipetting 100 µl of protein solution (1 mg/ml) onto the slide and the cover slip, incubated for 1 hour at room temperature. Protein solution was aspirated, and slides were washed with 1 M NaCl to remove residual DNA, followed by Milli Q water and 70% isopropanol. Washed slides and coverslips were dried in the desiccator at ambient pressure.

E. coli NCTC 12242 overnight culture was stained with LIVE/DEAD® BacLight™ Bacterial Viability Kit (ThermoFisher). A 1 ml aliquot of an overnight culture was harvested by centrifugation at 14,000 *g* and washed with 1 ml 0.9% w/v NaCl three times. Washed bacteria were resuspended in 1 ml 0.9% w/v NaCl supplemented with 3 µl SYTO9 and 6 µl propidium iodide and allowed to stain for 15 minutes protected from light. After staining, 5 µl of *E. coli* suspension was placed on a coated slide and covered with a coated coverslip and incubated for 5 hours at 37°C protected from light. Cells were imaged using ZEISS LSM 710 confocal laser scanning microscope using 63 x magnification with 594 nm and 488 nm laser lines for propidium iodide (excitation/emission maxima: 493/636 nm) and SYTO9 (excitation/emission maxima 483/503 nm), accordingly. Five random fields of vision were used to count total cells using 503 nm laser and membrane-compromised bacterial cells using 594nm laser. Images were processed using ZEN Blue software. Cells were counted using Fiji software with Cell Counter plugin. The data was compared using Student's t-test.

5.3.8. Plate-based biofilm recovery assays using cell biomass turbidity and resazurin reduction

Films of 4RepCT^{3Aha}, 4RepCT^{3Aha}-QAC (Br), 4RepCT^{3Aha}-QAC (I), and 4RepCT^{3Aha}-QAC (tosylate) were formed in a 96-well plate by adding 50 µl protein solution to each well ensuring that the bottom of the well is evenly wetted. The plate was dried in the desiccator overnight and washed with MilliQ water and 70% isopropanol, then dried overnight as described above.

E. coli NCTC12242 and *P. aeruginosa* were grown in LB media and *S. aureus* NCTC 6571 was grown in tryptic soy broth (TSB). A single bacterial colony was used to inoculate 5 ml of their respective media and incubated overnight at 37°C , 200 rpm. Bacteria were diluted thousandfold in fresh growth media and 100 µl of the diluted bacterial suspension was added to each well. Plate was incubated at 37°C overnight without agitation to encourage bacterial settling onto the coated surface. The spent media was discarded, and wells were washed with 300 µl PBS thrice to remove loosely attached bacterial cells.

For resazurin reduction assays, sterile growth media was supplemented with 1% w/v resazurin (0.22 µm-filtered) to the final concentration of 0.001%, and 200 µl of the solution was added to each well. The plate was incubated at 37°C for 6 hours. Reduction of resazurin to resorufin by bacterial metabolism was measured at 570 nm using TECAN SPARK plate reader and normalised against absorbance at 600 nm (OD_{570}-OD_{600}) as per PrestoBlue standard protocols (normalisation against turbidity).

For cell turbidity assays, 200 µl of fresh growth media was added to the wells. The plate was incubated at 37°C for 6 hours, and turbidity of the media was measured at 600nm using a TECAN SPARK plate reader.

The data was visualised using Prism software and the values were compared using one-way ANOVA and Tukey's post-hoc test.

5.4. Results

5.4.1. Clickable QAC conjugation to 4RepCT^{3Aha}

Conjugation was carried out in water due to excellent water solubility of the ligands. No observable precipitation was formed during the reaction or after 24-hour dialysis.

5.4.2. Investigation of the 4RepCT^{3Aha} and 4RepCT^{3Aha}-QAC (Br) film wettability

Aluminium surfaces coated with 4RepCT^{3Aha} and 4RepCT^{3Aha}-QAC (Br) showed different wettability properties when observed using environmental SEM with *in situ* freeze drying followed by re-wetting (Fig 5.2 A, freeze-dried). Films of 4RepCT^{3Aha}-QAC (Br) contained more aggregation compared to 4RepCT^{3Aha} films. At approximately 90% absolute humidity, 4RepCT^{3Aha}-coated aluminium surfaces were covered in distinct droplets. In contrast, as humidity of the eSEM chamber was increased to 90%, 4RepCT^{3Aha}-QAC (Br)-coated aluminium stubs were coated in a uniform water film and failed to form observable droplets at 500 x magnification.

Further investigation of the water contact angle (WCA) using sessile drop method on films formed on glass slides showed that the WCA of the 4RepCT^{3Aha}-QAC (Br) film was on average 4.19 degrees smaller than that of 4RepCT^{3Aha} (Fig. 5.2 B). This difference was not statistically significant (Student's t-test, n=10, p=0.0541).

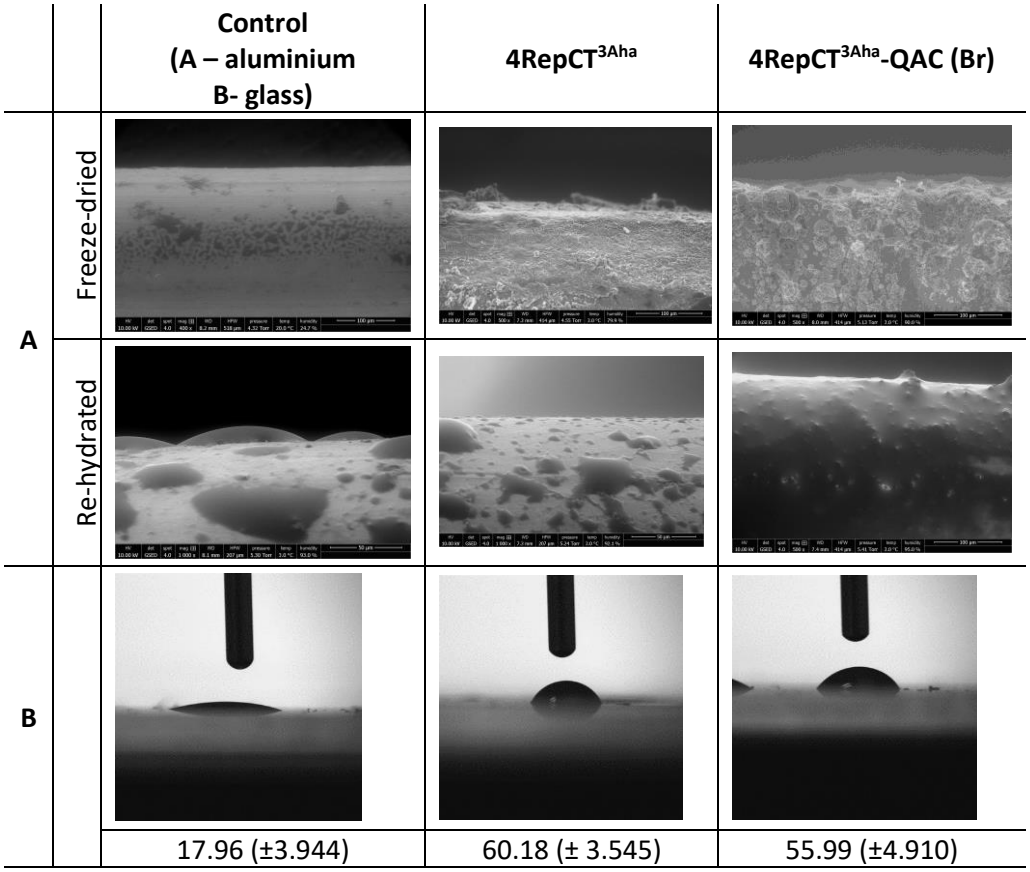

Figure 5.2. Wettability of 4RepCT^{3Aha} and 4RepCT^{3Aha}-QAC (Br) coated surfaces. **A**: *In situ* freeze-dried and re-wetted surfaces at 90% humidity using environmental SEM (control: aluminium) (scale bar: 100 µm). **B**: Water contact angle (WCA) images and measurements (n=10, ±SD) of a non-coated, 4RepCT^{3Aha}, and 4RepCT^{3Aha}-coated glass slide

5.4.3. Morphology of 4RepCT^{3Aha} and 4RepCT^{3Aha}-QAC (Br) films

Morphological assessment of 4RepCT^{3Aha} and 4RepCT^{3Aha}-QAC (Br) films was carried out using conventional SEM with gold-coated samples. These observations showed that 4RepCT^{3Aha} films have a smooth morphology with minimal aggregation (Fig.5.3 A). Under 5000 x magnification, 4RepCT^{3Aha} film exhibited morphology of a porous interconnected network (Fig. 5.3 B).

In contrast, 4RepCT^{3Aha}-QAC (Br) films have rougher morphology featuring aggregates with approximate diameter of 10-20 µm (Fig 5.3 A), as well as smaller aggregates of 10-20 nm diameter (Fig 5.3 B). Discrete fibrous structures were observed on 4RepCT^{3Aha}-QAC (Br) films at both 2000 x and 5000 x magnification.

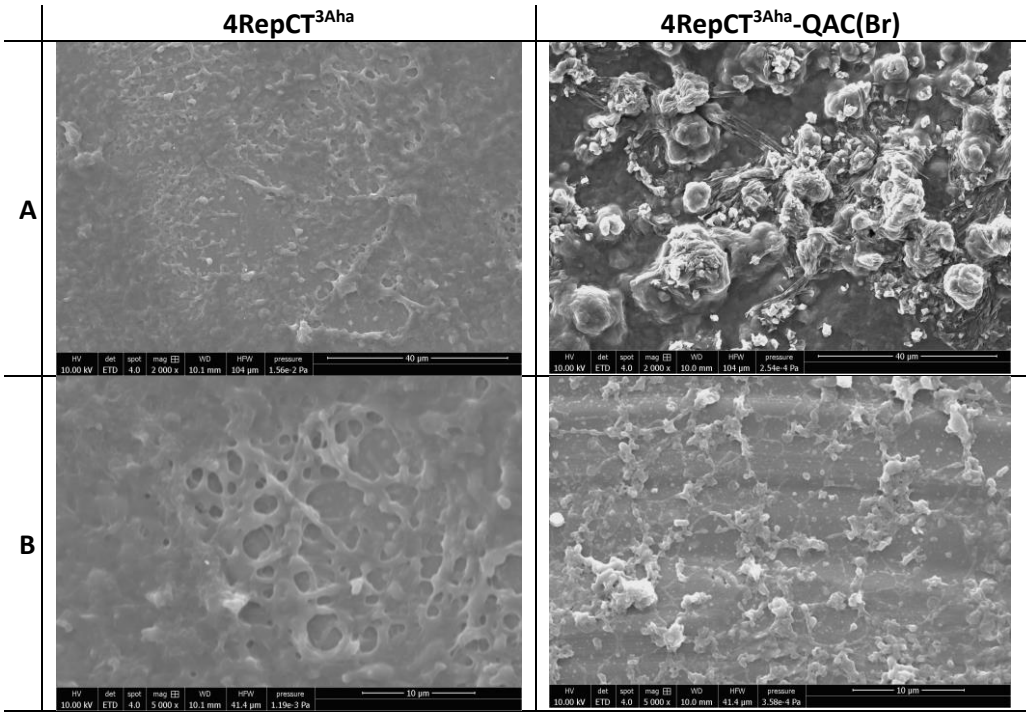

Figure 5.3. Surface morphology of 4RepCT^{3Aha} and 4RepCT^{3Aha}-QAC (Br) films using SEM. **A:** films under 2000 x magnification. Scale bar: 40 µm. **B:** films under 5000 x magnification. Scale bar: 10 µm.

5.4.4. Topology of 4RepCT^{3Aha} and 4RepCT^{3Aha}-QAC (Br) films

Preliminary topological assessment was carried out using atomic force microscopy (AFM) in tapping mode with contact current measurements at 10 V bias. Films formed by wet coating of 4RepCT^{3Aha} onto a glass slide showed topographical features ranging from -4.7 nm to 5.4 nm (Fig. 5.4) . In contrast, 4RepCT^{3Aha}-QAC (Br) showed rougher surface topology ranging from -19.9 nm to 36.5 nm with distinct spherical aggregates (Fig 5.4).

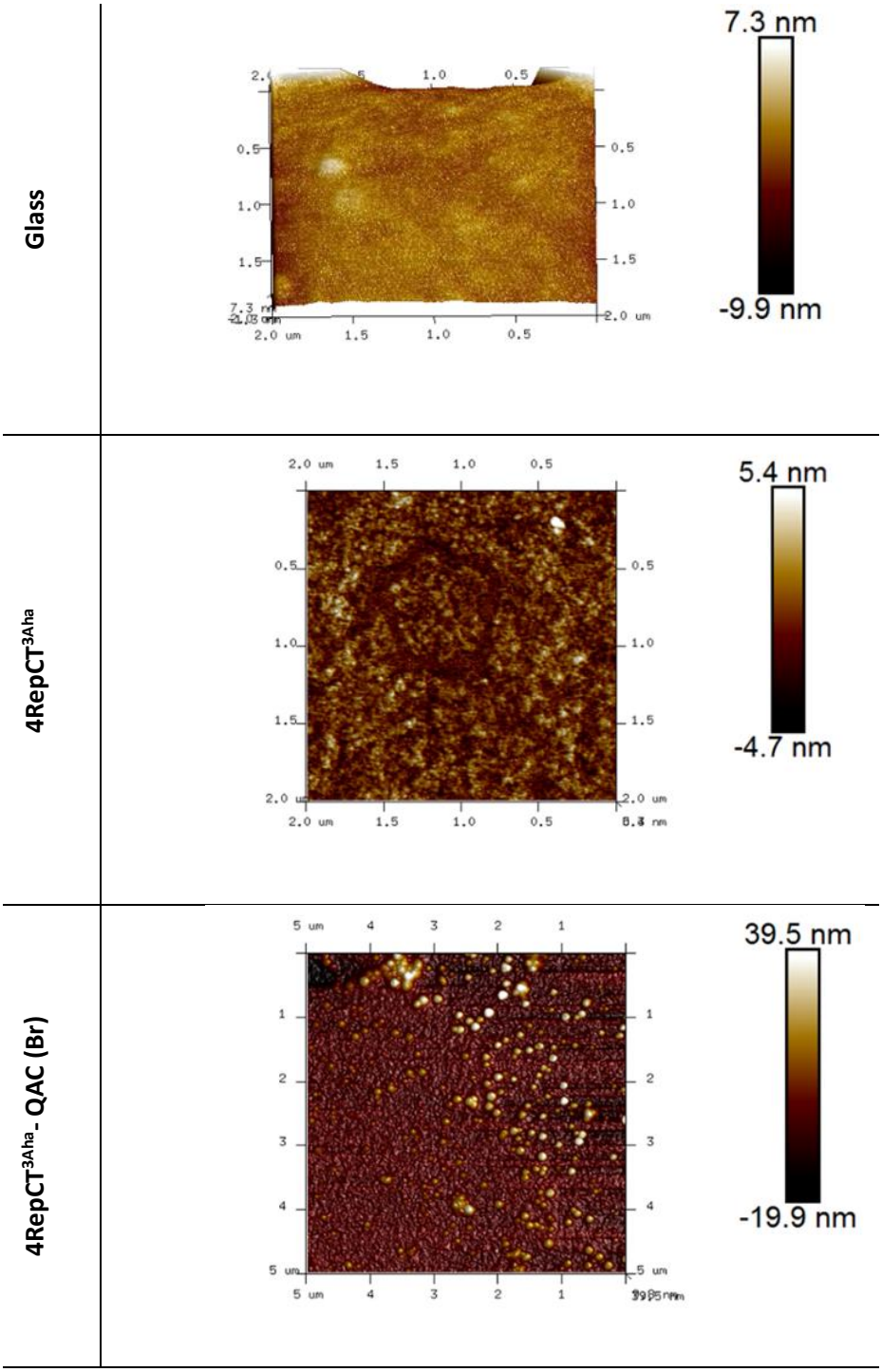

Figure 5.4. Atomic force microscopy images of a glass slide, 4RepCT^{3Aha} and 4RepCT^{3Aha}-QAC (Br).

5.4.5. Zone of inhibition study of 4RepCT^{3Aha} and 4RepCT^{3Aha}-QAC (Br) fibres

Zone of inhibition (ZOI) studies of 4RepCT^{3Aha} and 4RepCT^{3Aha}-QAC (Br) fibres were carried out to investigate whether conjugate fibres exhibit antimicrobial action via release of the QAC molecule from the material. No ZOI was observed on *E. coli* NCTC12242 lawns grown in presence of either 4RepCT^{3Aha}

or 4RepCT^{3Aha} fibres (Fig 5.5). Furthermore, five days after incubation, 4RepCT^{3Aha} fibres promoted bacterial growth as seen by increased confluent growth over the fibres. No increase in bacterial growth was observed on or around 4RepCT^{3Aha}-QAC (Br) fibres.

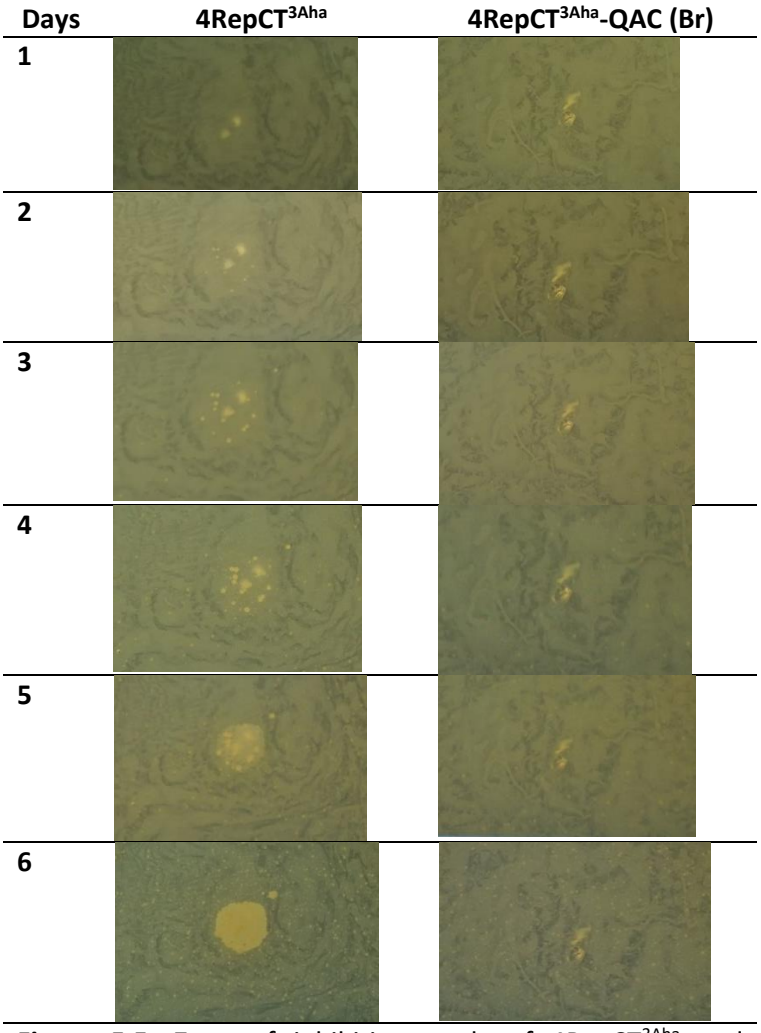

Figure 5.5. Zone of inhibition study of 4RepCT^{3Aha} and 4RepCT^{3Aha}-QAC (Br) fibres over six days.

5.4.6. Colony forming units of *E. coli* recovered from 4RepCT^{3Aha} and 4RepCT^{3Aha}-QAC (Br) coated surfaces

To investigate whether surface coating with 4RepCT^{3Aha} or 4RepCT^{3Aha}-QAC (Br) affected bacterial adhesion and surface-associated survival, glass spreading beads were coated with silk protein solution and incubated in liquid media inoculated with *E. coli* NCTC12242. Colony forming units (CFU) were recovered by sonication, grown on solid media, and counted.

The coating was confirmed using Coomassie Brilliant Blue protein stain. Both 4RepCT^{3Aha} and 4RepCT^{3Aha}-QAC (Br)-coated beads retained Coomassie dye resulting in a visibly blue colour (Fig. 5.6).

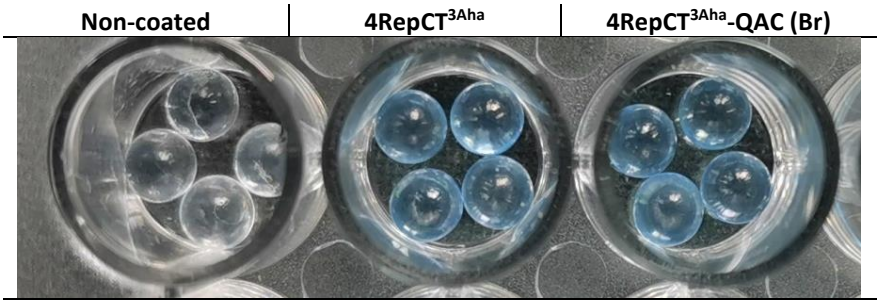

Figure 5.6. Glass beads coated with 4RepCT^{3Aha} and 4RepCT^{3Aha}-QAC (Br) and stained with a protein-specific dye Coomassie Brilliant Blue.

After incubation with a growing liquid culture of *E. coli* NCTC12242 overnight, beads were washed to remove loosely attached cells. Firmly surface-adherent cells were removed by sonication and plated on solid media. The highest number of colony forming units was recovered from the beads coated with 4RepCT^{3Aha} (104.3 (± 56.62) x10^3 CFU/ml) compared to non-coated (25.67 (±13.58) x 10^3 CFU/ml) and 4RepCT^{3Aha}-QAC (Br)-coated (2.667 (±0.57) x 10^3 CFU/ml) beads (Fig. 5.7). CFU recovery from beads coated with 4RepCT^{3Aha}-QAC was reduced by 89.6% and 97.4% compared to non-coated and 4RepCT^{3Aha}-coated beads, respectively. CFU recovery from beads coated with 4RepCT^{3Aha} was 75% higher than that of non-coated beads.

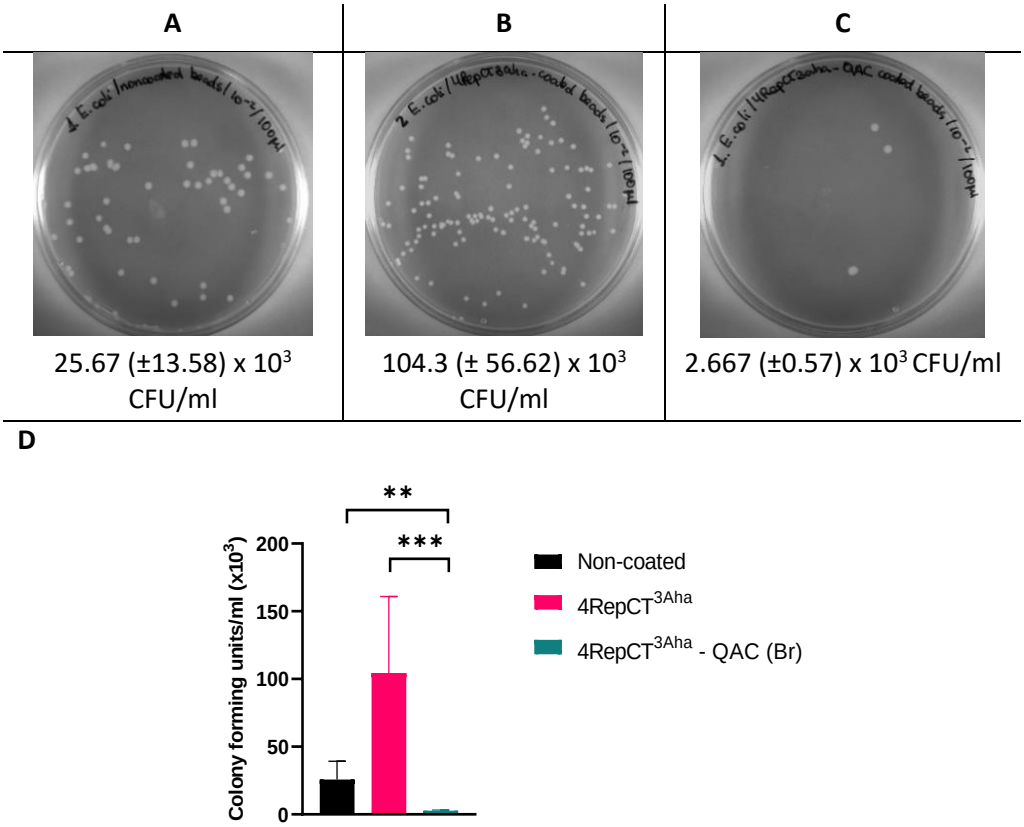

Figure 5.7. *E. coli* NCTC 12242 colony forming units recovered by sonication from **A** – non-coated, **B** – 4RepCT^{3Aha}-coated, **C** – 4RepCT^{3Aha}-QAC (Br) - coated beads after 18-hour growth in liquid culture. **D** -Number of colony forming units recovered from non-coated, 4RepCT^{3Aha}-coated, and 4RepCT^{3Aha}-QAC (Br) coated beads using sonication (Student's t test, ** - p<0.01, *** - p<0.001, n=3).

5.4.7. Live-dead microscopy

Survival of *E. coli* NCTC12242 on surfaces coated with 4RepCT^{3Aha} and 4RepCT^{3Aha}-QAC (Br) was observed using confocal fluorescence microscopy with SYTO9 and propidium iodide staining. Stained bacterial cells were placed between coated microscope slide and coverslip for six hours prior to visualisation. Significantly higher number of propidium iodide-stained cells was observed on slides coated with 4RepCT^{3Aha}-QAC (Br) (70% increase compared to 4RepCT^{3Aha}-coated slides, p=0.0014 (Fig. 5.8A). There was no difference in total cell count per field of vision as observed by SYTO9 staining (Fig. 5.8 B). The number of dead cells as a percentage of total cells per field of vision was 10% and 36% on 4RepCT^{3Aha} and 4RepCT^{3Aha}- QAC (Br) , respectively.

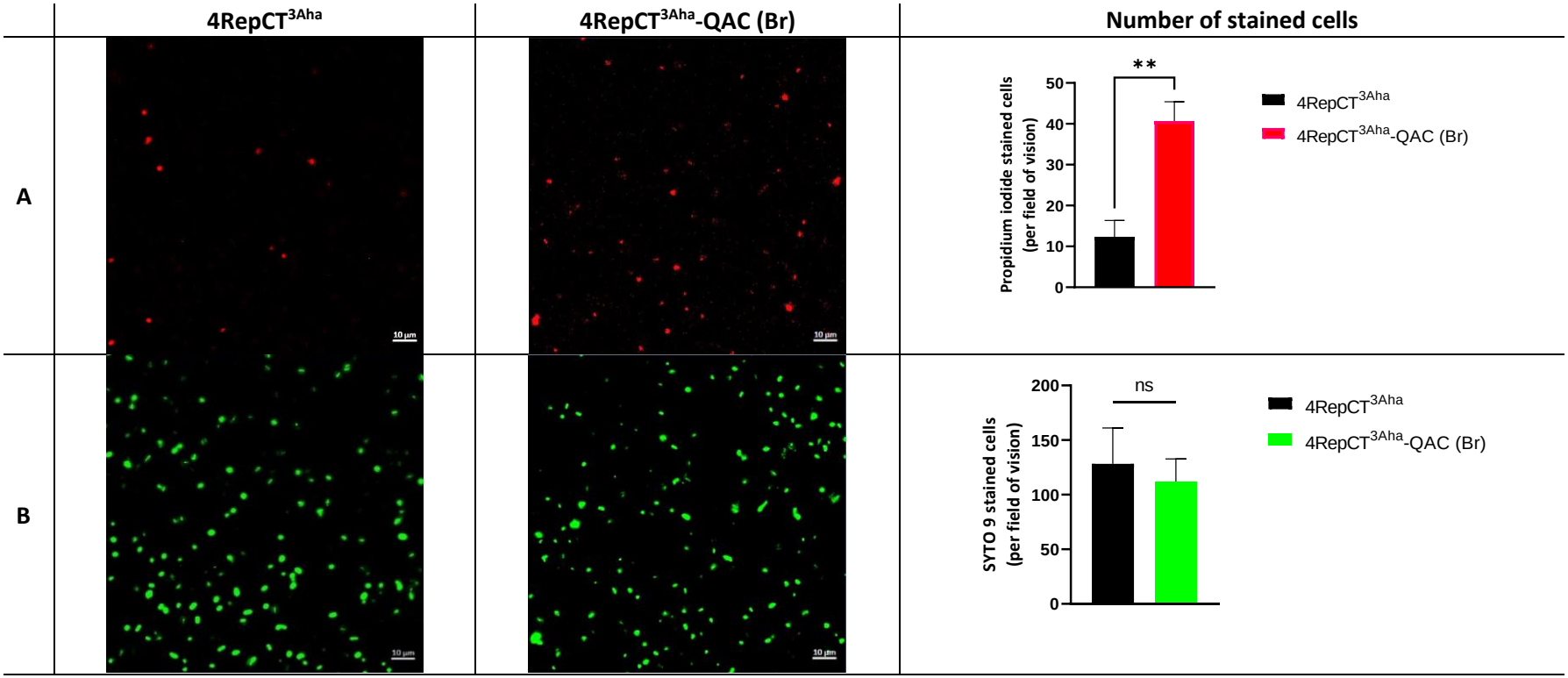

Figure 5.8. *E. coli* NCTC12242 cells stained with propidium iodide and SYTO9 using **A** -594nm (red) and **B**- 488nm (green) laser after 6-hour incubation on glass surfaces coated with 4RepCT^{3Aha} and4RepCT^{3Aha}-QAC (Br). SYTO9 indicates the total cell number as it stains all cells, whereas propidium iodide stains membrane-compromised cells only. A and B are representative images of the same field of vision; scale bar = 10 um. Student's t-test, n = 5, ** - $p<0.01$, ns – not significant, error bars denote standard deviation.

5.4.8. Plate-based biofilm recovery assays using metabolic reduction of resazurin and cell turbidity measurements.

To study the antimicrobial activity of surface-active QAC ligands, two parallel plate-based assays were designed based on metabolic reduction of resazurin to resorufin that was measured as absorbance at 570 nm, and an assay investigating the biomass turbidity of surface adherent cells using the absorbance at 600 nm. In parallel to QAC (Br), two additional quaternary ammonium ligands QAC (I) and QAC (tosylate) were tested. QAC (I) and QAC (tosylate) vary in their respective counterions (iodide and tosylate, respectively), as well as a longer linker compared to QAC (Br) (five carbon and two carbon chain, respectively; see Methods).

Resazurin reduction assay showed that metabolic activity of the *E. coli* NCTC 12242 cells adherent to 4RepCT^{3Aha}-QAC (Br), 4RepCT^{3Aha}-QAC (I), and 4RepCT^{3Aha}-QAC (tosylate) coated wells at six hours after the replacement of the growth media was significantly reduced compared to cells adherent to non-coated or 4RepCT^{3Aha}-coated wells (Fig. 5.9 A, $p<0.001$; the negative OD_{570} values are due to the subtraction of the reference wavelength, see Methods). There was no statistically significant difference in metabolic reduction of resazurin by surface-adherent cells growing on three assessed 4RepCT^{3Aha}-QAC ligand conjugates. Similarly, biomass turbidity at six hours was reduced by 54-55% in wells coated with 4RepCT^{3Aha}-QAC conjugates compared to non-coated or 4RepCT^{3Aha}-coated wells without statistically significant difference among the ligands (Fig. 5.9 B). Resazurin reduction assay of *S. aureus* NCTC 6571 biofilms showed that there was no statistically significant metabolic activity inhibition in any of the wells, however the variability of the absorbance values (SD 0.2579 – 0.4479) was larger compared to *E. coli* dataset (SD 0.2579 – 0.4478). No difference in *S. aureus* planktonic cell recovery from the biofilm was observed at OD600 (Fig. 5.9 B).

There was no statistically significant difference in resazurin metabolic reduction or planktonic cell recovery from *P. aeruginosa* biofilms grown on all coatings (Fig 5.9 A, B).

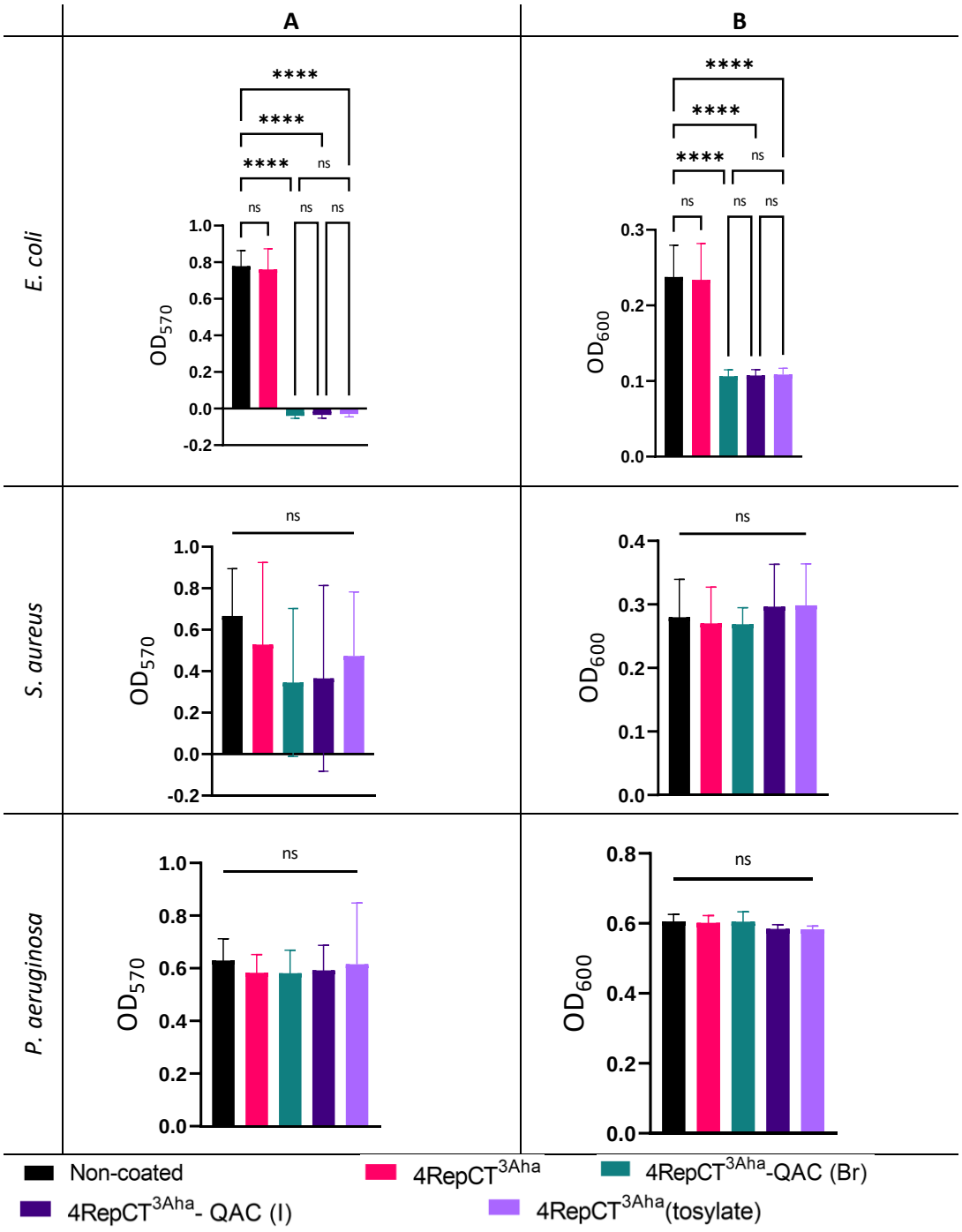

Figure 5.9. Absorbance of **A** – reduced resazurin at 570 nm and **B** -cell turbidity at 600 nm of surface-adherent *E. coli* NCTC12242, *S. aureus* NCTC 6571, and *P. aeruginosa* at 6 hours after the addition of a fresh growth media to a 24-hour biofilm. Absorbance of resazurin at 570 nm indicates cellular metabolism whilst OD600 indicates increase in bacterial biomass (One-way ANOVA with Tukey's multiple comparisons test, ns – $p > 0.05$, **** - $p<0.0001$, n=10, error bars denote standard deviation).

5.5. Discussion

5.5.1. Overview

This chapter focuses on films and fibres of 4RepCT^{3Aha} conjugates with non-releasable quaternary ammonium bearing ligands to create new contact-killing antimicrobial surfaces. Permanently surface-tethered QAC do not diffuse down their concentration gradient, contribute less to the antimicrobial resistance development, and allow to take advantage of their unique broad-spectrum antibacterial activity whilst reducing the risk of systemic and local toxicity making them a good candidate for contact killing surface development. Short chain QAC compounds were selected for conjugation to 4RepCT^{3Aha} due to the previously reported evidence that these compounds show antimicrobial activity when permanently tethered to a cellulose-based material surface[433].

Films of 4RepCT^{3Aha}-QAC (Br) showed some differences in surface wettability and morphology, compared to non-conjugated silk. The zone of inhibition assay showed that 4RepCT^{3Aha} – QAC (Br) fibres do not leach antimicrobial agent as displayed by the absence of a zone of inhibition around the fibres. Further, increase in bacterial growth on non-functionalised fibres was observed, whereas 4RepCT^{3Aha}-QAC fibres showed sustained fibrous morphology and no apparent increase in bacterial growth surrounding the material.

The colony forming unit recovery from glass surfaces coated with 4RepCT^{3Aha}-QAC (Br) was significantly lower than that of non-functionalised silk coating and non-coated glass. To that end, fluorescent microscopy analysis with live-dead staining was carried out, and the findings show increased cell death when cells are placed between 4RepCT^{3Aha}-QAC (Br) coated glass slide and a coverslip.

Lastly, a novel plate-based assay focusing on two distinct aspects of bacterial proliferation – biomass increase and metabolic activity – was designed. Using this assay, it was found that 4RepCT^{3Aha}-QAC (Br, I, tosylate) films significantly impact *E. coli* biomass increase and metabolic activity regardless of the QAC counterion. In contrast, *S. aureus* showed increased variability in cell proliferation and

metabolism that was not statistically significant from the controls. The 4RepCT^{3Aha}-QAC (Br, I, tosylate) did not show biocidal effects against surface-adherent *P. aeruginosa*.

5.5.2. Surface wettability using eSEM and water contact angle measurements

The differences in 4RepCT^{3Aha} and its conjugate film properties were compared using surface wettability, morphology, and topology investigations.

As an initial assessment, environmental SEM was used to *in situ* freeze-dry films formed on an aluminium surface followed by controlled re-hydration of the chamber up to 95% humidity, and the samples were observed until discrete water droplets formed. This approach was taken to acquire preliminary information on film surface properties including wettability, surface morphology, and other potential water-dependent behaviours[434]. Around 90-93% relative chamber humidity, discrete water droplets could be observed on 4RepCT^{3Aha} films (Fig 5.2). In contrast, individual water droplets could not be observed on 4RepCT^{3Aha}-QAC (Br) films; instead, 4RepCT^{3Aha}-QAC (Br) surface became coated with a confluent water film which suggests more hydrophilic properties and potentially swelling ability[435].

Water contact angle (WCA) measurement via a sessile drop method is a widely accepted quantitative measurement of surface wettability. It is expressed as the tangent angle at the solid, water, and gas (ambient air) contact point (three-phase contact point)[436]. WCA of assessed films was measured as an average of ten readings from three camera angles immediately at the timepoint of droplet contact onto the surface as it was observed that the microdroplet was absorbed into 4RepCT^{3Aha} and 4RepCT^{3Aha}-QAC (Br) films. This further suggests that protein films swell in presence of water. It was hypothesised that the WCA of 4RepCT^{3Aha}-QAC (Br) film will be smaller compared to 4RepCT^{3Aha} film due to strongly polar nature of the quaternary ammonium-bearing ligand. The WCA of 4RepCT^{3Aha} film was 60.18 (±3.545) degrees compared to WCA of 4RepCT^{3Aha}-QAC (Br) film of 55.99 (±4.910) (Fig 5.2 B). WCA measurements show a slightly increased wettability of 4RepCT^{3Aha}-QAC (Br) films compared to nonfunctionalized film, however this difference is not statistically significant ($p=0.0541$). This

finding is consistent to the results of a study by Harvey *et al.* where 4RepCT^{3Aha} conjugate to positively charged RGD peptide 4RepCT^{3Aha}-RGD similarly show marginal decrease in the WCA compared to non-functionalised film[192]. Unexpectedly, WCA reported in the Fig 5.2 B are within the range that is considered hydrophilic (<90°) whereas the study by Harvey *et al.* reports WCA ranging from 95.8° to 101.4°[192].

Several factors could have influenced this difference, likely the amount of protein in the film and film thickness: the measurements in Fig 5.2 B were made by drying 100 µl of 1 mg/ml protein solution onto a glass slide (100 µg protein per slide) ensuring edge-to-edge coating, whereas the study by Harvey *et al.* used 200 µg of protein per slide[192]. If the film formed by 100 µg of protein was not fully covering the glass, this could contribute to the measurement showing increased wettability of the surface. Other factors that could have influenced the difference in the WCA between these two sets of measurements are the purity of the protein preparation (and the biochemical nature of the carry-over bacteria-derived impurities), as we all as traces of salts and buffers within the film. Despite these variabilities, both findings suggest that conjugation of small ligands to 4RepCT^{3Aha} have marginal impact on overall wettability properties of the material.

5.5.3. Silk coating surface morphology

The eSEM images in Fig. 5.2 A showed preliminary differences in the surface morphologies of 4RepCT^{3Aha} and 4RepCT^{3Aha}-QAC-Br films, the latter showing more aggregation and fibrous structures compared to 4RepCT^{3Aha} films. The film morphology was observed using high vacuum scanning electron microscopy using gold-coated samples. The imaging showed that 4RepCT^{3Aha} films were smooth, with minimal aggregation (with 2-10 µm diameter) under 2000 x magnification and porous, interconnected network morphology under 5000 x magnification (Fig 5.3 A, B). In contrast, 4RepCT^{3Aha}-QAC (Br) film had rougher surface morphology with aggregates with 20-40 µm diameter (x 2000 magnification) and more pronounced fibrillar structures (Fig 5.3 A,B). This is consistent with previous findings by Widhe *et al.* where approx. 10 µm features were observed using SEM imaging of 4RepCT

protein[437]. Further, Harvey *et al.* reported that the 4RepCT^{3Aha}-RGD conjugate (made using copper catalysed click reaction) formed rougher films with larger aggregates (approximately 30 µm diameter) compared to non-functionalised 4RepCT^{3Aha} films[192]. The presence of aggregates in the 4RepCT^{3Aha} conjugate films could be among the factors contributing to overall slightly increased wettability because surface wettability properties are increased by surface morphology features in micrometre-range (whereas nanometre-range features tend to decrease wettability)[436].

5.5.4. Atomic force microscopy of silk surface topology

Surface topology was measured using atomic force microscopy (AFM) in tapping mode. In this imaging technique, a fine probe is tapped onto an uncoated sample under ambient conditions, and the resulting image contains quantitative information of the height of the film features. Consistently with electron microscopy findings in Fig. 5.3, 4RepCT^{3Aha}-QAC films had larger, more abundant spherical aggregates (up to 39.5 nm high in a 2 nm^2 area) compared to non-functionalised 4RepCT^{3Aha} (5.4 nm high) (Fig 5.4).

5.5.5. Zone of inhibition study

Zone of inhibition measurements on solid surface are a widely accepted method for investigation whether an antimicrobial molecule exhibits its action via release from the base material. It was hypothesised that 4RepCT^{3Aha}-QAC (Br) will not produce a zone of inhibition as the linker design does not include a labile bond compared to ester-bearing linker used in Chapter 4. Over the course of six days, 4RepCT^{3Aha}-QAC fibres did not produce a zone of inhibition (Fig 5.5). Interestingly, non-functionalised 4RepCT^{3Aha} fibres promoted bacterial growth around fibres starting from Day 5; this is in contrast to 4RepCT^{3Aha}-QAC (Br) fibres that did not show enhanced bacterial growth. This difference could be due to use of 4RepCT^{3Aha} fibres as a carbon source after the solid growth media has been depleted of nutrients, whereas 4RepCT^{3Aha}-QAC (Br) fibres resisted bacterial growth/digestion.

5.5.6. Colony forming unit recovery

Surface-active antimicrobial effects of 4RepCT^{3Aha}-QAC (Br) conjugate were further investigated by challenging a coated surface with *E. coli* NCTC 12242 grown in liquid media. Glass spreading beads were coated with 4RepCT^{3Aha} or 4RepCT^{3Aha}-QAC (Br) using wet coating method; this was carried out by incubating the beads in the protein solution under constant agitation. The beads coated with protein solution were stained by the Coomassie stain, and the retention of Coomassie Brilliant Blue dye was observed as a visually blue coating suggesting successful protein retention on the glass bead surface after wet coating (Fig 5.6).

Coated beads were incubated in a liquid media of *E. coli* overnight, then gently washed to remove loosely attached bacterial cells. Sonication was used to remove firmly attached bacterial cells that were then plated on solid media to investigate the number of viable surface-adherent cells expressed as a number of colony forming units (CFU). CFU recovery from 4RepCT^{3Aha}-QAC coated beads was significantly lower than the non-coated and non-functionalised controls (Fig. 5.7) which further suggests surface-active antimicrobial effect of 4RepCT^{3Aha}-QAC conjugate. Although the absolute numbers of bacteria surviving on the beads prior to sonication is likely to be higher as sonication is known to cause bacterial cell lysis, the relative decrease in colony forming unit recovery from 4RepCT^{3Aha}-coated beads could be caused by bacterial death on the coated surfaces, or the destabilisation of the adherent bacterial cell walls that were further disrupted by sonication.

In contrast, the CFU recovery from 4RepCT^{3Aha} coatings was 75% higher compared to non-coated glass beads(Fig. 5.7), possibly due to increased surface roughness and hydrophobicity that promotes bacterial attachment[438,439] .

5.5.7. Live-dead microscopy

Confocal fluorescence microscopy in combination with live-dead bacterial staining was used to further investigate bacterial survival on the surfaces. Live-dead staining and fluorescent microscopy allow to visualise dead and live cells in close contact with the coated surface without the need for cell removal

from its, thus excluding the potentially harmful bacterial detachment approaches such as sonication that are likely to introduce a bias. Further, unlike ZOI and CFU-based methods that analyse bacterial growth on solid media, live-dead microscopy uses selective uptake of a red fluorescent dye propidium iodide that stains those cells with increased membrane permeability as a measurement of cell death. The green fluorescent counterstain SYTO9 is taken up by all cells thus serving as a loading control. In essence, this approach allows us to study the number of cells that do not survive the attachment to the surface as opposed to counting the survival cells, thus providing a broader context to more traditional methods described above.

Both propidium iodide and SYTO9 are DNA-intercalating dyes that provide signal upon DNA binding. In context of imaging cells on recombinant protein-coated surfaces, this adds an additional challenge because recombinant proteins can be contaminated with residual DNA from the heterologous expression host. Upon staining, this contamination provides a strong background signal. To ensure exogenous DNA removal from the films, 1 M NaCl wash during protein purification and after film formation was used. Nevertheless, removal of exogenous DNA from dry-coated materials was challenging, therefore wet-coating method was used whereby the slide was incubated with protein solution followed by aspiration and 1 M NaCl wash. This method allows for thinner film to be made which resulted in better washing efficacy thus minimising the background staining signal. However, this approach allows for less conjugate to deposit on the surface which results in a lower charge density.

The number of propidium iodide-stained cells per field of vision on surfaces coated with 4RepCT^{3Aha}-QAC (Br) was 70% higher compared to 4RepCT^{3Aha} (Fig.5.8 A) whereas the total number of cells per field of vision was not statistically significantly different (Fig. 5.8 B). On 4RepCT^{3Aha}-QAC (Br) coated slides, 35% of total number of bacteria were stained by propidium iodide compared to 10% on 4RepCT^{3Aha}-coated slides.

Live-dead staining provides an interesting comparison of bacterial survival compared to CFU assays. Whilst the basic setup of these two experiments differs on the basis of the bacterial attachment (CFU count looks only at firmly attached cell survival whereas the described live-dead cell microscopy shows all cells including loosely attached cells), the reduction in CFUs (Fig. 5.6) is comparable to increase in membrane compromised cells (Fig 5.8). CFU count from 4RepCT^{3Aha} and 4RepCT^{3Aha}-QAC (Br) coated beads showed a 90-95% reduction in bacterial survival on the conjugate films, whereas live-dead staining shows a comparable 70% increase in the number of membrane-compromised cells.

Despite the highlighted advantages, there are several drawbacks to using live-dead staining to assess antimicrobial effects of surface-tethered, non-releasable ligands. Microscopy is a semi-quantitative approach because the observation can only be made in a single field and a single plane of vision. Further, despite the specificity of the stain and its popularity in microbiology, the topic of what is a dead bacterial cell remains hotly debated. Propidium iodide is known to permeate only those cells with compromised membrane, however, membrane compromise does not ultimately equate cell death. A number of studies have shown that membrane-compromised bacterial cells can recover and form CFU when the environmental pressure is removed[440,441].

With this in mind, flow cytometry using live-dead stain and cell sorting (FACS) could provide a quantitative insight into the proportions of membrane-compromised cells by sorting out dead cells that can be plated on a solid media to estimate the number of CFU on the same sample. This data would result in a more in-depth understanding of membrane damage and cell survival on 4RepCT^{3Aha} and 4RepCT^{3Aha}-QAC (Br) coated surfaces, however this would require a firmly attached cell removal method that would influence the final count (similarly to CFU assay) and a specialist containment level 2 FACS facility.

5.5.8. Plate-based assays for biofilm metabolic activity and planktonic cell recovery

Metabolic activity and the total biomass measurements are two emerging methods for characterisation of surface adherent bacteria growth. In biofilms, biomass increase does not always

correlate with metabolism, therefore both aspects should be taken into consideration for a comprehensive analysis[442,443]. The biomass is often measured using transmitted, absorbed, or scattered light using OD_{405} or OD_{600} reading (with or without crystal violet dye as an indicator, respectively)[443–445]. In cases where low inoculum (low number of surface-adherent cells) is expected, the biofilm can be incubated at growth conditions until signal is observed in a process called the biotimer assay[446–448].

A plate-based spectroscopic assay was developed to look at cell adherence and survival on 4RepCT^{3Aha} and 4RepCT^{3Aha}-QAC (Br) films. Firstly, bacteria were grown in coated wells for 24 hours to allow for initial cell attachment, followed by aspiration of the spent media and a gentle wash to remove loosely attached bacterial cells. Fresh media was added to each well to investigate the cellular metabolism and biomass. Cellular metabolism was measured via reduction of resazurin which produces signal at OD_{570}. Resazurin is a routinely used metabolic indicator in mammalian cell culture in assays such as PrestoBlue, as well as bacterial metabolic assays[449] (Fig 5.10). In parallel, the bacterial biomass was monitored as absorbance at 600 nm in media without resazurin.

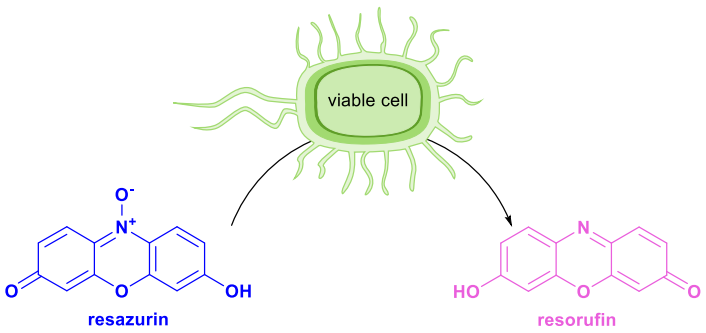

Figure 5.10. Resazurin (blue) is irreversibly reduced to resorufin (pink) by aerobic respiration of metabolically active cells.

To further investigate the mechanism of action of 4RepCT^{3Aha}-tethered QAC ligands, two additional quaternary ammonium-bearing ligands were synthesised in house. The QAC (I) and QAC (tosylate) ligands have a longer linker (five carbon chain) potentially allowing a greater distance from the base material which is reported to increase the antimicrobial activity as well as different counterions iodide and tosylate to investigate whether the antimicrobial activity of the QAC ligands is dependent on the

counterion (discussed in 5.1 Introduction). Taking advantage of the higher throughput nature of a plate-based assay, three QAC ligands were tested against three reference microorganisms.

The assay showed highly significant reduction in resazurin reduction and biomass density of *E. coli* NCTC 12242 in wells coated with 4RepCT-QAC ligand conjugates after 6 hours (Fig 5.9). There was no statistically significant difference in metabolism inhibition and biomass density in wells coated with 4RepCT^{3Aha}-QAC (Br), 4RepCT^{3Aha}-QAC (I), or 4RepCT^{3Aha}-QAC (tosylate) suggesting that the counterion or the linker length differences did not provide any additional antimicrobial effect at the surface level (Fig. 5.9).

The mean percentage reduction in biomass optical density of *E. coli* grown in wells coated with 4RepCT^{3Aha}-QAC conjugates was 55% which was the lowest relative growth inhibition across the experimental procedures described in this chapter. This could be explained by relatively mild sample processing conditions in this plate-based assay that uses bacterial growth media which allowed more cells to survive and proliferate.

In contrast to *E. coli*, statistically significant difference in resazurin reduction or biomass density was observed in wells with *S. aureus* NCTC6571 and *P. aeruginosa* (Fig. 5.9). Reportedly, both *S aureus* and *P. aeruginosa* exhibit QAC resistance by efflux pump upregulation[450,451], however this is not applicable in context of surface tethered QAC ligands. It is likely that the thickness of *S. aureus* cell wall and the viscid bacterial capsule of *P. aeruginosa* is not impacted by the cationic nature of 4RepCT^{3Aha}-QAC conjugates.

Further to this, *S. aureus* resazurin metabolism assays showed higher in-assay variability compared to *E. coli* – SD=0.3532 and SD=0.04909, respectively. This could indicate that there are subpopulations of *S. aureus* cells more susceptible to QAC inhibition. The mean percentage decrease in resazurin reduction in wells coated with 4RepCT^{3Aha}-QAC (Br), 4RepCT^{3Aha}-QAC (I), and 4RepCT^{3Aha}-QAC (tosylate) was 43%, 39%, and 21% compared to the non-coated wells ($p>0.05$). It is likely that the unexpected variability in the optical density was a consequence of bacterial death during the washing steps. Further investigation into survival of *S. aureus* and *P. aeruginosa* on 4RepCT^{3Aha}-QAC coated surfaces

using the methodology developed using *E. coli* as a model pathogen including microscopy and the conventional antimicrobial assays could provide more insight into the antimicrobial nature of the 4RepCT^{3Aha} conjugates.

As is the case with conjugates described in chapter 4, a significant weakness of this work is the inability to analytically describe the effectiveness of click chemistry reaction for the ligand conjugation to 4RepCT^{3Aha}. The method to quantify how many ligands can conjugate to the protein would provide a significantly better insight into the antimicrobial activity of the silk material. Theoretically, copper (I) catalysed azide-alkyne cycloaddition is extremely fast and high yielding (which is a defining feature of click chemistry reactions in general; discussed in more detail in section 1.4), however little is known about CuAAC reaction speed and efficiency with large molecules such as proteins that might be influenced by macromolecular crowding and folding that can obscure the azide moieties and reduce the reaction speed and efficiency. Overall, technical challenges associated with previous attempts of 4RepCT mass spectrometry and the need for a novel method development for 4RepCT^{3Aha} conjugate HPLC has halted further investigation in this area. With this in mind, the experimental work described in this chapter relies solely on the experimental controls, and the antimicrobial effect seen in 4RepCT^{3Aha} -QAC but not 4RepCT^{3Aha} is therefore attributed to the assumption that ligand has been conjugated to the protein.

5.6. Conclusions and future work

This chapter described a range of methods for analysing permanently surface tethered, contact-active antimicrobial quaternary ammonium bearing ligand conjugates to 4RepCT^{3Aha} materials. The 4RepCT^{3Aha}-QAC conjugate materials consistently showed significant antimicrobial activity against *E. coli* ranging from 30% to 95% growth inhibition. This data indicates that 4RepCT^{3Aha}-QAC based materials could be of interest in biomedical areas where *E. coli* colonisation and opportunistic infections are a concern, for instance abdominal surgical wounds, urinary catheters, and emergency surgeries (so called “dirty surgery”) .

Novel high-throughput compatible plate-based metabolic and biomass assays suggested marginal antibacterial effect of 4RepCT^{3Aha}-QAC against *S. aureus* and no effect against *P. aeruginosa*. Further investigation into *S. aureus* and *P. aeruginosa* survival on 4RepCT-QAC coated surfaces is required using live-dead microscopy and flow cytometry.

Lastly, 4RepCT^{3Aha} – QAC conjugates should be assessed for cytotoxicity against mammalian cells starting with fibroblasts. It is hypothesised that the conjugates will have some cytotoxicity, however mammalian cells in culture generally prefer positively charged, moderately hydrophobic surfaces[405,452], therefore it is important to assess both cell death and survival as an indicative fibroblast behaviour in wound remodelling.

6. General discussion and future work

6.1 Overview

The existing synthetic and animal-derived biomedical materials suffer from a range of disadvantages that can be alleviated by recombinant production of proteins in a controlled, animal-product free and scalable approach. Further, recombinant production of proteins enables finer tailoring of the protein amino acid sequence in terms of incorporation of solubility-enhancing domains or unnatural bio-orthogonally reactive amino acid incorporation.

The aim of this project was to create novel antimicrobial biomaterials based on scalable production of recombinant miniature spider silk using three different approaches: passive loading; covalent conjugation to an unnatural amino acid residue using a labile linker; and covalent conjugation to an unnatural amino acid using a non-labile linker. This work builds on existing methodologies of potassium phosphate mediated silk precipitation by Lammel *et al.*[137,153], and L-azidohomoalanine incorporation into spidroin's primary sequence for use bioconjugations by Harvey *et al.*[106,192]. The results presented in chapters 3, 4 and 5 showed that spider silk particles could be loaded with an antibiotic using non-covalent interactions, as well as covalent links via copper-catalysed azide-alkyne cycloaddition using labile and non-labile linkers. In addition, novel custom-tailored, high-throughput compatible plate based antimicrobial assays have been developed for quantification of antimicrobial effects keeping in mind distinct mechanisms of actions of the materials.

Each of these systems could be applied in a different biomedical scenario, such as implantation of antimicrobial material *in situ*; injectable embolic particles carrying a payload to the occlusion site; coating of an indwelling medical device; or various topical applications such as wound dressings.

6.2. Scale-up of recombinant silk production

As discussed in Chapter 1, bacterial recombinant silk hosts tend to show relatively low yields of protein that impedes the use of recombinant silk as a biomaterial due to resultant high production cost and

time. Some researchers focus on host strain engineering strategies, such as supplementing bacterial genome with additional copies of repetitive amino acid tRNAs, which theoretically could improve the yields however the yields are usually not reported[100,101]. Additionally, the issue is often tackled by adjusting the design of recombinant silk gene, such as inclusion of spidroin's N-terminal domain, that can provide a tenfold increase in yields (as exemplified by 4RepCT^{3Aha} and NT2RepCT yields, see Chapter 2). Besides the increase in protein yield per unit of cells, it is necessary to develop protocols for purification of protein on a larger scale (>2L biomass). As is the case for highly water soluble NT2RepCT, it is tolerant to most common precipitation methods including ammonium sulphate and organic solvents. This unique property was used to develop a purification method in Chapter 2 that is not limited by IMAC column volume whilst providing comparable yields and purity.

Further process development procedure for expression and purification of 4RepCT^{3Aha} protein are required to advance the progress on its material and conjugate characterisation. The main limitation of the current 4RepCT^{3Aha} expression protocol is the media swap procedure that removes methionine-supplemented growth media and replaces it with azidohomoalanine-supplemented media. This includes centrifugation of the bacterial biomass followed by washing steps, which is not feasible for processes on over 2L scale. The media swap step would not be required if the bacteria used up all methionine for cellular biomass increase prior to induction. To use this approach, it is necessary to determine methionine consumption rate by the bacteria via measuring the residual methionine concentration in the growth media over time. After the methionine has depleted and the biomass has reached the desirable optical density at 600nm (0.7-1 for shake flasks, 80-100 for a bioreactor high density culture), Aha and IPTG can be added to induce protein expression (Fig. 6.1).

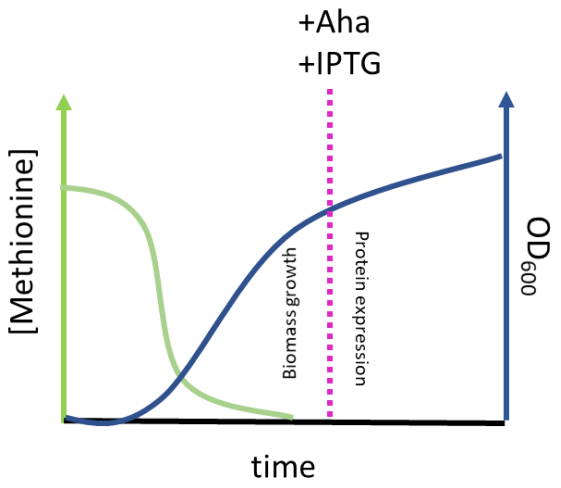

Figure 6.1. Expression of 4RepCT^{3Aha} using methionine depletion protocol. The concentration of methionine is limited so that it can support bacterial biomass growth to the desirable optical density, followed by addition of Aha and IPTG for protein expression.

6.3. Biocompatibility of silk-derived colloid systems

There is a significant body of evidence that illustrates the non-immunogenic and non-pyrogenic nature of both natural and recombinant silk fibres (see Chapter 1). However, to the date no assessment of the immunogenicity of colloidal silk particles has been carried out. As described in the Chapter 3, NT2RepCT is an appealing hydrophilic polymer for drug delivery applications due to its resorbable, pH sensitive nature. However, the immunogenicity of particles will require re-assessment due to the fact that protein aggregates can have a different immunological behaviour to soluble protein. This difference stems from the specifics of protein folding and unfolding: the aggregation of soluble protein into colloidal particles could expose those protein domains that are normally inaccessible to the solvent and thus the immune system.

6.4. Quantification of 4RepCT^{3Aha}-conjugated ligands

Using the established methodology, Aha incorporation into 4RepCT^{3Aha} is confirmed via conjugation of an alkyne-bearing fluorophore, such as FAM. However, the confirmation and quantification of non-fluorophore ligands remains a technical challenge. In experimental setting, conjugation is confirmed

by using controls in absence of a copper catalyst; these materials show no antimicrobial activity after non-conjugated ligand is removed by washing.

Mass spectrometry (MS) is a traditional technique for bioconjugate analysis aiming to determine how many ligand molecules are conjugated to the biopolymer. However, 4RepCT protein has been resistant to different MS techniques, including but not limited to matrix-associated laser desorption ionization (MALDI), electron spray ionisation (ESI), and tandem mass spectrometry (MS-MS). The assumption is that the lack of ionisable chemical groups in the repeat regions of 4RepCT are preventing molecule ionisation and subsequent flight in the electrical field, however this has not been experimentally confirmed. It could be further investigating by creating a genetic silk construct that only contains the C-terminal domain and using the resulting protein for Aha incorporation and conjugation. In 4RepCT protein, all methionine residues are located in the C-terminal domain, therefore this could provide some information about how many ligands can be conjugated to a single protein at once to investigate the current assumptions that, firstly, all methionine residues are replaced by Aha, and secondly, that all incorporated Aha residue side chains are sterically available for conjugation.

6.5. Conjugation of ligands to 4RepCT^{3Aha} scaffold and its effect on material properties

To date, most small organic molecule ligands could be successfully conjugated to 4RepCT^{3Aha} to deliver their functionality with little to no detrimental effect on protein's ability to form fibres and films[106,192] (Fig. 4.10, Fig. 5.4-5.6). However, the impact of conjugating larger polymeric molecules remains unknown. Attempts to immobilise high molecular weight polymers to 4RepCT^{3Aha} were carried out but as discussed in section 6.4, it is not possible to analytically determine the success of the reaction.

In light of this, tethering of high molecular weight polymers, especially carbohydrates, to 4RepCT^{3Aha} scaffolds could become the next step in building the conjugate library. For instance, 4RepCT^{3Aha} -PEG dendrimers could create a highly hydrophilic, non-fouling antimicrobial surface. Similarly to the 4RepCT^{3Aha} -erythromycin conjugate used in Chapter 4, silk could be conjugated to other aminoglycosides and macrolides with antimicrobial activity. Further, silk-carbohydrate conjugates

could be used in tissue engineering where these molecules plat important role in a huge diversity of cellular activities. Conjugates such as 4RepCT^{3Aha} -heparin, 4RepCT^{3Aha} -hyaluronic acid and 4RepCT^{3Aha} – keratosulfate could be useful in cell culture applications. Conjugation of carbohydrates would further highlight the key aspect of versatility offered by chemical conjugation approach compared to silk genetic modifications that can only fuse other protein-coding genes to silk's sequence.

6.6. Conclusions

Recombinant production of miniature spider silk proteins gives us a new potential to increase the availability of silk for biomedical applications. This, combined with the possibilities offered by bioconjugations using CuAAC, is a step change from current options of the functional material design. Recombinant silk- drug loaded and conjugated materials offer a unique combination of an animal-free, intelligently designed system with a tailorable degradation profile and non-toxic nature. The biological activity silk conjugates are dictated by the nature of the ligands, and this repertoire is constantly expanding as more drugs are being discovered for previously undruggable targets. With this in mind, the full biomedical capacity of recombinant spider silk conjugates is not yet explored.

Ultimately, the limitations of the material application are driven by biocompatibility. Extensive evidence suggests that silks have low immunogenicity, however, each novel conjugate poses a risk of creating an immunogenic motif. Little is known about the biological responses that might be mounted towards silk or silk conjugates upon repeat exposure, which is particularly important for applications where the material is delivered to the bloodstream.

In conclusion, silk biomaterial design, functionalisation, and characterisation are rapidly evolving fields, and chemical functionalisation offers a significant advantage over other techniques due to the streamlined nature of the ligand conjugation using click chemistry. Production cost-associated issues can be alleviated with the development of methodologies for scaled-up silk protein production with unnatural amino acid incorporation. Further, these processes can be applied to other structural proteins not limited to silks to create new, tailored biomedical materials.

7. References

1. Sutherland, T. D., Young, J. H., Weisman, S., Hayashi, C. Y. & Merritt, D. J. Insect silk: one name, many materials. *Annu. Rev. Entomol.* **55**, 171–188 (2010).

2. Garb, J. Spider Silk: An ancient biomaterial for the 21st century. in *Spider Research in the 21st Century: Trends & Perspectives* (ed. Penney, D.) 252–282 (Siri Scientific Press, 2013).

3. Eisoldt, L., Smith, A. & Scheibel, T. Decoding the secrets of spider silk. *Mater. Today* **14**, 80–86 (2011).

4. Forrest, R. D. Early history of wound treatment. *J. R. Soc. Med.* **75**, 198 (1982).

5. Morgan, E. Sticky Layers and Shimmering Weaves: A Study of Two Human Uses of Spider Silk. *J. Des. Hist.* **29**, 8–23 (2016).

6. Katie Hosmer. Collecting Golden Spider Silk for 3 Years to Create Cape. https://mymodernmet.com/simon-peers-nicholas-godley-golden-spider-silk-cape/ (2012).

7. Candelas, G. C. & Cintron, J. A spider fibroin and its synthesis. *J. Exp. Zool.* **216**, 1–6 (1981).

8. dos Santos-Pinto, J. R. A. *et al.* Structure and post-translational modifications of the web silk protein spidroin-1 from Nephila spiders. *J. Proteomics* **105**, 174–185 (2014).

9. Hu, X. *et al.* Molecular mechanisms of spider silk. *Cell. Mol. Life Sci.* **63**, 1986–1999 (2006).

10. Garb, J. E., Ayoub, N. A. & Hayashi, C. Y. Untangling spider silk evolution with spidroin terminal domains. *BMC Evol. Biol.* **10**, 243 (2010).

11. Rising, A., Hjälm, G., Engström, W. & Johansson, J. N-terminal nonrepetitive domain common to dragline, flagelliform, and cylindriform spider silk proteins. *Biomacromolecules* **7**, 3120–4 (2006).

12. Nilebäck, L. *et al.* Self-Assembly of Recombinant Silk as a Strategy for Chemical-Free Formation of Bioactive Coatings: A Real-Time Study. *Biomacromolecules* **5**, 326 (2017).

13. Gaines, W. A., Sehorn, M. G. & Marcotte, W. R. Spidroin N-terminal domain promotes a pH-dependent association of silk proteins during self-assembly. *J. Biol. Chem.* **285**, 40745–53 (2010).

14. Askarieh, G. *et al.* Self-assembly of spider silk proteins is controlled by a pH-sensitive relay. *Nature* **465**, 236–8 (2010).

15. Landreh, M. *et al.* A pH-Dependent Dimer Lock in Spider Silk Protein. *J. Mol. Biol.* **404**, 328–36 (2010).

16. Xu, M. & Lewis, R. V. Structure of a protein superfiber: spider dragline silk. *Proc. Natl. Acad. Sci.* **87**, 7120–24 (1990).

17. Hinman, M. B. & Lewis, R. V. Isolation of a clone encoding a second dragline silk fibroin. Nephila clavipes dragline silk is a two-protein fiber. *J. Biol. Chem.* **267**, 19320–4 (1992).

18. Parkhe, A. D., Seeley, S. K., Gardner, K., Thompson, L. & Lewis, R. V. Structural studies of spider silk proteins in the fiber. *J. Mol. Recognit.* **10**, 1–6 (1997).

19. Hinman, M. B., Jones, J. A. & Lewis, R. V. Synthetic spider silk: A modular fiber. *Trends Biotechnol.* **18**, 374–79 (2000).

20. Sponner, A. *et al.* The conserved C-termini contribute to the properties of spider silk fibroins. *Biochem. Biophys. Res. Commun.* **338**, 897–902 (2005).

21. Sponner, A., Unger, E., Grosse, F. & Weisshart, K. Conserved C-termini of spidroins are secreted by the major ampullate glands and retained in the silk thread. *Biomacromolecules* **5**, 840–5 (2004).

22. Hagn, F. *et al.* A conserved spider silk domain acts as a molecular switch that controls fibre assembly. *Nature* **465**, 239–42 (2010).

23. Rising, A. & Johansson, J. Toward spinning artificial spider silk. *Nat. Chem. Biol.* **11**, 309–315 (2015).

24. Andersson, M., Holm, L., Ridderstråle, Y., Johansson, J. & Rising, A. Morphology and Composition of the Spider Major Ampullate Gland and Dragline Silk. *Biomacromolecules* **14**, 2945–2952 (2013).

25. Vollrath, F. & Knight, D. P. Liquid crystalline spinning of spider silk. *Nature* **4001**, 541–548 (2001).

26. Viney, C. Natural silks: archetypal supramolecular assembly of polymer fibres. *Supramol. Sci.* **4**, 75–81 (1997).

27. Andersson, M. *et al.* Carbonic Anhydrase Generates CO2 and H+ That Drive Spider Silk Formation Via Opposite Effects on the Terminal Domains. *PLOS Biol.* **12**, e1001921 (2014).

28. Rammensee, S., Slotta, U., Scheibel, T. & Bausch, A. R. Assembly mechanism of recombinant spider silk proteins. *Proc. Natl. Acad. Sci.* **105**, 6590–6595 (2008).

29. Vollrath, F. & Knight, D. P. Structure and function of the silk production pathway in the Spider Nephila edulis. *Int. J. Biol. Macromol.* **24**, 243–249 (1999).

30. Rising, A. *et al.* Spider Silk Proteins – Mechanical Property and Gene Sequence. *Zoolog. Sci.* **22**, 273–281 (2005).

31. Chen, X., Zhengzhong, S. & Fritz, V. The spinning processes for spider silk. *Soft Matter* **2**, 448–451 (2006).

32. Breslauer, D. N., Lee, L. P. & Muller, S. J. Simulation of Flow in the Silk Gland. *Biomacromolecules* **10**, 49–57 (2008).

33. Römer, L. & Scheibel, T. The elaborate structure of spider silk: structure and function of a natural high performance fiber. *Prion* **2**, 154–161 (2008).

34. Riekel, C. *et al.* Aspects of X-ray diffraction on single spider fibers. *Int. J. Biol. Macromol.* **24**, 179–186 (1999).

35. Dicko, C., Kenney, J. M., Knight, D. & Vollrath, F. Transition to a β-sheet-rich structure in spidroin in vitro: The effects of pH and cations. *Biochemistry* **43**, 14080–14087 (2004).

36. Simmons, A., Ray, E. & Jelinski, L. W. Solid-State 13C NMR of Nephila clavipes Dragline Silk Establishes Structure and Identity of Crystalline Regions. *Macromolecules* **27**, 5235–5237 (2002).

37. Simmons, A. H., Michal, C. A. & Jelinski, L. W. Molecular Orientation and Two-Component Nature of the Crystalline Fraction of Spider Dragline Silk. *Science.* **271**, 84–7 (1996).

38. Gosline, J. M., Guerette, P. A., Ortlepp, C. S. & Savage, K. N. The mechanical design of spider silks: from fibroin sequence to mechanical function. *J. Exp. Biol.* **202**, 3295–303 (1999).

39. Renault, A. *et al.* Structure and mechanical properties of spider silk films at the air-water interface. *Langmuir* **29**, 7931–8 (2013).

40. Bunsell, A. R. *Handbook of properties of textile and technical fibres*. (Woodhead Publishing, 2009).

41. Agnarsson, I., Kuntner, M. & Blackledge, T. A. Bioprospecting Finds the Toughest Biological Material: Extraordinary Silk from a Giant Riverine Orb Spider. *PLoS One* **5**, e11234 (2010).

42. Stauffer, S. L., Coguill, S. L. & Lewis, R. V. Comparison of Physical Properties of Three Silks from Nephila clavipes and Araneus gemmoides. *J. Arachnol.* **22**, 5–11 (1994).

43. Köhler, T. & Vollrath, F. Thread biomechanics in the two orb-weaving spiders Araneus diadematus (Araneae, Araneidae) and Uloborus walckenaerius (Araneae, Uloboridae). *J. Exp. Zool.* **271**, 1–17 (1995).

44. Madsen, B., Shao, Z. Z. & Vollrath, F. Variability in the mechanical properties of spider silks on three levels: interspecific, intraspecific and intraindividual. *Int. J. Biol. Macromol.* **24**, 301–306 (1999).

45. Zhengzhong Shao, Fritz Vollrath, Yong Yang & Hans Thøgersen. Structure and Behavior of Regenerated Spider Silk. *Macromolecules* **36**, 1157–1161 (2003).

46. Liu, Y., Shao, Z. & Vollrath, F. Relationships between supercontraction and mechanical properties of spider silk. *Nat. Mater. 2005 412* **4**, 901–905 (2005).

47. Liu, D. *et al.* Spider dragline silk as torsional actuator driven by humidity. *Sci. Adv* **5**, 9183 (2019).

48. Cohen, N., Levin, M. & Eisenbach, C. D. On the Origin of Supercontraction in Spider Silk. *Biomacromolecules* **22**, 993–1000 (2021).

49. Lewis, R. V. Spider silk: the unraveling of a mystery. *Acc. Chem. Res.* **25**, 392–398 (2002).

50. Qin, Z. & Buehler, M. J. Spider silk: Webs measure up. *Nat. Mater.* **12**, 185–7 (2013).

51. Pérez-Rigueiro, J., Elices, M. & Guinea, G. V. Controlled supercontraction tailors the tensile behaviour of spider silk. *Polymer (Guildf).* **44**, 3733–3736 (2003).

52. Elices, M., Plaza, G. R., Pérez-Rigueiro, J. & Guinea, G. V. The hidden link between supercontraction and mechanical behavior of spider silks. *J. Mech. Behav. Biomed. Mater.* **4**, 658–669 (2011).

53. Bell, F. I., McEwen, I. J. & Viney, C. Supercontraction stress in wet spider dragline. *Nat. 2002 4166876* **416**, 37 (2002).

54. Greco, G. *et al.* Tyrosine residues mediate supercontraction in biomimetic spider silk. *Commun. Mater.* **2**, 1–10 (2021).

55. Hayashi, C. Y. & Lewis, R. V. Evidence from flagelliform silk cDNA for the structural basis of elasticity and modular nature of spider silks. *J. Mol. Biol.* **275**, 773–784 (1998).

56. Shao, Z. & Vollrath, F. The effect of solvents on the contraction and mechanical properties of spider silk. *Polymer (Guildf).* **40**, 1799–1806 (1999).

57. Rising, A. *et al.* Major ampullate spidroins from Euprosthenops australis: multiplicity at protein, mRNA and gene levels. *Insect Mol. Biol.* **16**, 551–561 (2007).

58. Vollrath, F., Barth, P., Basedow, A., Engstrom, W. & List, H. Local tolerance to spider silks and protein polymers in vivo. *In Vivo (Brooklyn).* **16**, 229–34 (2002).

59. Schäfer-Nolte, F. *et al.* Biomechanics and biocompatibility of woven spider silk meshes during

remodeling in a rodent fascia replacement model. *Ann. Surg.* **259**, 781–792 (2014).

60. Gellynck, K. *et al.* Biocompatibility and biodegradability of spider egg sac silk. *J. Mater. Sci. Mater. Med.* **19**, 2963–2970 (2008).

61. Allmeling, C., Jokuszies, A., Reimers, K., Kall, S. & Vogt, P. M. Use of spider silk fibres as an innovative material in a biocompatible artificial nerve conduit. *J. Cell. Mol. Med.* **10**, 770–777 (2006).

62. Allmeling, C., Radtke, C. & Vogt, P. M. Technical and biomedical uses of nature's strongest fiber: Spider silk. in *Spider Ecophysiology* (ed. Nentwig, W.) (Springer, 2013).

63. Kornfeld, T. *et al.* Spider silk nerve graft promotes axonal regeneration on long distance nerve defect in a sheep model. *Biomaterials* **271**, 120692 (2021).

64. Kuhbier, J. W. *et al.* Influence of direct or indirect contact for the cytotoxicity and blood compatibility of spider silk. *J. Mater. Sci. Mater. Med.* **28**, 1–9 (2017).

65. Liebsch, C. *et al.* Preliminary investigations of spider silk in wounds in vivo — Implications for an innovative wound dressing. *Burns* **44**, 1829–1838 (2018).

66. Wright, S. & Goodacre, S. L. Evidence for antimicrobial activity associated with common house spider silk. *BMC Res. Notes* **5**, 326 (2012).

67. Keiser, C. N., DeMarco, A. E., Shearer, T. A., Robertson, J. A. & Pruitt, J. N. Putative microbial defenses in a social spider: immune variation and antibacterial properties of colony silk. *J. Arachnol.* **43**, 394–399 (2015).

68. Roozbahani, H., Asmar, M., Ghaemi, N. & Issazadeh, K. Evaluation of Antimicrobial Activity of Spider Silk Pholcus Phalangioides Against Two Bacterial Pathogens in Food Borne. *Int. J. Adv. Biol. Biomed. Res.* **2**, 2197–2199 (2014).

69. Esteves, F. G. *et al.* Revealing the Venomous Secrets of the Spider's Web. *J. Proteome Res.* **19**, 3044–3059 (2020).

70. Wang, Y. *et al.* The spider venom peptide lycosin-II has potent antimicrobial activity against clinically isolated bacteria. *Toxins (Basel).* **8**, 119 (2016).

71. Zhang, S. *et al.* Nitrogen inaccessibility protects spider silk from bacterial growth. *J. Exp. Biol.* **222**, jeb214981 (2019).

72. Prince, J. T., McGrath, K. P., DiGirolamo, C. M. & Kaplan, D. L. Construction, Cloning, and Expression of Synthetic Genes Encoding Spider Dragline Silk. *Biochemistry* **34**, 10879–85 (1995).

73. Lewis, R. V, Hinman, M., Kothakota, S. & Fournier, M. J. Expression and purification of a spider silk protein: a new strategy for producing repetitive proteins. *Protein Expr. Purif.* **7**, 400–6 (1996).

74. Xu, H. T. *et al.* Construct synthetic gene encoding artificial spider dragline silk protein and its expression in milk of transgenic mice. *Anim. Biotechnol.* **18**, 1–12 (2007).

75. Fahnestock, S. R. & Bedzyk, L. A. Production of synthetic spider dragline silk protein in Pichia pastoris. *Appl. Microbiol. Biotechnol.* **47**, 33–39 (1997).

76. Scheller, J., Gührs, K. H., Grosse, F. & Conrad, U. Production of spider silk proteins in tobacco and potato. *Nat. Biotechnol.* **19**, 573–7 (2001).

77. Whittall, D. R., Baker, K. V., Breitling, R. & Takano, E. Host Systems for the Production of

Recombinant Spider Silk. *Trends Biotechnol.* **39**, 560–573 (2020).

78. Blackledge, T. A. Silken toolkits: biomechanics of silk fibers spun by the orb web spider Argiope argentata. *J. Exp. Biol.* **209**, 2452–61 (2006).

79. Ortlepp, C. S. & Gosline, J. M. Consequences of forced silking. *Biomacromolecules* **5**, 727–31 (2004).

80. Tucker, C. L. *et al.* Mechanical and physical properties of recombinant spider silk films using organic and aqueous solvents. *Biomacromolecules* **15**, 3158–70 (2014).

81. Jones, J. A. *et al.* Importance of heat and pressure for solubilization of recombinant spider silk proteins in aqueous solution. *Int. J. Mol. Sci.* **17**, 1955 (2016).

82. Karatzas, C., Turner, J. & Lazaris-Karatzas, A. Patent for production of biofilaments in transgenic animals. (2007).

83. Li, H., Chen, S., Piao, S., An, T. & Wang, C. Production of artificial synthetic spidroin gene 4S-transgenic cloned sheep embryos using somatic cell nuclear transfer. *Anim. Biotechnol.* **14**, 1532–2378 (2020).

84. Kuwana, Y., Sezutsu, H., Nakajima, K. I., Tamada, Y. & Kojima, K. High-toughness silk produced by a transgenic silkworm expressing spider (Araneus ventricosus) dragline silk protein. *PLoS One* **9**, e105325 (2014).

85. Wen, H. *et al.* Transgenic silkworms (Bombyx mori) produce recombinant spider dragline silk in cocoons. *Mol. Biol. Rep.* **37**, 1815–21 (2010).

86. Teule, F. *et al.* Silkworms transformed with chimeric silkworm/spider silk genes spin composite silk fibers with improved mechanical properties. *Proc. Natl. Acad. Sci.* **109**, 923–9 (2012).

87. Zhang, X. *et al.* CRISPR/Cas9 Initiated Transgenic Silkworms as a Natural Spinner of Spider Silk. *Biomacromolecules* **20**, 2252–2264 (2019).

88. Zhao, S. *et al.* Recombinant silk proteins with additional polyalanine have excellent mechanical properties. *Int. J. Mol. Sci.* **22**, 1–14 (2021).

89. Scheller, J., Henggeler, D., Viviani, A. & Conrad, U. Purification of spider silk-elastin from transgenic plants and application for human chondrocyte proliferation. *Transgenic Res.* **13**, 51–7 (2004).

90. Hauptmann, V. *et al.* Native-sized spider silk proteins synthesized in planta via intein-based multimerization. *Transgenic Res.* **22**, 369–77 (2013).

91. Menassa, R. *et al.* Spider dragline silk proteins in transgenic tobacco leaves: Accumulation and field production. *Plant Biotechnol. J.* **2**, 431–8 (2004).

92. Yang, J., Barr, L. A., Fahnestock, S. R. & Liu, Z.-B. High yield recombinant silk-like protein production in transgenic plants through protein targeting. *Transgenic Res.* **14**, 313–24 (2005).

93. Candelas, G. C. & López, F. Synthesis of fibroin in the cultured glands of Nephila clavipes. *Comp. Biochem. Physiol.* **74**, 637–641 (1983).

94. Candelas, G. C., Arroyo, G., Carrasco, C. & Dompenciel, R. Spider silkglands contain a tissue-specific alanine tRNA that accumulates in vitro in response to the stimulus for silk protein synthesis. *Dev. Biol.* **140**, 215–20 (1990).

95. Lazaris, A. *et al.* Spider silk fibers spun from soluble recombinant silk produced in mammalian

cells. *Science (80-.).* **295**, 472–6 (2002).

96. Huemmerich, D. *et al.* Novel assembly properties of recombinant spider dragline silk proteins. *Curr. Biol.* **14**, 2070–4 (2004).

97. Miao, Y. *et al.* Expression of spider flagelliform silk protein in Bombyx mori cell line by a novel Bac-to-Bac/BmNPV baculovirus expression system. *Appl. Microbiol. Biotechnol.* **71**, 192–199 (2006).

98. Lyda, T. A. *et al.* A Leishmania secretion system for the expression of major ampullate spidroin mimics. *PLoS One* **12**, (2017).

99. Widmaier, D. M. *et al.* Engineering the Salmonella type III secretion system to export spider silk monomers. *Mol. Syst. Biol.* **5**, 309 (2009).

100. Xia, X.-X. *et al.* Native-sized recombinant spider silk protein produced in metabolically engineered Escherichia coli results in a strong fiber. *Proc. Natl. Acad. Sci.* **107**, 14059–63 (2010).

101. Bowen, C. H. *et al.* Recombinant Spidroins Fully Replicate Primary Mechanical Properties of Natural Spider Silk. *Biomacromolecules* **19**, 3853–3860 (2018).

102. M, A. *et al.* Biomimetic spinning of artificial spider silk from a chimeric minispidroin. *Nat. Chem. Biol.* **13**, 262–264 (2017).

103. Jia, Q., Wen, R. & Meng, Q. Novel highly soluble chimeric recombinant spidroins with high yield. *Int. J. Mol. Sci.* **21**, 1–13 (2020).

104. Schacht, K. & Scheibel, T. Processing of recombinant spider silk proteins into tailor-made materials for biomaterials applications. *Curr. Opin. Biotechnol.* **29**, 62–9 (2014).

105. Margareta Stark *et al.* Macroscopic Fibers Self-Assembled from Recombinant Miniature Spider Silk Proteins. *Biomacromolecules* **8**, 1695–1701 (2007).

106. Harvey, D., Bardelang, P., Goodacre, S. L., Cockayne, A. & Thomas, N. R. Antibiotic Spider Silk: Site-Specific Functionalization of Recombinant Spider Silk Using “Click” Chemistry. *Adv. Mater.* **29**, 1604245 (2017).

107. Kvick, M. *et al.* Cyclic Expansion/Compression of the Air–Liquid Interface as a Simple Method to Produce Silk Fibers. *Macromol. Biosci.* **21**, 2000227 (2020).

108. Lin, Z., Deng, Q., Liu, X.-Y. & Yang, D. Engineered Large Spider Eggcase Silk Protein for Strong Artificial Fibers. *Adv. Mater.* **25**, 1216–1220 (2013).

109. Ruiz, V. *et al.* Preparation and characterization of Nephila clavipes tubuliform silk gut. *Soft Matter* **15**, 2960–2970 (2019).

110. Gnesa, E. *et al.* Conserved C-Terminal Domain of Spider Tubuliform Spidroin 1 Contributes to Extensibility in Synthetic Fibers. *Biomacromolecules* **13**, 304–312 (2012).

111. Xia, X.-X. *et al.* Native-sized recombinant spider silk protein produced in metabolically engineered Escherichia coli results in a strong fiber. *Proc. Natl. Acad. Sci. U. S. A.* **107**, 14059–63 (2010).

112. Hu, C.-F., Qian, Z.-G., Peng, Q., Zhang, Y. & Xia, X.-X. Unconventional Spidroin Assemblies in Aqueous Dope for Spinning into Tough Synthetic Fibers. *ACS Biomater. Sci. Eng.* **7**, 3608–3617 (2021).

113. Belbéoch, C., Lejeune, J., Vroman, P. & Salaün, F. Silkworm and spider silk electrospinning: a

review. *Environ. Chem. Lett.* **19**, 1737–1763 (2021).

114. Jean S. Stephens *et al.* Effects of Electrospinning and Solution Casting Protocols on the Secondary Structure of a Genetically Engineered Dragline Spider Silk Analogue Investigated via Fourier Transform Raman Spectroscopy. *Biomacromolecules* **6**, 1405–1413 (2005).

115. Yu, Q. *et al.* Structure–property relationship of regenerated spider silk protein nano/microfibrous scaffold fabricated by electrospinning. *J. Biomed. Mater. Res. Part A* **102**, 3828–3837 (2014).

116. DeSimone, E., Aigner, T. B., Humenik, M., Lang, G. & Scheibel, T. Aqueous electrospinning of recombinant spider silk proteins. *Mater. Sci. Eng. C* **106**, 110145 (2020).

117. Konwarh, R., Gupta, P. & Mandal, B. B. Silk-microfluidics for advanced biotechnological applications: A progressive review. *Biotechnol. Adv.* **34**, 845–858 (2016).

118. Renberg, B., Andersson-Svahn, H. & Hedhammar, M. Mimicking silk spinning in a microchip. *Sensors Actuators B Chem.* **195**, 404–408 (2014).

119. Wang, X. *et al.* Nanolayer biomaterial coatings of silk fibroin for controlled release. *J. Control. Release* **121**, 190–9 (2007).

120. Zha, R. H. *et al.* Universal nanothin silk coatings via controlled spidroin self-assembly. *Biomater. Sci.* **7**, 683–695 (2019).

121. Wohlrab, S., Spieß, K. & Scheibel, T. Varying surface hydrophobicities of coatings made of recombinant spider silk proteins. *J. Mater. Chem.* **22**, 22050–22054 (2012).

122. Tucker, C. L. *et al.* Mechanical and physical properties of recombinant spider silk films using organic and aqueous solvents. *Biomacromolecules* **15**, 3158–3170 (2014).

123. Huemmerich, D. *et al.* Primary structure elements of spider dragline silks and their contribution to protein solubility. *Biochemistry* **43**, 13604–12 (2004).

124. Spiess, K., Lammel, A. & Scheibel, T. Recombinant spider silk proteins for applications in biomaterials. *Macromol. Biosci.* **10**, 998–1007 (2010).

125. Borkner, C. B., Elsner, M. B. & Scheibel, T. Coatings and films made of silk proteins. *ACS Appl. Mater. Interfaces* **6**, 15611–15625 (2014).

126. Perry, H., Gopinath, A., Kaplan, D. L., Negro, L. D. & Omenetto, F. G. Nano- and micropatterning of optically transparent, mechanically robust, biocompatible silk fibroin films. *Adv. Mater.* **20**, 3070–2 (2008).

127. Kumari, S., Bargel, H., Anby, M. U., Lafargue, D. & Scheibel, T. Recombinant Spider Silk Hydrogels for Sustained Release of Biologicals. *ACS Biomater. Sci. Eng.* **4**, 1750–1759 (2018).

128. Luo, F., Qian, Z.-G. & Xia, X.-X. Responsive Protein Hydrogels Assembled from Spider Silk Carboxyl-Terminal Domain and Resilin Copolymers. *Polymers (Basel).* **10**, 915 (2018).

129. Schacht, K. & Scheibel, T. Controlled Hydrogel Formation of a Recombinant Spider Silk Protein. *Biomacromolecules* **12**, 2488–2495 (2011).

130. Qian, Z.-G., Zhou, M.-L., Song, W.-W. & Xia, X.-X. Dual Thermosensitive Hydrogels Assembled from the Conserved C-Terminal Domain of Spider Dragline Silk. *Biomacromolecules* **16**, 3704–3711 (2015).

131. Rammensee, S., Huemmerich, D., Hermanson, K. D., Scheibel, T. & Bausch, A. R. Rheological characterization of hydrogels formed by recombinantly produced spider silk. *Appl. Phys. A* **82**,

261–264 (2005).

132. Earlam, R. Recombinant spider silk protein hydrogels. (University of Nottingham, 2021).

133. Arndt, T., Laity, P. R., Johansson, J., Holland, C. & Rising, A. Native-like Flow Properties of an Artificial Spider Silk Dope. *ACS Biomater. Sci. Eng.* **7**, 462–471 (2021).

134. Steiner, D. *et al.* Enhanced vascularization and de novo tissue formation in hydrogels made of engineered RGD-tagged spider silk proteins in the arteriovenous loop model. *Biofabrication* **13**, Online ahead of print (2021).

135. Neubauer, V. J., Trossmann, V. T., Jacobi, S., Döbl, A. & Scheibel, T. Recombinant Spider Silk Gels Derived from Aqueous–Organic Solvents as Depots for Drugs. *Angew. Chemie Int. Ed.* **60**, 11847–11851 (2021).

136. Doblhofer, E., Heidebrecht, A. & Scheibel, T. To spin or not to spin: spider silk fibers and more. *Appl. Microbiol. Biotechnol.* **99**, 9361–9380 (2015).

137. Lammel, A., Schwab, M., Slotta, U., Winter, G. & Scheibel, T. Processing conditions for the formation of spider silk microspheres. *ChemSusChem* **1**, 413–6 (2008).

138. Mohammadi, P. *et al.* Controllable coacervation of recombinantly produced spider silk protein using kosmotropic salts. *J. Colloid Interface Sci.* **560**, 149–160 (2020).

139. Slotta, U. K., Rammensee, S., Gorb, S. & Scheibel, T. An Engineered Spider Silk Protein Forms Microspheres. *Angew. Chemie Int. Ed.* **47**, 4592–4594 (2008).

140. Lucke, M., Winter, G. & Engert, J. The effect of steam sterilization on recombinant spider silk particles. *Int. J. Pharm.* **481**, 125–131 (2015).

141. Elsner, M. B., Herold, H. M., Müller-Herrmann, S., Bargel, H. & Scheibel, T. Enhanced cellular uptake of engineered spider silk particles. *Biomater. Sci.* **3**, 543–55 (2015).

142. Jastrzebska, K. *et al.* The method of purifying bioengineered spider silk determines the silk sphere properties. *Sci. Rep.* **6**, 28106 (2016).

143. Dams-Kozlowska, H. *et al.* Purification and cytotoxcicity of tag-free bioengineered spider silk proteins. *J. Biomed. Mater. Res. A* **101**, 456 (2013).

144. Fredriksson, C. *et al.* Tissue response to subcutaneously implanted recombinant spider silk: An in vivo study. *Materials (Basel).* **2**, 1908–1922 (2009).

145. Gomes, S. *et al.* In Vivo Biological Responses to Silk Proteins Functionalized with Bone Sialoprotein. *Macromol. Biosci.* **13**, 444–54 (2013).

146. Hedhammar, M. Y. *et al.* Sterilized recombinant spider silk fibers of low pyrogenicity. *Biomacromolecules* **11**, 953–959 (2010).

147. Zeplin, P. H. *et al.* Spider Silk Coatings as a Bioshield to Reduce Periprosthetic Fibrous Capsule Formation. *Adv. Funct. Mater.* **24**, 2658–2666 (2014).

148. Moisenovich, M. M. *et al.* In vitro and in vivo biocompatibility studies of a recombinant analogue of spidroin 1 scaffolds. *J. Biomed. Mater. Res. Part A* **96A**, 125–131 (2011).

149. Saha, A. & Robertson, E. S. Mechanisms of B-Cell Oncogenesis Induced by Epstein-Barr Virus. *J. Virol.* **93**, (2019).

150. Pelassa, I. *et al.* Association of polyalanine and polyglutamine coiled coils mediates expansion disease-related protein aggregation and dysfunction. *Hum. Mol. Genet.* **23**, 3402–3420

(2014).

151. Dinjaski, N. *et al.* Predicting rates of in vivo degradation of recombinant spider silk proteins. *J. Tissue Eng. Regen. Med.* **12**, e97–e105 (2018).

152. Müller-Herrmann, S. & Scheibel, T. Enzymatic Degradation of Films, Particles, and Nonwoven Meshes Made of a Recombinant Spider Silk Protein. *ACS Biomater. Sci. Eng.* **1**, 247–259 (2015).

153. Lammel, A., Schwab, M., Hofer, M., Winter, G. & Scheibel, T. Recombinant spider silk particles as drug delivery vehicles. *Biomaterials* **32**, 2233–40 (2011).

154. Hofer, M., Winter, G. & Myschik, J. Recombinant spider silk particles for controlled delivery of protein drugs. *Biomaterials* **33**, 1554–62 (2012).

155. Doblhofer, E. & Scheibel, T. Engineering of recombinant spider silk proteins allows defined uptake and release of substances. *J. Pharm. Sci.* **104**, 988–994 (2015).

156. Blüm, C. & Scheibel, T. Control of Drug Loading and Release Properties of Spider Silk Sub-Microparticles. *Bionanoscience* **2**, 67–74 (2012).

157. Florczak, A., Mackiewicz, A. & Dams-Kozlowska, H. Functionalized spider silk spheres as drug carriers for targeted cancer therapy. *Biomacromolecules* **15**, 2971–81 (2014).

158. Kumari, S., Bargel, H., Anby, M. U., Lafargue, D. & Scheibel, T. Recombinant Spider Silk Hydrogels for Sustained Release of Biologicals. *ACS Biomater. Sci. Eng.* **4**, 1750–1759 (2018).

159. Bini, E. *et al.* RGD-functionalized bioengineered spider dragline silk biomaterial. *Biomacromolecules* **7**, 3139–45 (2006).

160. Gomes, S. C., Leonor, I. B., Mano, J. F., Reis, R. L. & Kaplan, D. L. Antimicrobial functionalized genetically engineered spider silk. *Biomaterials* **32**, 4255–66 (2011).

161. Currie, H. A., Deschaume, O., Naik, R. R., Perry, C. C. & Kaplan, D. L. Genetically engineered chimeric silk-silver binding proteins. *Adv. Funct. Mater.* **21**, 2889–95 (2011).

162. Dakal, T. C., Kumar, A., Majumdar, R. S. & Yadav, V. Mechanistic basis of antimicrobial actions of silver nanoparticles. *Front. Microbiol.* **7**, 1831 (2016).

163. Seijsing, F. *et al.* Recombinant spider silk coatings functionalized with enzymes targeting bacteria and biofilms. *Microbiol. Open* **9**, e993 (2020).

164. Dorr, B. M., Ham, H. O., An, C., Chaikof, E. L. & Liu, D. R. Reprogramming the specificity of sortase enzymes. *Proc. Natl. Acad. Sci.* **111**, 13343–13348 (2014).

165. Petzold, J. *et al.* Surface Features of Recombinant Spider Silk Protein eADF4(κ16)-Made Materials are Well-Suited for Cardiac Tissue Engineering. *Adv. Funct. Mater.* **27**, 1701427 (2017).

166. Numata, K., Subramanian, B., Currie, H. A. & Kaplan, D. L. Bioengineered silk protein-based gene delivery systems. *Biomaterials* **30**, 5775–84 (2009).

167. Numata, K., Hamasaki, J., Subramanian, B. & Kaplan, D. L. Gene delivery mediated by recombinant silk proteins containing cationic and cell binding motifs. *J. Control. Release* **146**, 136–43 (2010).

168. Esser, T. U., Trossmann, V. T., Lentz, S., Engel, F. B. & Scheibel, T. Designing of spider silk proteins for human induced pluripotent stem cell-based cardiac tissue engineering. *Mater. Today Bio* **11**, 100114 (2021).

169. Widhe, M., Johansson, U., Hillerdahl, C. O. & Hedhammar, M. Recombinant spider silk with cell binding motifs for specific adherence of cells. *Biomaterials* **34**, 8223–34 (2013).

170. Åstrand, C., Chotteau, V., Falk, A. & Hedhammar, M. Assembly of FN-silk with laminin-521 to integrate hPSCs into a three-dimensional culture for neural differentiation. *Biomater. Sci.* **8**, 2514–2525 (2020).

171. Tasiopoulos, C. P., Gustafsson, L., Wijngaart, W. van der & Hedhammar, M. Fibrillar Nanomembranes of Recombinant Spider Silk Protein Support Cell Co-culture in an In Vitro Blood Vessel Wall Model. *ACS Biomater. Sci. Eng.* **7**, 3332–3339 (2021).

172. Johansson, U. *et al.* Integration of Primary Endocrine Cells and Supportive Cells Using Functionalized Silk Promotes the Formation of Prevascularized Islet-like Clusters. *ACS Biomater. Sci. Eng.* **6**, 1186–95 (2020).

173. Chouhan, D. *et al.* Silkworm Silk Scaffolds Functionalized with Recombinant Spider Silk Containing a Fibronectin Motif Promotes Healing of Full-Thickness Burn Wounds. *ACS Biomater. Sci. Eng.* **5**, 4634–4645 (2019).

174. Chouhan, D. *et al.* Silkworm Silk Matrices Coated with Functionalized Spider Silk Accelerate Healing of Diabetic Wounds. *ACS Biomater. Sci. Eng.* **5**, 3537–3548 (2019).

175. Johansson, U. *et al.* Integration of Primary Endocrine Cells and Supportive Cells Using Functionalized Silk Promotes the Formation of Prevascularized Islet-like Clusters. *ACS Biomater. Sci. Eng.* **6**, 1186–95 (2019).

176. Pereira, A. M. *et al.* Silk-based biomaterials functionalized with fibronectin type II promotes cell adhesion. *Acta Biomater.* **47**, 50–9 (2017).

177. Numata, K., Reagan, M. R., Goldstein, R. H., Rosenblatt, M. & Kaplan, D. L. Spider silk-based gene carriers for tumor cell-specific delivery. *Bioconjug. Chem.* **22**, 1605–10 (2011).

178. Numata, K. & Kaplan, D. L. Silk-based gene carriers with cell membrane destabilizing peptides. *Biomacromolecules* **11**, 3189–95 (2010).

179. Petrou, G. *et al.* Genetically Engineered Mucoadhesive Spider Silk. *Biomacromolecules* **19**, 3268–79 (2018).

180. Wong Po Foo, C. *et al.* Novel nanocomposites from spider silk-silica fusion (chimeric) proteins. *Proc. Natl. Acad. Sci.* **103**, 9428–33 (2006).

181. Martín-Moldes, Z., López Barreiro, D., Buehler, M. J. & Kaplan, D. L. Effect of the silica nanoparticle size on the osteoinduction of biomineralized silk-silica nanocomposites. *Acta Biomater.* **120**, 203–212 (2021).

182. Huang, J., Wong, C., George, A. & Kaplan, D. L. The effect of genetically engineered spider silk-dentin matrix protein 1 chimeric protein on hydroxyapatite nucleation. *Biomaterials* **28**, 2358–67 (2007).

183. Neubauer, V. J. & Scheibel, T. Spider Silk Fusion Proteins for Controlled Collagen Binding and Biomineralization. *ACS Biomater. Sci. Eng.* **6**, 5599–5608 (2020).

184. Chouhan, D. *et al.* Recombinant Spider Silk Functionalized Silkworm Silk Matrices as Potential Bioactive Wound Dressings and Skin Grafts. *ACS Appl. Mater. Interfaces* **10**, 23560–72 (2018).

185. Huemmerich, D., Slotta, U. & Scheibel, T. Processing and modification of films made from recombinant spider silk proteins. *Appl. Phys. A Mater. Sci. Process.* **82**, 219–22 (2006).

186. Spieß, K., Wohlrab, S. & Scheibel, T. Structural characterization and functionalization of engineered spider silk films. *Soft Matter* **6**, 4168–74 (2010).

187. Wohlrab, S. *et al.* Cell adhesion and proliferation on RGD-modified recombinant spider silk proteins. *Biomaterials* **33**, 6650–9 (2012).

188. Herold, H. M., Döbl, A., Wohlrab, S., Humenik, M. & Scheibel, T. Designed Spider Silk-Based Drug Carrier for Redox- or pH-Triggered Drug Release. *Biomacromolecules* **21**, 4904–4912 (2020).

189. Humenik, M. & Scheibel, T. Nanomaterial building blocks based on spider silk-oligonucleotide conjugates. *ACS Nano* **8**, 1342–9 (2014).

190. Humenik, M., Drechsler, M. & Scheibel, T. Controlled hierarchical assembly of spider silk-DNA chimeras into ribbons and raft-like morphologies. *Nano Lett.* **14**, 3999–4004 (2014).

191. Humenik, M., Preiß, T., Gödrich, S., Papastavrou, G. & Scheibel, T. Functionalized DNA-spider silk nanohydrogels for controlled protein binding and release. *Mater. Today Bio* **6**, 100045 (2020).

192. Harvey, D. *et al.* Cyclo(RGDfK) Functionalized Spider Silk Cell Scaffolds: Significantly Improved Performance in Just One Click. *Macromol. Biosci.* **20**, 2000255 (2020).

193. Kolb, H. C., Finn, M. G. & Sharpless, K. B. Click Chemistry: Diverse Chemical Function from a Few Good Reactions. *Angew. Chemie - Int. Ed.* **40**, 2004–21 (2001).

194. Baskin, J. M. & Bertozzi, C. R. Bioorthogonal click chemistry: Covalent labeling in living systems. *QSAR Comb. Sci.* **26**, 1211–9 (2007).

195. Ahmad Fuaad, A. A. H., Azmi, F., Skwarczynski, M. & Toth, I. Peptide conjugation via CuAAC 'click' chemistry. *Molecules* **18**, 13148–74 (2013).

196. Abel, G. R., Calabrese, Z. A., Ayco, J., Hein, J. E. & Ye, T. Measuring and Suppressing the Oxidative Damage to DNA during Cu(I)-Catalyzed Azide-Alkyne Cycloaddition. *Bioconjug. Chem.* **27**, 698–704 (2016).

197. Zhu, L., Brassard, C. J., Zhang, X., Guha, P. M. & Clark, R. J. On the Mechanism of Copper(I)-Catalyzed Azide–Alkyne Cycloaddition. *Chem. Rec.* **16**, 1501–1517 (2016).

198. Gaetke, L. M., Chow-Johnson, H. S. & Chow, C. K. Copper: Toxicological relevance and mechanisms. *Arch. Toxicol.* **88**, 1929 (2014).

199. Li, L. & Zhang, Z. Development and applications of the copper-catalyzed azide-alkyne cycloaddition (CuAAC) as a bioorthogonal reaction. *Molecules* **21**, 1393 (2016).

200. Agard, N. J., Prescher, J. A. & Bertozzi, C. R. A strain-promoted [3 + 2] azide-alkyne cycloaddition for covalent modification of biomolecules in living systems. *J. Am. Chem. Soc.* **126**, 15046–47 (2004).

201. Anderton, G. I. *et al.* Accelerating Strain-Promoted Azide-Alkyne Cycloaddition Using Micellar Catalysis. *Bioconjug. Chem.* **26**, 1687–91 (2015).

202. Dommerholt, J., Rutjes, F. P. J. T. & van Delft, F. L. Strain-Promoted 1,3-Dipolar Cycloaddition of Cycloalkynes and Organic Azides. *Top. Curr. Chem.* **374**, 16 (2016).

203. Hedhammar, M. *et al.* Structural Properties of Recombinant Nonrepetitive and Repetitive Parts of Major Ampullate Spidroin 1 from Euprosthenops australis: Implications for Fiber Formation. *Biochemistry* **47**, 3407–3417 (2008).

204. Grip, S., Johansson, J. & Hedhammar, M. Engineered disulfides improve mechanical properties of recombinant spider silk. *Protein Sci.* (2009) doi:10.1002/pro.111.

205. Sandri, M., Rizzi, C., Catani, C. & Carraro, U. Selective Removal of Free Dodecyl Sulfate from 2-Mercaptoethanol-SDS-Solubilized Proteins before KDS-Protein Precipitation. *Anal. Biochem.* **213**, 34–39 (1993).

206. T, G., G, R. & AK, G. Colloidal drug delivery systems: current status and future directions. *Crit. Rev. Ther. Drug Carrier Syst.* **32**, 89–147 (2015).

207. Sung, Y. K. & Kim, S. W. Recent advances in polymeric drug delivery systems. *Biomater. Res.* **24**, 1–12 (2020).

208. Liechty, W. B., Kryscio, D. R., Slaughter, B. V. & Peppas, N. A. Polymers for Drug Delivery Systems. *Annu. Rev. Chem. Biomol. Eng.* **1**, 149 (2010).

209. Lengyel, M., Kállai-Szabó, N., Antal, V., Laki, A. J. & Antal, I. Microparticles, Microspheres, and Microcapsules for Advanced Drug Delivery. *Sci. Pharm.* **87**, 20 (2019).

210. Fröhlich, E. The role of surface charge in cellular uptake and cytotoxicity of medical nanoparticles. *Int. J. Nanomedicine* **7**, 5577 (2012).

211. Grossen, P., Witzigmann, D., Sieber, S. & Huwyler, J. PEG-PCL-based nanomedicines: A biodegradable drug delivery system and its application. *J. Control. Release* **260**, 46–60 (2017).

212. Schöttler, S. *et al.* Protein adsorption is required for stealth effect of poly(ethylene glycol)- and poly(phosphoester)-coated nanocarriers. *Nat. Nanotechnol.* **11**, 372–377 (2016).

213. Suk, J. S., Xu, Q., Kim, N., Hanes, J. & Ensign, L. M. PEGylation as a strategy for improving nanoparticle-based drug and gene delivery. *Adv. Drug Deliv. Rev.* **99**, 28 (2016).

214. Aliberti, C. *et al.* Chemoembolization Adopting Polyethylene Glycol Drug-Eluting Embolics Loaded With Doxorubicin for the Treatment of Hepatocellular Carcinoma. *Vasc. Interv. Radiol.* **209**, 430–434 (2017).

215. Pereira, P. L. *et al.* An in-vitro evaluation of three types of drug-eluting microspheres loaded with irinotecan. *Anticancer. Drugs* **27**, 873–878 (2016).

216. Fiorentini, G. *et al.* A review discussing the use of polyethylene glycol microspheres in the treatment of hepatocellular carcinoma. *Futur. Med.* **15**, 695–703 (2018).

217. Anselmo, A. C. & Mitragotri, S. Nanoparticles in the clinic: An update. *Bioeng. Transl. Med.* **4**, e10143 (2019).

218. Yu, J. J. *et al.* Bio-distribution and anti-tumor efficacy of PEG/PLA nano particles loaded doxorubicin. *J. Drug Target.* **15**, 279–284 (2007).

219. Vila, A. *et al.* PEG-PLA nanoparticles as carriers for nasal vaccine delivery. *J. Aerosol Med.* **17**, 174–185 (2004).

220. Eğri, S. & Eczacıoğlu, N. Sequential VEGF and BMP-2 releasing PLA-PEG-PLA scaffolds for bone tissue engineering: I. Design and in vitro tests. *Artif. Cells, Nanomedicine Biotechnol.* **45**, 321–329 (2017).

221. Essa, S., Louhichi, F., Raymond, M. & Hildgen, P. Improved antifungal activity of itraconazole-loaded PEG/PLA nanoparticles. *J. Microencapsul.* **30**, 205–217 (2013).

222. Kawai, F. Biodegradation of Polyethers (Polyethylene Glycol, Polypropylene Glycol, Polytetramethylene glycol, and Others). in *Biopolymers Online* (ed. Steinbüchel, A.) (Wiley-

VCH Verlag GmbH & Co. KGaA, 2001).

223. Ishida, T., Wang, X. Y., Shimizu, T., Nawata, K. & Kiwada, H. PEGylated liposomes elicit an anti-PEG IgM response in a T cell-independent manner. *J. Control. Release* **122**, 349–355 (2007).

224. Lubich, C. *et al.* The Mystery of Antibodies Against Polyethylene Glycol (PEG) - What do we Know? *Pharm. Res.* **33**, 2239–2249 (2016).

225. Sellaturay, P., Nasser, S., Islam, S., Gurugama, P. & Ewan, P. W. Polyethylene glycol (PEG) is a cause of anaphylaxis to the Pfizer/BioNTech mRNA COVID-19 vaccine. *Clin. Exp. Allergy* **51**, 861–863 (2021).

226. Morão, A. & de Bie, F. Life Cycle Impact Assessment of Polylactic Acid (PLA) Produced from Sugarcane in Thailand. *J. Polym. Environ.* **27**, 2523–2539 (2019).

227. Lee, B. K., Yun, Y. & Park, K. PLA Micro- and Nano-Particles. *Adv. Drug Deliv. Rev.* **107**, 176 (2016).

228. Ramot, Y., Haim-Zada, M., Domb, A. J. & Nyska, A. Biocompatibility and safety of PLA and its copolymers. *Adv. Drug Deliv. Rev.* **107**, 153–162 (2016).

229. Kumari, B., Khansili, A., Phougat, P. & Kumar, M. Comprehensive review of the role of acrylic acid derivative polymers in floating drug delivery system. *Polymers (Basel).* **49**, 71–79 (2019).

230. Cook, G. E. *et al.* Infection in orthopaedics. *J. Orthop. Trauma* **29**, S19–S23 (2015).

231. Seligson, D. & Berling, S. Antibiotic-laden PMMA bead chains for the prevention of infection in compound fractures: current state of the art. *Eur. J. Orthop. Surg. Traumatol.* **25**, 969–974 (2015).

232. Arruebo, M. & Sebastian, V. Batch and microfluidic reactors in the synthesis of enteric drug carriers. in *Nanotechnology for Oral Drug Delivery* (eds. Martins, J. P. & Hélder, A. S.) 317–357 (Academic Press, 2020).

233. Lam, H. T., Zupančič, O., Laffleur, F. & Bernkop-Schnürch, A. Mucoadhesive properties of polyacrylates: Structure – Function relationship. *Int. J. Adhes. Adhes.* **107**, 102857 (2021).

234. Jorge, J. H., Giampaolo, E. T., Machado, A. L. & Vergani, C. E. Cytotoxicity of denture base acrylic resins: A literature review. *J. Prosthet. Dent.* **90**, 190–193 (2003).

235. Yoshii, E. Cytotoxic effects of acrylates and methacrylates: relationships of monomer structures and cytotoxicity. *J. Biomed. Mater. Res.* **37**, 517–524 (1997).

236. Bull, J. E., Henderson, D. C. & Turk, J. L. Immunogenicity of acrylate chemicals as assessed by antibody induction. *Int. Arch. Allergy Appl. Immunol.* **83**, 310–314 (1987).

237. Mitchell, M. J. *et al.* Engineering precision nanoparticles for drug delivery. *Nat. Rev. Drug Discov.* **20**, 101–124 (2020).

238. Beija, M. *et al.* Colloidal systems for drug delivery: from design to therapy. *Trends Biotechnol.* **30**, 485–496 (2012).

239. Allen, T. M. & Cullis, P. R. Liposomal drug delivery systems: From concept to clinical applications. *Adv. Drug Deliv. Rev.* **65**, 36–48 (2013).

240. Soleimanian, Y., Goli, S. A. H., Shirvani, A., Elmizadeh, A. & Marangoni, A. G. Wax-based delivery systems: Preparation, characterization, and food applications. *Compr. Rev. Food Sci. Food Saf.* **19**, 2994–3030 (2020).

241. Hamada, J. *et al.* Embolization with cellulose porous beads, I: An experimental study. *AJNR. Am. J. Neuroradiol.* **17**, 1895–1899 (1996).

242. Halib, N. *et al.* Potential Applications of Nanocellulose-Containing Materials in the Biomedical Field. *Materials (Basel).* **10**, 977 (2017).

243. Liu, Z., Jiao, Y., Wang, Y., Zhou, C. & Zhang, Z. Polysaccharides-based nanoparticles as drug delivery systems. *Adv. Drug Deliv. Rev.* **60**, 1650–1662 (2008).

244. Mohammed, M. A., Syeda, J. T. M., Wasan, K. M. & Wasan, E. K. An Overview of Chitosan Nanoparticles and Its Application in Non-Parenteral Drug Delivery. *Pharmaceutics* **9**, 53 (2017).

245. González-Aramundiz, J. V., Lozano, M. V., Sousa-Herves, A., Fernandez-Megia, E. & Csaba, N. Polypeptides and polyaminoacids in drug delivery. *Expert Opin. Drug Deliv.* **9**, 183–201 (2012).

246. Chan, Y.-P., Meyrueix, R., Kravtzoff, R., Nicolas, F. & Lundstrom, K. Review on Medusa®:a polymer-based sustained release technology for protein and peptide drugs. *Expert Opin. Drug Deliv.* **4**, 441–451 (2007).

247. Chen, S., Yu, H., Xiaobo, F. & Dehao, F. ε-Polylysine and next-generation dendrigraft poly-L-lysine: chemistry, activity, and applications in biopharmaceuticals. *J. Biomater. Sci. Polym. Ed.* **26**, 1343–1356 (2015).

248. Karimi, M. *et al.* Nanocaged Platforms: Modification, Drug Delivery and Nanotoxicity Opening Synthetic Cages to Release the Tiger: Nanocages for Drug Delivery. *Nanoscale* **9**, 1356 (2017).

249. Zhang, Y. *et al.* Design, fabrication and biomedical applications of zein-based nano/micro-carrier systems. *Int. J. Pharm.* **513**, 191–210 (2016).

250. Paliwal, R. & Palakurthi, S. Zein in controlled drug delivery and tissue engineering. *J. Control. Release* **189**, 108–122 (2014).

251. Elzoghby, A., Freag, M., Mamdouh, H. & Elkhodairy, K. Zein-based Nanocarriers as Potential Natural Alternatives for Drug and Gene Delivery: Focus on Cancer Therapy. *Curr. Pharm. Des.* **23**, 5261–71 (2018).

252. Feroz, S., Muhammad, N., Ranayake, J. & Dias, G. Keratin - Based materials for biomedical applications. *Bioact. Mater.* **5**, 496 (2020).

253. Zheng, D.-W. *et al.* Hierarchical Micro-/Nanostructures from Human Hair for Biomedical Applications. *Adv. Mater.* **30**, 1800836 (2018).

254. Lewis, A. L. *et al.* Comparative in vitro evaluation of microspherical embolisation agents. *J. Mater. Sci. Mater. Med.* **17**, 1193–1204 (2006).

255. Moskowitz, R. W. Role of collagen hydrolysate in bone and joint disease. *Semin. Arthritis Rheum.* **30**, 87–99 (2000).

256. Elzoghby, A. O. Gelatin-based nanoparticles as drug and gene delivery systems: Reviewing three decades of research. *J. Control. Release* **172**, 1075–1091 (2013).

257. Tomeh, M. A., Hadianamrei, R. & Zhao, X. Silk fibroin as a functional biomaterial for drug and gene delivery. *Pharmaceutics* **11**, 494 (2019).

258. Holland, C., Numata, K., Rnjak-Kovacina, J. & Seib, F. P. The Biomedical Use of Silk: Past, Present, Future. *Adv. Healthc. Mater.* **8**, 1800465 (2019).

259. Huang, W., Ling, S., Li, C., Omenetto, F. G. & Kaplan, D. L. Silkworm silk-based materials and devices generated using bio-nanotechnology. *Chem. Soc. Rev.* **47**, 6486–6504 (2018).

260. Wenk, E., Merkle, H. P. & Meinel, L. Silk fibroin as a vehicle for drug delivery applications. *J. Control. Release* **150**, 128–141 (2011).

261. Rockwood, D. N. *et al.* Materials fabrication from Bombyx mori silk fibroin. *Nat. Protoc.* **6**, 1612–1631 (2011).

262. Dewair, M., Baur, X. & Ziegler, K. Use of immunoblot technique for detection of human IgE and IgG antibodies to individual silk proteins. *J. Allergy Clin. Immunol.* **76**, 537–542 (1985).

263. Panilaitis, B. *et al.* Macrophage responses to silk. *Biomaterials* **24**, 3079–3085 (2003).

264. Sharma, A., Dour, P. & Gupta, P. Screening of Enterobacterial Contamination During Gelatin Production and its Effect on Pharmaceutical Grade Gelatin. *World J. Microbiol. Biotechnol.* **22**, 1049–1054 (2006).

265. De Clerck, E. & De Vos, P. Study of the Bacterial Load in a Gelatine Production Process Focussed on Bacillus and Related Endosporeforming Genera. *Syst. Appl. Microbiol.* **25**, 611–617 (2002).

266. De Clerck, E. *et al.* Isolation, characterization, and identification of bacterial contaminants in semifinal gelatin extracts. *Appl. Environ. Microbiol.* **70**, 3664–3672 (2004).

267. Colchester, A. C. F. & Colchester, N. T. H. The origin of bovine spongiform encephalopathy: The human prion disease hypothesis. *Lancet* **366**, 856–861 (2005).

268. Mackenzie, G. & Will, R. Creutzfeldt-Jakob disease: recent developments. *F1000 Res.* **6**, 2053 (2017).

269. Frandsen, J. L. & Ghandehari, H. Recombinant protein-based polymers for advanced drug delivery. *Chem. Soc. Rev.* **41**, 2696–2706 (2012).

270. Olsen, D. *et al.* Recombinant collagen and gelatin for drug delivery. *Adv. Drug Deliv. Rev.* **55**, 1547–1567 (2003).

271. Guo, T. *et al.* Recombinant human hair keratin proteins for halting bleeding. *Artif. Cells, Nanomedicine, Biotechnol.* **46**, 456–461 (2018).

272. Gao, F. *et al.* Recombinant Human Hair Keratin Nanoparticles Accelerate Dermal Wound Healing. *ACS Appl. Mater. Interfaces* **11**, 18681–18690 (2019).

273. Zhao, Z., Li, Y. & Xie, M.-B. Silk Fibroin-Based Nanoparticles for Drug Delivery. *Int. J. Mol. Sci.* **16**, 4880 (2015).

274. Niknejad, H. & Mahmoudzadeh, R. Comparison of different crosslinking methods for preparation of docetaxel-loaded albumin nanoparticles. *Iran. J. Pharm. Res.* **14**, 385–394 (2015).

275. Tello, F., Prata, A. S., Rodrigues, R. A. F., Sartoratto, A. & Grosso, C. R. F. Improving the performance of transglutaminase-crosslinked microparticles for enteric delivery. *Food Res. Int.* **88**, 153–158 (2016).

276. James, A. M., Derry, M. J., Train, J. S. & Dawson, R. Dispersible microporous diblock copolymer nanoparticles via polymerisation-induced self-assembly. *Polym. Chem.* **10**, 3879–3886 (2019).

277. Creamer, A. *et al.* Post-polymerisation functionalisation of conjugated polymer backbones

and its application in multi-functional emissive nanoparticles. *Nat. Commun.* **9**, 1–11 (2018).

278. Kumar, M., Bishnoi, R. S., Shukla, A. K. & Jain, C. P. Techniques for Formulation of Nanoemulsion Drug Delivery System: A Review. *Prev. Nutr. Food Sci.* **24**, 225 (2019).

279. Martínez Rivas, C. J. *et al.* Nanoprecipitation process: From encapsulation to drug delivery. *Int. J. Pharm.* **532**, 66–81 (2017).

280. Hyde, A. M. *et al.* General Principles and Strategies for Salting-Out Informed by the Hofmeister Series. *Org. Process Res. Dev.* **21**, 1355–1370 (2017).

281. Galindo-Rodriguez, S., Allémann, E., Fessi, H. & Doelker, E. Physicochemical parameters associated with nanoparticle formation in the salting-out, emulsification-diffusion, and nanoprecipitation methods. *Pharm. Res.* **21**, 1428–1439 (2004).

282. Merchant, Z. *et al.* Engineering hydrophobically modified chitosan for enhancing the dispersion of respirable microparticles of levofloxacin. *Eur. J. Pharm. Biopharm.* **88**, 816–829 (2014).

283. Ungaro, F. *et al.* Dry powders based on PLGA nanoparticles for pulmonary delivery of antibiotics: Modulation of encapsulation efficiency, release rate and lung deposition pattern by hydrophilic polymers. *J. Control. Release* **157**, 149–159 (2012).

284. Sosnik, A. & Seremeta, K. P. Advantages and challenges of the spray-drying technology for the production of pure drug particles and drug-loaded polymeric carriers. *Adv. Colloid Interface Sci.* **223**, 40–54 (2015).

285. Xie, J., Jiang, J., Davoodi, P., Srinivasan, M. P. & Wang, C. H. Electrohydrodynamic atomization: A two-decade effort to produce and process micro-/nanoparticulate materials. *Chem. Eng. Sci.* **125**, 32–57 (2015).

286. Kopeček, J. & Yang, J. Hydrogels as smart biomaterials. *Polym. Int.* **56**, 1078–1098 (2007).

287. Desimone, E., Schacht, K., Jungst, T., Groll, J. & Scheibel, T. Biofabrication of 3D constructs: Fabrication technologies and spider silk proteins as bioinks. *Pure Appl. Chem.* **87**, 737–49 (2015).

288. Fu, J. *et al.* Self-assembled Nucleic Acid Nanostructures for Cancer Theranostic Medicines. *Curr. Top. Med. Chem.* **17**, 1815–1828 (2017).

289. Reverchon, E. & Adami, R. Nanomaterials and supercritical fluids. *J. Supercrit. Fluids* **37**, 1–22 (2006).

290. Brigger, I., Dubernet, C. & Couvreur, P. Nanoparticles in cancer therapy and diagnosis. *Adv. Drug Deliv. Rev.* **54**, 631–651 (2002).

291. Rejman, J., Oberle, V., Zuhorn, I. S. & Hoekstra, D. Size-dependent internalization of particles via the pathways of clathrin-and caveolae-mediated endocytosis. *Biochem. J.* **377**, 159–169 (2004).

292. Foged, C., Brodin, B., Frokjaer, S. & Sundblad, A. Particle size and surface charge affect particle uptake by human dendritic cells in an in vitro model. *Int. J. Pharm.* **298**, 315–322 (2005).

293. Gustafson, H. H., Holt-Casper, D., Grainger, D. W. & Ghandehari, H. Nanoparticle Uptake: The Phagocyte Problem. *Nano Today* **10**, 487 (2015).

294. Young, M., Coffey, W. & Mikhail, L. N. Uterine Fibroid Embolization. in *Statpearls* (Statpearls

Publishing, 2021).

295. Chen, Y. P., Zhang, J. L., Zou, Y. & Wu, Y. L. Recent advances on polymeric beads or hydrogels as embolization agents for improved transcatheter arterial chemoembolization (TACE). *Front. Chem.* **7**, 408 (2019).

296. McLucas, B., Adler, L. & Perrella, R. Uterine fibroid embolization: Nonsurgical treatment for symptomatic fibroids. *J. Am. Coll. Surg.* **192**, 95–105 (2001).

297. Pieper, C. C. *et al.* Temporary Arterial Embolization of Liver Parenchyma with Degradable Starch Microspheres (EmboCept®S) in a Swine Model. *Cardiovasc. Intervent. Radiol.* **38**, 435–441 (2015).

298. Embolic Particles/Beads - Endovascular Today. *Endovascular Today - US Device Guide - Embolic Particles/Beads* https://evtoday.com/device-guide/us/embolic-particlesbeads (2020).

299. Patra, J. K. *et al.* Nano based drug delivery systems: recent developments and future prospects. *J. Nanobiotechnology 2018 161* **16**, 1–33 (2018).

300. Longmire, M., Choyke, P. L. & Kobayashi, H. Clearance Properties of Nano-sized Particles and Molecules as Imaging Agents: Considerations and Caveats. *Nanomedicine (Lond).* **3**, 703 (2008).

301. Elmowafy, E. M., Tiboni, M. & Soliman, M. E. Biocompatibility, biodegradation and biomedical applications of poly(lactic acid)/poly(lactic-co-glycolic acid) micro and nanoparticles. *J. Pharm. Investig.* **49**, 347–380 (2019).

302. Elsner, M. B., Herold, H. M., Müller-Herrmann, S., Bargel, H. & Scheibel, T. Enhanced cellular uptake of engineered spider silk particles. *Biomater. Sci.* **3**, 543–551 (2015).

303. Eliakim-Raz, N. *et al.* Efficacy and safety of chloramphenicol: joining the revival of old antibiotics? Systematic review and meta-analysis of randomized controlled trials. *J. Antimicrob. Chemother.* **70**, 979–996 (2015).

304. Lucke, M. *et al.* Engineered hybrid spider silk particles as delivery system for peptide vaccines. *Biomaterials* **172**, 105–115 (2018).

305. Shnoudeh, A. J. *et al.* Synthesis, Characterization, and Applications of Metal Nanoparticles. in *Biomaterials and Bionanotechnology* (ed. Tekade, R.) 527–612 (Academic Press, 2019).

306. Gumustas, M., Sengel-Turk, C. T., Gumustas, A., Ozkan, S. A. & Uslu, B. Effect of Polymer-Based Nanoparticles on the Assay of Antimicrobial Drug Delivery Systems. in *Multifunctional Systems for Combined Delivery, Biosensing and Diagnostics* (ed. Grumezescu, A. M.) 67–108 (Elsevier, 2017).

307. Bazant, M. Z. Electrokinetic Motion of Heterogeneous Particles. in *Encyclopedia of Microfluidics and Nanofluidics* 518–522 (Springer, 2008).

308. Sheth, R. A. *et al.* Endovascular Embolization by Transcatheter Delivery of Particles: Past, Present, and Future. *J. Funct. Biomater.* **8**, 12 (2017).

309. Bysell, H., Månsson, R., Hansson, P. & Malmsten, M. Microgels and microcapsules in peptide and protein drug delivery. *Adv. Drug Deliv. Rev.* **63**, 1172–1185 (2011).

310. Scheffold, F. Pathways and challenges towards a complete characterization of microgels. *Nat. Commun.* **11**, 1–13 (2020).

311. Otikovs, M. *et al.* Degree of Biomimicry of Artificial Spider Silk Spinning Assessed by NMR

Spectroscopy. *Angew. Chemie - Int. Ed.* **56**, 12571–12575 (2017).

312. Kronqvist, N. *et al.* Sequential pH-driven dimerization and stabilization of the N-terminal domain enables rapid spider silk formation. *Nat. Commun.* **5**, 3254 (2014).

313. Hermanson, G. T. *Bioconjugate Techniques*. (Elsevier Science, 2013).

314. Migneault, I., Dartiguenave, C., Bertrand, M. J. & Waldron, K. C. Glutaraldehyde: behavior in aqueous solution, reaction with proteins, and application to enzyme crosslinking. *Biotechniques* **37**, 790–802 (2018).

315. Farris, S., Song, J. & Huang, Q. Alternative reaction mechanism for the cross-linking of gelatin with glutaraldehyde. *J. Agric. Food Chem.* **58**, 998–1003 (2010).

316. Olde Damink, L. H. H. *et al.* Glutaraldehyde as a crosslinking agent for collagen-based biomaterials. *J. Mater. Sci. Mater. Med.* **6**, 460–472 (1995).

317. Salem, M., Mauguen, Y. & Prangé, T. Revisiting glutaraldehyde cross-linking: the case of the Arg–Lys intermolecular doublet. *Acta Crystallogr. Sect. F Struct. Biol. Cryst. Commun.* **66**, 225 (2010).

318. Yan, E.-K. *et al.* Preparation of cross-linked hen-egg white lysozyme crystals free of cracks. *Sci. Reports 2016 61* **6**, 1–9 (2016).

319. Gonenc, I. & Us, F. Effect of Glutaraldehyde Crosslinking on Degree of Substitution, Thermal, Structural, and Physicochemical Properties of Corn Starch. *Starch - Stärke* **71**, 1800046 (2019).

320. Bruschi, M. Main mechanisms to control the drug release. in *Strategies to Modify the Drug Release from Pharmaceutical Systems* (ed. Bruschi, M. L. B. T.-S. to M. the D. R. from P. S.) 37–62 (Woodhead Publishing, 2015).

321. Bruschi, M. Mathematical models of drug release. in *Strategies to Modify the Drug Release from Pharmaceutical Systems* (ed. Bruschi, M. L. B. T.-S. to M. the D. R. from P. S.) 63–86 (Woodhead Publishing, 2015).

322. Eronen, P., Österberg, M. & Jääskeläinen, A.-S. Effect of alkaline treatment on cellulose supramolecular structure studied with combined confocal Raman spectroscopy and atomic force microscopy. *Cellulose* **16**, 167–178 (2008).

323. Kamaruzzaman, N. F. *et al.* Targeting the Bacterial protective armour; challenges and novel strategies in the treatment of microbial biofilm. *Materials (Basel).* **11**, 1705 (2018).

324. Clean Care is Safer Care Team. Report on the Burden of Endemic Health Care-Associated Infection Worldwide Clean Care is Safer Care. *Report on the Burden of Endemic Health Care-Associated Infection Worldwide: A systematic review of the literature* (2011).

325. Stone, P. W. Economic burden of healthcare-associated infections: An American perspective. *Expert Rev. Pharmacoeconomics Outcomes Res.* **9**, 417–422 (2009).

326. Guest, J. F., Keating, T., Gould, D. & Wigglesworth, N. Modelling the annual NHS costs and outcomes attributable to healthcare-associated infections in England. *BMJ Open* **10**, e033367 (2020).

327. Sievert, D. M. *et al.* Antimicrobial-Resistant Pathogens Associated with Healthcare-Associated Infections Summary of Data Reported to the National Healthcare Safety Network at the Centers for Disease Control and Prevention, 2009–2010. *Infect. Control Hosp. Epidemiol.* **34**, 1–14 (2013).

328. Hsieh, E. *et al.* Neonatal fungal infections: When to treat? *Early Hum. Dev.* **88**, S6 (2012).

329. Flemming, H. C. *et al.* Biofilms: An emergent form of bacterial life. *Nat. Rev. Microbiol.* **14**, 563–575 (2016).

330. Davies, D. Understanding biofilm resistance to antibacterial agents. *Nat. Rev. Drug Discov.* **2**, 114–122 (2003).

331. Del Pozo, J. L., Rouse, M. S. & Patel, R. Bioelectric effect and bacterial biofilms. A systematic review. *Int. J. Artif. Organs* **31**, 786–95 (2008).

332. Lewis, K. Persister cells, dormancy and infectious disease. *Nat. Rev. Microbiol.* **5**, 48–56 (2007).

333. Mah, T. F. Biofilm-specific antibiotic resistance. *Future Microbiol.* **7**, 1061–1072 (2012).

334. Busscher, H. J. *et al.* Biomaterial-associated infection: Locating the finish line in the race for the surface. *Sci. Transl. Med.* **4**, 153rv10-153rv10 (2012).

335. Adlhart, C. *et al.* Surface Modifications For Antimicrobial Effects in the Healthcare Setting: A Critical Overview. *J. Hosp. Infect.***99**, 239-249 (2018).

336. Tiller, J. C. Antimicrobial Surfaces. in *Bioactive Surfaces* (eds. Borner, H. G. & Lutz, J.-F.) (Springer, 2010).

337. Zhu, X. & Jun Loh, X. Layer-by-layer assemblies for antibacterial applications. *Biomater. Sci.* **3**, 1505–1518 (2015).

338. Zhuk, I. *et al.* Self-defensive layer-by-layer films with bacteria-triggered antibiotic release. *ACS Nano* **8**, 7733–7745 (2014).

339. Jameson, S. S. *et al.* Antibiotic-loaded bone cement is associated with a lower risk of revision following primary cemented total knee arthroplasty: An analysis of 731 214 cases using national joint registry data. *Bone Jt. J.* **101**-**B**, 1331–1347 (2019).

340. NICE. Surgical site infections: prevention and treatment. *Guidance* (2018).

341. Anagnostakos, K. Therapeutic Use of Antibiotic-loaded Bone Cement in the Treatment of Hip and Knee Joint Infections. *J. Bone Jt. Infect.* **2**, 29–37 (2017).

342. Chen, M. *et al.* Antibacterial Micelles with Vancomycin-Mediated Targeting and pH/Lipase-Triggered Release of Antibiotics. *ACS Appl. Mater. Interfaces* **10**, 36814–36823 (2018).

343. Murdan, S. Electro-responsive drug delivery from hydrogels. *J. Control. Release* **92**, 1–17 (2003).

344. Davidson, H. *et al.* Tetracycline tethered to titanium inhibits colonization by Gram-negative bacteria. *J. Biomed. Mater. Res. - Part B Appl. Biomater.* **103**, 1381–1389 (2015).

345. Jose, B., Antoci, V., Zeiger, A. R., Wickstrom, E. & Hickok, N. J. Vancomycin covalently bonded to titanium beads kills Staphylococcus aureus. *Chem. Biol.* **12**, 1041–1048 (2005).

346. Rottman, M., Goldberg, J. & Hacking, S. A. Titanium-Tethered Vancomycin Prevents Resistance to Rifampicin in Staphylococcus aureus in vitro. *PLoS One* **7**, e52883 (2012).

347. Tanihara, M., Suzuki, Y., Nishimura, Y., Suzuki, K. & Kakimaru, Y. Thrombin-sensitive peptide linkers for biological signal-responsive drug release systems. *Peptides* **19**, 421–425 (1998).

348. Yue, S. *et al.* Photo-triggered release of an antibiotic from an in situ forming hydrogel for antibacterial wound dressings. *Front. Bioeng. Biotechnol.* **4**, 626–34 (2016).

349. Shi, Y. *et al.* Light-triggered release of ciprofloxacin from an in situ forming click hydrogel for antibacterial wound dressings. *J. Mater. Chem. B* **3**, 8771–8774 (2015).

350. Chen, C. P. & Wickstrom, E. Self-protecting bactericidal titanium alloy surface formed by covalent bonding of daptomycin bisphosphonates. *Bioconjug. Chem.* **21**, 1978–1986 (2010).

351. Zhang, Z., Suner, S. S., Blake, D. A., Ayyala, R. S. & Sahiner, N. Antimicrobial activity and biocompatibility of slow-release hyaluronic acid-antibiotic conjugated particles. *Int. J. Pharm.* **576**, 119024 (2020).

352. Lequeux, I., Ducasse, E., Jouenne, T. & Thebault, P. Addition of antimicrobial properties to hyaluronic acid by grafting of antimicrobial peptide. *Eur. Polym. J.* **51**, 182–190 (2014).

353. Ketonis, C. *et al.* Antibiotic Modification of Native Grafts: Improving Upon Nature's Scaffolds. *Tissue Eng. Part A* **16**, 2041 (2010).

354. Jones, R. D., Jampani, H. B., Newman, J. L. & Lee, A. S. Triclosan: A review of effectiveness and safety in health care settings. *Am. J. Infect. Control* **28**, 184–196 (2000).

355. Heath, R. J. *et al.* Mechanism of triclosan inhibition of bacterial fatty acid synthesis. *J. Biol. Chem.* **274**, 11110–11114 (1999).

356. Alfhili, M. A. & Lee, M.-H. H. Triclosan: An Update on Biochemical and Molecular Mechanisms. *Oxid. Med. Cell. Longev.* **2019**, 1607304 (2019).

357. Assadian, O. *et al.* Minimum inhibitory (MIC) and minimum microbicidal concentration (MMC) of polihexanide and triclosan against antibiotic sensitive and resistant Staphylococcus aureus and Escherichia coli strains. *GMS Krankenhhyg. Interdiszip.* **6**, 006 (2011).

358. Escalada, M. G., Harwood, J. L., Maillard, J.-Y. & Ochs, D. Triclosan inhibition of fatty acid synthesis and its effect on growth of Escherichia coli and Pseudomonas aeruginosa. *J. Antimicrob. Chemother.* **55**, 879–882 (2005).

359. Russell, A. D. Whither triclosan? *J. Antimicrob. Chemother.* **53**, 693–695 (2004).

360. Davison, J. & Maillard, J. *Opinion on triclosan - Antimicrobial resistance*. *Scientific Committee on Consumer Safety* (2010).

361. Tang, Z. W. *et al.* Antiadhesive zwitterionic poly-(sulphobetaine methacrylate) brush coating functionalized with triclosan for high-efficiency antibacterial performance. *Prog. Org. Coatings* **97**, 277–287 (2016).

362. Chen, Z., Chisholm, B. J., Stafslien, S., He, J. & Patel, S. Novel, UV-curable coatings containing a tethered biocide: Synthesis, characterization, and antimicrobial activity. *J. Biomed. Mater. Res. Part A* **95A**, 486–494 (2010).

363. Wu, H. X. *et al.* Highly efficient antibacterial surface grafted with a triclosan-decorated poly(N-hydroxyethylacrylamide) brush. *ACS Appl. Mater. Interfaces* **7**, 7008–7015 (2015).

364. Park, S. H. *et al.* Triclosan-immobilized polyamide thin film composite membranes with enhanced biofouling resistance. *Appl. Surf. Sci.* **443**, 458–466 (2018).

365. Long, K. S. & Porse, B. T. A conserved chloramphenicol binding site at the entrance to the ribosomal peptide exit tunnel. *Nucleic Acids Res.* **31**, 7208–7215 (2003).

366. Wiest, D. B., Cochran, J. B. & Tecklenburg, F. W. Chloramphenicol Toxicity Revisited: A 12-Year-Old Patient With a Brain Abscess. *J. Pediatr. Pharmacol. Ther.* **17**, 182–188 (2012).

367. CLSI. *Performance Standards for Antimicrobial Susceptibility Testing*. (Clinical and Laboratory

Standards Institute, 2020).

368. Fernández, M. *et al.* Mechanisms of resistance to chloramphenicol in Pseudomonas putida KT2440. *Antimicrob. Agents Chemother.* **56**, 1001–1009 (2012).

369. Magoulas, G. E. *et al.* Synthesis and antimicrobial activity of chloramphenicol-polyamine conjugates. *Bioorganic Med. Chem.* **23**, 3163–3174 (2015).

370. Yacoby, I., Shamis, M., Bar, H., Shabat, D. & Benhar, I. Targeting antibacterial agents by using drug-carrying filamentous bacteriophages. *Antimicrob. Agents Chemother.* **50**, 2087–2097 (2006).

371. Hooper, D. C. Emerging mechanisms of fluoroquinolone resistance. *Emerg. Infect. Dis.* **7**, 337–341 (2001).

372. Anderson, V. R. & Perry, C. M. Levofloxacin: A review of its use as a high-dose, short-course treatment for bacterial infection. *Drugs* **68**, 535–565 (2008).

373. Jalvandi, J. *et al.* Polyvinyl alcohol composite nanofibres containing conjugated levofloxacin-chitosan for controlled drug release. *Mater. Sci. Eng. C* **73**, 440–446 (2017).

374. Lu, C. *et al.* Hyaluronic acid-based levofloxacin nanomicelles for nitric oxide-triggered drug delivery to treat bacterial infections. *Carbohydr. Polym.* **229**, 115479 (2020).

375. Zhu, Z. *et al.* Mechanical properties of regenerated Bombyx mori silk fibers and recombinant silk fibers produced by transgenic silkworms. *J. Biomater. Sci. Polym. Ed.* **21**, 395–411 (2010).

376. Parwe, S. P. *et al.* Synthesis of ciprofloxacin-conjugated poly (L-lactic acid) polymer for nanofiber fabrication and antibacterial evaluation. *Int. J. Nanomedicine* **9**, 1463–1477 (2014).

377. Schmidt, M. *et al.* Conjugation of ciprofloxacin with poly(2-oxazoline)s and polyethylene glycol via end groups. *Bioconjug. Chem.* **26**, 1950–1962 (2015).

378. Tenson, T., Lovmar, M. & Ehrenberg, M. The mechanism of action of macrolides, lincosamides and streptogramin B reveals the nascent peptide exit path in the ribosome. *J. Mol. Biol.* **330**, 1005–1014 (2003).

379. Menninger, J. R. Peptidyl transfer RNA dissociates during protein synthesis from ribosomes of Escherichia coli. *J. Biol. Chem.* **251**, 3392–3398 (1976).

380. Langsrud, S., Sundheim, G. & Holck, A. L. Cross-resistance to antibiotics of Escherichia coli adapted to benzalkonium chloride or exposed to stress-inducers. *J. Appl. Microbiol.* **96**, 201–208 (2004).

381. Morar, M., Pengelly, K., Koteva, K. & Wright, G. D. Mechanism and diversity of the erythromycin esterase family of enzymes. *Biochemistry* **51**, 1740–1751 (2012).

382. Fallah, F., Zargar, M., Yousefi, M. & Alam, A. N. Synthesis of the erythromycin-conjugated nanodendrimer and its antibacterial activity. *Eur. J. Pharm. Sci.* **123**, 321–326 (2018).

383. Bosnjakovic, A. *et al.* Poly(amidoamine) dendrimer-erythromycin conjugates for drug delivery to macrophages involved in periprosthetic inflammation. *Nanomedicine Nanotechnology, Biol. Med.* **7**, 284–294 (2011).

384. Wijma, R. A., Huttner, A., Koch, B. C. P., Mouton, J. W. & Muller, A. E. Review of the pharmacokinetic properties of nitrofurantoin and nitroxoline. *J. Antimicrob. Chemother.* **73**, 2916–2926 (2018).

385. El Sakka, N. & Gould, I. M. Role of old antimicrobial agents in the management of urinary

tract infection. *Expert Rev. Clin. Pharmacol.* **9**, 1047–1056 (2016).

386. Mirkovic, B. *et al.* Nitroxoline impairs tumor progression in vitro and in vivo by regulating cathepsin B activity. *Oncotarget* **6**, 19027–19042 (2015).

387. Chan-On, W. *et al.* Quinoline-based clioquinol and nitroxoline exhibit anticancer activity inducing FoxM1 inhibition in cholangiocarcinoma cells. *Drug Des. Devel. Ther.* **9**, 2033–2047 (2015).

388. Sobke, A. *et al.* The Urinary Antibiotic 5-Nitro-8-Hydroxyquinoline (Nitroxoline) Reduces the Formation and Induces the Dispersal of Pseudomonas aeruginosa Biofilms by Chelation of Iron and Zinc. *Antimicrob. Agents Chemother.* **56**, 6021–6025 (2012).

389. Antoci, V. *et al.* Vancomycin covalently bonded to titanium alloy prevents bacterial colonization. *J. Orthop. Res.* **25**, 858–866 (2007).

390. Sharma, P. C., Jain, A., Jain, S., Pahwa, R. & Yar, M. S. Ciprofloxacin: review on developments in synthetic, analytical, and medicinal aspects. *J. Enzyme Inhib. Med. Chem.* **25**, 577–589 (2010).

391. *NCTC ® Antimicrobial Resistance Reference Strains and Antimicrobial Susceptibility Testing Control Strains* . www.phe-culturecollections.org.uk.

392. Kugel, A. J. *et al.* Combinatorial materials research applied to the development of new surface coatings XII: Novel, environmentally friendly antimicrobial coatings derived from biocide-functional acrylic polyols and isocyanates. *J. Coatings Technol. Res.* **6**, 107–121 (2009).

393. Ding, C. & Li, Z. A review of drug release mechanisms from nanocarrier systems. *Mater. Sci. Eng. C* **76**, 1440–1453 (2017).

394. Bargh, J. D., Isidro-Llobet, A., Parker, J. S. & Spring, D. R. Cleavable linkers in antibody-drug conjugates. *Chem. Soc. Rev.* **48**, 4361–4374 (2019).

395. Larsen, E. M. & Johnson, R. J. Microbial esterases and ester prodrugs: An unlikely marriage for combating antibiotic resistance. *Drug Dev. Res.* **80**, 33–47 (2019).

396. Wagh, A., Song, H., Zeng, M., Tao, L. & Das, T. K. Challenges and new frontiers in analytical characterization of antibody-drug conjugates. *MAbs* **10**, 222–243 (2018).

397. Kumar, A. & Balbach, J. Real-time protein NMR spectroscopy and investigation of assisted protein folding. *Biochim. Biophys. Acta - Gen. Subj.* **1850**, 1965–1972 (2015).

398. Barclay, T., Ginic-Markovic, M., Johnston, M. R., Cooper, P. D. & Petrovsky, N. Analysis of the hydrolysis of inulin using real time 1H NMR spectroscopy. *Carbohydr. Res.* **352**, 117–125 (2012).

399. Bureš, F. Quaternary Ammonium Compounds: Simple in Structure, Complex in Application. *Top. Curr. Chem.* **377**, 1–21 (2019).

400. Jiao, Y. *et al.* Quaternary ammonium-based biomedical materials: State-of-the-art, toxicological aspects and antimicrobial resistance. *Prog. Polym. Sci.* **71**, 53 (2017).

401. Minbiole, K. P. C. *et al.* From antimicrobial activity to mechanism of resistance: the multifaceted role of simple quaternary ammonium compounds in bacterial eradication. *Tetrahedron* **72**, 3559–3566 (2016).

402. Morrison, K. R., Allen, R. A., Minbiole, K. P. C. & Wuest, W. M. More QACs, more questions: Recent advances in structure activity relationships and hurdles in understanding resistance

mechanisms. *Tetrahedron Lett.* **60**, 150935 (2019).

403. Xu, W. Z., Gao, G. & Kadla, J. F. Synthesis of antibacterial cellulose materials using a 'clickable' quaternary ammonium compound. *Cellulose* **20**, 1187–1199 (2013).

404. Asri, L. A. T. W. T. W. *et al.* A Shape-adaptive, Antibacterial-coating of immobilized Quaternary-ammonium compounds tethered on hyperbranched polyurea and its mechanism of action. *Adv. Funct. Mater.* **24**, 346–355 (2014).

405. Ganewatta, M. S. *et al.* Antibacterial and Biofilm-Disrupting Coatings from Resin Acid-Derived Materials. *Biomacromolecules* **16**, 3336–3344 (2015).

406. Lin, J., Qiu, S., Lewis, K. & Klibanov, A. M. Mechanism of bactericidal and fungicidal activities of textiles covalently modified with alkylated polyethylenimine. *Biotechnol. Bioeng.* **83**, 168–172 (2003).

407. Marks, M. A., Kalaitzidou, K. & Gutekunst, W. R. Synthesis and Characterization of Cationic Dendrimer-PDMS Hybrids. *Macromol. Rapid Commun.* **42**, 2000652 (2021).

408. Chris Zhisheng Chen, † *et al.* Quaternary Ammonium Functionalized Poly(propylene imine) Dendrimers as Effective Antimicrobials: Structure−Activity Studies. *Biomacromolecules* **1**, 473–480 (2000).

409. Dong, J. J. *et al.* Contact killing of Gram-positive and Gram-negative bacteria on PDMS provided with immobilized hyperbranched antibacterial coatings. *Langmuir* **35**, 14108–14116 (2019).

410. Hassan, M. M. Binding of a quaternary ammonium polymer-grafted-chitosan onto a chemically modified wool fabric surface: assessment of mechanical, antibacterial and antifungal properties. *RSC Adv.* **5**, 35497–35505 (2015).

411. Tiller, J. C. Antimicrobial Surfaces. *Adv. Polym. Sci.* **240**, 193–217 (2010).

412. Tiller, J. C., Lee, S. B., Lewis, K. & Klibanov, A. M. Polymer surfaces derivatized with poly(vinyl-N-hexylpyridinium) kill airborne and waterborne bacteria. *Biotechnol. Bioeng.* **79**, 465–71 (2002).

413. Gilbert, P. & Moore, L. E. Cationic antiseptics: diversity of action under a common epithet. *J. Appl. Microbiol.* **99**, 703–715 (2005).

414. Gozzelino, G., Tobar, D. E. R., Chaitiemwong, N., Hazeleger, W. & Beumer, R. Antibacterial activity of reactive quaternary ammonium compounds in solution and in nonleachable coatings. *J. Food Prot.* **74**, 2107–2112 (2011).

415. Xue, Y., Xiao, H. & Zhang, Y. Antimicrobial Polymeric Materials with Quaternary Ammonium and Phosphonium Salts. *Int. J. Mol. Sci.* **16**, 3626 (2015).

416. Cavallaro, A., Mierczynska, A., Barton, M., Majewski, P. & Vasilev, K. Influence of immobilized quaternary ammonium group surface density on antimicrobial efficacy and cytotoxicity. *Biofouling* **32**, 13–24 (2015).

417. Murata, H., Koepsel, R. R., Matyjaszewski, K. & Russell, A. J. Permanent, non-leaching antibacterial surfaces: How high density cationic surfaces kill bacterial cells. *Biomaterials* **28**, 4870–4879 (2007).

418. Kaur, R. & Liu, S. Antibacterial surface design – Contact kill. *Prog. Surf. Sci.* **91**, 136–153 (2016).

419. Tezvergil-Mutluay, A. *et al.* The inhibitory effects of quaternary ammonium methacrylates on soluble and matrix-bound MMPs. *J. Dent. Res.* **90**, 535–540 (2011).

420. Umer, D., Yiu, C. K. Y., Burrow, M. F., Niu, L. N. & Tay, F. R. Effect of a novel quaternary ammonium silane on dentin protease activities. *J. Dent.* **58**, 19–27 (2017).

421. Gill, S. E. & Parks, W. C. Metalloproteinases and their inhibitors: Regulators of wound healing. *Int. J. Biochem. Cell Biol.* **40**, 1334–1347 (2008).

422. Miot-Noirault, E. *et al.* Small rigid platforms functionalization with quaternary ammonium: Targeting extracellular matrix of chondrosarcoma. *Nanomedicine Nanotechnology, Biol. Med.* **10**, 1887–1895 (2014).

423. Miladi, I. *et al.* Doxycycline and its quaternary ammonium derivative for adjuvant therapies of chondrosarcoma. *Cancer Chemother. Pharmacol.* **80**, 517–526 (2017).

424. Moraes, I. Q. S. de *et al.* Inhibition of matrix metalloproteinases: a troubleshooting for dentin adhesion. *Restor. Dent. Endod.* **45**, (2020).

425. Zhang, Y., Chen, Y., Hu, Y., Huang, F. & Xiao, Y. Quaternary ammonium compounds in dental restorative materials. *Dent. Mater. J.* **37**, 183–191 (2018).

426. Hegstad, K. *et al.* Does the Wide Use of Quaternary Ammonium Compounds Enhance the Selection and Spread of Antimicrobial Resistance and Thus Threaten Our Health? *Microb. Drug Resist.* **16**, 91–104 (2010).

427. Buffet-Bataillon, S., Tattevin, P., Bonnaure-Mallet, M. & Jolivet-Gougeon, A. Emergence of resistance to antibacterial agents: the role of quaternary ammonium compounds—a critical review. *Int. J. Antimicrob. Agents* **39**, 381–389 (2012).

428. Oh, S. *et al.* Microbial community degradation of widely used quaternary ammonium disinfectants. *Appl. Environ. Microbiol.* **80**, 5892–5900 (2014).

429. Jennings, M. C., Minbiole, K. P. C. & Wuest, W. M. Quaternary Ammonium Compounds: An Antimicrobial Mainstay and Platform for Innovation to Address Bacterial Resistance. *ACS Infect. Dis.* **1**, 288–303 (2015).

430. Elena, P. & Miri, K. Formation of contact active antimicrobial surfaces by covalent grafting of quaternary ammonium compounds. *Colloids Surf B Biointerfaces* **169**, 195–205 (2018).

431. Hoven, V. P., Tangpasuthadol, V., Angkitpaiboon, Y., Vallapa, N. & Kiatkamjornwong, S. Surface-charged chitosan: Preparation and protein adsorption. *Carbohydr. Polym.* **68**, 44–53 (2007).

432. Pei, A., Butchosa, N., Berglund, L. A. & Zhou, Q. Surface quaternized cellulose nanofibrils with high water absorbency and adsorption capacity for anionic dyes. *Soft Matter* **9**, 2047–2055 (2013).

433. Xu, W. Z., Gao, G. & Kadla, J. F. Synthesis of antibacterial cellulose materials using a “clickable” quaternary ammonium compound. *Cellul. 2013 203* **20**, 1187–1199 (2013).

434. Jenkins, L. M. & Donald, A. M. Use of the environmental scanning electron microscope for the observation of the swelling behaviour of cellulosic fibres. *Scanning* **19**, 92–97 (1997).

435. Zhong, Z. & Xiao, C. Fabric composition testing. in *Fabric Testing* (ed. Hu, J.) 48–89 (Woodhead Publishing, 2008).

436. Yuan, Y. & Lee, T. R. Contact Angle and Wetting Properties. *Springer Ser. Surf. Sci.* **51**, 3–34

(2013).

437. Widhe, M. *et al.* Recombinant spider silk as matrices for cell culture. *Biomaterials* **31**, 9575–85 (2010).

438. Cheng, Y., Feng, G. & Moraru, C. I. Micro-and nanotopography sensitive bacterial attachment mechanisms: A review. *Front. Microbiol.* **10**, 191 (2019).

439. Krasowska, A. & Sigler, K. How microorganisms use hydrophobicity and what does this mean for human needs? *Front. Cell. Infect. Microbiol.* **4**, 112 (2014).

440. Netuschil, L., Auschill, T. M., Sculean, A. & Arweiler, N. B. Confusion over live/dead stainings for the detection of vital microorganisms in oral biofilms - which stain is suitable? *BMC Oral Health* **14**, 2 (2014).

441. Boulos, L., Prévost, M., Barbeau, B., Coallier, J. & Desjardins, R. LIVE/DEAD®BacLight™: application of a new rapid staining method for direct enumeration of viable and total bacteria in drinking water. *J. Microbiol. Methods* **37**, 77–86 (1999).

442. Corte, L., Pierantoni, D. C., Tascini, C., Roscini, L. & Cardinali, G. Biofilm Specific Activity: A Measure to Quantify Microbial Biofilm. *Microorganisms* **7**, (2019).

443. Bakke, R., Kommedal, R. & Kalvenes, S. Quantification of biofilm accumulation by an optical approach. *J. Microbiol. Methods* **44**, 13–26 (2001).

444. Pierantoni, D. C., Corte, L., Roscini, L. & Cardinali, G. High-throughput rapid and inexpensive assay for quantitative determination of low cell-density yeast cultures. *Microorganisms* **7**, 32 (2019).

445. Dhale, R. P., Ghorpade, M. V. & Dharmadhikari, C. A. Comparison of Various Methods Used to Detect Biofilm Production of Candida Species. *J. Clin. Diagn. Res.* **8**, DC18 (2014).

446. Pantanella, F. *et al.* BioTimer Assay, a new method for counting Staphylococcus spp. in biofilm without sample manipulation applied to evaluate antibiotic susceptibility of biofilm. *J. Microbiol. Methods* **75**, 478–84 (2008).

447. Rosa, L. *et al.* Biotimer assay: A reliable and rapid method for the evaluation of central venous catheter microbial colonization. *J. Microbiol. Methods* **143**, 20–25 (2017).

448. Rosa, L. *et al.* BioTimer assay as complementary method to vortex-sonication-vortex technique for the microbiological diagnosis of implant associated infections. *Sci. Reports 2019 91* **9**, 1–10 (2019).

449. Travnickova, E. *et al.* Resazurin assay for assessment of antimicrobial properties of electrospun nanofiber filtration membranes. *AMB Express 2019 91* **9**, 1–11 (2019).

450. M, E. S. Z., S, B. & K, M. Molecular study of resistance of Staphylococcus aureus to antiseptic quaternary ammonium compounds. *J. Glob. Antimicrob. Resist.* **17**, 94–97 (2019).

451. Tabata, A. *et al.* Correlation between Resistance of Pseudomonas aeruginosa to Quaternary Ammonium Compounds and Expression of Outer Membrane Protein OprR. *Antimicrob. Agents Chemother.* **47**, 2093 (2003).

452. Webb, K., Hlady, V. & Tresco, P. A. Relative importance of surface wettability and charged functional groups on NIH 3T3 fibroblast attachment, spreading, and cytoskeletal organization. *J. Biomed. Mater. Res.* **41**, 422 (1998).

Appendix 1. Media compositions and equipment

Procedure	Equipment
Centrifugation of volumes over 100mL	Beckman Avanti J25 with JA10 rotor
Centrifugation of volumes up to 30ml, >25000 g	Beckman Avanti J25 with JA25.50 rotor
Centrifugation of volumes up to 30ml < 5000 g	Beckman Spinchon 15 with S4180 rotor
Centrifugation of volumes up to 1.5ml	Heraeus Biofuge Primo benchtop centrifuge
Plate incubation	Binder KB115 at 37 °C
Shake flask incubation	Lab Companion IS 971R
Analytical microbalance	Sartorius R160P analytical balance
Cuvette spectrophotometry (for OD600)	WPA UV 1101 photometer
Microvolume spectrophotometry	TECAN SPARK multimode microplate reader
Gel electrophoresis	Biorad Mini-PROTEAN Tetra Cell system with Biorad PowerPac™ Basic Power Supply
Gel visualisation	Syngene G.Box Chemi 16 Gel Doc System

SDS PAGE components	
15% (w/v) resolving gel (10ml)	
Water	2.3 ml
30% w/v acrylamide	5 ml
1.5M Tris pH8.8	2.5 ml
10% w/v SDS	0.1 ml
10% w/v ammonium persulfate	0.1 ml
TEMED	0.004 ml
5% stacking gel (5ml)	
Water	3.4 ml
30% w/v acrylamide	0.83 ml
1.5M Tris pH8.8	0.63 ml
10% w/v SDS	0.05 ml
10% w/v ammonium persulfate	0.05 ml
TEMED	0.005 ml
10x running buffer (diluted to 1x before use)	
Tris	30 g
Glycine	144 g
SDS	10 g
MilliQ ultrapure water	to 1 L
4x reducing loading buffer (stock)	
Double distilled glycerol	2 ml
1M Tris pH6.8	1 ml
Bromophenol blue	0.01 mg
DTT	0.3 g
SDS	0.4 g
MilliQ ultrapure water	to 5 ml

M9 minimal media	
Biomass growth	
10x M9 salt solution (Sigma) pH7	100 ml

20% w/v glucose	30 ml
Methionine	0.1 g
1 M $MgSO_4$	1 ml
1 M $CaCl_2$	0.3 ml
1 mg/ml biotin + 1 mg/ml thiamine suspension	1 ml
100x Trace element solution	10 ml
Kanamycin (50 mg/ml)	1 ml
MilliQ ultrapure water	to 1 L

Induction

10x M9 salt solution (Sigma) pH 7	100 ml
20% w/v glucose	20 ml
80% v/v sterile glycerol	10 ml
1 M $MgSO_4$	1 ml
1 M $CaCl_2$	0.3 ml
1 mg/ml biotin + 1 mg/ml thiamine suspension	1 ml
100x Trace element solution	10 ml
Kanamycin (50 mg/ml)	1 ml
1 M IPTG	1 ml
L-azidohomoalanine	0.1 g
MilliQ ultrapure water	to 1 L

100X Trace element solution pH 7.5

EDTA	5 g
$FeCl_3$-$6H_2O$	0.83 g
$ZnCl_2$	84 mg
$CuCl_2$-2H2O	13 mg
$CoCl_2$-2H2O	10 mg
H_3BO_3	10 mg
$MnCl_2$-4H2O	1.6 mg

Protein purification buffers

Buffer A for Ni IMAAC	20 mM Tris pH 8, 300 mM NaCl, 30 mM imidazole
Buffer B for Ni IMAAC	20 mM Tris pH 8, 300 mM NaCl, 700 mM imidazole
Buffer A Co^{2+}	20 mM Tris pH 8, 300 mM NaCl
Buffer B Co^{2+}	20 mM Tris pH 8, 300 mM NaCl, 300 mM imidazole
Buffer B Q	20 mM Tris pH 8, 1 M NaCl

Appendix 2. Clickable ligand synthesis data

All chemical syntheses were carried out by Dr Tom Armstrong except clickable levofloxacin that was synthesised by Dr Francesco Zamberlan.

Scheme S.1. General synthesis procedure J (see methods below).R – triclosan, nitroxoline; a -5-hexynoic acid, DCC, DMAP, CH_2Cl_2, r.t., 18h.

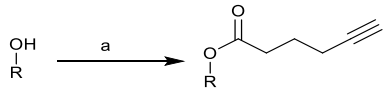

5-Chloro-2-(2,4-dichlorophenoxy)phenyl hex-5-ynoate (208) [releasable triclosan]

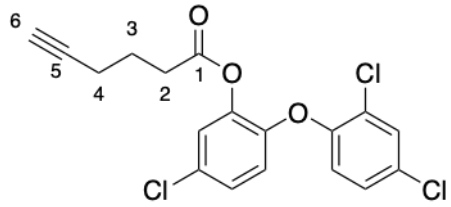

The title compound was prepared according to General Procedure J from 5-Hexynoic acid (1.00 g, 8.91 mmol), DCC (2.02 g, 9.81 mmol), Triclosan (2.84 g, 9.81 mmol) and DMAP (54 mg, 5 mol%). Purification was performed by flash column chromatography (Hexane/EtOAc, 9:1) to yield the title compound as a dense, clear oil (2.90 g, 85%). ^{1}H NMR (400 MHz, $CDCl_3$) δ 7.47 (d, *J* = 2.5 Hz, 1H, ArH), 7.25 – 7.15 (m, 3H, ArH), 6.87 (dd, *J* = 8.8, 4.7 Hz, 2H, ArH), 2.66 (t, *J* = 7.4 Hz, 2H, H-2), 2.29 (td, *J* = 6.9, 2.6 Hz, 2H, H-4), 2.01 (t, *J* = 2.7 Hz, 1H, H-6), 1.89 (p, *J* = 7.1 Hz, 2H, H-3). ^{13}C NMR (101 MHz, $CDCl_3$) δ 175.7 (C-1), 151.5 (ArC), 146.1 (ArC), 141.8 (ArC), 130.5 (ArC), 129.5 (ArC), 129.3 (ArC), 128.2 (ArC), 127.0 (ArC), 125.8 (ArC), 124.4 (ArC), 120.3 (ArC), 118.4 (ArC), 83.9 (C-5), 71.4 (C-6), 32.4 (C-2), 23.4 (C-3), 17.7 (C-4). HRMS (ESI) *m/z* calcd for $C_{18}H_{13}O_3{}^{35}Cl3Na$ [M + Na]+, 404.9822 found 404.9818.

5-Nitroquinolin-8-yl hex-5-ynoate (209) [nitroxoline]

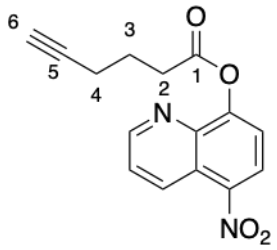

The title compound was prepared according to General Procedure J from 5-Hexynoic acid (0.64 g, 5.78 mmol), DCC (1.21 g, 5.78 mmol), Nitroxoline (1.00 g, 5.26 mmol) and DMAP (32 mg, 5 mol%). Purification was performed by flash column chromatography (Hexane/EtOAc, 6:4) to yield the title compound as a yellow solid (1.05 g, 70%). ^{1}H NMR (400 MHz, $CDCl_3$) δ 9.10 (dd, *J* = 8.9, 1.6 Hz, 1H, ArH), 9.03 (dd, *J* = 4.1, 1.6 Hz, 1H, ArH), 8.47 (d, *J* = 8.5 Hz, 1H, ArH), 7.70 (dd, *J* = 8.9, 4.1 Hz, 1H, ArH), 7.57 (d, *J* = 8.5 Hz, 1H, ArH), 3.00 (t, *J* = 7.3 Hz, 2H, CH2, H-2), 2.49 (td, *J* = 6.9, 2.7 Hz, 2H, H-4), 2.16 – 2.10 (m, 2H, H-3), 2.07 (t, *J* = 2.6 Hz, 1H, H-6). ^{13}C NMR (101 MHz, $CDCl_3$) δ 171.2 (C-1), 152.8 (ArC), 151.3 (ArC), 142.9 (ArC), 140.9 (ArC), 132.4 (ArC), 125.3 (ArC), 124.5 (ArC), 122.7 (ArC), 119.8 (ArC), 83.2 (C-5), 69.4 (C-6), 32.9 (C-2), 23.7 (C-3), 17.8 (C-4). HRMS (ESI) *m/z* calcd for $C_{15}H_{13}N_2O_4Na$ [M + Na]+, 285.0870, found 285.0876.

Scheme S.2. Synthesis of 'clickable' Ciprofloxacin

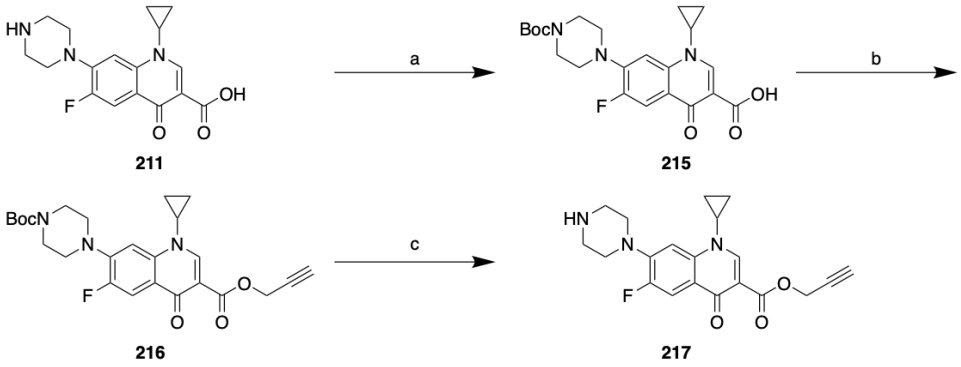

a) (Boc)2O, NaOH (aq), THF, r.t., 18 h, quant. b) Propargyl bromide, K2CO3, DMF, 130 ºC, 80%. c) TFA, CH2Cl2, r.t., 30 min, 46%

***N*-Boc Ciprofloxacin (215)**

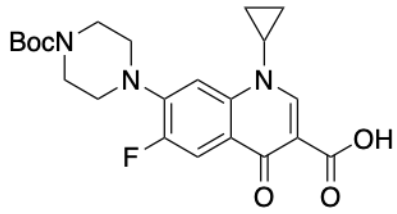

Ciprofloxacin (1.00 g, 3.02 mmol) was suspended in THF (25 mL). Upon addition of 1M NaOH (aq) (6.00 mL, 6.00 mmol) a clear solution formed to which $(Boc)_2O$ (725 mg, 3.31 mmol) was added. The reaction mixture was then allowed to stir at r.t. for 18 h. The organic solvent was removed under reduced pressure and the resulting aqueous phase was acidified to pH 3-4 using 1M HCl (aq). The resulting solid was isolated by filtration and washed with EtOAc before being dried under reduced pressure to yield the title compound as a white solid (1.42 g, quant.) which was used without further purification. ^{1}H NMR (400 MHz, $CDCl_3$:MeOD, 2:1) δ 9.25 (s, 1H, CH), 8.44 (d, *J* = 12.9 Hz, 1H, ArH), 7.98 – 7.91 (m, 1H, ArH), 4.20 – 4.09 (m, 5H, NCH_2), 3.87 – 3.78 (m, 4H, CH_2), 1.98 (s, 9H, $(CH_3)_3$), 1.95 – 1.89 (m, 2H,

CH_2), 1.75 – 1.68 (m, 2H, CH_2). ^{13}C NMR (101 MHz, $CDCl_3$:MeOD, 2:1) δ 177.07 (CO), 167.92 (CO), 154.90 (CO), 152.49 (*C*=CH), 147.80 (CH), 145.88 (d, *J* = 10.3 Hz, ArC), 139.21 (ArC), 119.82 (d, *J* = 8.0 Hz, ArC), 112.11 (d, *J* = 23.6 Hz, ArCF), 107.35 (ArC), 105.40 (d, *J* = 3.4 Hz, ArC), 80.72 (C), 49.57 (CH_2), 35.61 (CH), 28.11 ((CH_3)$_3$), 7.99 (CH_2). ^{19}F NMR (376 MHz, CDCl3) δ -117.05 (dd, *J* = 12.9, 7.0 Hz). HRMS (ESI) m/z calcd for $C_{22}H_{26}O_5N_3FNa$ $[M + Na]^+$, 454.1749, found 454.1760

_N_-Boc Ciprofloxacin propargyl ester (216)

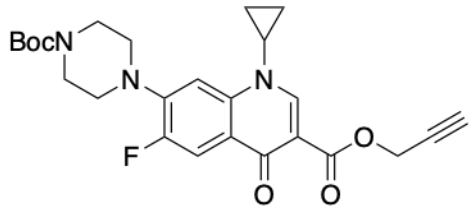

Acid **215** (400 mg, 0.93 mmol) was suspended in DMF (20 mL) followed by the sequential addition of K_2CO_3 (256 mg, 1.86 mmol) and propargyl bromide (165 mg, 1.40 mmol). The reaction mixture was heated to reflux and the resulting solution was stirred for 18 h. The reaction mixture was allowed to cool to 0 ºC and diluted with H_2O (20 mL) before being extracted with EtOAc (3 × 30 mL). The combined organic layers were then washed with $NaHCO_3$ (aq), H_2O and Brine (30 mL each). The organic layer was dried over $MgSO_4$, filtered and concentrated under reduced pressure. Purification was performed by flash column chromatography (0 -> 100%, Hexane/EtOAc) to yield the title compound as a white solid (357 mg, 80%) ^1H NMR (400 MHz, $CDCl_3$) δ 8.51 (s, 1H, CH), 7.97 (d, *J* = 13.1 Hz, 1H, ArH), 7.28 – 7.22 (m, 1H, ArH), 4.90 (d, *J* = 2.5 Hz, 2H, C*H*$_2$CCH), 3.68 – 3.60 (m, 4H, NCH_2), 3.42 (dt, *J* = 7.0, 3.2 Hz, 1H, CH), 3.21 (dd, *J* = 6.1, 4.0 Hz, 4H, CH_2), 2.48 (t, *J* = 2.4 Hz, 1H, CH_2CCH), 1.49 (s, 9H, (CH_3)$_3$), 1.36 – 1.28 (m, 2H, CH_2), 1.18 – 1.11 (m, 2H, CH_2). ^{13}C NMR (101 MHz, CDCl3) δ 172.8 (CO), 164.6 (CO), 154.6 (CO), 148.6 (CH), 144.4 (ArC), 137.9 (ArC), 113.4 (d, J = 22.8 Hz, ArCF), 109.4 (ArC), 105.1 (ArC), 80.2 (C), 78.1 (C), 74.8 (CH_2), 52.1 (CH), 49.9 (CH_2), 34.7 (CH), 28.4 ((CH_3)$_3$), 8.2 (CH_2). ^{19}F NMR (376 MHz,

$CDCl_3$) δ -123.50 (dd, *J* = 13.1, 7.0 Hz). HRMS (ESI) m/z calcd for $C_{25}H_{28}O_5N_3F^3Na$ $[M + Na]^+$, 492.1905, found 492.1915

Ciprofloxacin propargyl ester (217)

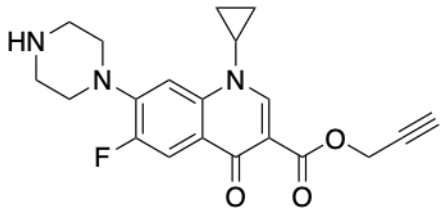

Carbamate **216** (47 mg, 0.10 mmol) was dissolved in a 9:1 mixture of CH_2Cl_2:TFA (20 mL). The reaction mixture was allowed to stir for 30 min before being concentrated under reduced pressure. The residue was suspended in $NaHCO_3$ and the resulting solid was isolated by filtration to yield the title compound as an off-white solid (17 mg, 46%). ^{1}H NMR (400 MHz, $CDCl_3$) δ 8.53 (s, 1H, CH), 7.99 (d, *J* = 13.3 Hz, 1H, ArH), 7.25 (d, *J* = 6.9 Hz, 2H, ArH, under solvent peak), 4.90 (d, *J* = 2.4 Hz, 2H, CH_2), 3.43 (tt, *J* = 7.1, 4.0 Hz, 1H, CH), 3.31 – 3.20 (m, 4H, CH_2), 3.09 (dd, *J* = 6.3, 3.4 Hz, 4H, CH_2), 2.48 (t, *J* = 2.4 Hz, 1H, CH), 1.35 – 1.29 (m, 2H, CH_2), 1.17 – 1.11 (m, 2H, CH_2). ^{13}C NMR (101 MHz, $CDCl_3$) δ 172.9 (CO), 164.8 (CO), 152.3 (*C*=CH), 148.5 (CH), 145.1 (d, *J* = 10.4 Hz, ArC), 138.0, 122.9 (d, *J* = 7.0 Hz, ArC), 113.3 (d, *J* = 23.2 Hz), 109.3, 104.8 (d, *J* = 3.2 Hz). 78.2 (C), 74.7 (CH), 52.1 (CH_2), 51.1 (*C*H_2CCH), 46.0 (CH_2), 34.6 (CH), 8.2 (CH_2). ^{19}F NMR (376 MHz, CDCl3) δ -123.3 (dd, *J* = 13.3, 7.1 Hz). HRMS (ESI) m/z calcd for $C_{20}H_{20}O_3N_3FNa$ $[M + Na]^+$, 392.1381, found 392.1397

Scheme S.3. Synthesis of 'clickable' Chloramphenicol

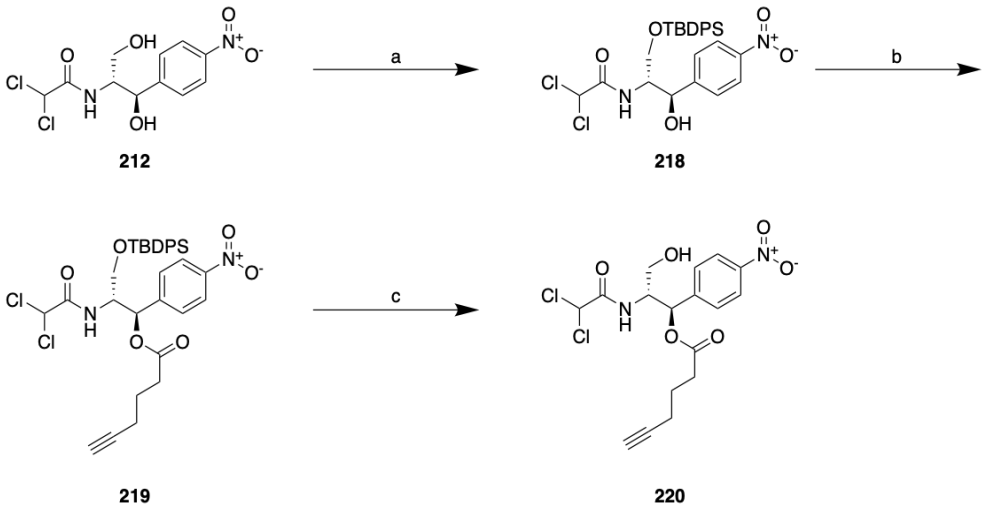

a) TBDPSCl, Imidazole, DMF, r.t., 18 h, 82%. b) 5-Hexynoic acid, DCC, DMAP (5 mol%), CH2Cl2, r.t., 18 h, 83%. c) TBAF, THF, r.t., 18 h, 70%

N-((1*R*,2*R*)-3-((*tert*-Butyldiphenylsilyl)oxy)-1-hydroxy-1-(4-nitrophenyl)propan-2-yl)-2,2-dichloroacetamide (218)

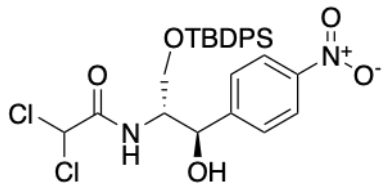

Chloramphenicol (3.00 g, 9.30 mmol) was dissolved in anhydrous DMF (50 mL). Imidazole (0.94 g, 13.90 mmol) and TBDPSCl (2.81 g, 10.20 mmol) were added sequentially and the reaction mixture was stirred at r.t. for 18 h. The reaction mixture was then diluted with H_2O (50 mL) before being extracted with EtOAc (3 × 100 mL). The combined organic layers were then sequentially washed with $NaHCO_3$ (aq), H_2O and Brine (100 mL). The organic layer was then dried over $MgSO_4$, filtered and concentrated under reduced pressure. Purification was performed by flash column chromatography (CH_2Cl_2/MeOH, 98:2) to yield the title compound as a dense yellow oil which crystallised upon standing (6.40 g, 82%).

^{1}H NMR (400 MHz, $CDCl_3$) δ 8.20 – 8.13 (m, 2H, ArH), 7.68 (dq, *J* = 6.7, 1.3 Hz, 4H, ArH), 7.58 – 7.36 (m, 8H, ArH), 5.79 (s, 1H, $CHCl_2$), 5.31 (d, *J* = 2.8 Hz, 1H, C*H*OH), 4.21 (dtd, *J* = 9.0, 4.6, 2.9 Hz, 1H, CH), 3.92 (d, *J* = 4.6 Hz, 2H, CH_2), 1.13 (s, 9H, $(CH_3)_3$). ^{13}C NMR (101 MHz, $CDCl_3$) δ 171.3 (NCO), 148.2 (ArC), 147.5 (ArC), 135.6 (ArC), 135.5 (ArC), 128.1 (ArC), 128.0 (ArC), 126.8 (ArC), 123.5 (ArC), 71.9 (CHOH), 66.2 ($CHCl_2$), 63.8 (CH_2), 55.9 (CH), 27.5 $(CH_3)_3$), 19.2 (C). HRMS (ESI) *m/z* calcd for $C_{27}H_{30}O_6N_2{}^{35}Cl_2Si$ [M + H]+, 561.1373, found 561.1377.

(1*R*,2*R*)-3-((*tert*-Butyldiphenylsilyl)oxy)-2-(2,2-dichloroacetamido)-1-(4-nitrophenyl)propyl hex-5-ynoate (219)

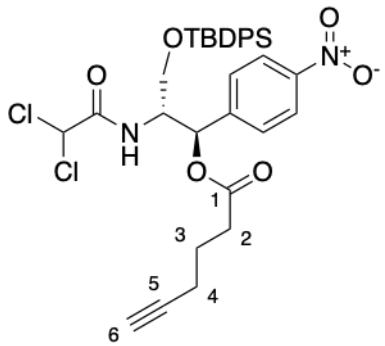

The title compound was prepared according to General Procedure J from 5-Hexynoic acid (1.07 g, 9.54 mmol), DCC (2.15 g, 10.42 mmol), **218** (5.00 g, 8.92 mmol) and DMAP (51 mg, 5 mol%). Purification was performed by flash column chromatography (CH_2Cl_2/MeOH, 98:2) to yield the title compound as a dense colourless oil (4.80 g, 83%). ^{1}H NMR (400 MHz, $CDCl_3$) δ 8.16 – 8.09 (m, 2H, ArH), 7.57 (ddd, *J* = 8.1, 3.1, 1.5 Hz, 4H, ArH), 7.49 – 7.33 (m, 8H, ArH), 6.20 (d, *J* = 7.9 Hz, 1H, C*H*OH), 5.88 (s, 1H, $CHCl_2$), 4.35 (dddd, *J* = 9.5, 7.6, 4.4, 2.8 Hz, 1H, CH), 3.67 (dd, *J* = 10.8, 4.4 Hz, 1H, CH_2'), 3.41 (dd, *J* = 10.8, 2.8 Hz, 1H, CH_2), 2.50 (td, *J* = 7.3, 1.7 Hz, 2H, H-2), 2.22 (tdd, *J* = 6.6, 2.7, 1.3 Hz, 2H, H-4), 1.95 (t, *J* = 2.7 Hz, 1H, H-6), 1.81 (p, *J* = 7.1 Hz, 2H, H-3), 1.13 (s, 9H). ^{13}C NMR (101 MHz, $CDCl_3$) δ 172.1 (NCO), 164.6 (C-1), 147.6 (ArC), 143.9 (ArC), 135.6 (ArC), 135.5 (ArC), 130.3 (ArC), 128.1 (ArC), 128.0 (ArC), 123.2

(ArC), 82.9 (C-5), 72.5 (C-6), 69.5 (CO), 65.2 ($CHCl_2$), 61.8 (CH_2), 54.3 (CH), 33.1 (C-2), 26.4 ($(CH_3)_3$), 23.2 (C-3), 17.7 (C). HRMS (ESI) *m/z* calcd for $C_{33}H_{36}O_7N_2{}^{35}Cl_2Si$ [M + H]+, 655.1792, found 655.1777.

(1*R*,2*R*)-2-(2,2-Dichloroacetamido)-3-hydroxy-1-(4-nitrophenyl)propyl hex-5-ynoate (220)

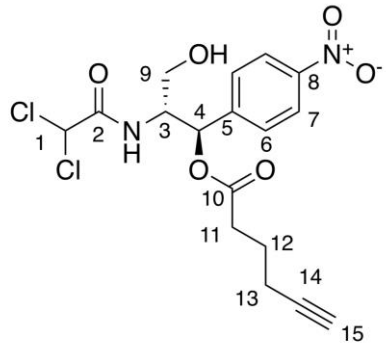

Compound **219** (4.80 g, 7.33 mmol) was dissolved in anhydrous THF. TBAF (1M solution in THF, 10.70 mL, 10.70 mmol) was added dropwise and the reaction mixture was stirred for 18 h. The reaction mixture was then diluted with saturated aqueous NH_4Cl and Et_2O (50 mL), the layers were separated and the aqueous layer was washed with Et_2O (3 × 50 mL). The combined organic layers were dried over $MgSO_4$, filtered and concentrated under reduced pressure. Purification was performed by flash column chromatography (CH_2Cl_2/MeOH, 98:2) to yield the title compound as a dense yellow oil (1.95 g, 70%). ^{1}H NMR (400 MHz, $CDCl_3$) δ 8.27 – 8.22 (m, 2H, ArH-7), 7.61 – 7.56 (m, 2H, ArH-6), 6.89 (d, *J* = 8.9 Hz, 1H, NH), 5.79 (s, 1H, H-1), 5.11 (d, *J* = 2.4 Hz, 1H, H-4), 4.50 (dd, *J* = 10.9, 7.0 Hz, 1H, H-9), 4.47 – 4.39 (m, 1H, H-3), 4.25 (dd, *J* = 10.9, 6.1 Hz, 1H, H-9'), 2.57 (t, *J* = 7.4 Hz, 2H, H-11), 2.32 (td, *J* = 6.9, 2.7 Hz, 2H, H-13), 2.02 (t, *J* = 2.6 Hz, 1H, H-15), 1.89 (p, *J* = 7.1 Hz, 2H, H-12). ^{13}C NMR (101 MHz, $CDCl_3$) δ 173.5 (C-10), 164.4 (C-2), 147.7 (ArC), 147.0 (ArC), 126.8 (C-8), 123.8 (C-7), 82.9 (C-14), 70.8 (C-15), 69.5 (C-4), 66.0 (C-1), 62.6 (C-9), 54.1 (C-3), 32.6 (C-11), 23.3 (C-12), 17.8 (C-13). HRMS (ESI) *m/z* calcd for $C_{17}H_{18}O_6{}^{35}Cl_2N2Na$ $[M + Na]^+$, 439.0434, found 439.0432.

Scheme 2.4. Selective functionalisation of Erythromycin.

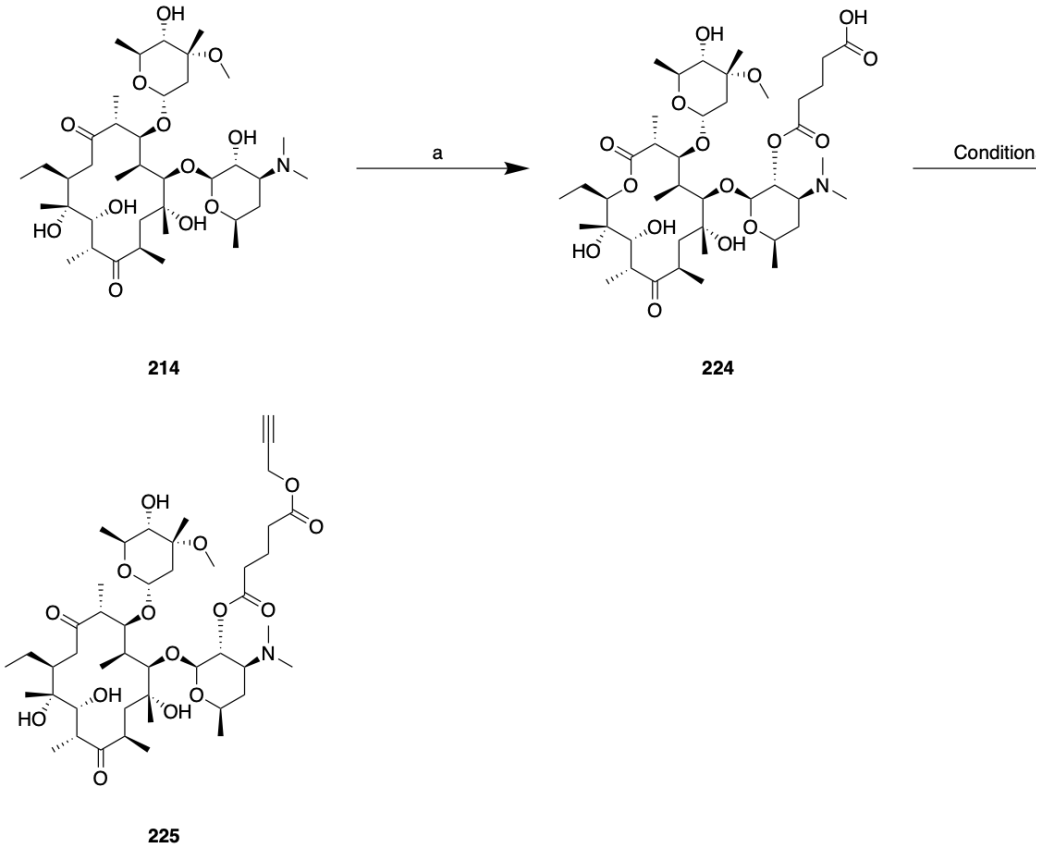

a) Glutaric anhydride, Et3N, DMF, r.t., 3 d,

Erythromycin-2'-glutarate (224)

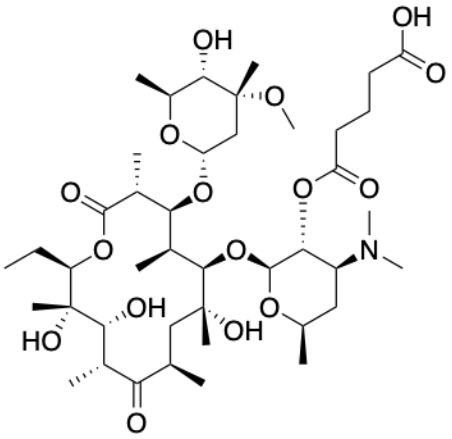

The title compound was prepared using a modified version of the procedure detailed by Bosniakovic *et al*. Erythromycin (500 mg, 0.68 mmol) and glutaric anhydride (155 mg, 1.36 mmol) were dissolved in DMF (10 mL) and placed under a nitrogen atmosphere. Et_3N (137 mg, 1.36 mmol) was added and the reaction mixture was allowed to stir for 72 h at r.t. before being concentrated under reduced pressure. Purification was performed by flash column chromatography (MeOH/EtOAc/Hexane, 5:2:2) to yield the title compound as a white solid (435 mg, 75%) ^{1}H NMR (400 MHz, $CDCl_3$) δ 5.02 (dd, *J* = 10.9, 2.3 Hz, 1H), 4.89 – 4.84 (m, 2H), 4.58 (d, *J* = 7.2 Hz, 1H), 3.91 (dd, *J* = 12.9, 8.0 Hz, 2H), 3.77 (s, 1H), 3.50 (ddd, *J* = 26.2, 10.5, 4.7 Hz, 2H), 3.35 (s, 3H), 3.03 (dd, *J* = 14.1, 8.0 Hz, 3H), 2.83 (td, *J* = 15.9, 13.4, 5.8 Hz, 1H), 2.64 (t, *J* = 9.1 Hz, 1H), 2.41 (s, 6H), 2.36 – 2.19 (m, 4H), 2.01 – 1.66 (m, 7H), 1.62 – 1.50 (m, 2H), 1.41 (s, 3H), 1.28 – 1.06 (m, 23H), 0.89 (d, *J* = 7.4 Hz, 3H), 0.82 (t, *J* = 7.4 Hz, 3H). ^{13}C NMR (101 MHz, $CDCl_3$) δ 175.5, 172.4, 100.4, 96.1, 83.6, 79.7, 77.9, 76.9, 74.8, 74.6, 72.8, 70.8, 69.0, 67.6, 65.7, 62.5, 49.5, 45.1, 44.8, 39.3, 39.0, 38.1, 37.9, 35.9, 35.0, 34.8, 29.0, 27.0, 21.5, 21.2, 18.7, 18.2, 16.4, 16.0, 12.0, 10.6, 9.2. HRMS (ESI) *m/z* calcd for $C_{42}H_{74}NO_{16}$ $[M + H]^+$, 848.5002, found 848.5055.

Erythromycin-2'-glutarate propargyl ester (225)

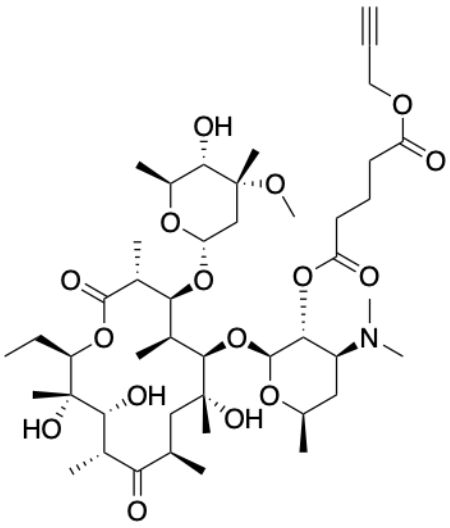

Carboxylic acid **224** (200 mg, 0.23 mmol) was dissolved in DMF (10 mL) followed by the addition of K_2CO_3 (65 mg, 0.46 mmol) and propargyl bromide (28 mg, 0.23 mmol). The reaction mixture was allowed to stir for 18 h at r.t. before being concentrated under reduced pressure. Purification was perfumed by flash column chromatography (5:2:2, MeOH/Hexane/EtOAc) to yield the title compound as a white solid (180 mg, 88%). ^{1}H NMR (400 MHz, DMSO) δ 5.10 (dd, *J* = 10.7, 2.5 Hz, 1H), 4.78 – 4.48 (m, 4H), 4.41 (d, *J* = 7.5 Hz, 1H), 4.27 (s, 1H), 4.00 (dd, *J* = 9.4, 6.2 Hz, 1H), 3.91 (d, *J* = 9.2 Hz, 1H), 3.85 (d, *J* = 5.4 Hz, 1H), 3.72 (dt, *J* = 9.0, 4.5 Hz, 2H), 3.53 (t, J = 2.5 Hz, 1H), 3.44 (d, J = 6.5 Hz, 1H), 3.24 (s, 3H), 2.96 – 2.92 (m, 1H), 2.88 – 2.75 (m, 3H), 2.63 (td, *J* = 15.6, 15.2, 3.3 Hz, 1H), 2.46 – 2.22 (m, 6H), 2.14 (s, 5H), 1.93 – 1.65 (m, 6H), 1.63 – 1.47 (m, 2H), 1.30 – 0.96 (m, 27H), 0.84 (d, *J* = 7.4 Hz, 3H), 0.76 (t, *J* = 7.4 Hz, 3H). ^{13}C NMR (101 MHz, DMSO) δ 175.19, 172.30, 99.57, 95.18, 78.90, 77.96, 77.80, 76.22, 75.16, 73.73, 73.19, 71.82, 67.52, 65.40, 63.06, 52.00, 49.27, 44.58, 36.26, 35.33, 33.48, 32.75, 32.23, 31.25, 29.77, 26.90, 21.70, 21.59, 21.40, 20.36, 19.01, 18.75, 17.72, 15.97, 12.06, 11.14, 9.46. HRMS (ESI) *m/z* calcd for $C_{45}H_{76}NO_{16}$ $[M + H]^+$, 886.5159, found 886.5194.

Scheme .52. Synthesis of quaternary ammonium salts

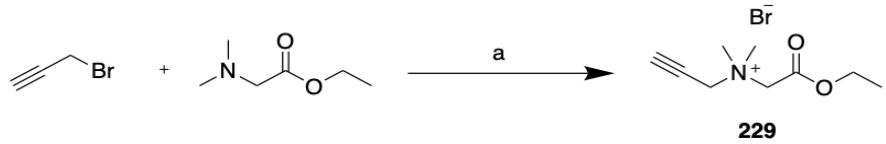

a) THF, r.t., 18 h, 96%

Note: three different counterions were used (Br, I, tosylate)

***N*-(2-Ethoxy-2-oxoethyl)-N,N- dimethylprop-2-yn-1-aminium bromide (229)**

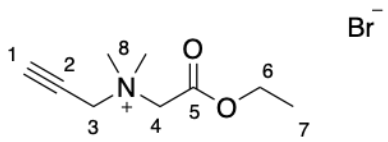

N,N-Dimethylglycine ethyl ester (3.99 g, 30.41 mmol) was dissolved in anhydrous THF (30 mL). Propargyl bromide (2.94 g, 20.00 mmol) was added dropwise over 2 min and the reaction mixture was stirred at r.t. for 18 h. The resulting solid was extracted by filtration and washed repeatedly with Hexane before being dried under reduced pressure to yield the title compound as white solid (4.78 g, 96%). ^{1}H NMR (400 MHz, DMSO) δ 4.62 (d, *J* = 2.6 Hz, 2H, H-3), 4.54 (s, 2H, H-4), 4.25 (q, *J* = 7.1 Hz, 2H, H-6), 4.16 (t, *J* = 2.5 Hz, 1H, H-1), 3.30 (s, 6H, H-8), 1.26 (t, *J* = 7.1 Hz, 3H, H-7). ^{13}C NMR (101 MHz, DMSO) δ 165.5 (CO), 83.5 (C), 72.2 (CH), 62.7 (CH_2), 60.5 (CH_2), 57.1 (CH_3), 52.3 (CH_2), 9.7 (CH_3). HRMS (ESI) *m/z* calcd for $C_9H_{16}N_1O_2$ $[M]^+$, 170.1176 found 170.1194.

Cllickable levofloxacin (synthesised by Dr Francesco Zamberlan)

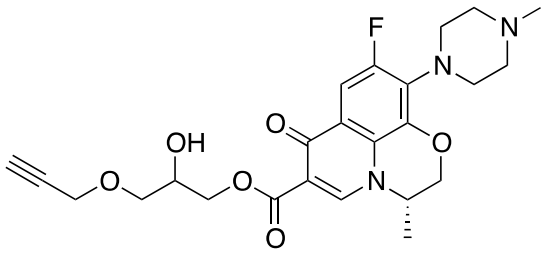

Levofloxacin (0.1 g, 0.277 mmol) was suspended in toluene (5 ml) in a microwave sealable flask. Propargyl glycidyl ether (2 eq., 74 ul, 0.553 mmol) and two spatula tips of tetrabutylphosphonium bromide (around 5 mol %) were then added, and the flask was sealed and refluxed overnight. The solution became clear and transparent. The reaction was monitored via TLC (9:1 DCM/MeOH with 3% ammonia in methanol) and MS. Upon completion, the reaction was worked up: ethyl acetate (10 ml) was added, and the solution washed once with sodium bicarbonate saturated solution (10 ml). The water phase was extracted twice with ethyl acetate (10 ml), dried over anhydrous magnesium sulfate and concentrated in vacuo, to yield 0.171 g of crude. This was purified by column chromatography and HPLC, to obtain 3.8 mg of pure product.

^{1}H-NMR (400 MHz; CD_3OD, d): 8.75 (s, 1H), 7.58 (d, 1H), 4.65 (m, 1H), 4.54 (m, 1H) 4.40 (m, 2H), 4.29 (m, 1H), 4.24 (d, 2H), 4.12 (m, 1H), 3.68 (d, 2H), 3.48 (br d, 4H), 2.89 (m, 5H), 2.57 (s, 3H), 2.17 (s, 1H), 1.55 (d, 3H).

^{13}C-NMR (101 MHz; $CDCl_3$, d): 173.0, 166.2, 156.9, 154.5, 145.3, 139.5, 131.9, 123.8, 123.1, 109.7, 105.3, 79.5, 74.8, 70.7, 68.4, 68.1, 66.7, 58.7, 55.7, 54.8, 50.6, 46.4, 29.7, 18.3.

HRMS (ESI): $[M+Na]^+$ calcd for $C_{24}H_{28}FN_3NaO_6$, 496.1854; found, 496.1852.